Spin Density Matrix Element Extraction for the ρ^0 Vector Meson on Hydrogen and Deuterium Targets at HERMES

Craig Shearer

Doctor of Philosophy Thesis

University of Glasgow

Faculty of Physical Sciences

Department of Physics and Astronomy

Nuclear Physics Group

September 2005

Abstract

The HERMES experiment in Hamburg, Germany, consists of a large forward spectrometer which studies various physics processes related to the nucleon and its internal structure. The main focus of the analysis presented in this thesis is based on the angular decay distributions of the decay products of the ρ^0 vector meson. By examining the angular decay of the outgoing decay products the Spin Density Matrix Elements (SDMEs) for the ρ^0 can be determined. The extraction of the ρ^0 data sample from the raw HERMES output data is explained and the method used to extract exclusive, diffractive ρ^0s is given. The analysis procedure and the method used to analyse the data samples is then explained with consideration given to the description of the method used to extract the spin density matrix elements.

In the autumn of 2005 a new detector known as the Recoil Detector will be commissioned in the front region of the HERMES experiment. The Recoil Detector will advance the analysis presented in this thesis in some regards, ie the improved t-resolution at low t which will improve exclusive measurements including vector meson production. Several contributions to the Recoil Detector are presented in detail. In particular the research of the HELIX128-3.0 readout chip and its development towards the final readout of the silicon detector and the integration of the Recoil Detector into the Hermes Monte Carlo.

Contents

List of Tables

List of Figures

Chapter 1

Introduction

The HERMES experiment which is based in Hamburg, Germany, consists of a large forward Spectrometer which studies various physics processes related to the nucleon and its internal structure. The second chapter introduces the experimental apparatus and its components in some detail.

In the Autumn of 2005 a new detector known as the Recoil Detector will be commissioned in the front region of the HERMES experiment. The main aim of the Recoil Detector is to measure exclusive physics events and to improve the experimental resolution of t, the four momentum transfer to the target, which is currently limited by the forward spectrometer. Using the Recoil Detector to analyse reactions such as DVCS (deeply virtual compton scattering) and Meson Production, access to different combinations of GPDs will be possible. The improved t resolution will allow a t-dependance of such processes to be measured which at present is not feasible.

Chapter three will present the components which comprise the Recoil Detector in some detail. In chapter four special attention is given to the research done on the HELIX128-3.0 readout chip and its development towards the final readout of the silicon detector. In chapter five the integration of the Recoil Detector into the Hermes Monte Carlo is explained with details on the modifications and development of the code given in considerable detail.

The physics analysis undertaken as part of this research is presented in the concluding chapters. The main focus of the analysis presented in this thesis is based on the angular decay distributions of the decay products of the ρ^0 vector meson. By examining the angular decay of the outgoing decay products the Spin Density Matrix Elements (SDMEs) for the ρ^0 can be determined. Chapter six introduces the physics theory and theoretical models used in this analysis, the kinematical variables used later are also described and defined. In chapter seven the data structures and experimental basis on which the analysis relies is presented with the Monte Carlo used in this analysis being described and shown in some detail.

The extraction of the ρ^0 data sample from the raw HERMES output data is explained and the method used to extract exclusive, diffractive ρ^0s is given in chapter eight. The analysis procedure and the method used to analyse the data samples are then explained with consideration given to the method used to extract the spin density matrix elements.

The results and values obtained for different data samples are then presented, both for hydrogen and deuterium targets. In this analysis all 23 polarised spin density matrix elements in a single, average Q^2 are extracted and presented. The 15 unpolarised matrix elements are also extracted in 4 different Q^2 bins allowing a Q^2-dependence to be observed for the 15 unpolarised matrix elements.

In chapter nine, conclusions are presented and the relevance of the results obtained in the analysis are drawn.

Chapter 2

The HERMES Experiment

The HERMES Experiment is located at the Deutsches Elektronen Synchrotron (DESY) in Hamburg, Germany. The experiment is situated in the eastern part of the HERA (Hadron-Elektron Ring Anlage) collider ring, which has a circumference of 6.3 km. The collider consists of two storage rings with counter-rotating beams of protons and positrons (or electrons). The proton beam has an energy of 920 GeV since 2001 and the positron beam an energy of 27.5 GeV. In the years analysed in this thesis the lepton beam was a positron beam. In figure 2.1 is a schematic diagram of the layout of the HERA facility. The ZEUS and H1 experiments, which are also on the ring, analyse reactions produced by colliding positrons and protons together, in order to study the structure of the proton over a wide kinematical range in unpolarised deep inelastic scattering. HERA-B, when it was operational, studied CP-violation in B-Meson production by colliding the proton beam with a thin metal wire target which was introduced into the beam.

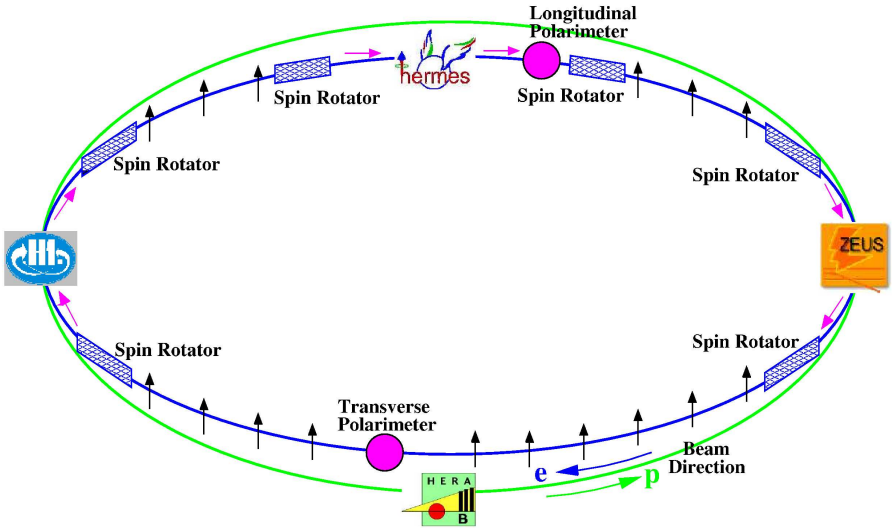

Figure 2.1: Schematic overview of the HERA collider ring at DESY

The HERMES experiment was designed for measurements of the spin structure functions of the proton and neutron by the analysis of inclusive and semi-inclusive spin asymeteries in polarised deep inelastic lepton-nucleon scattering. It utilises the longitudinally po-

larised, circulating HERA positron beam in combination with a longitudinally polarised internal gas target. The HERMES forward spectrometer is optimised for the detection of semi-inclusive events. Semi-inclusive events are those in which both the scattered lepton and hadrons are detected. Apart from the wide acceptance the experiment also has excellent particle identification abilities. HERMES also allows the option to use a variety of unpolarised gas targets rather than just the polarised gas target in order to study hadronisation in nuclei and nuclear effects in lepton-lepton scattering.

2.1 Polarised Beam

The lepton beam is initially unpolarised when it is injected into the HERA ring. However a transverse polarisation of the positron (electron) beam parallel (anti-parallel) to the magnetic dipole builds up naturally through the Sokolov-Ternov effect [1]; the circular motion of the positrons (electrons) accelerated in a synchrotron causes the charged leptons to emit synchrotron radiation. The emission of synchrotron radiation sometimes causes the leptons to flip their spins, resulting in a beam which has a transverse polarisation. The beam polarisation rises exponentially with time:

$$P = P_{max}(1 - e^{-t/\tau}) \tag{2.1}$$

where t is the time elapsed since the injection of the beam into the accelerator ring and τ is the so-called build up time, the time taken to reach $(1 - \frac{1}{e}) \approx 64\%$ of the maximum possible polarisation P_{max}. In an idealised accelerator in the absence of any depolarising effects, the maximum attainable polarisation is $P_{ST} = 92.4\%$ [2], with the build up time of τ_{ST}, where τ_{ST} is a property of the accelerator and is equal to 37 minutes for HERA at 27.5 GeV. P_{max} is then given by:

$$P_{max} = \frac{\tau}{\tau_{ST}} P_{ST} \tag{2.2}$$

Therefore P_{max} is a function of τ only, where τ depends on the many factors that affect the beam conditions such as the depolarising effects which are caused by horizontal magnetic fields, spin diffusion and depolarisation resonances that cause precession of the positron spin[3]. The average beam polarisation at HERA is about 55%, while the maximum polarisation reached is about 70%.

To obtain a longitudinal beam polarisation at HERMES, the transverse spin direction is rotated by 90° by a combination of magnets known as a spin rotator. A second spin rotator behind the experiment restores the transverse polarisation (figure 2.1).

2.2 Beam Polarimetry

In order to determine the degree of polarisation of the lepton beam, which is vital to the operation of the experiment, the longitudinal and transverse beam polarisations are measured by two Compton polarimeters situated close to the East and West halls respectively.

The design of the longitudinal polarimeter is based on the Compton scattering of circularly polarised photons on the longitudinally polarised beam. With fixed energies, the polarised Compton cross section depends on the longitudinal polarisation of the positron [4]:

$$\frac{d\sigma}{dE_\gamma} = \frac{d\sigma_0}{dE_\gamma}[1 - P_\lambda P_e A_z(E_\gamma)] \tag{2.3}$$

where $d\sigma_0/dE_\gamma$ is the unpolarised cross section, E_γ is the energy of the backscattered Compton photon, P_λ is the circular polarisation for the two helicity states $\lambda = \pm 1$, P_e is the longitudinal positron polarisation, and $A_z(E_\gamma)$ is the longitudinal asymmetry function. With the values of $d\sigma_0/dE_\gamma$ and $A_z(E_\gamma)$ well known, and with P_λ and E_γ fixed, $d\sigma/dE_\gamma$ is a function of longitudinal polarisation only.

Figure 2.2 shows the beam polarisation for one positron fill of the 1997 data taking period, measured with the transverse and longitudinal polarimeters. The polarisation quickly rises at the beginning and stays stable for the entire length of the fill.

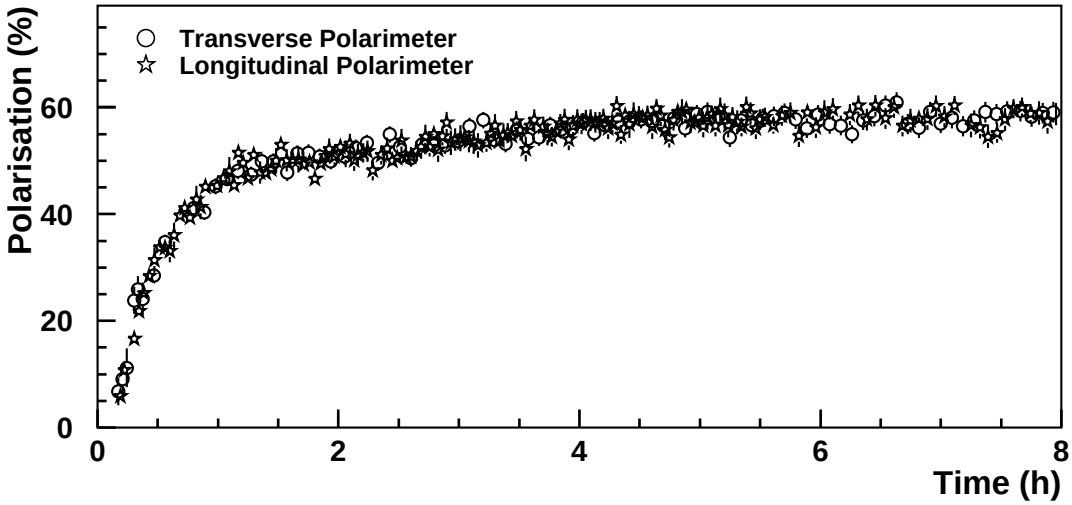

Figure 2.2: Polarisation of the HERA positron beam for one fill.

2.3 HERMES Internal Gas Target

HERMES uses an internal gas target, where the polarised target gas is injected into a windowless storage cell directly in the vacuum of the positron beam pipe. This technique has the advantage that a single atomic species at a high degree of polarisation is injected, free from dilution by material such as target windows. Polarised gas targets allow a rapid reversal of the polarisation state, reducing the systematic uncertainties of the asymmetry measurement. HERMES used a polarised Helium-3 target in 1995, and a polarised hydrogen target in 1996 and 1997. In 1998, 1999 and 2000 the polarised gas target was deuterium. In 1996-1997 the unpolarised gases were hydrogen (H_2) and deuterium (D_2) and for 1998, 1999 and 2000 the unpolarsised target gases used were also hydrogen (H_2) and deuterium (D_2). HERMES also has the option of using other, heavier, unpolarised gas targets such as Helium-3 (^3He) and Nitrogen (N_2), up to Krypton and Xenon.

Figure 2.3 shows a schematic view of the target region. The target gas is injected through a side tube into the middle of the storage cell that is a 400 mm long open-ended thin aluminium tube of elliptical cross section, confining the target gas around the beam. After the diffusion of the target gas to the ends of the cell it is pumped away by a differential vacuum pump system that maintains the ultra high vacuum in the beam pipe. A triangular density distribution of the target gas is generated by the equilibrium of the injection at the center and the diffusion to the ends of the storage cell, reflected by the shape of the z-vertex distribution which is shown in figure 2.4. A set of collimators in front of the target protects the target cell and the spectrometer from synchrotron radiation and secondary particle

showers. A thin 0.3 mm stainless steel exit window allows the scattered particles to emerge into the spectrometer. The gaps between the storage cell and the up- and down-stream end of the beam pipe are bridged by wake field suppressors to ensure the continuity of the beam enclosure, hence reducing radio frequency (RF) excitations induced by the bunch structure of the beam.

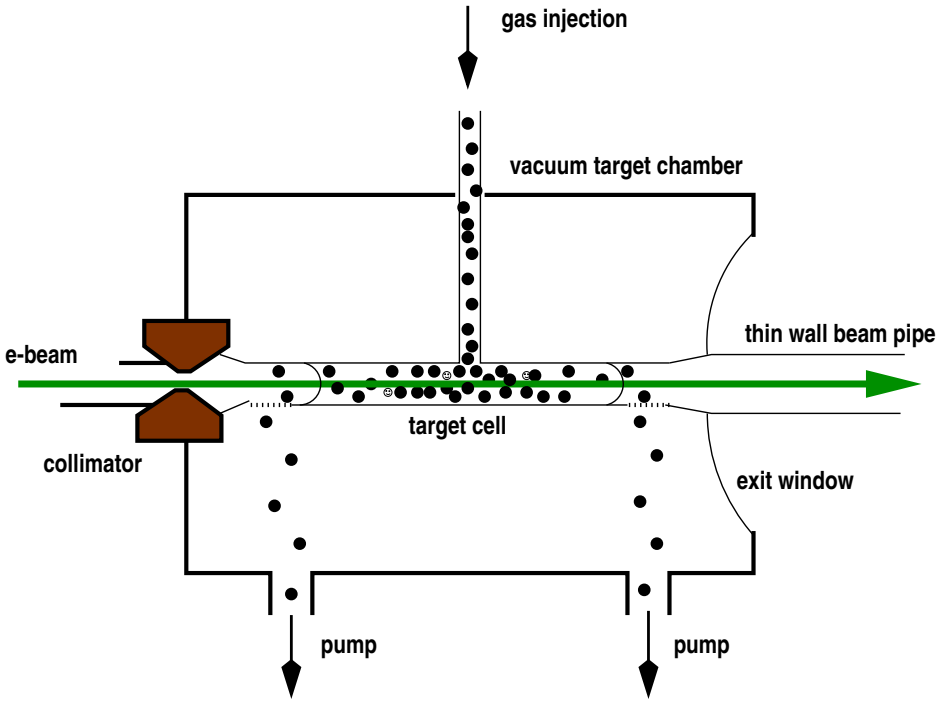

Figure 2.3: Schematic of the HERMES target region.

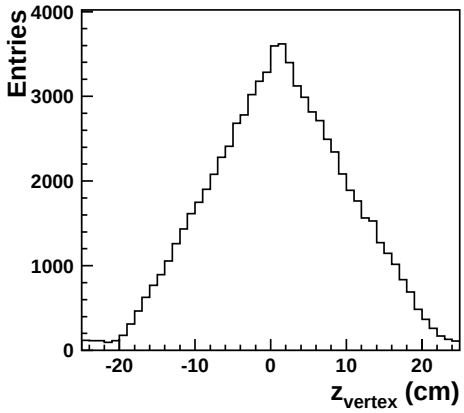

Figure 2.4: Z-vertex distribution in the target cell.

2.3.1 Polarised H-D Target

The polarised H-D target is shown in figure 2.5. The system consists mainly of an atomic beam source, the target analyser and the Breit-Rabbi polarimeter.

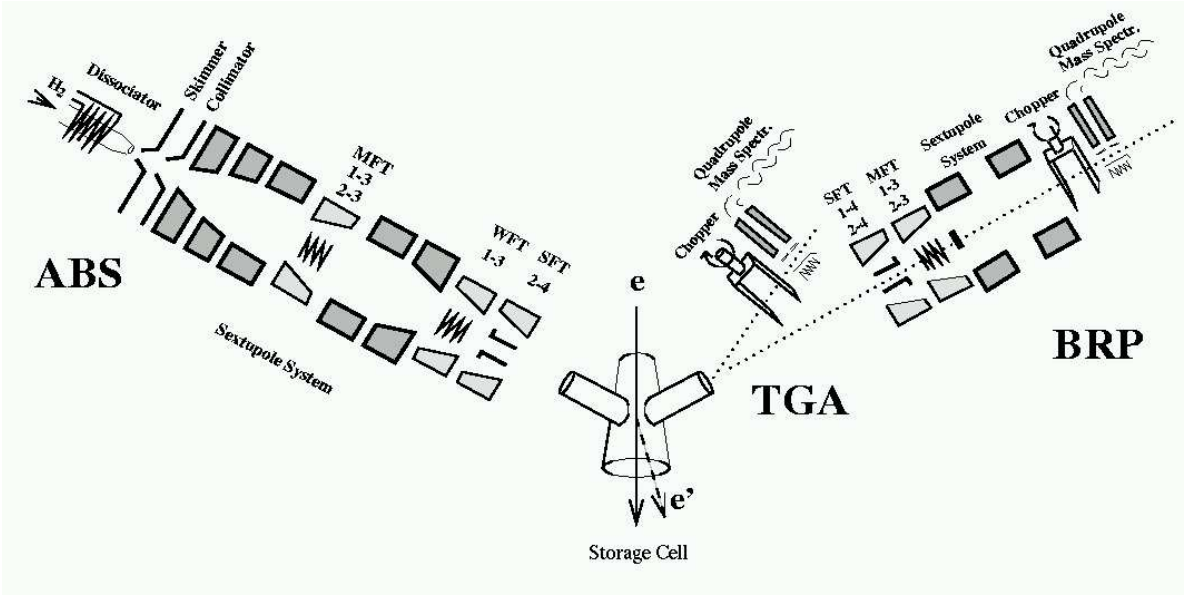

Figure 2.5: The polarised H-D target consisting of the atomic beam source (ABS), Breit-Rabi polarimeter (BRP) and the target gas analyser (TGA).

The polarised gas is provided by the atomic beam source (ABS) which makes use of Stern-Gerlach spin separation by multipole magnets. The molecular gas H_2 is dissociated by a 13.56 MHz RF discharge into H atoms. A cooled nozzle and skimmer form an atomic thermal velocity beam , which is fed through a system of five sextupole magnets. The upper hyperfine states $|1>$ and $|2>$ are focused by the magnets, while states $|3>$ and $|4>$ are deflected. The electron polarisation of the atomic beam is transferred to the protons by the means of adiabatic RF transitions, induced by units at the end of the magnet system. When the transition units are switched off the atomic beam was electron polarised only. A transition from state $|1>$ to $|3>$ provided negative nuclear polarisations, while the $|2>$ to $|4>$ transition gave positive polarisation. The polarised atomic beam is focused by the sextupole magnets into the entrance tube of the storage cell.

A superconducting magnet produces a 335 mT holding field providing the quantisation axis for the target polarisation. The storage cell is coated with a thin layer of ice in order to minimise randomisation of the nucleon spins or molecular recombination through interactions with the cell walls. The cell temperature is kept at 100 k which is the lowest temperature possible without causing substantial degradation of polarisation and increased recombination while maximising the target density [5].

The target polarisation is monitored by the Breit-Rabi polarimeter (BRP). A gas sample from the middle of the storage cell diffuses into an extraction tube, which feeds the sample through a system of transition units and sextupole magnets. The sextupoles remove the states with the negative electron spin projection, $|3>$ and $|4>$, from the gas sample while states $|1>$ and $|2>$ remain in the beam and are seen by an atomic beam detector. The atomic beam detector consists of a chopper and a quadrapole mass spectrometer. Switching on certain certain RF transitions therefore changes the beam flux. The four hyperfine states defining the nuclear and electron polarisation could be determined from combining measurements with different RF transitions switched on [6].

A target gas analyser (TGA) with a mass spectrometer determines the relative amount of molecular and atomic hydrogen in the target cell. The target polarisation P_T is calculated using the following expression:

$$P_T = \alpha_0(\alpha_r + (1-\alpha_r)\beta)P_T^{atom} \tag{2.4}$$

where α_0 is the initial atomic fraction of 0.99± 0.01(syst), α_r is the fraction of hydrogen atoms that do not recombine in the target cell, and $(1-\alpha_r)$ is the fraction of recombined molecules with relative polarisation β. Since the target gas is not analysed from directly within the target cell, small Monte Carlo corrections have to be applied to the measurements of the BRP and the TGA [7]

2.3.2 Unpolarised Target

The unpolarised gas feed system (UGFS) is a simple device, where the target gas is simply blown into the target cell. The gas target allows a fast exchange of the target material and at least two target gases were alternated on an hourly basis to reduce the uncertainty in the relative normalisation. The density of the polarised hydrogen gas target is restricted by the intensity of the polarised source. In contrast, the density of the unpolarised target, is restricted only by the fact that the reduction in the beam life time must not exceed a certain limit if the unpolarised measurements are being performed in parallel to other HERA experiments. In the case of dedicated HERMES data taking, the target density is mainly restricted by the maximum throughput of the data acquisition system (DAQ).

2.4 The HERMES Spectrometer

The HERMES experiment uses an open magnet spectrometer [8] shown in figure 2.6. The experiment is split into a symmetric upper and lower half by the positron and proton beam lines. A dipole spectrometer magnet provides an integrated field strength of 1.3 Tm. A large iron plate shields the beams as they travel through the magnet. This large plate determines the acceptance of the spectrometer at low scattering angles. The vertical and horizontal acceptances of the detector cover $40 < |\theta_y| < 140$ mrad and $|\theta_x| < 170$ mrad respectively. Positrons incident on the target gas are scattered into the acceptance of the HERMES detector where they are tracked and the identities of the detected particles determined.

2.4.1 Tracking Detectors

As the scattered particles pass through the detector their paths have to be determined. The tracking of particles is performed by wire chambers, each of which reacts to the passage of particles through one of its channels with an electrical signal.

The wire chambers are high voltage devices with an array of wires spanning the inside of each chamber. An electric field is formed within the chamber as a result of the potential difference between the anode wires and cathode planes. Passage of particles through the gaseous medium between the wires ionises the gas which creates a signal within the neighbouring wires. The wire chambers themselves contain many wires, usually with a least two wire planes, where the planes are at angles to one another in a grid pattern. The location of a particle within the chamber is established by the presence of an electric signal from two (or more) wires in different planes. Based on the mechanism of the electric field distortion, several types of wire chambers exist[9]. At HERMES, proportional and drift chambers are the two types which are used.

In a proportional wire chamber, a particle that enters the chamber ionises the gas mixture within the chamber. The resulting free charges drift to the oppositely charged electrodes, the electrons drifting to the anodes, the positive ions drifting to the cathodes.

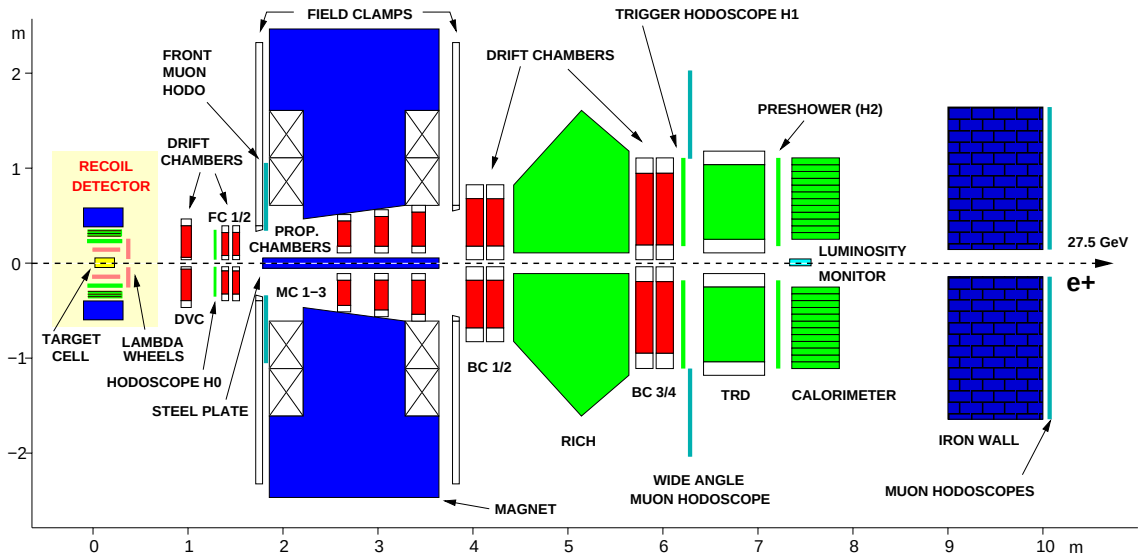

Figure 2.6: The HERMES spectrometer with the Recoil Detector position illustrated.

When the electrons' proximity to the wires increases the drifting electrons are accelerated by the intense electric field. The acceleration of the electrons ionises the gas medium surrounding them, which produces more drifting electrons which in turn also ionise the medium. In this way the initial electron incident on the drift chamber produces an avalanche of ionisation within the chamber. In a proportional chamber the rate of multiplication, and therefore the net current, is proportional to the energy deposited by the incident charged particle. The proportional chambers used at HERMES are the Magnet Chambers (MC) located inside the magnet, and the readout chambers of the TRD.

In a drift chamber, the particle incident upon the detector also ionises the gas mixture within the detector. However, unlike the proportional drift chamber the total electron drift time within the chamber is used to locate the track of the particle. Measurement of the length of the drift time within the chamber allow the distance of the particle from the wire to be determined, assuming that the speed is constant. Most wire chambers at HERMES are drift chambers rather than proportional wire chambers. The drift chambers used at HERMES are: the Drift Vertex Chambers (DVC), a pair of Front Chambers (FC) which are in front of the magnet and four Back Chambers (BC) which are behind the magnet. For a period in 1997 the Vertex Chambers (VC) were also installed in the experiment [10]. In this analysis the Vertex Chambers were not used in the event reconstruction.

2.4.2 Trigger Hodoscopes

The trigger is an electrical signal supplied to the data acquisition system when a physics event of interest is detected. Arrays of scintillators, referred to as hodoscopes (figure 2.6) are used as the triggers. As particles pass through the scintillating material of the hodoscopes light is scintillated by the particle. The array of narrow scintillators provides a fast detector response to the particle. At HERMES energies the intensity of the light produced depends linearly on the energy deposited by the particle.

The optical response in each scintillator within a hodoscope is transformed into an electrical signal by a Photo Multiplier Tube (PMT). The anode current of the PMT depends linearly on the light intensity at the photocathode.

Three hodoscopes, H0, H1 and H2(the preshower detector), are currently used in the HERMES experiment. H2 is used as a Particle Identification (PID) detector.

2.5 PID Detectors

The HERMES spectrometer provides an excellent positron-hadron separation using four Particle Identification (PID) detectors: the Transition Radiation Detector (TRD), the Preshower detector (H2), the electromagnetic calorimeter and for 1995-1997 the Cerenkov Detector and for 1998 onwards the Ring Imaging Cerenkov (RICH) detector. Each of the four detectors is able to differentiate between hadrons and positrons, however each detector varies with regard to its relative effectiveness to do so. In order to improve the separation of the hadron and positrons the hadron-positron identification for each of the four detectors are combined.

2.5.1 The Threshold Cerenkov Detector

Cerenkov Radiation is emitted in a medium by a particle whose velocity exceeds the speed of light in that medium. For optical density (index of refraction) n, the threshold function is given by [11]:

$$N_0 = C_0\big(1 - \frac{1}{(n\beta)^2}\big) \tag{2.5}$$

where C_0 is a constant. β is defined for a particle i with a rest mass M_i as:

$$\beta_i = \frac{v_i}{c} = \frac{p_i}{E_i} = \frac{p}{\sqrt{M_i^2 + p_i^2}} \tag{2.6}$$

With background noise subtracted N_0 is equal to the number of Cerenkov photoelectrons. Due to the fact that the mass of the positron is much smaller than that of the pion (the lightest hadron), the value $(1 - 1/\beta^2)$ is much larger for positrons. For n close to 1, this implies that the yield depends on the particle mass. For a given n it is possible to compute the threshold momentum above which the particle emits Cerenkov radiation. The values of threshold momentum for the positron and pion define the lower and upper bounds of the operational momentum range, respectively. Within the operational range, such that separation between positrons and hadrons is possible, only positrons emit Cerenkov radiation.

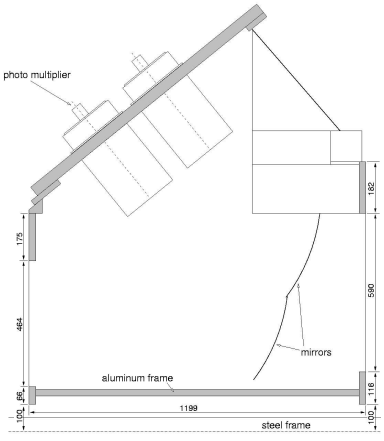

Figure 2.7: Side cross-section of the top half of the Cerenkov detector. The upper and lower halves of the Cerenkov are identical.

The Cerenkov detector used at HERMES in 1995-1997 (figure 2.7), contained a mixture of C_4F_{10} (30 %) and N_2 (70 %) gases at atmospheric pressure. The index of refraction for the mixture was n =1.0066181. The resulting operational momentum range is 0.014 to 3.9 GeV. In addition, pion-kaon and kaon-proton separation is also possible for momentum ranges between 3.9 and 13.6 GeV and 13.6 and 25.8 GeV respectively. Separation between positrons and hadrons in the Cerenkov detector is shown in figure 2.8.

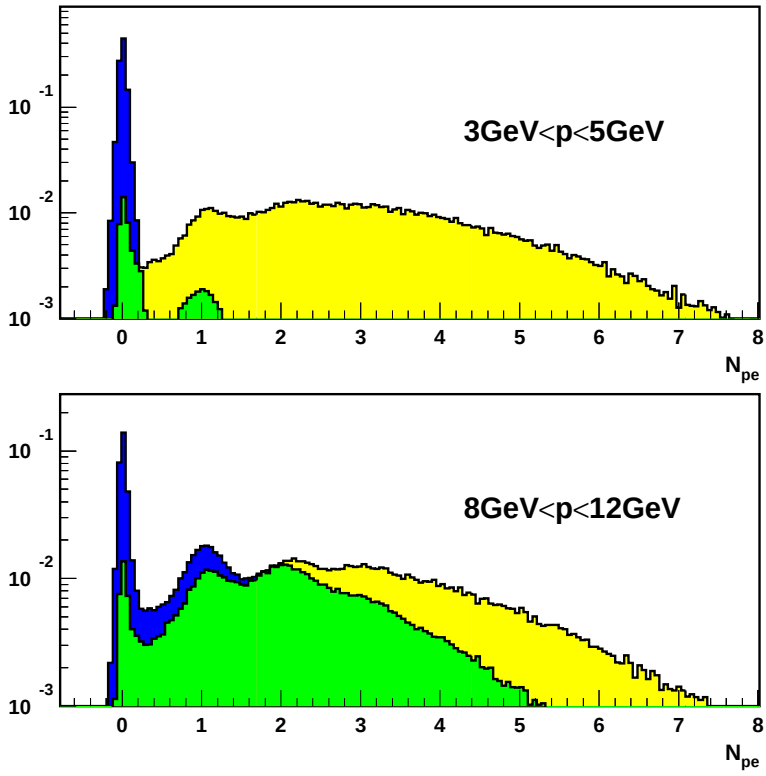

Figure 2.8: Photoproduction response of the Cerenkov detector below and above the pion threshold. Light and Dark shading represent positron and hadron distributions respectively. The intermediate shading represents the region where the two distributions overlap. Good positron-hadron separation exists only below the threshold.

2.5.2 The Ring Imaging Cerenkov Detector

During the shutdown in 1998 the threshold Cerenkov counter was replaced by a Ring Imaging Cerenkov (RICH) detector. The RICH consists of two symmetric halves located above and below the HERA beamline. A schematic of one half of the detector is shown in figure 2.9. It shows the detector body containing the aerogel radiator directly behind the entrance window, a reflecting mirror system and a photomultiplier (PMT) matrix on top. The geometrical design of the RICH was constrained by the requirement that it had to fit into the position which the Cerenkov detector previously occupied. The body of the detector is constructed of aluminium and has a volume of around 4000 l. The entrance and exit windows are made of 1 mm thick aluminium. The main volume is filled with C_4F_{10} radiator gas which is slightly above atmospheric pressure. The segmented mirror section is made from 8 parts (2 rows of 4) and has a radius of 2.20 m.

The RICH was designed to cover the momentum range for hadrons (π, K and p) between around 2 and 15 GeV. To cover this momentum range a dual radiator is used: a C_4F_{10} gas

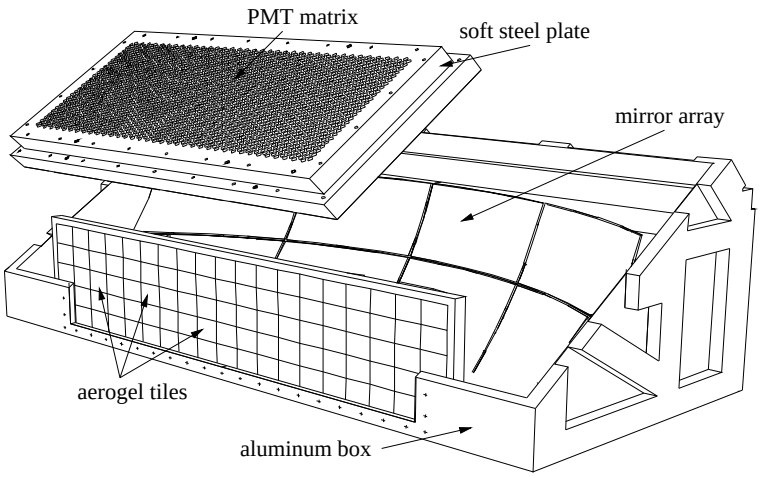

Figure 2.9: Cutaway drawing of the RICH. The aerogel radiator at the entrance of the detector, the segmented spherical mirror and the PMT matrix mounted on top can be seen.

radiator and a clear silica aerogel radiator wall. The Cerenkov angles for both are shown in figure 2.10. The gas with an index of refraction 1.00137, covers the PID in the higher momentum range above about 10 GeV and gives a pion, kaon and proton threshold of 2.7, 9.4, and 17.9 GeV respectively. The aerogel takes up the PID in the low momentum region between roughly 2 and 10 GeV. For this reason the index of refraction for the aerogel was chosen to be about $n = 1.03$, leading to a pion, kaon and proton threshold of 0.6, 2.0 and 3.8 GeV respectively.

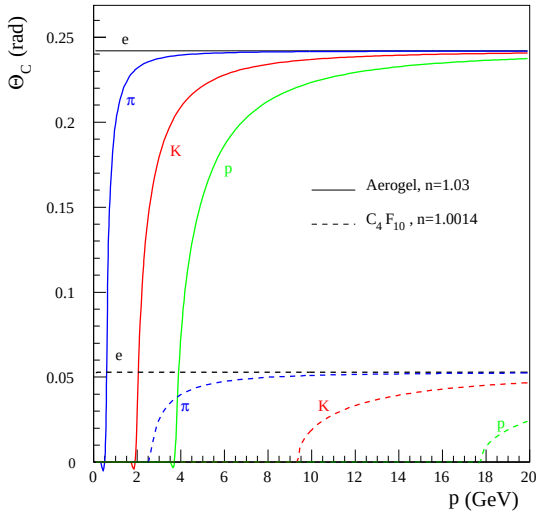

Figure 2.10: The Cerenkov angle as a function of the particle momentum for e, π, K and p for the aerogel and the gas radiators.

For the hadron identification, the threshold behaviour in the two radiators as well as the information of the photon angles are used. Cerenkov photons are emitted in a cone around the particle trajectory with an opening angle:

$$\cos\theta_c = \frac{1}{\beta n}. \tag{2.7}$$

2.5.3 The Transition Radiation Detector

Transition Radiation (TR) is emitted by charged particles that cross a boundary between two media which have different dielectric constants. Usually TR belongs to the X-ray region of the electromagnetic spectrum. The probability for a particle to emit a photon per interface is approximately $\frac{2}{3}\alpha$, where $\alpha = 1/137$ is the fine structure constant. In the ultra-relativistic regime, the mean energy W of the emitted TR caused by the passage of a particle i from vacuum into a medium with plasma frequency ω_p depends linearly on $\gamma = E_i/M_i$ [12]:

$$W = \frac{2}{3}\alpha\omega_p\gamma. \tag{2.8}$$

The plasma frequency in a material is a function of its electron density n_e:

$$\omega_p = 4\pi\alpha\frac{n_e}{M_e} \tag{2.9}$$

where M_e is the rest mass of the electron. Since γ is much higher for positrons than for hadrons, the dependence of the TR energy yield on γ is a useful property for differentiating between positrons and hadrons.

From 2.8 and 2.9 it can be shown that the optimal radiator material should have a high electron density. In order to increase the probability of TR emissions in the HERMES TR Detector (TRD), multiple boundaries are necessary. The material should also be highly transparent to the X-rays. These requirements are satisfied by a polypropylene radiator. The choices of fibre thickness (17-20 μm) and packing density (0.10 g/cm^3) of this porous material are optimised for the electron energy range of the experiment [10]. The bulk thickness of the radiator is limited by the X-ray absorption and is chosen to be 6.5 cm.

In addition to the radiator described above, the HERMES TRD contains planar proportional wire chambers as X-ray detectors (there are a total of 12 MWPCs). For optimal X-ray absorption, a high Z gas is required. For this reason the wire chamber is filled with a mixture of Xenon (90%) and CH_4 (10%) gas. CH_4 is used as a quenching agent to control the electron multiplication in the chamber.

A radiator and a wire chamber constitute one module of the TRD. Each half of the detector consists of 6 such modules used in succession (figure 2.11). When particles ionise the medium, secondary high energy electrons are frequently produced. These are known as δ-rays and constitute the background to the TRD signal. Use of several modules in succession permits a module by module comparison of energy deposition, which in turn allows the elimination of the majority of the δ-rays. A truncated mean method may be used for illustration: since δ-rays are characterised by high energy deposition the module with highest energy deposition is excluded from the calculation of the mean value of energy deposition for each hit. As shown in figure 2.12, use of the 6 module and the truncated mean method improves the positron-hadron separation.

2.5.4 The Preshower Detector

Energy loss per unit thickness dE/dz is significantly higher for positrons than for hadrons: in addition to collisions with electrons within the material, a significant portion of the energy is lost through radiation [9]. At HERMES energies where the radiative energy loss dominates, the radiated photons are sufficiently energetic to produce e^+e^- pairs. These

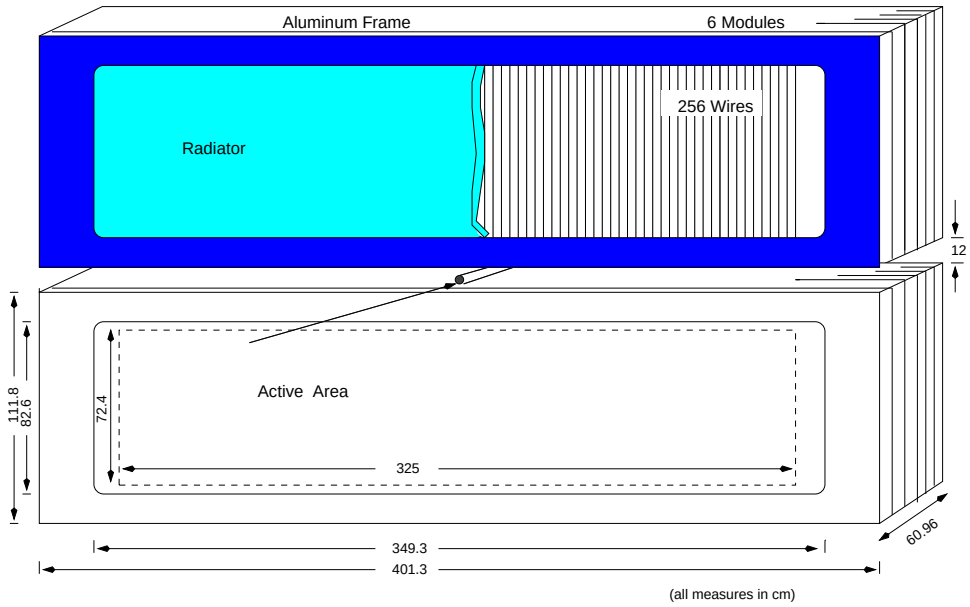

Figure 2.11: Schematic view of the TRD.

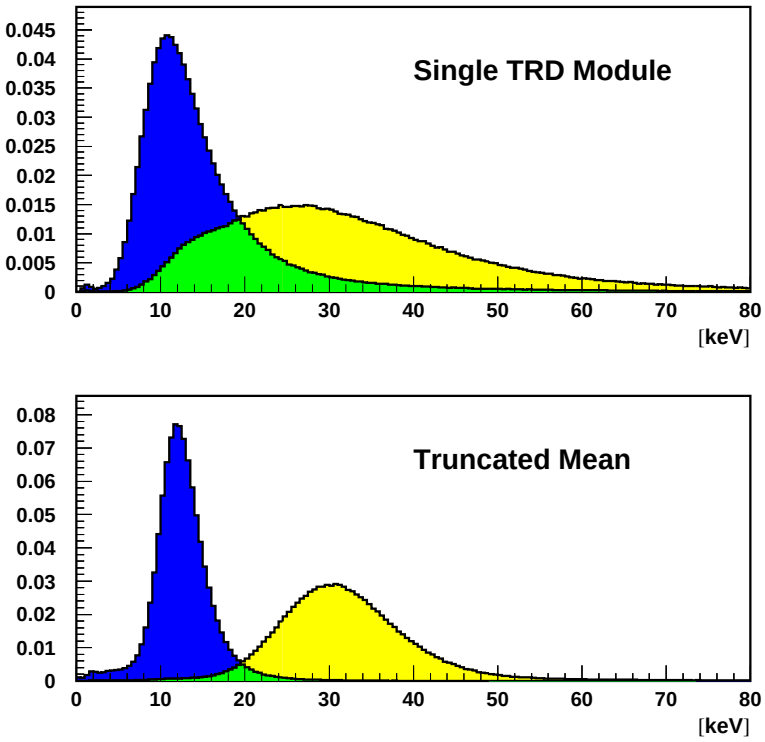

Figure 2.12: Response of the TRD detector for a single module and with the truncated mean. Light and dark shading shading represents positron and hadron distributions respectively. The intermediate shading represents the region where the two distributions overlap [13].

pairs also radiate, with subsequent pair production. Rapid multiplication of the numbers of electrons and positrons occur and an electromagnetic shower is produced. With a suffi-

ciently thick material of high Z it is possible to use the high dE/dz for positrons to initiate an electromagnetic shower. This principle is used in the preshower detector at HERMES which consists of 42 plastic scintillator bars (figure 2.13).

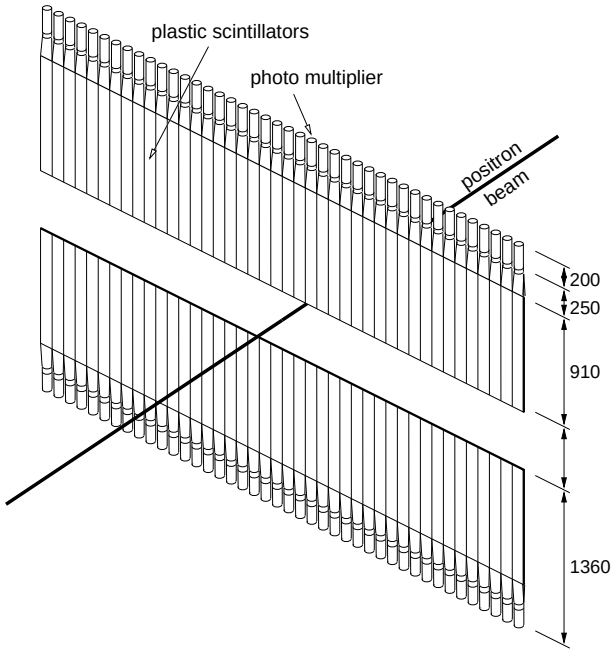

Figure 2.13: Schematic diagram of the preshower detector.

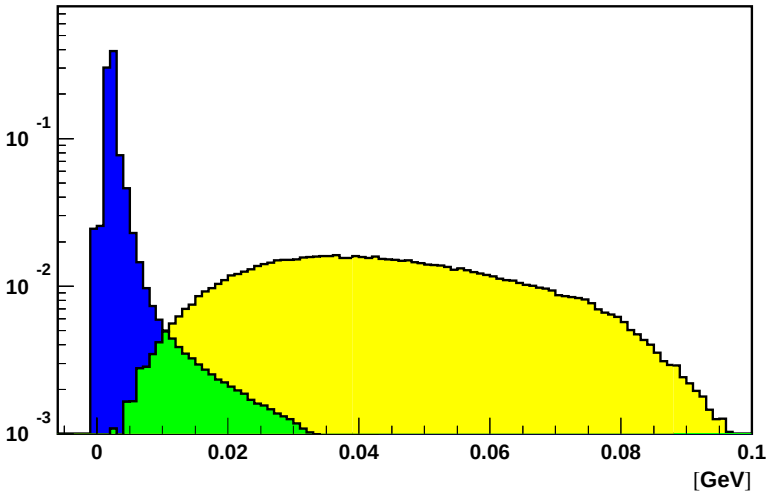

Figure 2.14: Normalised response of the preshower detector. Light and dark shading represents positron and hadron distributions respectively. The intermediate shading represents the region where the two distributions overlap.

An 11 mm thick plate of lead, placed immediately before hodoscope H2, is two radiations lengths thick. That is, the original positron would retain, on average, only $1/e^2$ of its initial energy as it leaves the plate. The remaining energy is contained in the electromagnetic shower, which propagates to the scintillators of the hodoscope. In this way, a parent positron registers a large net multi-particle signal from the shower in the hodoscope,

whereas a hadron leaves the lead plate without producing a shower and registers a single particle signal of smaller amplitude. The response of the preshower detector is shown in figure 2.14.

2.5.5 The Electromagnetic Calorimeter

The HERMES electromagnetic calorimeter, which is constructed from lead glass blocks, is able to fully contain an electromagnetic shower. With a calorimeter of sufficient thickness the electromagnetic shower is able to progress until all positrons and electrons are of such low energy that they no longer radiate, but interact through ionisation of atoms which eventually causes them to stop.

This leads to a ratio of $E_{calo}/p \simeq 1$ for positrons at HERMES energies, where E_{calo} is the energy deposition in the calorimeter, and p is the momentum of the positron measured by analysing the degree of track deflection by the magnet.

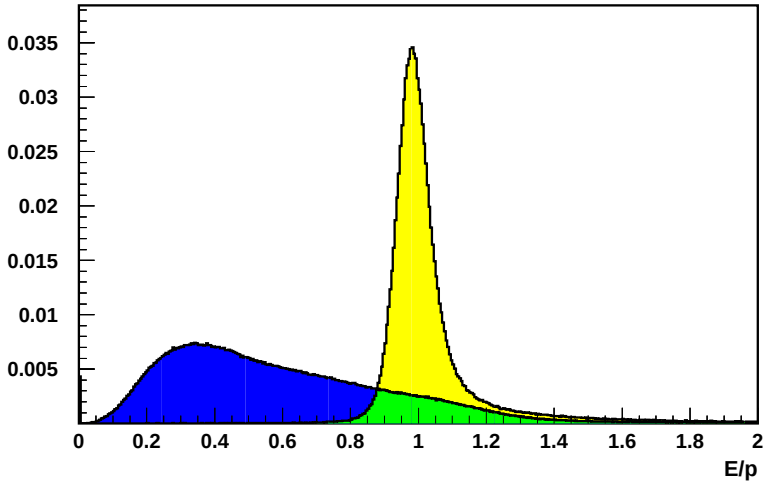

Figure 2.15: Normalised response of the calorimeter. Light and dark shading represents positron and hadron distributions respectively. The intermediate shading represents the region where the two distributions overlap.

The behaviour of hadrons within the calorimeter is different, since they lose energy through ionising atomic collisions and through nuclear interactions only. The hadrons may still produce other particles as a result of collisions within the material, which may result in further hadron production and emission of photons. The photons and neutral pions create e^+e^- pairs, and electromagnetic cascades result. The entire process of multiple particle creation as a result of interaction of hadrons with matter, known as a hadronic shower, does not begin immediately in the calorimeter and is often not fully contained within the calorimeter. Due to loss of neutrons and nuclear binding energy $E_{calo}/p < 1$ for hadrons.

The different behaviour of positrons and hadrons in E_{calo}/p in the calorimeter allows a good degree of separation between the two (figure 2.15). The HERMES calorimeter (figure 2.16) contains 420 cells in each half of the detector. The cells, which are square in cross section, are constructed from a glass made of 51.23% Pb_3O_4, 41.57% SiO_2, 7% K_2O and 0.2% Ce in weight proportions. The glass blocks have a radiation length of 2.78 cm and an index of refraction of 1.65 [14]. With cell dimensions of 9×9×50 cm, each cell is 18 radiation lengths thick. As the shower is quenched in the cells, particles emit Cerenkov radiation which is detected by the PMT tubes. Each cell is coupled to a photomultiplier tube thereby forming a total of 840 channels. Due to the fact that showers may extend

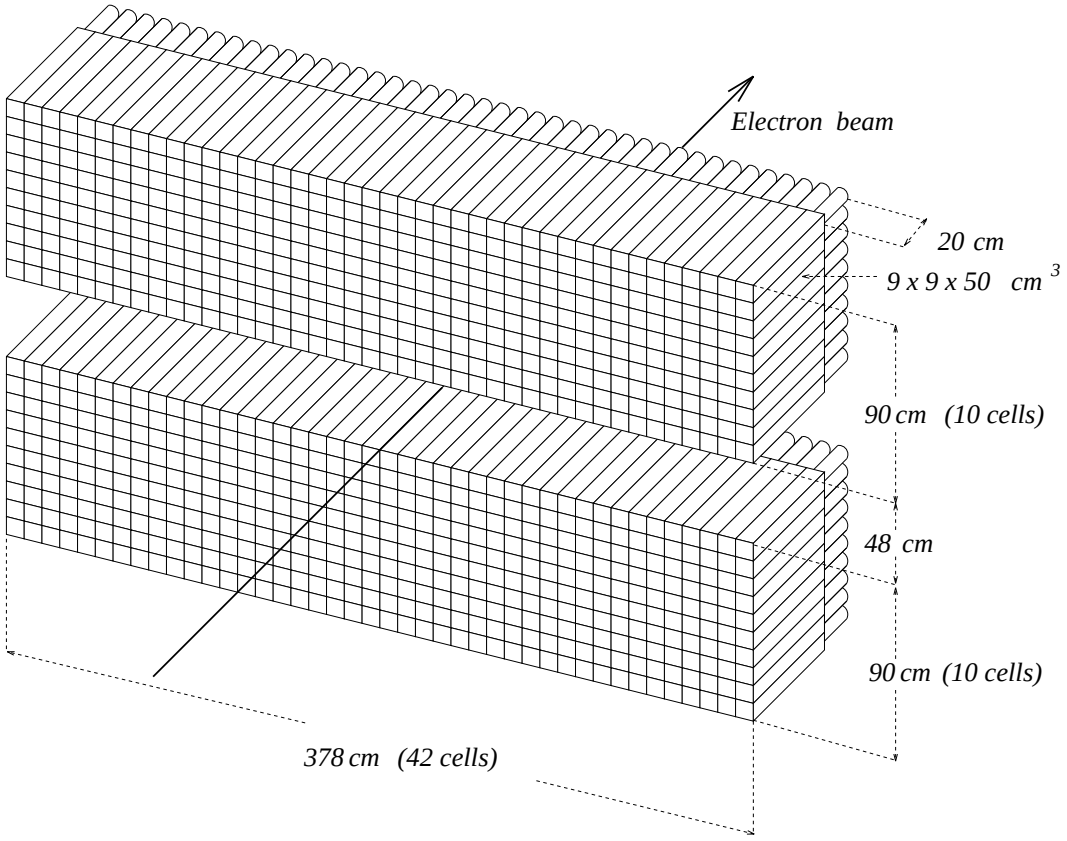

Figure 2.16: Schematic diagram of the HERMES electromagnetic calorimeter.

over adjacent cells the measurements are summed over a 3×3 block array with the centre of the shower in the middle of the block with the most energy.

2.6 The Luminosity Monitor

The luminosity is a characteristic quantity which represents the product of the beam flux and the surface target density. At HERMES the luminosity is measured by means of a luminosity monitor [15](figure 2.17). The luminosity monitor consists of a calorimeter made from 24 radiation hard $NaBi(WO_4)_2$ blocks, with each block coupled to a photomultiplier tube. Since it is not possible to place a detector directly into the beam, the luminosity is measured indirectly by accessing the rates of Bhabha scattering $e^+e^- \rightarrow e^+e^-$ from the atomic electrons in the target gas, which is related to the beam luminosity through:

$$R = L\sigma \tag{2.10}$$

where L, R and σ denote the luminosity, the process rate and the Bhabha cross section respectively. The luminosity is related to the beam current I and the surface density of the target ρ through:

$$L = \frac{I\rho}{e} \tag{2.11}$$

where e is the elementary charge.

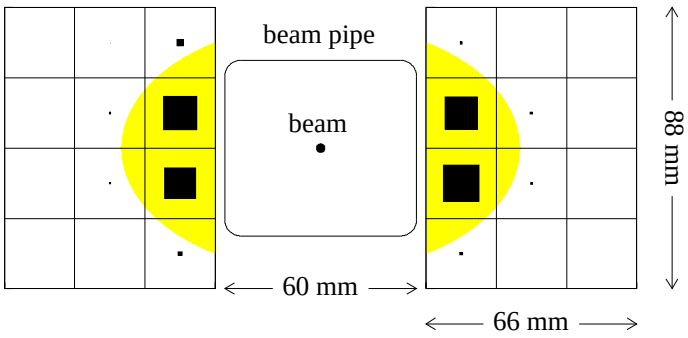

Figure 2.17: Front view of the luminosity monitor, with the shaded region showing the detector acceptance.

2.7 Data Acquisition

The HERMES data acquisition system is based on FastBus, using two CERN host interfaces as bus masters. All drift chambers are read out by FastBus TDC's (time to digital converters), while the vertex and magnet chambers are read out by a PCOS IV system that allows only one bit per channel. All photomultipliers and the TRD photon detectors are read out by ADC's (analogue to digital converters). In addition, trigger hodoscopes are read out by TDC's to allow time of flight determination. The electronics are located in a trailer separated by a shielding wall from the experiment. During a fill of the positron beam that typically lasts for around 8 hours, the data is written onto staging disks in the online computer system. Once the fill has ended the data is transferred by a FDDI link to a tape robot at the DESY main site and a backup is written to local DLT tapes. The HERMES data acquisition is capable of reading out the detector information at rates up to 500 MHz with dead times below 10%.

Chapter 3

The HERMES Recoil Detector

In the autumn of 2005, a new upgrade to the HERMES experiment will be installed. The new apparatus is known as the Recoil Detector. The Recoil Detector will bring several improvements to the current setup. Exclusivity will be determined on an event level, that is, the non-exclusive background levels will be reduced to below 1%. At present the energy and position resolution of the HERMES spectrometer is limited and exclusivity can only be determined for a data sample and not for individual events. A second advantage which the Recoil Detector will have is that it will improve the t resolution of the experiment, where t is related to the four momentum of the recoil proton and the target proton, $t = (p' - p)^2$. At present the resolution in t provided by the spectrometer is only 0.17 GeV^2 for BH/DVCS (Bethe-Heitler/Deeply Virtual Compton Scattering) events. The Recoil Detector will have an improved t resolution measurement and will be capable of measuring t-dependency of such processes, which at present is not possible.

3.1 Recoil Detector Components

The Recoil Detector consists of three separate detectors, all surrounded by a superconducting (SC) 1 Tesla solenoid magnet (figure 3.1). The silicon detector is the innermost and surrounds the target cell within the beam vacuum of the HERA ring. The next detector from the inside out is the scintillating fibre detector, or SciFi detector. The outermost detector is the photon detector which consists of several layers of converter and scintillator material, located within the magnet, and surrounding the SciFi detector. As mentioned, all three sub-detectors are within a 1 Tesla longitudinal magnetic field which is generated by the SC solenoidal magnet. This section will describe each of the sub-detectors in more detail along with their expected performance.

3.1.1 Target Cell

The design of the target cell for the Recoil Detector is very similar to the target design used currently by the HERMES experiment, although the active length is shorter. The length of the target cell is 15 cm and it is placed 5 cm downstream from the centre of the current 40 cm long target cell.

The target cell is an aluminium tube with a wall thickness of 50 μm. The cell has an elliptical cross section, with a major (minor) axis of 2.1 (0.9) cm. Unpolarised gas is injected through a small capillary located on the underside of the cell, running along the centre of the tube. The thin wall thickness of the target cell determines the low momentum cut-off for the silicon detector.

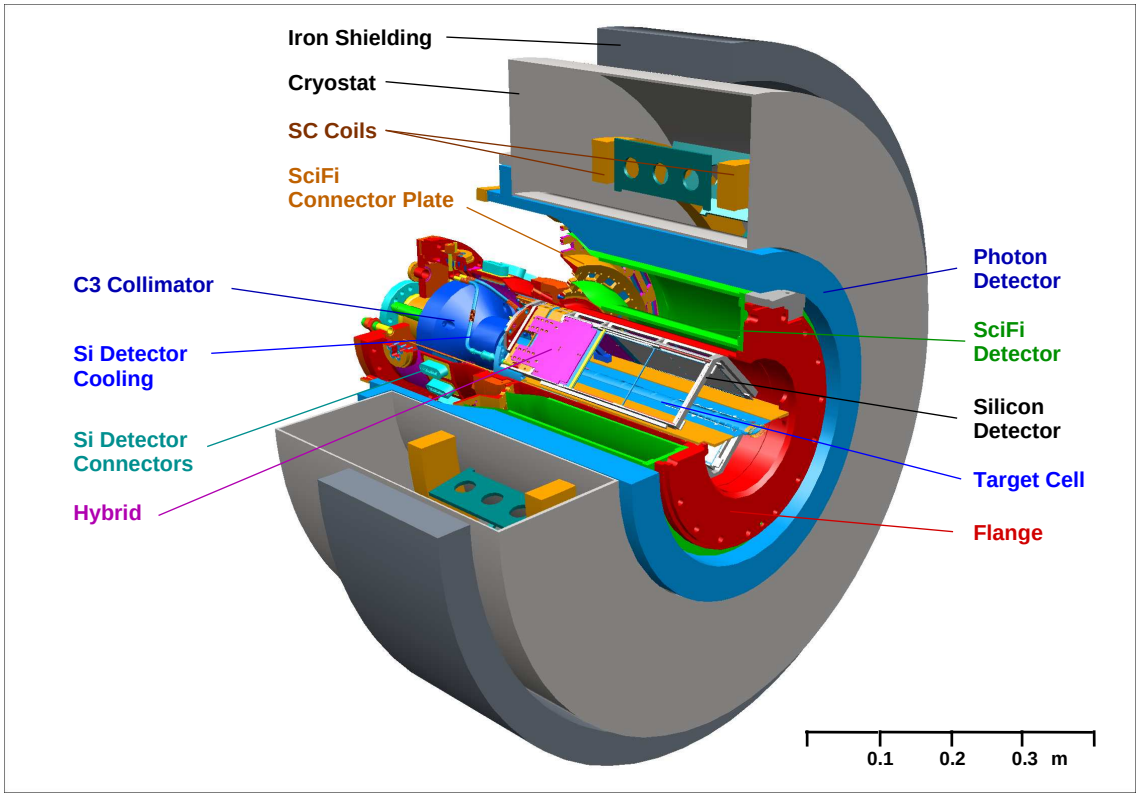

Figure 3.1: 3-dimensional cut through CAD model of the Recoil Detector.

The estimated heating power of the HERA beam is 15 Watts. To counteract this a water-cooled mass is thermally coupled to one end of the cell. The layout of the target cell is shown in figure 3.2.

3.1.2 Silicon Detector

The main purpose of the silicon detector is to detect the recoiling protons from DVCS events and to reject events with intermediate Δ-resonances which constitute the background for this process. From Monte Carlo simulations [16], it was observed that the DVCS protons in events, where the scattered positron produces a trigger in the HERMES spectrometer, are produced with a polar angle of $10° < \theta < 80°$. The Recoil Detector is designed to cover this angular acceptance. The majority of the full 2π azimuthal acceptance is also covered by the Recoil Detector. The momentum and particle type of the detected particle are determined from the energy deposited in the silicon layers. Therefore, a poor angular resolution is acceptable for the silicon detector and for this reason a relatively large strip pitch of $\sim$ 1 mm is chosen. The recoil detected protons have a momentum between 0.135 and 1.4 GeV/c which corresponds to a kinetic energy between 9 and 750 MeV.

Due to the very low energy of the recoil protons it is necessary to minimise the amount of material between the interaction point and the detector. Therefore the silicon detector will be mounted inside the HERA ring vacuum in a newly commissioned scattering chamber (figure 3.3). For this reason, all of the components and techniques used for the silicon detector must be vacuum compatible. HERMES has experience with operating silicon detectors in the HERA vacuum with both the Silicon Test Counter and the Lambda Wheels operating within the HERA ring vacuum. The silicon detector employs many approaches and technology developed by the HERMES NIKHEF group.

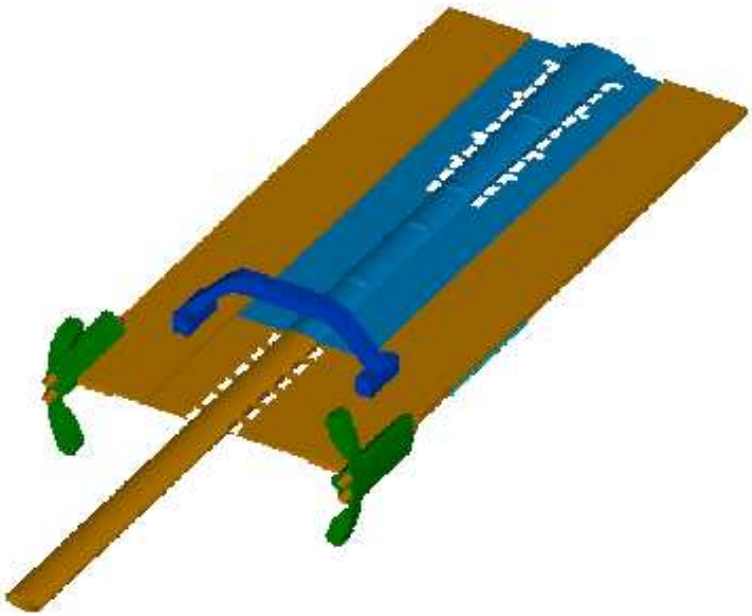

Figure 3.2: The target cell and its support structure. The cooling masses are shown in green (dark grey, upstream left and right), the foil and holding frame in blue and the support plates in red (light grey).

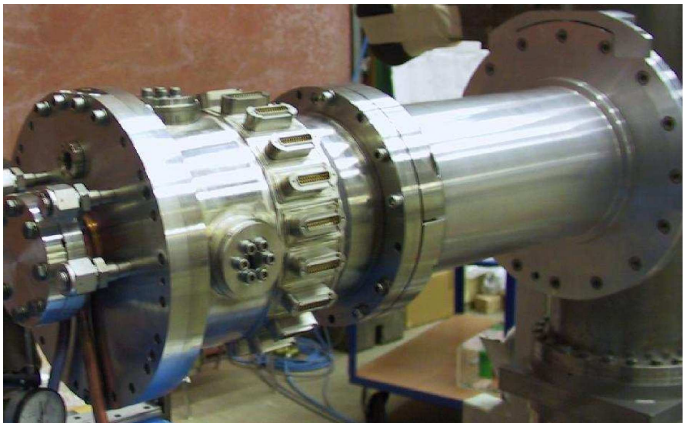

Figure 3.3: Service chamber (with connectors for the cooling system and silicon detector readout) and the scattering chamber.

The silicon detector uses TIGRE [17] silicon microstrip detectors from MICRON Semiconductor Ltd [18]. The dimensions of each silicon detector are 99 mm$\times$ 99 mm which are the largest square double sided detector available. The detectors have a thickness of 300 μm and a strip pitch of 758 μm, with 128 strips on each side. Diagrams of the TIGRE sensor are shown in figure 3.4. The specifications for the sensors are shown in table 3.1.

The recoil silicon detector consists of four modules mounted symmetrically around the HERMES target cell, inside the HERA vacuum. The layout of the silicon detector can be seen in figure 3.6. A module consists of 2 layers of double sided silicon strip detectors separated by a gap of 15 mm between the layers. Each of the 2 layers is itself made from 2 TIGRE sensors; the second orientated immediately downstream from the first. The total surface area of the 16 silicon sensors constituting the recoil silicon detector is 0.16 m^2. The

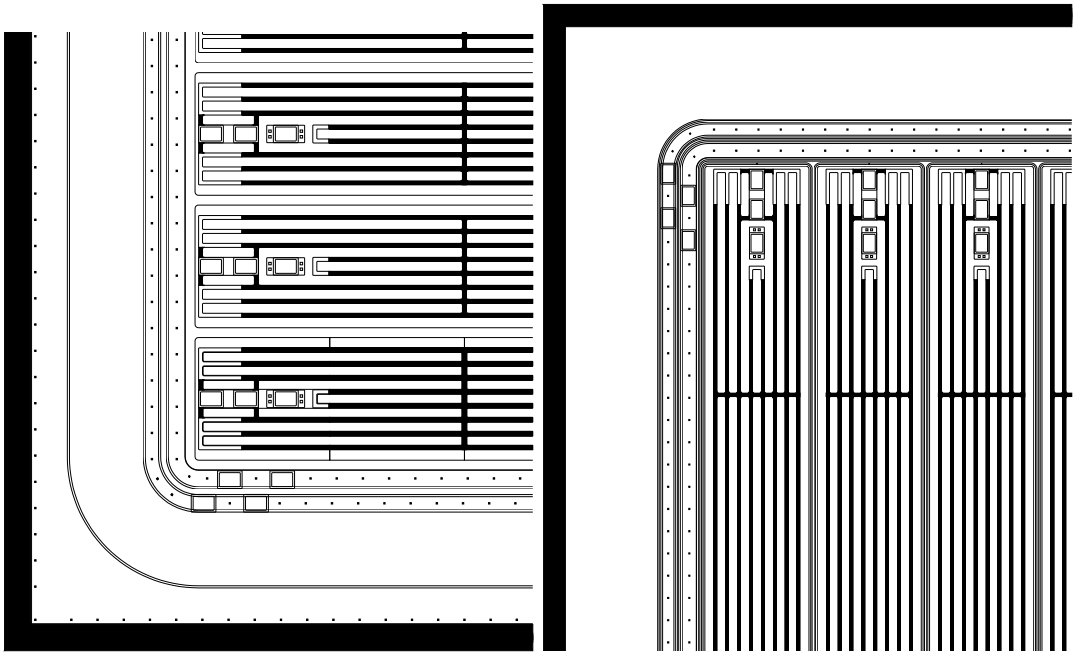

Figure 3.4: Two corners of the TIGRE sensors are shown illustrating the design of the readout end of the sensor. The figure on the left (right) corresponds to the p-side (n-side).

Parameter	Value
Sensor size	99 mm × 99 mm
Active area	97.3 mm × 97.3 mm
Silicon thickness	300 μm
Strip pitch	758 μm
Strip separation	56 μm
Coupling capacitance	1 nF
Total strip capacitance	25 pF
Polysilicon bias resistor	50 M Ω
Depletion voltage	50 V Max

Table 3.1: Specifications of the MICRON TIGRE silicon microstrip sensor.

detector hybrid is a circuit board containing the HELIX3.0 readout chip and on board electronics. One hybrid is required per silicon sensor. To increase the dynamic range, signals are split into a high gain and a low gain channel. Flexfoils are used to connect the individual silicon strips with the readout electronics (figure 3.5).

3.1.3 Scintillating Fibre Detector

The scintillating fibre detector is designed to detect and identify charged pions and protons in the momentum range from 0.3 GeV/c up to 1.4 GeV/c. The detector contributes to the recoil particle detection with a good azimuthal and polar angular resolution. The momentum resolution above $p = 0.4$ GeV/c is expected to be good. Charge determination is obtained by examining the bending behaviour of the particle in the magnetic field, and the discrimination between pions and protons will result from the analysis of the amount of scintillation light that an incident particle produces. The expected angular range of the

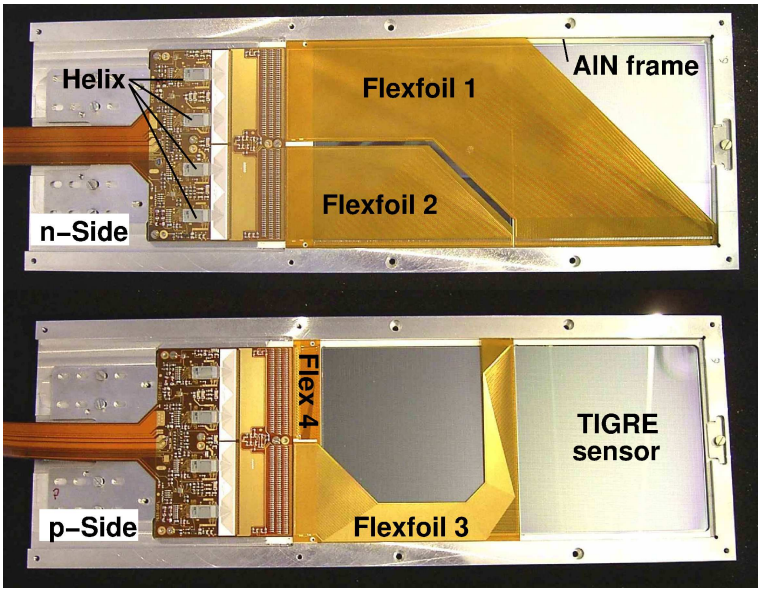

Figure 3.5: p- and n- side of a silicon detector module.

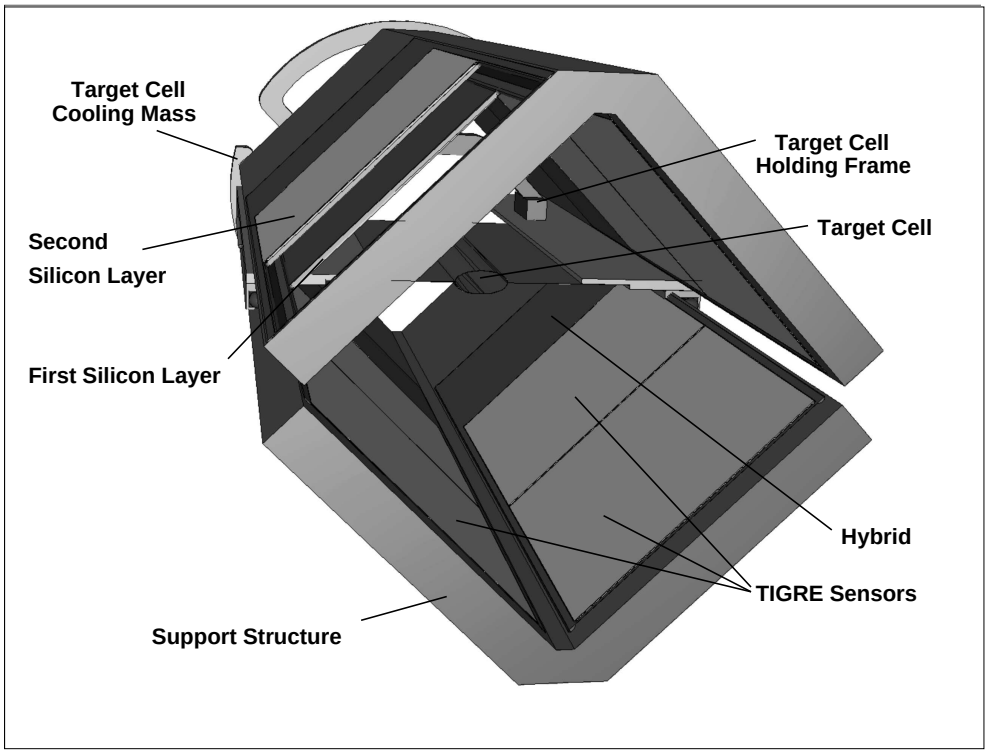

Figure 3.6: Schematic layout of the silicon detectors for the HERMES Recoil Detector. The figure shows the 3D model of the detector and support structure, looking upstream. The upper left TIGRE sensors are not shown so that the double structure is clear.

SciFi detectors acceptance is designed to cover large angles from up to around 90° down to around the region where the acceptance of the Lambda Wheels takes over the particles' detection.

The scintillating fibre detector consists of two cylindrical scintillating fibre modules (SciFi1 and SciFi2) with an inner radius of 108 mm and 183 mm respectively and a thickness of 4 mm each. A photgraph of the SciFi detector is shown in figure 3.7. Each module consists of an inner layer with fibres parallel to the beam axis and an outer layer (stereo layer) with fibres at an angle of 10° with respect to the beam axis (figure 3.8). Each layer of the SciFi1 (SciFi2) is a dense packing of fibres where 2 fibres per layer define one radial road and are read out by the same PMT channel. Fibre diameters of 1 mm were chosen for all SciFi layers.

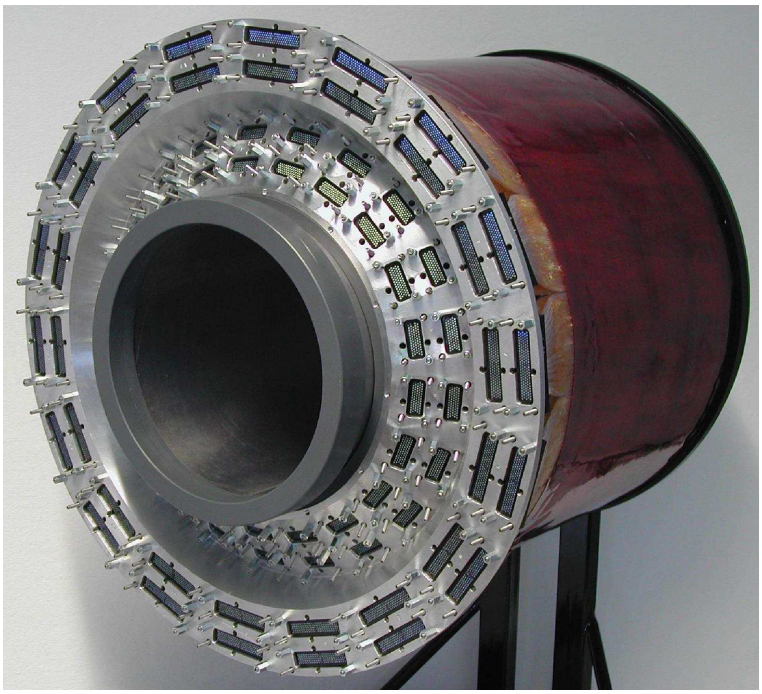

Figure 3.7: View of the Scintillating Fibre Tracking detector.

The azimuthal angle ϕ and the transverse momentum of a track can be resolved from the two inner parallel layers of SciFi1 and SciFi2 alone. This requires the assumption that the track comes from the primary vertex at the lepton beam position. Tracks from secondary vertices can only be reconstructed if at least one additional space point is provided by the silicon detector. The two stereo layers are required to define the particles track in space, i.e to measure the longitudinal vertex position and polar angle. The small stereo angle of 10° was chosen to minimise any track ambiguities and to facilitate the detector fabrication.

The active length of the detector modules is 280 mm. This part of the detector modules is a glued, self supporting fibre structure which is attached to a supporting ring structure at both ends. The downstream ring is attached to the flange of the HERMES pumping cross and ensures a relative alignment of the two modules with respect to one another and the beam pipe. At this end the fibres are polished and coated with a reflecting surface to minimise light losses. At the upstream end the fibres are bundled, over a length of 72 mm, upstream of the active area into roads and fixed to connectors which attach the scintillating fibres to clear light guide fibres. The connectors themselves will be attached to another ring support structure (figure 3.7). The total weight of the SciFi detector is roughly 3kg.

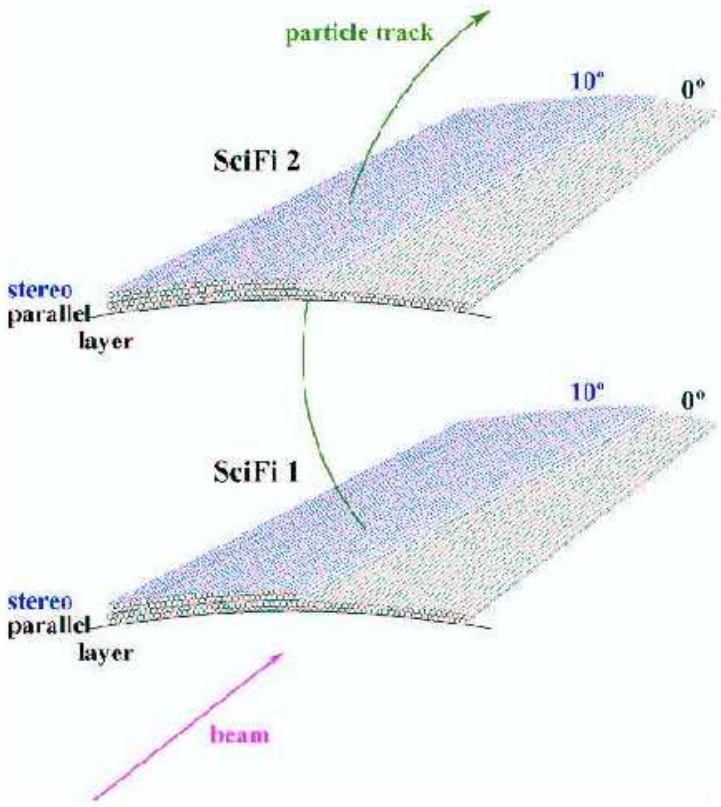

Figure 3.8: Schematic showing the fibre positioning and layering structure of the inner and outer SciFi. The inner (outer) layer has a stereo angle of 0° (10°) with respect to the direction of the beam.

3.1.4 Photon Detector

The primary aim of the photon detector is to reduce the background from events in which an intermediate Δ-resonance is produced. This is accomplished through the detection of (at least one of) the photons emitted by the decay of neutral pions created in the decay of the Δ. It may also be feasible to use the photon detector as an actual detector for π^0's, if the two decay photons are detected and separated. The photon detector will provide a cosmic trigger which will be used for alignment purposes in the final experimental setup and allow alignment of sub-detectors with respect to one another to be done.

The photon detector consists of three converter layers made from Tungsten. Tungsten is chosen as it is a high Z material, which when struck, produces particle showers which are in turn detected by three scintillating fibre detector layers. The modules are made of multiple segmented sections which constitute the overall barrel shape of the detector which is contained within the inner radius of the magnet. The inner layer has 60 strips orientated parallel to the beam, the second and third layer each contain 44 strips at an angle of $\pm 45°$. For mechanical protection the entire detector is contained in a fiberglass cage (figure 3.9).

The kinematic distributions of pions and their decay photons were studied for the case

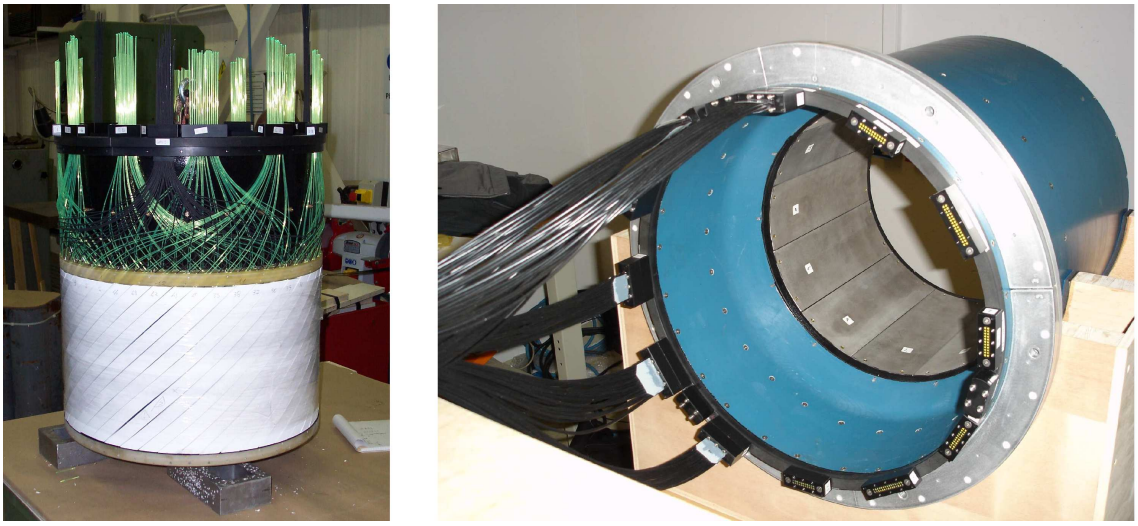

Figure 3.9: The photon detector during assembly(left); the scintillator strips of the outer layer are visible together with the wavelength shifting fibers and the connector ring. The detector after completion (right) is shown together with some lightguides attached to the front fibre connector ring; the blue fiberglass cage and the segmented preshower converter of the inner layer are visible on the inside of the detector.

of DVCS leading to a Δ^+ final state [16], when both the scattered lepton and the DVCS photon are detected in the standard HERMES acceptance. Neutral pions from the resulting Δ decay have emission angles centred around 63 degrees, with a momentum around 250 MeV/c. The decay photons have a wider distribution, while the average emission angle between the two photons is about 50 degrees. This means that for a segmented scintillator barrel with strips with an individual angular aperture of 6 degrees only about 10% of the events will not be resolved over the entire kinematic range covered by the detector.

3.1.5 Superconducting Magnet

The magnet in the Recoil Detector fulfills a double function: It provides the magnetic field which is used for the tracking in the SciFi detector. The magnet also removes Møller electrons by allowing them to spiral forward and in this way protects the silicon detector from this background.

In order to allow a smooth connection between the momentum resolution of the SciFi and silicon detectors the magnet requires a field strength of around 1 Tesla. For the same reason the homogeneity of the field should be better than 20% in either direction. The reduction of Møller electrons is adequate for fields above 0.7 Tesla. A superconducting coil was chosen due to space constraints within the experimental area. Liquid helium is supplied to the magnet to allow it to be cooled down to a working temperature.

The magnet was designed and built by the Efremov Institute, St Petersburg. A picture showing the Recoil Detector magnet is shown in figure 3.10 [19].

3.2 Physics Prospects

This section will focus on the main physics processes which the Recoil Detector will investigate and measure. A look will be taken at Deeply Virtual Compton Scattering

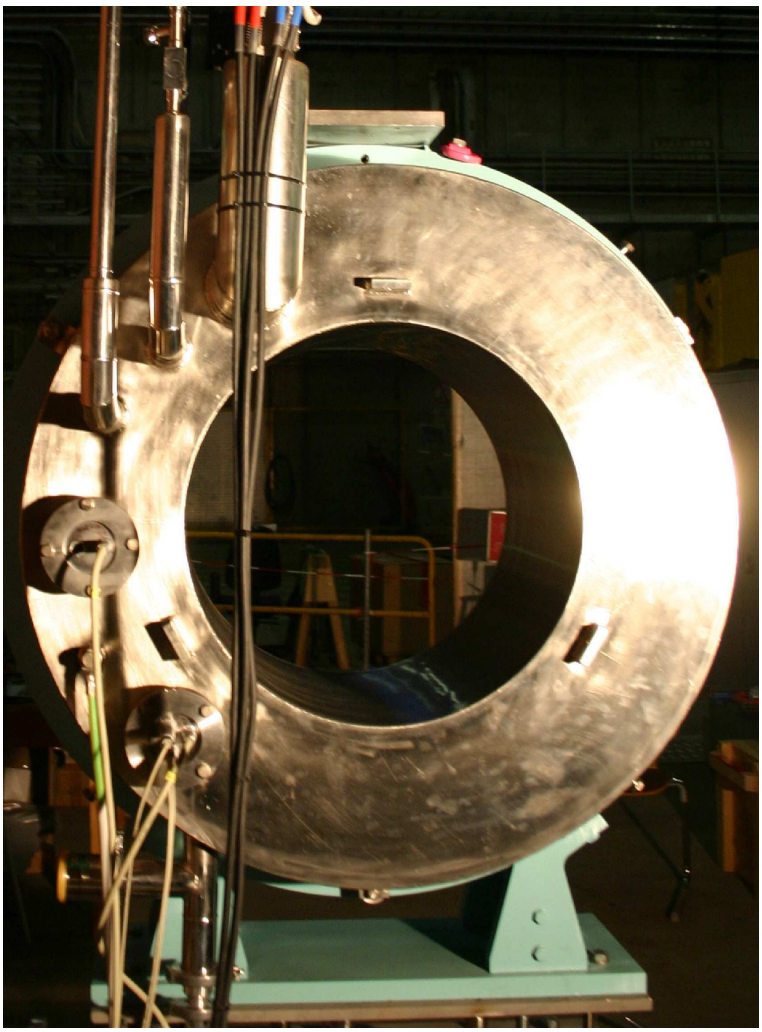

Figure 3.10: Picture of the superconducting solenoidal HERMES Recoil Detector magnet.

(DVCS), which is a process that can access the so called Generalised Parton Distributions (GPD's)[20].

3.2.1 Generalised Parton Distributions

In inclusive and semi-inclusive deep inelastic scattering the structure of the nucleon is described in the framework of QCD by unpolarised and polarised parton distribution functions (PDF's). A generalisation of these parton distributions are the so called generalised parton distributions (GPD's), which are sometimes referred to as skewed or off-forward parton distributions. They allow a unified theoretical approach to a wide variety of exclusive processes in perturbative QCD and provide an interpretation of these reactions in terms of the nucleon structure. Recent theoretical interest for these GPD's has arisen since it was shown [21][22] that the second moment of these distributions is related to the contribution of the spin and orbital angular momentum of the quarks to the nucleon spin.

A good example [23] to demonstrate the meaning of these GPD's and how they are connected to the usual parton densities is provided by the amplitude for virtual Compton scattering. The optical theorem links the imaginary part of the Compton amplitude $\gamma^* p \rightarrow \gamma^* p$ to the inclusive deep-inelastic scattering cross section $\gamma^* p \rightarrow X$. In the Bjorken limit

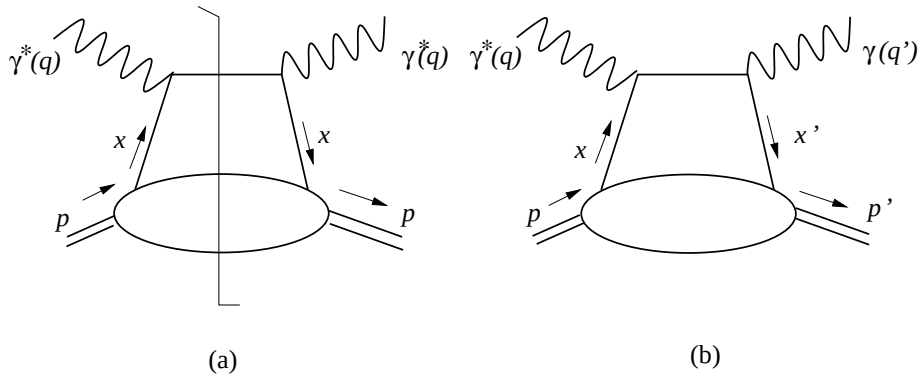

Figure 3.11: (a) The Born level diagram of the forward Compton amplitude. The blob denotes the quark and antiquark distributions in the proton. (b) The Born diagram for deep virtual Compton scattering. In this case the blob is described by GPD's.

this can be calculated as a parton-photon scattering amplitude times the usual parton distributions in the proton. As depicted in figure 3.11(a), no momentum is transferred across the cut in the diagram ($t = 0$) and the parton lines connecting to the proton have the same momentum fractions, equal to Bjorken-x. If now the virtual photon on the righthand side of the diagram is replaced by a real photon as in figure 3.11(b), one obtains the amplitude of the deep virtual Compton scattering (DVCS) $\gamma^* p \to \gamma p$ process. In this case there is a momentum transfer $t = \Delta^2 = (p' - p)^2 = (q - q')^2$ between the proton on the left and right side. The parton lines connecting with the proton have different momentum fractions, which introduces a sort of imbalance or skewedness in the graph. The factorisation shown in the so-called handbag diagram in figure 3.11 (b) is valid for the DVCS amplitude at large Q^2 and fixed Bjorken-x, and small and fixed t. The amplitude is factorised in a hard scattering part calculable in pQCD, and a non-perturbative nucleon structure part which is described in terms of GPD's. In [24] a general proof of factorisation was given also for hard exclusive production by longitudinal photons of vector mesons (ρ, ω,...) and pseudo-scalar mesons (π, η,...) so that GPD's can be accessed via these reactions too.

The nucleon structure information contained in these handbag diagrams can be parameterised in leading order QCD in terms of generalised structure functions, which in the notation of [21][22] are the GPD's H_f, $\widetilde{H}_f$, E_f and $\widetilde{E}_f$ for each quark flavour f (u, d and s). The GPD's are functions of three independent kinematical variables denoted as x, ξ and t. These variables are defined in a frame where the virtual photon momentum q^μ and nucleon momentum P^μ are collinear along the z-axis and in the opposite direction. The physical momenta are then expressed as a function of the two lightlike 4-vectors $p^\mu = P^+/\sqrt{2} \cdot (1, 0, 0, 1)$ and $n^\mu = 1/\sqrt{2}P^+ \cdot (1, 0, 0, -1)$, where the light-cone components are defined as $a^\pm = (a^0 \pm a^3)/\sqrt{2}$. x is the light-cone momentum fraction of the exchanged parton with respect to the incoming nucleon as defined by $x = k/P^+$; the variable $\xi = -\Delta^+/2P^+$, where $\Delta = p' - p$ and $t = \Delta^2$. In the Bjorken limit one has $2\xi \to x_B/(1 - x_B/2)$ with x_B the Bjorken-x variable. The light cone momentum fraction is restricted to $[-1, 1]$, where positive (negative) values correspond to quarks (antiquarks). The difference between the parton fractional momenta $x - x'$ is approximately equal to Bjorken-x.

The usual parton densities are matrix elements of an operator between identical nucleon states. They express the squared amplitude or probability for a nucleon to emit a parton

of given momentum fraction x. The GPD's are matrix elements of the same operators, but now between different nucleon states. They represent the amplitude for a nucleon to emit a parton with momentum fraction x times the conjugated amplitude expressing the absorption of a parton with a different momentum fraction x'. In the case $x > 0$ and $x' < 0$, one can interpret the parton with negative momentum x' as an antiparton with positive momentum fraction $-x'$, which leads to the picture of a nucleon emitting a quark-antiquark pair.

In the forward direction the GPD's H and $\widetilde{H}$ reduce to the familiar quark density and spin distributions:

$$H_f^q(x,0,0) = q_f(x), \qquad \widetilde{H}_f^q(x,0,0) = \Delta q_f(x), \tag{3.1}$$

The first moments of the GPD's are related [21][22] to the elastic form factors:

$$\int_{-1}^{+1} dx H(x,\xi,t) = F_1(t), \qquad \int_{-1}^{+1} dx E(x,\xi,t) = F_2(t) \tag{3.2}$$

$$\int_{-1}^{+1} dx\, \widetilde{H}(x,\xi,t) = G_A(t), \qquad \int_{-1}^{+1} dx\, \widetilde{E}(x,\xi,t) = G_P(t) \tag{3.3}$$

where F_1 and F_2 are the Dirac and Pauli form factors and G_A and G_P are the axial-vector and psuedo-scalar form factors. The second moments of the unpolarised GPD's at $t = 0$ give:

$$\frac{1}{2}\int_{-1}^{+1} dx x[H^q(x,\xi,0) + E^q(x,\xi,0)] = \frac{1}{2}\Delta\Sigma + L_q = J_q \tag{3.4}$$

where $\Delta\Sigma/2$ and L_q are the quark spin and orbital angular momentum contribution to the nucleon spin. The former quantity is also accessed in polarised DIS measurements, so that the measurement of the sum rule (3.4) would lead to the determination of the quark orbital momentum contribution to the nucleon spin according to:

$$\frac{1}{2} = J_q + J_g \tag{3.5}$$

and also to the total gluon contribution J_g. A unique feature of this GPD framework is that it gives access to nucleon spin information without the need for a polarised beam or target.

As already mentioned, these GPD's provide a tool to describe various types of exclusive reactions. However, different types of exclusive processes are related to different (combinations of the) GPD's. At leading order pQCD the longitudinally polarised vector meson channels (ρ_L, ω_L, ϕ_L) are sensitive to the unpolarised GPD H and E only, whereas the psuedo-scalar meson channels (π, η) have sensitivity to the polarised $\widetilde{H}$ and $\widetilde{E}$ [24]. All four GPD's contribute in the description of deeply virtual Compton scattering (DVCS) [21][22]

3.2.2 Deeply Virtual Compton Scattering

A particularly promising way of studying the nucleon structure is through the DVCS process, where a virtual photon couples to the proton, and a real photon is emitted ($\gamma^* + p \rightarrow \gamma + p$), as illustrated in figure 3.12. The proton is left intact. The DVCS process combines the advantages of deep inelastic scattering (DIS) and Compton scattering. The initial photon is off-shell, thus opening an additional dimensional parameter with respect to real Compton scattering, because the virtuality can be 'tuned' (in the given kinematical limits).

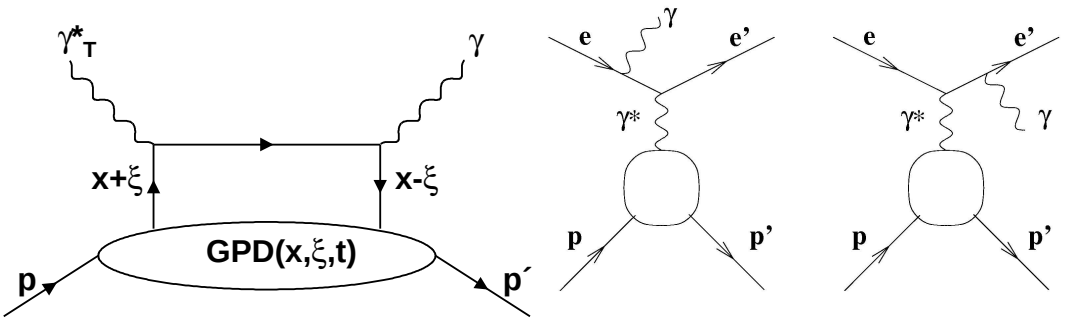

Figure 3.12: Handbag diagram for DVCS(left). Handbag diagram for Bethe-Heitler process (middle and right)

In electron (or positron) scattering experiments there exists an other process that leads to the same final state as DVCS, namely the Bethe-Heitler (BH) process (figure 3.12), in which the incoming or outgoing electron radiates a bremsstrahlung photon in the Coulomb field of the proton. Hence in the process $ep \rightarrow ep\gamma$ the amplitudes of DVCS and BH are interfering, thus prohibiting the measurement of the pure DVCS process. The relative contributions of BH and DVCS to the total BH/DVCS amplitude depend strongly on the lepton energy. At HERMES energies, the BH contribution is mostly dominant, except at larger values of the Bjorken variable x_B and Q^2. This situation is used as an opportunity [20], since the interference of the two amplitudes offers a way to access both the real and imaginary part of the DVCS amplitude (see below). At higher energies, where the DVCS amplitude dominates over the BH amplitude, only the square of the DVCS amplitude can be accessed [20].

The process amplitudes describing DVCS, BH and their interference can be expanded into a power series in $1/Q$. They exhibit different characteristics as functions of the azimuthal angle ϕ between the scattering plane and the production plane (see figure 3.13), and can be expressed using moments $\langle \cos n\phi \rangle$ and $\langle \sin n\phi \rangle$. These cosine and sine moments are sensitive to the real and imaginary parts of the DVCS helicity amplitudes, respectively. In order to project out the various moments, measurements are carried out for different beam helicity and charge. Under the assumption of the handbag diagram (figure 3.12), each moment has its own characteristic fall-off with $(1/Q)^n$ at fixed x_B and t. The first cosine moment is then dominant with a $1/Q$ fall-off, while higher moments fall-off with powers of 2 or higher [20].

A theoretical picture of the DVCS process has been developed in a number of papers [20][25][26][27]. Explicit expressions for the amplitudes of the DVCS, Bethe-Heitler and interference terms, including the first subleading correction in $1/Q$ for different kinds of polarised and unpolarised initial particles have been calculated [28].

To access, in a first step , the nucleon helicity conserving GPD $H(x,\xi,t)$ at HERMES with a Recoil Detector an unpolarised target is sufficient. In this case two different types of measurement are possible. In the leading twist-2 approximation:

I) *lepton charge asymmetry* is proportional to the difference of the cross sections for scattering of unpolarised leptons of either charge off an unpolarised target:

$$d\Delta\sigma_{ch} \equiv d\sigma(e^+p) - d\sigma(e^-p) \sim \cos(\phi) \times Re\mathcal{A} \tag{3.6}$$

II) *lepton beam helicity asymmetry* is proportional to the difference of the cross sections for scattering of a longitudinally (L) polarised positron (electron) beam off an unpolarised

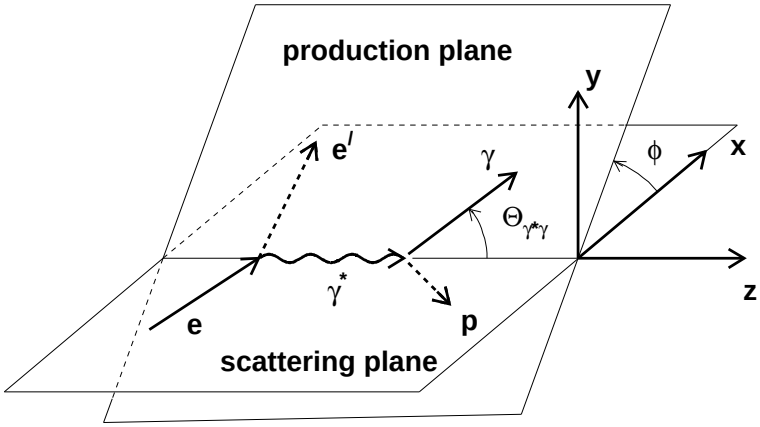

Figure 3.13: Schematic of the azimuthal angle ϕ between the scattering and the production plane. It is equally valid for DVCS and meson production.

(U) target:

$$d\Delta\sigma_{LU} \equiv d\sigma(\overrightarrow{e^{\pm}}p) - d\sigma(\overleftarrow{e^{\pm}}p) \sim \mp \sin(\phi) \times Im\mathcal{A}. \tag{3.7}$$

These asymmetries give access to the real and imaginary parts of the same combination of DVCS amplitudes:

$$\mathcal{A} = F_1(t)\mathcal{H}_1(\xi,t) + \xi(F_1(t)+F_2(t))\,\widetilde{\mathcal{H}}_1\,(\xi,t) - \frac{t}{4M^2}F_2(t)\mathcal{E}_1(\xi,t) \tag{3.8}$$

where the skewdness ξ can be related to the Bjorken variable $\xi = x_B/(2-x_B)$. Note that the contribution of the amplitude $\widetilde{\mathcal{H}}_1$ is suppressed at small values of x_B while the contribution of the amplitude $\mathcal{E}_1$ is suppressed at small values of t. The main contribution to the asymmetries in the HERMES kinematical region comes from the amplitude $\mathcal{H}_1$.

To leading order in α_s, the imaginary and real parts of the DVCS amplitude are related to the GPD's:

$$\begin{aligned}
Im\mathcal{H}_1 &= -\pi \sum_q e_q^2 (H^q(\xi,\xi,t) - H^q(-\xi,\xi,t)) \\
Im\,\widetilde{\mathcal{H}}_1 &= -\pi \sum_q e_q^2 (\widetilde{H}^q\,(\xi,\xi,t) + \widetilde{H}^q\,(-\xi,\xi,t)) \\
Re\mathcal{H}_1 &= \sum_q e_q^2 \big[P \int_{-1}^{+1} H^q(x,\xi,t)\big(\frac{1}{x-\xi} + \frac{1}{x+\xi}\big)dx\big] \\
Re\,\widetilde{\mathcal{H}}_1 &= \sum_q e_q^2 \big[P \int_{-1}^{+1} \widetilde{H}^q\,(x,\xi,t)\big(\frac{1}{x-\xi} - \frac{1}{x+\xi}\big)dx\big]
\end{aligned} \tag{3.9}$$

where P denotes Cauchy's principle value. Analogous expressions are valid for the DVCS amplitudes $\mathcal{E}_1$ and $\widetilde{\mathcal{E}}_1$.

At HERMES, results of the DVCS analysis has been presented [29] and published [30]. Projections of the DVCS measurements at HERMES possible with the Recoil Detector have also been made [31][32] with the projected improvements to measured asymmetries presented.

3.2.3 Hard Exclusive Meson Production

Whereas DVCS provides the theoretically cleanest access to generalised parton distributions, meson production processes offer a wealth of additional information.

According to the meson quantum numbers, their production is sensitive to different combinations of GPDs and thus offer a way to disentangle the various quark flavours (see table 3.2) and gluon contributions (for an overview see [33]). Note that, contrary to DVCS, a meson production process involves either the parton helicity-independent functions H or E or the helicity-dependent ones $\widetilde{H}$ and $\widetilde{E}$ which reduces the number of unknowns in the analysis.

Produced particle	Quark flavour structure of proton GPDs
γ	$\frac{4}{9}H^u + \frac{1}{9}H^d + \frac{1}{9}H^s$, $\frac{4}{9}\widetilde{H}^u + \frac{1}{9}\widetilde{H}^d + \frac{1}{9}\widetilde{H}^s$
ρ^0_L	$\frac{1}{\sqrt{2}}\{\frac{2}{3}H^u + \frac{1}{3}H^d\}$
ω_L	$\frac{1}{\sqrt{2}}\{\frac{2}{3}H^u - \frac{1}{3}H^d\}$
ϕ_L	$\frac{1}{3}H^s$
π^0	$\frac{1}{\sqrt{2}}\{\frac{2}{3}\widetilde{H}^u + \frac{1}{3}\widetilde{H}^d\}$
η	$\frac{1}{\sqrt{6}}\{\frac{2}{3}\widetilde{H}^u - \frac{1}{3}\widetilde{H}^d + \frac{2}{3}\widetilde{H}^s\}$
ρ^+	$H^u - H^d$
π^+	$\widetilde{H}^u - \widetilde{H}^d$

Table 3.2: Examples of the quark flavour structure of proton GPDs accessible in electroproduction. In the production of ρ^0_L, ω^0_L and ϕ^0_L gluon distributions contribute at the same order in α_s. Flavour SU(3) symmetry is assumed for the η meson wave function.

The main task of the Recoil Detector is to detect and identify recoil protons that are produced in conjunction with a neutral particle entering the HERMES spectrometer (rows 1-6 of table 3.2). If a positive meson is detected instead (rows 7-8 of table 3.2), the recoil particle is a neutron whose detection is experimentally difficult.

Some channels, such as $ep \rightarrow ep\rho^0$, have quite large production rates, and thus provide sufficient statistics for detailed studies like simultaneous binning in different variables. One important example for a two-dimensional spectrum is the dependence on Q^2 at a given fixed value of x_B. This dependence is predicted by the factorisation theorem, up to logarithmic modifications due to radiative corrections. Its verification constitutes one of the key tests whether the measurement takes place in a kinematic region where this theorem can be used.

To illustrate the potential of such high statistic channels, figure 3.14 shows projected spectra in t and Q^2 for two bins in x_B for exclusive ρ production.

The HERMES Recoil Detector, which will become fully operational in 2006/07, will also bring some likely improvements to the current vector meson analysis. The main areas in which the Recoil Detector will alter or improve the current analysis are:

- The t-resolution will be improved at low t from the resolution that is available using the HERMES Spectrometer alone [10](figure 3.15). This improvement is possible due to the detection of the recoiling proton directly, rather than reconstructing the $t \sim t'$ value indirectly from the ρ^0 decay products, which is the current analysis procedure at HERMES. This approach is used as the recoiling proton is not normally within the acceptance of the forward spectrometer.

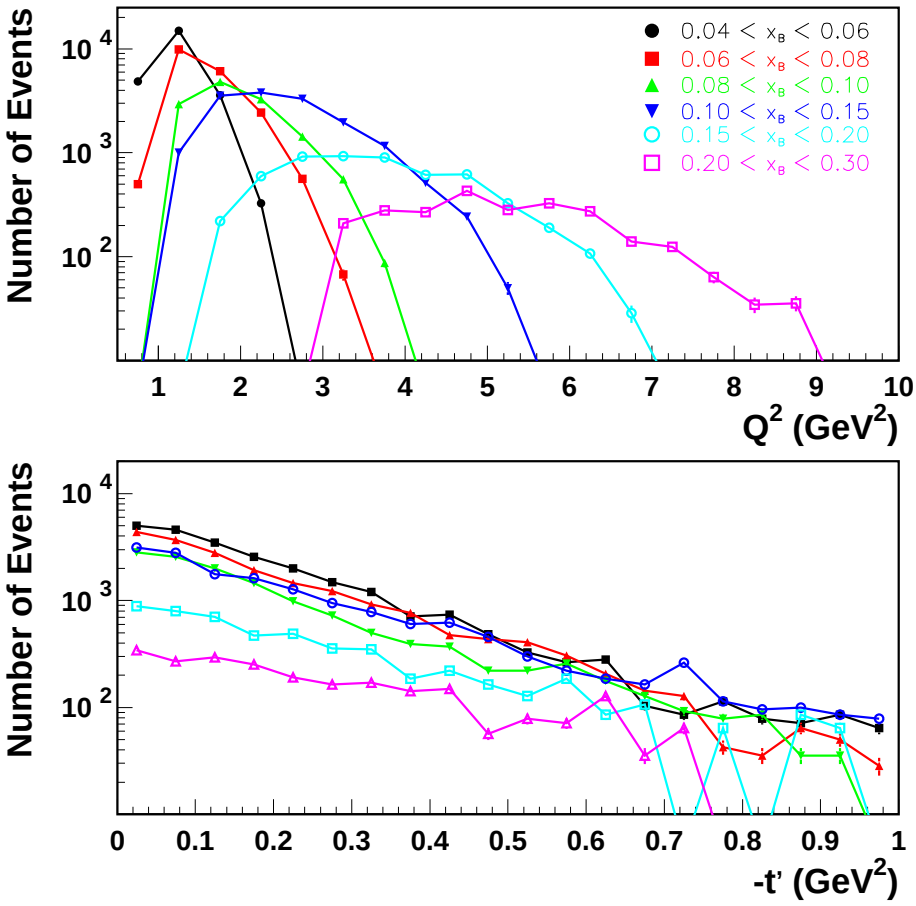

Figure 3.14: Projected spectra in Q^2 and t for $ep \rightarrow ep\rho$ for 6 bins in x_B. They are extrapolated from the spectra measured at HERMES and scaled to an integrated luminosity of 2 fb^{-1}, including the acceptance of the Recoil Detector. Statistical errors are covered by the symbols.

The improved t-resolution will be useful for analysing, for example, the deuterium target. As a composite target, consisting of more than just a single nucleon, deuterium has both a coherent and an incoherent contribution which both contribute at low t. The improved resolution may allow a cleaner separation of these two overlapping distributions and hence a better understanding of the coherent process where all nucleons within the nucleus are scattered upon.

- There will also be the possibility with the Recoil Detector to remove the ΔE cut (shown in figure 8.2), which in the current analysis is used to remove as much of the DIS background from the data sample which contaminates the exclusive peak. This cut removes a lot of the unwanted DIS events, however a large number of exclusive events are also removed which is undesirable.

  The coplanarity cut used by the Recoil Detector will decrease the overall statistics and it remains to be analysed whether this cut produces a net benefit for a vector meson analysis with respect to the removal of the ΔE cut applied at present.

- Another improvement the data taken with the Recoil Detector will bring is an increase in overall statistics for vector meson analysis. Using an unpolarised hydrogen (and deuterium) gas target during operational running, the data collected during the

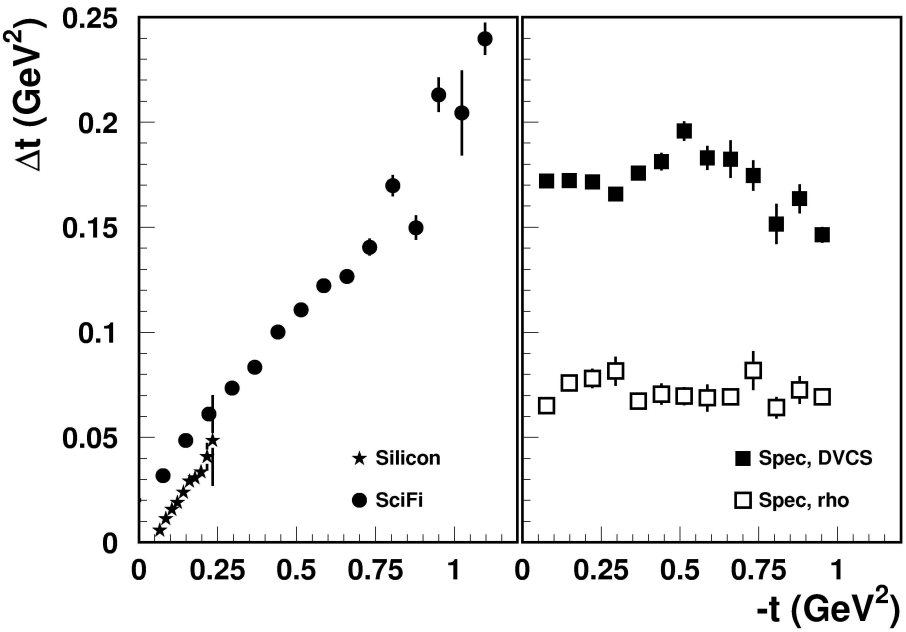

Figure 3.15: t-resolution comparison for the Recoil Detector and HERMES Spectrometer. Left: The projected t- resolutions for the silicon detector and scintillating fibre detector. Right: The current t-resolution of the HERMES Spectrometer, shown for both DVCS and vector meson analysis.

lifetime of the Recoil Detector will greatly increase the size of the data sample which can be analysed in a vector meson analysis in the near future.

This will help to increase the statistical accuracy of results which are obtained previously with the statistics collected by the HERMES Spectrometer. This, for example will help to improve the accuracy of the knowledge of the SDME's for both hydrogen and deuterium, allowing different hypotheses and theoretical models to be tested more rigourously.

Chapter 4

Helix 3.0 Readout Chip

In this section the process of energy deposition in a layer of silicon will be presented with emphasis on the energy range in which the Recoil Detector will operate. The HELIX128-3.0 readout chip will then be described and the experimental method used to investigate the functionality of the chip will be shown. The suitability for this readout chip to be used within the silicon recoil detector will be discussed and the results obtained from experimental measurements shown.

4.1 Energy Deposition in Silicon

Ionising radiation creates electron-hole pairs in the n-doped silicon. Holes drift towards the p+ and electrons to the n+ side of the detector. In general the average energy loss (stopping power) of an ionising particle inside a material is given by the Bethe-Bloch formula [34]:

$$-\frac{1}{\rho}\frac{\mathrm{d}E}{\mathrm{d}x} = -\kappa z^2 \frac{Z}{A}\frac{1}{\beta^2}\left(\frac{1}{2}\ln\frac{2m_e c^2\beta^2\gamma^2 T_{\max}}{I^2} - \beta^2 - \frac{\delta}{2}\right), \tag{4.1}$$

where:

κ = $4\pi N_A r_e^2 m_e c^2$ ($= 0.3071 \frac{\mathrm{MeVcm}^2}{\mathrm{g}}$)
$Z(A)$ = Atomic number(mass) of the medium
z = Charge of incident particle (in units of elementary charge)
$T_{\max}$ = Maximum kinetic energy transfered to an electron in a single collision.
$= 2m_e c^2\beta^2\gamma^2$ (if $\frac{2\gamma\ m_e}{M} << 1$ where M = mass incident particle)
I = Mean excitation energy (= 173.0 eV for Silicon)
δ = 'Density effect′ correction to energy loss by ionisation.

This formula has been plotted in figure 4.1 for ionising protons passing through a 300 μm thick silicon layer for the momentum range relevant for the Recoil Detector. The density effect has been neglected since only momenta up to 1.6 GeV are expected. Particles with an energy corresponding to the minimum plateau of the Bethe-Bloch are defined as 'minimum ionising particles' (≡MIP).

A particle traveling through a certain material becomes more ionising towards the end of its path, therefore its energy loss versus penetration depth is a typical Bragg curve. The range R of a particle with a kinetic energy E_0 which stops inside the absorbing material is calculated by integrating the Bethe-Bloch formula 4.1:

$$\mathrm{R}(E_0) = \int_0^{E_0}\left(\frac{\mathrm{d}E}{\rho\mathrm{d}x}\right)^{-1}\mathrm{d}E. \tag{4.2}$$

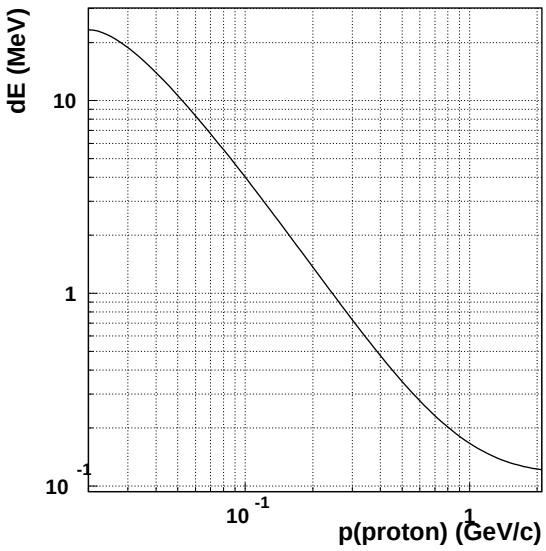

Figure 4.1: Bethe-Bloch for protons in a 300 μm silicon layer.

For low energies the Bethe-Bloch formula goes as $\sim \frac{1}{\beta^2} (=\sim \frac{1}{E_0})$, so the range can be approximated to be:

$$\mathrm{R}(E_0) = \int_0^{E_0} \frac{1}{\rho} \frac{\mathrm{d}E}{cE^a} = \frac{1}{\rho} c_r E_0^b$$

with b and c_r fitting parameters. Using the measured energy range the parameters c_r and b have been fitted in the range 40 to 170 $\frac{\mathrm{MeV}}{\mathrm{c}}$ and are:

$$\begin{aligned} c_r &= 3.258 \times 10^{-3} \tfrac{\mathrm{g}}{\mathrm{cm}^2} \\ b &= 1.70. \end{aligned}$$

For other energies fitting parameters are given in [35].

A particle traveling through the silicon deposits an energy of

$$E_{\mathrm{dep}} = E_0 - E_{\mathrm{fin}} \tag{4.3}$$

where E_{fin} is the energy of the particle after passing the silicon. If now the range of a particle in a piece of silicon is t then it has lost an amount of energy equal to $E_0 - E_{\mathrm{fin}}$. Hence:

$$\int_{E_{\mathrm{fin}}}^{E_0} \left(\frac{\mathrm{d}E}{\rho \mathrm{d}x} \right)^{-1} \mathrm{d}E = t.$$

Calculating now the range $\mathrm{R}(E_{\mathrm{fin}})$ of a particle with energy E_{fin}:

$$\begin{aligned} \int_0^{E_{\mathrm{fin}}} \left(\frac{\mathrm{d}E}{\rho \mathrm{d}x} \right)^{-1} \mathrm{d}E &= \int_0^{E_0} \left(\frac{\mathrm{d}E}{\rho \mathrm{d}x} \right)^{-1} \mathrm{d}E + \int_{E_{\mathrm{fin}}}^{E_0} \left(\frac{\mathrm{d}E}{\rho \mathrm{d}x} \right)^{-1} \mathrm{d}E, \quad \text{and} \\ \frac{1}{\rho} c_R E_{\mathrm{fin}}^b &= \frac{1}{\rho} c_R E_0^b - t. \end{aligned}$$

Then from equation 4.3:

$$E_{\mathrm{dep}} = E_0 - \left(E_0^b - \frac{t\rho}{c_R} \right)^{\frac{1}{b}}. \tag{4.4}$$

Applying this formula the energy deposition in the two silicon layers can be calculated. In figure 4.2 the energy deposition in the first layer is plotted versus the energy deposition in the second layer for protons hitting the detector perpendicularly. Protons with momenta lower than $\sim 106 \frac{\mathrm{MeV}}{\mathrm{c}}$ get stuck in the first layer of silicon. Protons with momenta between ~ 106 and ~ 130 $\frac{\mathrm{MeV}}{\mathrm{c}}$ punch through the first layer but get stuck in the second layer. If the momentum of a proton is higher than ~ 130 $\frac{\mathrm{MeV}}{\mathrm{c}}$ it punches through both silicon layers.

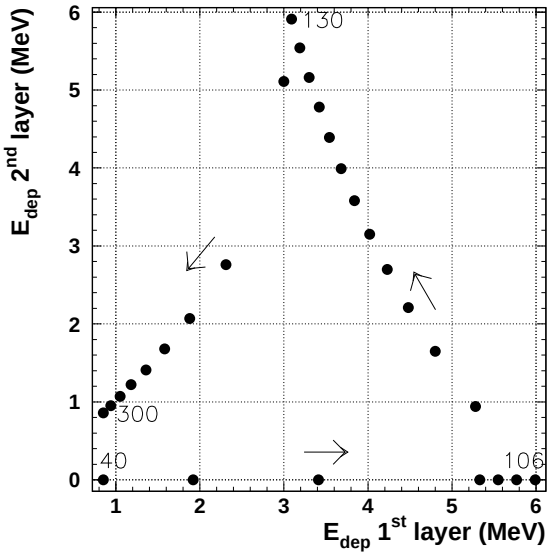

Figure 4.2: Energy deposition in two layers of 300 μm silicon for protons hitting the silicon perpendicularly. The arrows indicate increasing proton momenta. Protons with $p \lesssim 106$ $\frac{\mathrm{MeV}}{\mathrm{c}}$ get stuck in the first layer, if $106 \lesssim p \lesssim 130$ $\frac{\mathrm{MeV}}{\mathrm{c}}$ then the protons punch through the first layer but get stuck in the second. For $p \gtrsim 130$ $\frac{\mathrm{MeV}}{\mathrm{c}}$ the proton punches through both layers.

Due to the possibility of large energy transfer in a single collision, the energy deposition inside thin layers of detector material is not Gaussian. Therefore a difference between the most probable and the average energy deposition arises. The distribution should be approximated by a Landau curve [36]:

$$\begin{aligned} L(\lambda) &= \frac{1}{\sqrt{2\pi}}\, e^{-\frac{1}{2}(\lambda + e^{-\lambda})} \\ \lambda &= \frac{\Delta E - \Delta E^W}{\xi} \end{aligned} \tag{4.5}$$

where $\xi = \frac{\kappa}{2}\rho\frac{Z}{A}(\frac{z}{\beta})^2$, ΔE the actual energy loss, and ΔE^W the most probable energy loss. ΔE^W can be determined by taking the mean of equation 4.5:

$$\Delta E^W = -\xi < \lambda > + < \Delta E > \tag{4.6}$$

The mean energy loss $< \Delta E >$ of a proton in a silicon layer is known from the Bethe-Bloch formula (equation 4.1). $< \lambda >$ can be calculated by:

$$< \lambda >= \frac{1}{\sqrt{2\pi}} \int_{-\infty}^{+\infty} \lambda e^{-\frac{1}{2}(\lambda + e^{-\lambda})} \mathrm{d}\lambda = \gamma + \ln 2$$

where γ is Euler's constant. Evaluating equation 4.6 for a MIP gives $\Delta E^W = 85.5$ keV. Knowing that 3.6 eV is needed to create one electron-hole pair in silicon a signal of ~ 24000 electrons is 'most probable' appearing for the energy deposition of a MIP. The Landau distribution for minimum ionising protons is shown in figure 4.3.

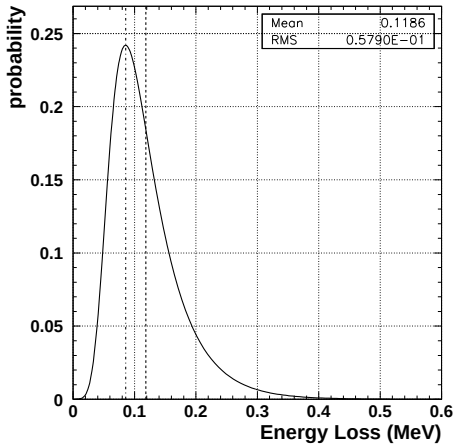

Figure 4.3: Energy loss distribution for minimum ionising protons in silicon. The distribution is represented by a Landau curve. The dashed (dash-dotted) line represents the average (most probable) energy loss.

Looking back at figure 4.2 the expected signals can now be calculated for the mentioned momenta: a proton with momentum 106 $\frac{\text{MeV}}{\text{c}}$ will deposit ~ 6 MeV in the first energy layer, corresponding with a signal of ~ 51 MIP. For a momentum of 130 $\frac{\text{MeV}}{\text{c}}$ there will be a deposition of $\sim 3.1(\sim 5.9)$ MeV in the first(second) layer, corresponding with a signal of $\sim 26(\sim 50)$ MIP. A 300 $\frac{\text{MeV}}{\text{c}}$ proton will deposit ~ 0.8 MeV in both layers, giving a signal of about 7 MIP. Most recoil particles will cross the silicon detector not perpendicularly but at an angle of between around 0.8-1.4 rad (5.19). A dynamic range of |70| MIPs ensures that those particles can be detected.

If in the future a deuterium instead of a proton target will be used, the energy deposition will be different. Scattering on ^2H has two interesting contributions. On one hand there will be spectator protons if the virtual photon interacts with the neutron. 10% of these spectator protons are expected to deposit more than 6 MeV in the silicon; 2.5% more than 7 MeV [37]. On the other hand there's elastic scattering on the ^2H target, where the deuterium as a whole ends up in the silicon, depositing an energy up to 8 MeV, corresponding to a signal of ~ 68 MIP. So a range of at least |70| would be needed in order to have a sufficient safety margin if the recoil deuterons are to be detected.

4.2 HELIX128-3.0

HELIX128-3.0 [38] was designed by the ASIC laboratory of the Heidelberg University and manufactured in the 0.8μm CMOS process by AMS [39]. The chip contains 128 channels, each of them (figure 4.4) has a charge sensitive preamplifier, followed by a shaper whose output is sampled into an analog pipeline with 128 memory cells which store the charge until the trigger signal arrives. Data from one of the 128 pipeline channels, selected by the trigger, is transferred via a multiplexer to a serial output readout line. Characteristics of all the amplification stages can be adjusted via programming of digital-to-analog registers.

This allows the selection of the most appropriate operating point for the chip and reduces the negative effects of radiation damage.

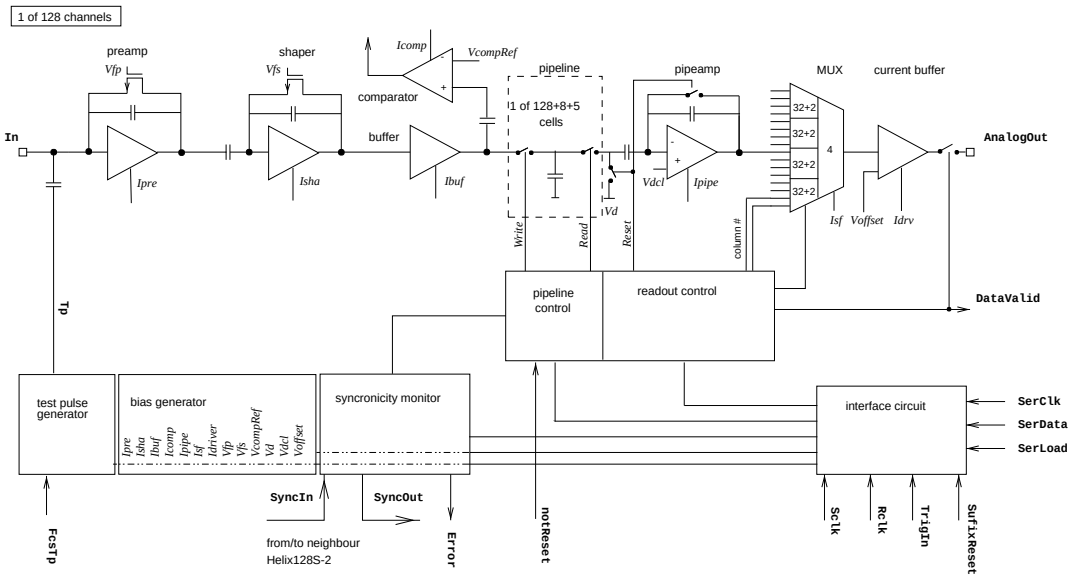

Figure 4.4: Schematic diagram of HELIX128

The HELIX128 has been designed for the HERA collider experiments at DESY, so that the input signal can be sampled with 10.4 MHz clock frequency (bunch crossing frequency at HERA) with a shaper peaking time of about 50ns. The storage time depth is about $10\mu s$ $(96ns \cdot 128)$ to compensate for the trigger delay. Up to eight triggered events can be stored allowing equalisation of statistical fluctuations in trigger rate. Several HELIX128 chips can be daisy-chained in order to make the data transfer from them to the serial output easier. A special feature of the HELIX128-3.0 version is a failsafe token, which allows the exclusion of broken chips from the readout chain.

4.3 Charge Injection Experiment

In this section the dynamic range of the HELIX128-3.0 is investigated and possible techniques to increase the dynamic range of the readout chip are presented. For the HELIX128-3.0 a range of $|10|$ MIPs was observed with a signal to noise of ≈ 10 for 1 MIP. Using a charge sharing method the dynamic range of the HELIX128-3.0 can be extended. The results and the method applied used are described in the following sections.

4.3.1 General Setup Considerations

The first step of the chip study was to measure the detector independent properties. For this purposes ZEUS (HELIX) hybrids have been used with no detector attached. The charge equivalent to that produced by particles of various energies has been injected into a chip's channel and the response has been measured. The charge injection system is shown in figure 4.5. Applying the following formula one gets an input charge in units of MIP with one MIP corresponding to 24000 electrons:

$$Q = C_c \cdot V_{\text{in}} = C_c \cdot \frac{V_{\text{gen}} 10^{-\frac{\text{At}}{20}}}{1.6 \times 10^{-19}} \frac{1}{24000}, \tag{4.7}$$

where At is the attenuation coefficient in dB and V_{gen} the output of the pulse generator. For convenience the injected charge will be quoted in units of MIP.

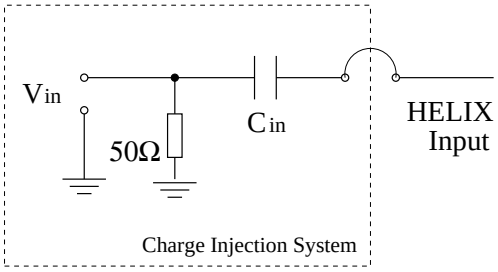

Figure 4.5: Charge injection system schematic. V_{in} is a signal from the pulse generator, attenuated to get the required input charge. C_{in} is an input capacitance. It defines the amount of charge: $dq = C_{in} \cdot du$.

The chip's output signal PH_i^k can be described as a sum of the following components:

$$PH_i^k = S_i^k + P^k + N_i^k + C_i, \tag{4.8}$$

where i and k denote the event and the channel number respectively;

S_i^k is the chip response to the injected charge;

P^k is the DC-offset of the channel (pedestal level);

N_i^k is the individual random noise contribution of the channel (Gaussian distributed); and

C_i is a random voltage offset, common for all channels of the chip, event independent and Gaussian distributed, usually called common mode noise.

During the pedestal measurements ($S_i^k = 0$) the pedestal level of each channel is measured:

$$P_k = \frac{1}{N_{events}} \sum_{i=1}^{N_{events}} PH_i^k. \tag{4.9}$$

The common mode noise (CMN) can be calculated for each event individually by

$$C_i = \frac{1}{N^*_{channels}} \sum_{k=1}^{N^*_{channels}} (PH_i^k - P_k) \tag{4.10}$$

where P_k is taken from the pedestal measurements (equation 4.9) and averaging is done over the channels without hits ($N^*_{channels}$ is a number of such channels and $N^*_{channels} = N_{channels}$ in the case $S_i^k = 0$, where $N_{channels}$ is the total number of channels taken for the analysis). The CMN can now be extracted from the final data

$$S_i^k + N_i^k = PH_i^k - P_k - C_i. \tag{4.11}$$

For the case of pedestal measurements ($S_i^k = 0$) the rms of each channel N_i^k distribution can be extracted, which gives the channel's noise levels.

4.3.2 Experimental Setup

The test stand used (figure 4.6) has been designed by the ZEUS collaboration [40] to test the HELIX128-3.0 based Micro Vertex Detector (MVD) [41]. In the original configuration the test stand was used to measure the detector response to a laser beam test pulse. The laser was not used during these measurements. The test stand consists of a pattern generator (SEQSI) which controls the HELIX128 chips and a SIROCO ADC for the readout. The interface of the DAQ was a LABVIEW program which was used to address the SEQSI. A

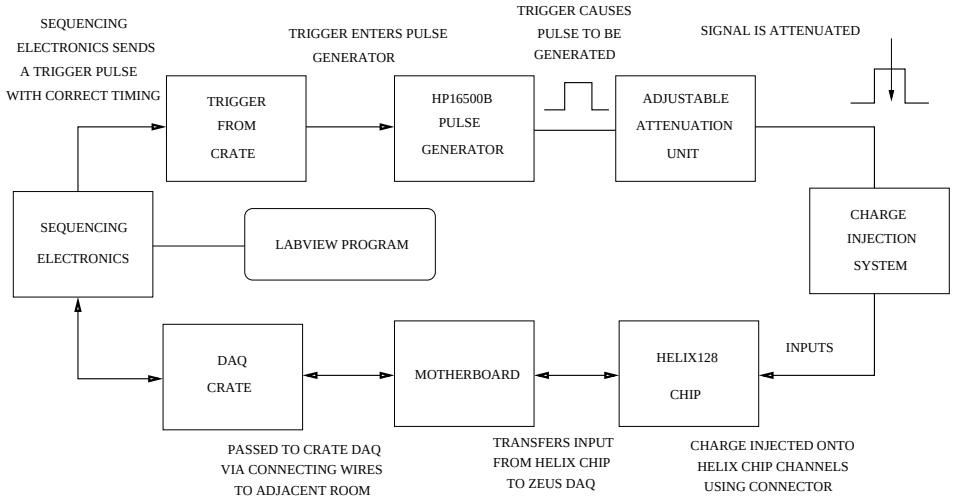

Figure 4.6: Diagram of experimental setup used for HELIX128 property studies.

pulse step (V_{gen}) of 2V height and 20μs length from the pulse generator is divided by the attenuator and applied via the charge injection system to the HELIX128 input. This may simulate the detector response for particles over a wide energy range. The dependence of the input charge on the attenuation (of V_{gen}) is given by equation (4.7), where $C_{in} = 4.4pF$ (figure 4.5).

4.3.3 Results of the HELIX128-3.0

The measured noise distribution of an unbonded HELIX128 channel is shown in figure 4.7 (N_i^k with pedestal offset P^k, see eq. (4.8)). It shows the "pure" noise of the HELIX128 front end electronics. The noise of a bonded channel is 1.5 times higher and with connected charge injection system it is 2.4 times as high as for an unbonded channel. In the final configuration the signal to noise ratio depends on the load capacitance of the silicon detector connected.

The chip noise dependence on the load capacitance has been studied in other collaborations [42], and it was shown to be linear in the range from 1pF to 60pF. These measurements have been repeated in our experimental setup but contained an external influence for low capacitances which we could not extract (figure 4.8). The detailed study of the ZEUS test setup was out of the scope of this work, so an independent noise slope study and other tests were postponed until the set up of a test stand for the HERMES Recoil Detector project at DESY Zeuthen [43][44].

The HELIX128 dynamic range is shown in the upper plot of figure 4.9. The dependence of the chip's response (S_i^k in equation (4.8)) on the injected charge is linear in the range of $\pm$10 MIPs. This is not sufficient to detect slow protons (up to 60 MIPs $\approx$ 7 MeV deposited energy).

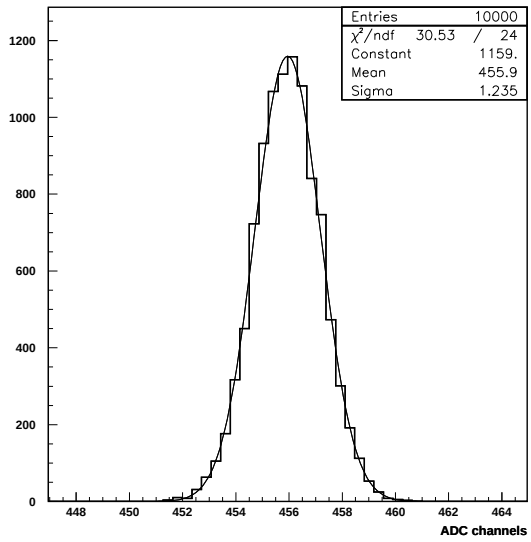

Figure 4.7: The noise distribution with constant offset of an unbonded ("open") channel.

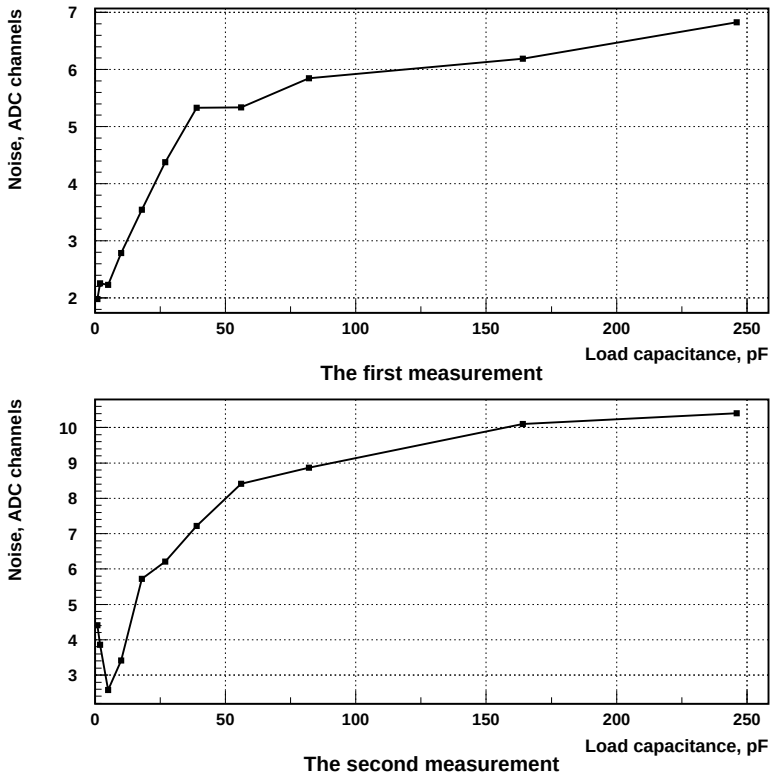

Figure 4.8: Measurements of the noise slope. The dependence should be linear up to 60pF.

The signal to noise ratio is shown in the lower plot of figure 4.9. With the charge injection system connected the signal to noise ratio is approximately 10 for 1 MIP and it is up to 200 for the saturated chip.

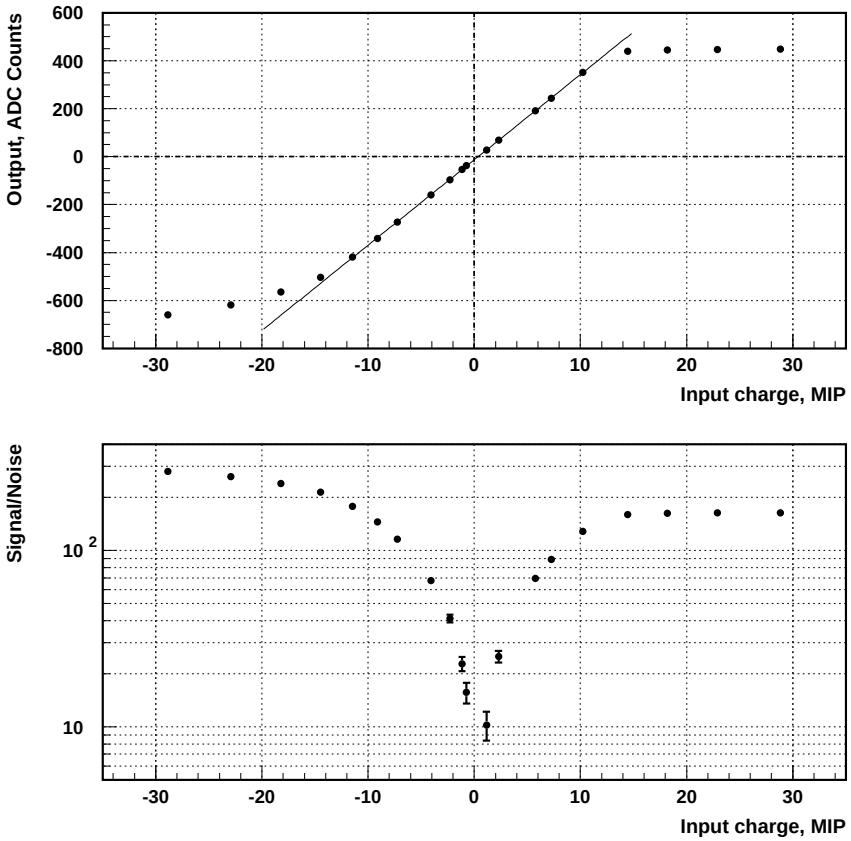

Figure 4.9: Upper plot: HELIX128 dynamic range, fitted by a straight line $kx + b$ ($k = 35.6 \pm 0.2$, $b = -13.5 \pm 1.5$). Lower plot: signal to noise ratio of a channel connected to the charge injection system.

One observed problem was a cross talk effect in the chip (figure 4.10). When charge is injected into one channel, a response of the two neighboring channels is observed (every other channel was bonded, so the neighboring channels are unbonded). This effect is asymmetric and it depends on the physical number of the channel. For positive charge injected into the even channels the cross talk is bigger in the following channel than in the previous one. Charge injected into odd channels causes bigger cross talk in the previous channel then in the following one (the channels are counted from 1). It varies from 10% for a non saturated channel up to 20% for highly saturated channels . The same effect has been observed in the ZEUS collaboration [41]. There it was measured for minimum ionising particles only, when HELIX128 is still in the linear range. The cross talk effect has been observed for negative input charge as well.

Because of the wide energy range of particles to be detected by the Recoil Detector, there will be a non–constant cross talk behavior (figure 4.10) in the HELIX128 and therefore one can correct for this effect for non–saturated channels only.

A possible way to extend the dynamic range is charge division. The chosen method is shown in figure 4.11b. The signal from the detector can be divided by a coupling capacitor into high gain and low gain readout channels. In order to avoid difficulties caused by the cross talk, independent chips for the high gain and the low gain channels are used.

The response of two channels, coupled by a 10pF capacitor to the injected positive charge can be seen in figure 4.12. In such a configuration the dynamic range is extended to ± 40 MIPs for the low gain channel. It can be made even wider by decreasing the

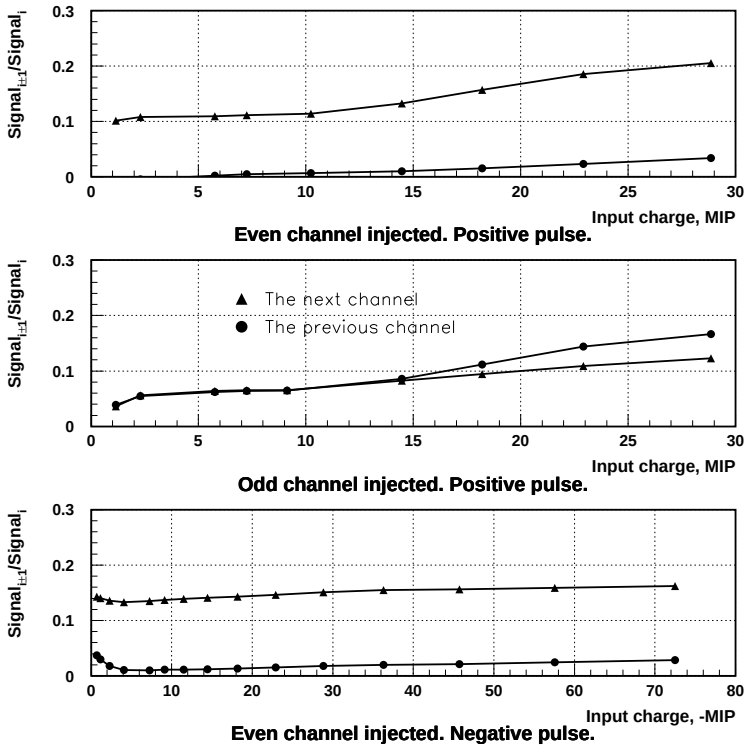

Figure 4.10: Cross talk observed in the neighbouring channels to the injected one. The two upper plots show the cross talk for the positive charge injected into even and odd channels. The lowest plot shows this effect for negative charge injected into an even channel. The neighboring channels are not bonded. The channels are counted from 1.

value of the coupling capacitor. In the final configuration for the silicon detector the 10pF capacitors result in a dynamic range of ±70 MIP (see section 4.4.3).

The fraction of the charge flowing into the high and low gain channels can be calculated from this data: the charge sensitive preamplifier of HELIX128 can be parameterized as an "effective" capacitance $C_{eff} = G \cdot C$ (figure 4.11a), where G is the gain of the amplifier. With the charge division measurements one can estimate the "effective" input capacitance. Using two coupled HELIX128 channels as shown in figure 4.11b and knowing the parameters of the dynamic range linear fit ($k_{high,low}x + b_{high,low}$ (figure 4.12)), one can derive

$$C_{eff} = C \cdot G = \frac{C_c - k \cdot C_c}{k} = 24.9 \pm 0.7\ pF \tag{4.12}$$

where $k = k_{low}/k_{high} = 0.286 \pm 0.006$, $C_c = 10\ pF$, and indexes $high$ and low correspond to the high and the low gain channels, respectively.

Now a charge division ratio can be derived (figure 4.11) as

$$\frac{q_{low}}{q_{high}} = \frac{C_c}{C_{eff} + C_c} \tag{4.13}$$

where q_{low} and q_{high} are the charges after the division in low and high gain channels. Using the results of equations (4.12) and (4.13) one can estimate the fractions of the produced

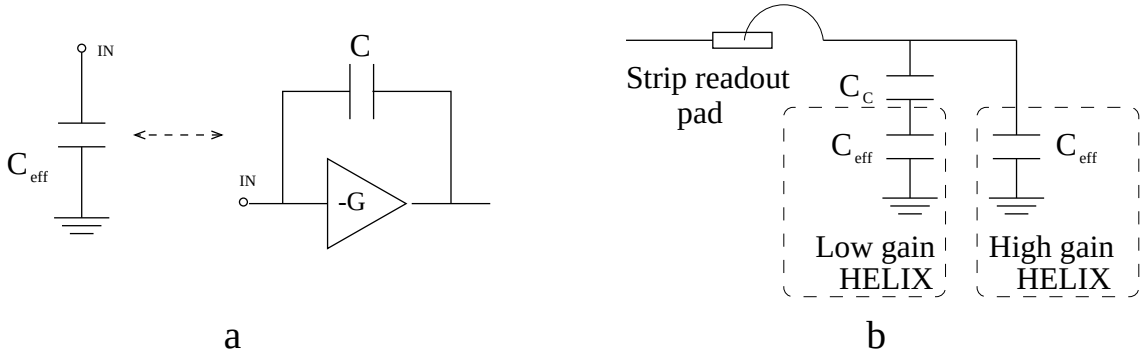

Figure 4.11: **a.** Equivalent schematic of the charge sensitive HELIX128 preamplifier. It can be represented as effective capacitance $C_{eff} = G \cdot C$, where G - the gain of the preamplifier. **b.** Schematic view of charge division. Capacitance C_c can be varied for the dynamic range adjustment.

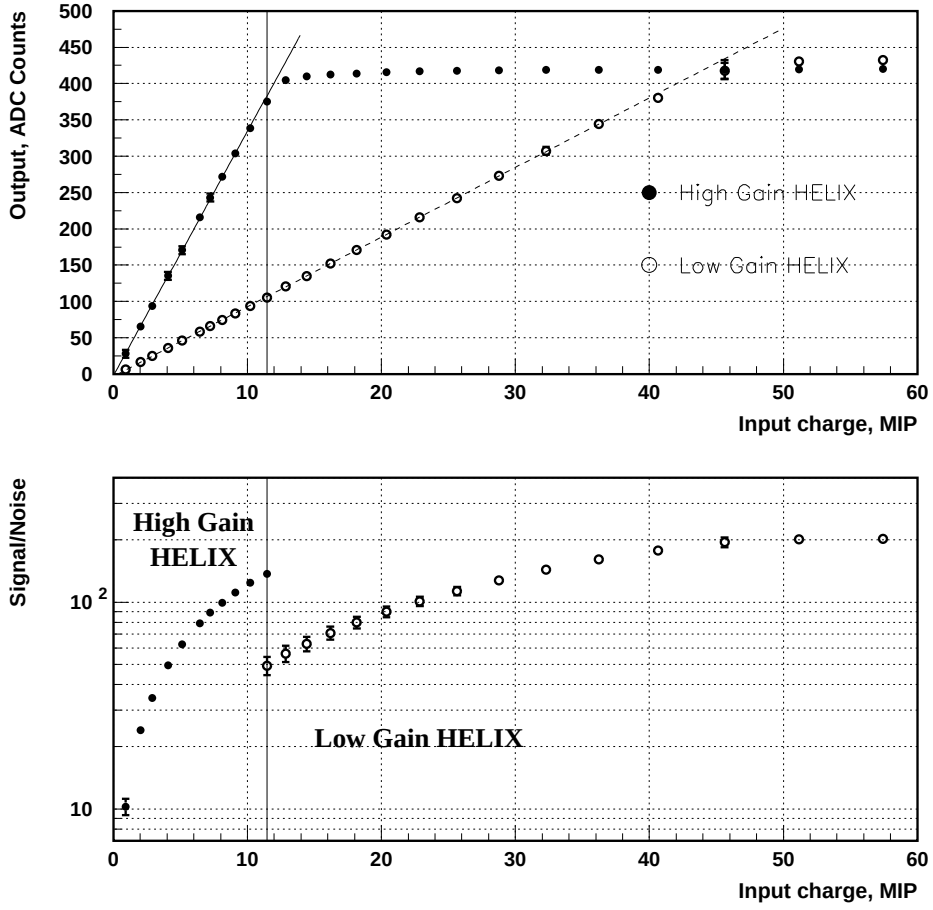

Figure 4.12: Responses of high gain and low gain HELIX128 channels coupled by a 10pF capacitor. Upper plot: HELIX128 dynamic range, fitted by straight lines $k_{high,low}x + b_{high,low}$. High gain channel $k_{high} = 33.6 \pm 0.6$, $b_{high} = -2 \pm 3.6$. Low gain channel $k_{low} = 9.6 \pm 0.1$, $b_{low} = -3.1 \pm 1.9$. Lower plot: signal to noise ratio. If the high gain channel gets saturated, the signal from the low gain channel is used.

charge $q_0 = q_{low} + q_{high}$ in the high and the low gain channels

$$\frac{q_{high}}{q_0} = \frac{C_{eff} + C_c}{C_{eff} + 2C_c} = 78\%, \qquad \frac{q_{low}}{q_0} = \frac{C_c}{C_{eff} + 2C_c} = 22\%.$$

The charge division measurements have been done for $C_c = 22pF$ as well. The dynamic range for 22pF is smaller and signal to noise ratio is worse for the high gain channel (figure 4.13). Following the calculations in equation (4.12) and using $k = k_{low}/k_{high} = 0.489 \pm 0.012$ and $C_c = 22pF$ instead, one gets $C_{eff} = 23.0 \pm 1.1\ pF$ which is consistent with the $C_c = 10pF$ result. The fractions of the detector response in the high and the low gain channels in this case are (see equation (4.13)):

$$\frac{q_{high}}{q_0} = \frac{C_{eff} + C_c}{C_{eff} + 2C_c} = 67\%, \qquad \frac{q_{low}}{q_0} = \frac{C_c}{C_{eff} + 2C_c} = 33\%.$$

Some measurements of HELIX128 characteristics were done with 5MHz sampling frequency. The dynamic range and cross talk of the chip in this mode are the same as at

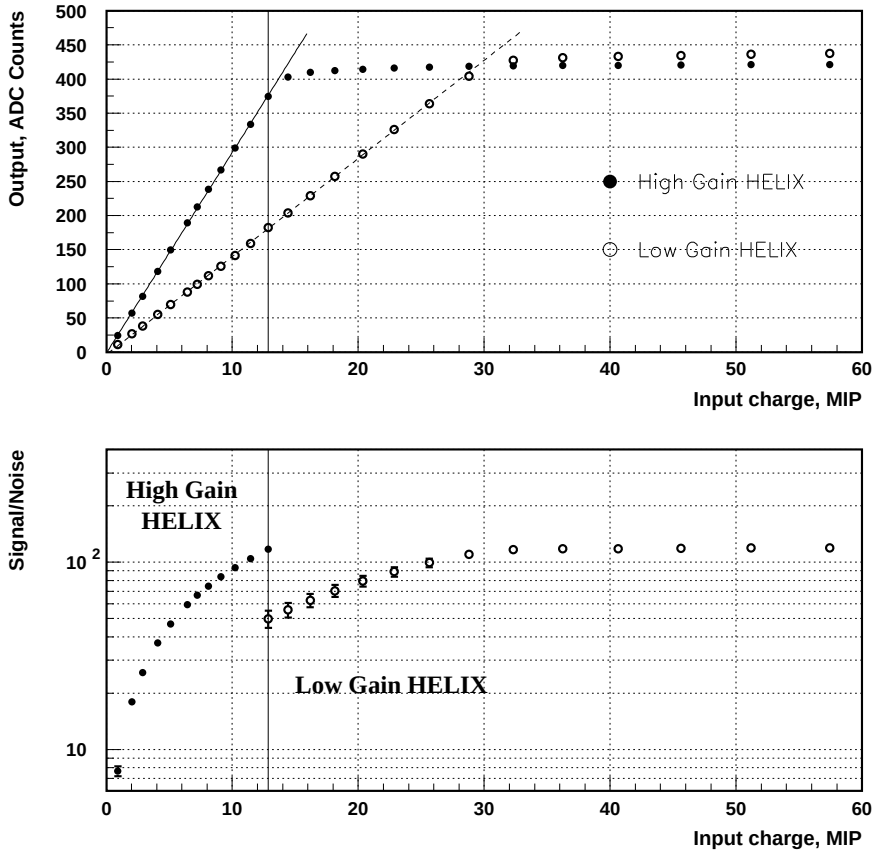

Figure 4.13: Responses of high gain and low gain HELIX128 channels coupled by a 22pF capacitor. Upper plot: HELIX128 dynamic range, fitted by straight lines $k_{high,low}x + b_{high,low}$. High gain channel $k_{high} = 29.4 \pm 0.4$, $b_{high} = -1.5 \pm 3.1$. Low gain channel $k_{low} = 14.4 \pm 0.2$, $b_{low} = -3.8 \pm 2.2$. Lower plot: signal to noise ratio. If the high gain channel gets saturated, the signal from the low gain channel is used.

10MHz, but the common mode noise contribution is less: for 10MHz sampling clock frequency the contribution of the common mode noise is 30% of the total channel noise, but at 5MHz it is only 5% (under our experimental conditions).

4.4 Test Beam Experiment

In this section the results obtained from the first prototype of the HERMES Silicon Recoil Detector using the DESY II electron beam are presented. The use of the charge sharing by capacitive coupling method is tested to investigate the increase in the dynamic range of the HELIX128-3.0 readout chip with a prototype detector attached.

4.4.1 Experimental Setup

The measurements presented in this section were performed with two different experimental setups. For data with minimal ionising particles (MIP) a test beam telescope at the DESYII electron beam was used. Charge injection measurements were mainly done using a readout system of a ZEUS laser test stand. In order to compare both measurements, the charge injection system was connected to the telescope readout as well.

Test Beam Setup

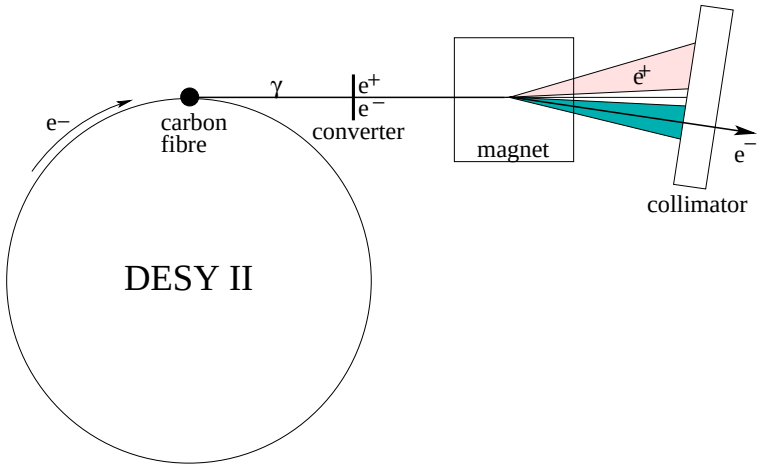

Figure 4.14: Generation of electrons for the test beam area 22 [45].

The beam telescope of the ZEUS Micro Vertex Detector (MVD) collaboration was used for a first beam test. It is installed at the beam line 22 at the DESY II accelerator at DESY Hamburg. The electrons of this beam are generated as depicted in Figure 4.14: a Bremsstrahlung beam is generated by a carbon fibre in the circulating electron synchrotron beam DESY II, a metal plate is used to convert this Bremsstrahlung photons into electron/positron pairs, a dipole magnet spreads the beam out into a horizontal fan, and a set of collimators form the extracted beam. The magnet is also used to control the energy of the beam. This parasitic test beam provides electron energies from 1 to 6 GeV. In this range the electrons are minimal ionising particles (MIPs) [46].

The silicon telescope, depicted in Figure 4.15, consists of four scintillating counters for triggering, three reference detectors, and a device under test (DUT) movable via an xyϕ table. All devices are positioned on an optical bench and the modules can be shifted in $\pm$z

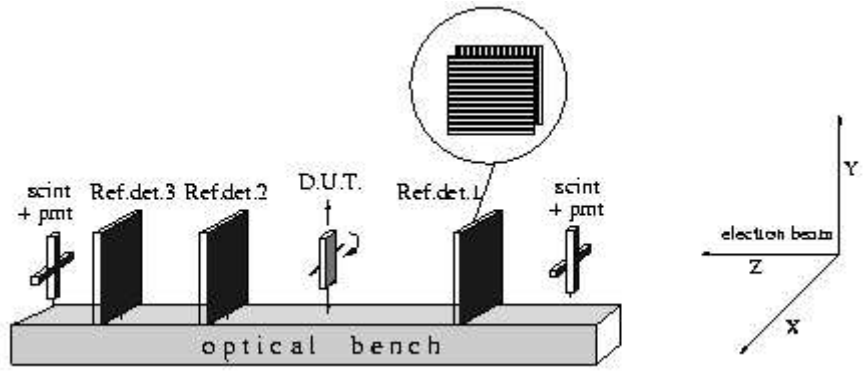

Figure 4.15: Sketch of the beam telescope at DESY II. The telescope consists of three reference detectors, a DUT movable via an xyϕ table, and four scintillating counters for triggering [47].

direction. Figure 4.16 shows a photograph of the beam telescope at DESY II. A coincidence of up to four scintillating finger counters each (1 cm wide), two at the front and two at the back of the telescope, provides a trigger for the readout. Due to the width of these scintillators, the trigger accepts events in roughly a 1 cm by 1 cm window.

Each of the silicon reference modules has two high resolution single sided strip sensors (x–y orientation). The reference detectors define precise tracks, but for the results presented in this thesis the data from the reference system was not used. The DUT is positioned between the second and the third reference detector.

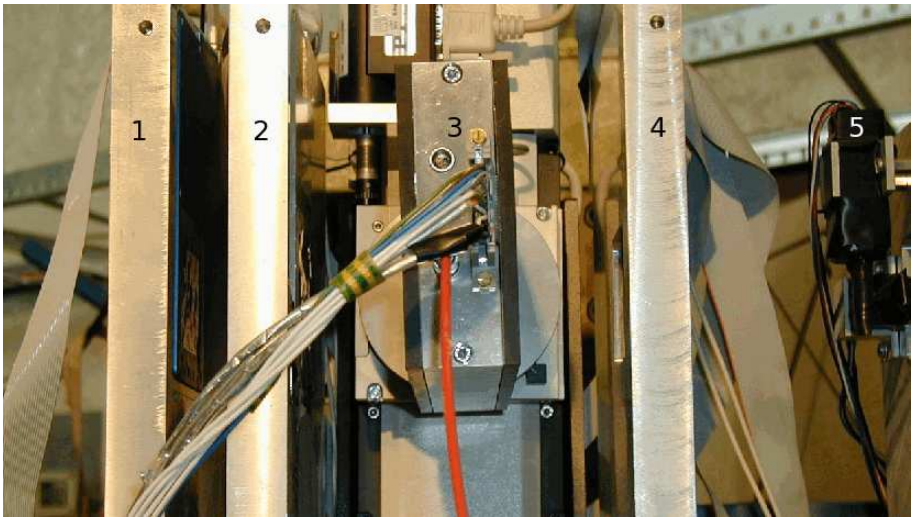

Figure 4.16: Photograph of the beam telescope at DESY II. From left to right: two reference detectors in aluminium boxes, the DUT on an xyϕ table, and the third reference detector; at the very right end two of the four scintillating trigger counters.

The DUT is programmed by a sequencer (SEQSI) [48] and read out via an ADC (V550) [49]. The setup is run using a 1 MHz clock, which is phase locked to the DESY II 1 MHz RF system. A detailed description of the complete test stand can be found in [41].

All measurements presented in this section were carried out with 1 GeV electrons.

Charge Injection Setup

The dynamic range of the HELIX128 3.0 with charge sharing system was studied using direct charge injection [50]. The setup was also used to calibrate these results with 1 MIP particles.

A MIP passing a 300 μm thick silicon layer generates about 24000 electron/hole pairs. This amount of charge was created using a pulse generator, an attenuator, and a coupling capacitor C_{in}. The function of the charge injection system is shown in Figure 4.5. Figure 4.17 shows the ZEUS hybrid which was used for these tests. The attenuated signal

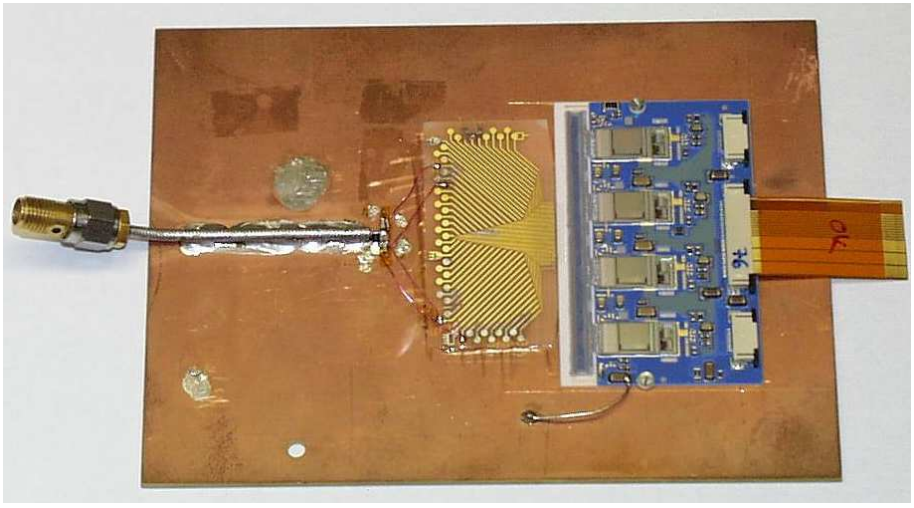

Figure 4.17: Photograph of the ZEUS hybrid used for the charge injection measurements.

is fed into the connector at the left side. The capacitors are not visible due to their small size.

4.4.2 Device Under Test

First Prototype

A module for the HERMES Silicon Recoil Detector will consist of sensors for particle detection, the analog readout, and the necessary control- and supply circuits. The TIGRE sensors from MICRON Semiconductors Ltd. are 99 mm × 99 mm square, double sided and have a thickness of 300 μm. The strip pitch is 758 μm and they have 128 strips per side (p-side and n-side). The n-side uses strip separation by p^+-stops around all structures. As analog readout chip for the Silicon Detector the programmable HELIX128 3.0 was chosen [50]. One of the advantages of this chip is, that it is already used in the Lambda Wheel Detector of HERMES [51]. Therefore the same control- and readout electronics can be used with minor modifications for the final readout.

The HELIX128 is an analog chip designed for gas microstrip detectors and silicon strip detectors. Each of its 128 channels has an amplifier stage, a shaper and a pipeline capacitor array. A detailed description of the chip's architecture and registers can be found in [47, 38]. This chip is able to store acquired signals in a pipeline cell. Thus the chip can be read out after a trigger decision.

The HELIX128 is mounted on a hybrid circuit, which also provides the appropriate layout of the inputs and outputs. For the prototype modules a ZEUS hybrid[1] with four

[1] a PCB for the ZEUS Micro Vertex Detector (MVD)

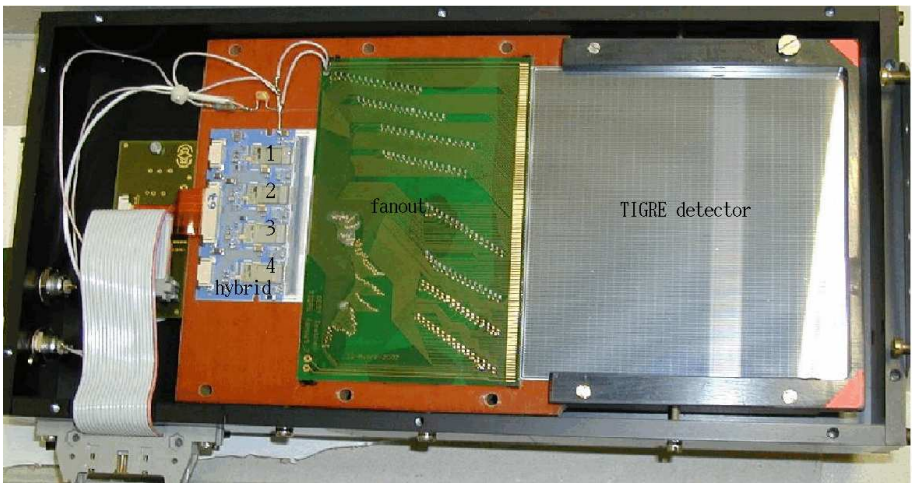

Figure 4.18: Photograph of the first prototype for the HERMES Silicon Recoil Detector. The main parts are the TIGRE sensor (large reflecting square, right), the "fanout" (middle) and the hybrid (left of fanout).

HELIX128 3.0 used. Another advantage of the use of the ZEUS hybrid is the available interface at the test beam readout. Later tests were performed with the final hybrid for the HERMES silicon project [43][52][53].

The first prototype module was prepared for the beam tests including the charge sharing. The principle of charge sharing is depicted in Figure 4.11.

Figure 4.18 shows this prototype module in a special frame. The main parts are the sensor (large reflecting square, right), the "fanout" (middle) and the hybrid (left of fanout). The TIGRE sensor (device #1869-17) is connected to two HELIX128 chips, one as high and one as low gain chip. Since the sensor has a pitch of 758 μm whereas the ZEUS hybrid has a pitch of 125 μm a pitch adapter is necessary. A special PCB, the so-called fanout, was designed for this purpose. Its design includes the pitch adapter and the charge dividing capacitors. Furthermore, it allows the possibility to route the high and low gain channels to separate HELIX128 chips. Only the second and third HELIX128 were connected to the fanout with Helix #2 (#3) being the low (high) gain chip.

The complete module was shielded in an aluminium box in order to attach it to a support frame on an xyϕ table in the telescope. Furthermore, this box protects the module from damage and light. Thin aluminium foil windows in front of and behind the sensor allow the 1 GeV electrons to pass the through the sensor with minimal multiple scattering.

General Settings

Numerous operating parameters of the HELIX128 chip can be controlled by setting values in the chip's internal registers. During the beam measurements all settings were kept constant to have comparable sets of data. Table 4.1 summaries the standard register settings with corresponding currents and voltages. They were used during the test described here. A detailed description of these parameters can be found in [38, 47]. Fine tuning of the parameters may yield a better signal to noise ratio (S/N), but due to limited time the default parameters were used. Fine tuning was done later for the final detector during laboratory tests with a finalised hybrid in Zeuthen[44][54].

The supply voltages were set to $\pm$2.1 V, measured at the driver board close to the telescope. The silicon sensor was biased with 60 V. The sensor of the DUT, #1869-17, is fully depleted at voltages larger than 50 V.

Name	DAC-counts	I(μA)	Name	DAC-counts	U(V)
I_{pre}	80	200	V_{fp}	142	0.219
I_{sha}	40	100	V_{fs}	226	1.531
I_{buf}	40	100	V_{d}	69	-0.922
I_{pipe}	16	40	V_{dcl}	194	1.031
I_{sf}	40	100	V_{offset}	110	-0.281
I_{driver}	36	90	$V_{compRef}$	142	0.219
I_{comp}	20	50			

Table 4.1: Standard HELIX128 settings (register values with corresponding currents and voltages) used during the beam tests.

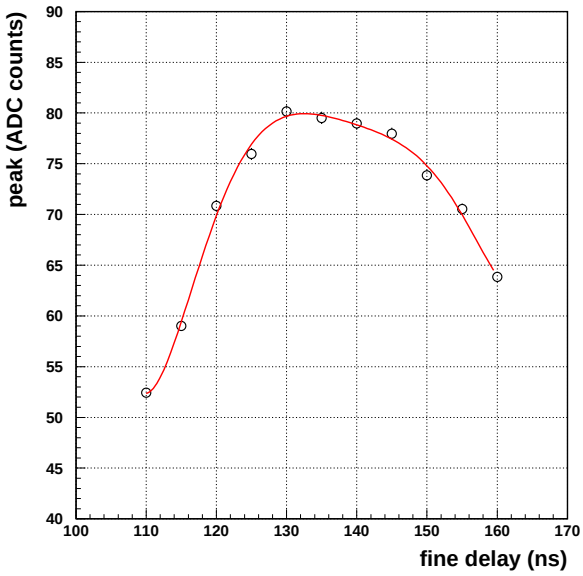

Figure 4.19: Most probable peak of the Landau energy deposition distribution for 1 GeV electrons in 300 μm silicon (n-side) versus the delay.

Timing

The HELIX128 preamplifier output voltages are stored in a sample&hold capacitor array of 129 $\times$ 141 cells. Each cell capacitor is connected by a read switch to a read line and by a write switch to the write line. The timing of the readout system has to be set such that the pipeline column in which the event was stored is marked to be read out. Therefore the readout pointer marking the readout column has to be delayed. This delay (latency) can be set by means of the *Latency* register. The latency gives the time (in number of clock cycles) between the trigger pointer and the write pointer within the HELIX128 [38]. An additional fine tuning of the timing is necessary to sample the shaper peak of the signal. The measurement of such a delay curve helps to find this peak. The fine delay is adjusted by a delay unit which can be adjusted in 1 ns steps. For several fine delay settings 5000 events were taken. Plotting the most probable peak of the Landau distribution (see Section 4.4.3) versus the time gives the delay curve. Figure 4.19 shows the delay curve for the n-side measurement. The centre of the plateau is located at around 135 ns. The delay curve for

the p-side is shifted by 10 ns to shorter delays due to the difference in the mobility of holes and electrons and thus different charge collection times: p-side slow, n-side fast.

Pedestals and Noise

The use of a complete sensor with all strips connected to the readout gave the possibility to measure the pedestal distribution of each strip. Figure 4.20 depicts a sample of such a pedestal distribution. The common mode noise is subtracted. The noise of the strips is defined as standard deviation σ of the Gaussian fit of this distribution. In Figure 4.21

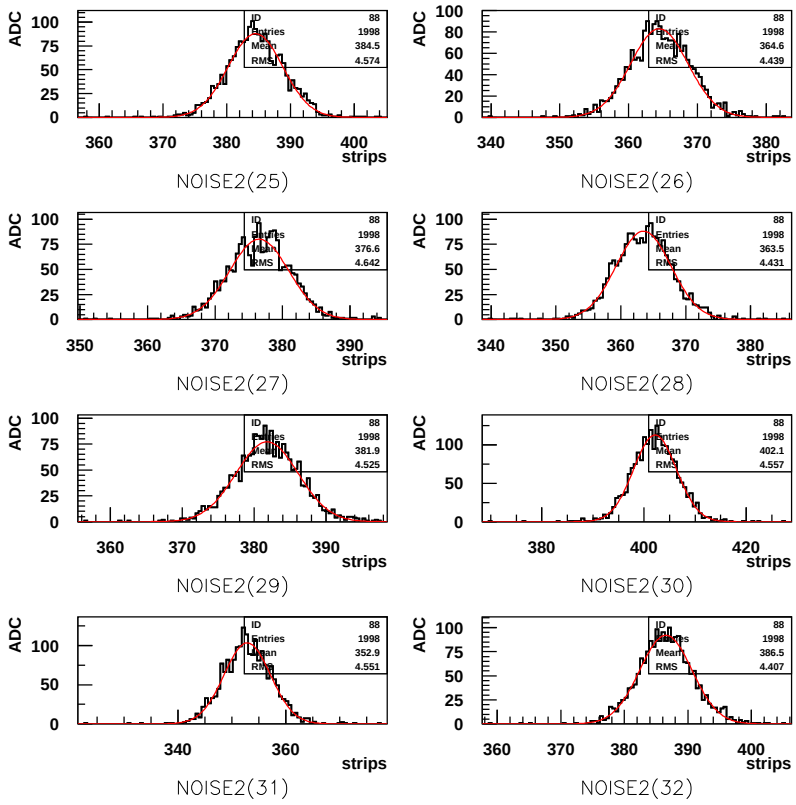

Figure 4.20: The Gaussian distributed pedestals (common mode subtracted) for a sample of low gain strips. The noise is defined as the σ of the Gaussian fit. Due to lack of space, the σ is not depicted in the plots.

the noise of the low gain HELIX128 (upper part) and high gain HELIX128 (lower part) is depicted. In the case of the low gain chip a clear dependence on the coupling capacitor is visible since the coupling capacitor mainly determines the input capacitance. The noise increases with an increasing coupling capacitance from 4.2 ADC counts for a 4.7 pF coupling capacitor up to 6.1 ADC counts for a 22 pF coupling capacitor. During a second test beam period this noise had increased up to 10 ADC channels due to an unknown problem with the setup. Since the noise of the module didn't increase when tested in the laser test stand this was clearly a problem of the test beam setup. Since no future tests are planned with this test stand no detailed noise studies were done.

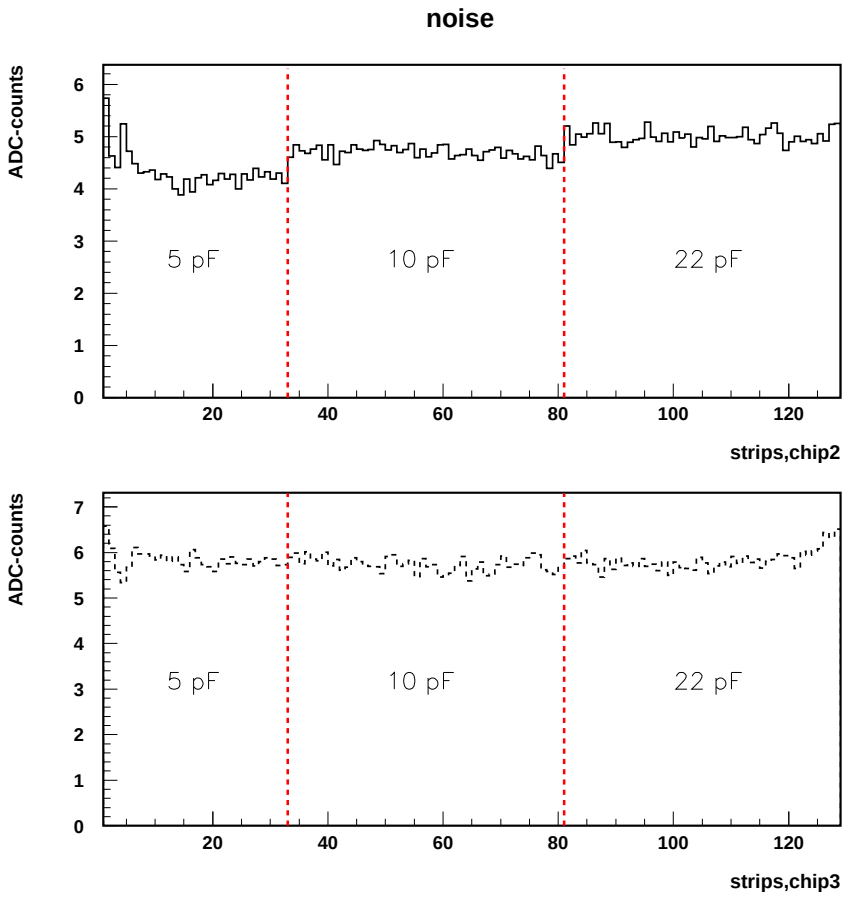

Figure 4.21: Noise of the low gain (chip 2) and high gain (chip 3) versus the strip number.

4.4.3 Calibration

Energy Loss Distribution of all Hit Strips

In Figure 4.22 the energy loss distribution of the electrons in the high gain chip is depicted. With the given beam size usually about 13 strips are covered by the trigger counter area. For every event the strip with the maximum ADC value was taken into account, but only if this signal was larger than the 3σ threshold. Using this cut the Gaussian distributed noise is eliminated leaving only the signal. The resulting distribution is fitted with an approximation of the Landau distribution

$$L(\lambda) = \frac{1}{\sqrt{2\pi}} \exp(-\frac{1}{2}(\lambda + e^{-\lambda})) \tag{4.14}$$

with

$$\lambda = \frac{\Delta E - \Delta E_p}{\xi} \tag{4.15}$$

$$\xi = 2\pi N_A r_e^2 m_e c^2 z^2 \frac{Z}{A\beta^2} \rho x \tag{4.16}$$

where ΔE is the energy loss in a layer and ΔE_p the most probable energy loss in a layer [36]. The most probable peak (parameter P2 in the fit procedure) of the Landau is defined as the actual signal size. A fit using a truncated Bethe-Bloch formalism would yield a better agreement with the data, but this would have no effect on the conclusions from this work.

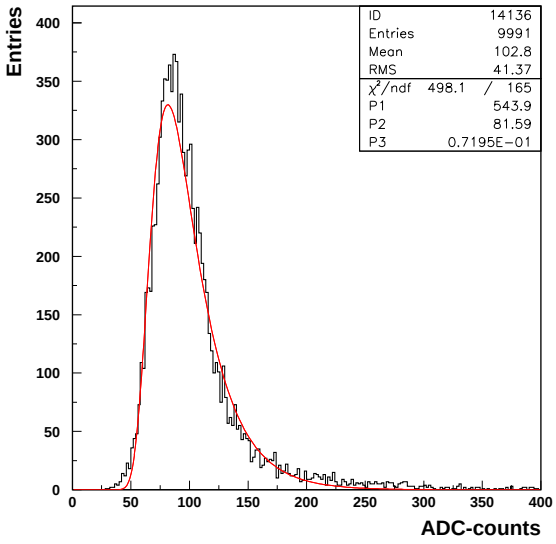

Figure 4.22: Landau distribution for a 10000 event run taken with the n-side of the sensor connected. All hit strips of the 4.7 pF high gain channels were taken into account.

Energy Loss Distribution in Single Sensor Strips

Due to the large width of the strips the energy of the passing electron is mainly deposited in one strip. Therefore it is possible to extract the distribution of the deposited charge from a single channel. Histogramming the ADC counts of one high gain strip for each event results in a distribution of the type depicted in Figure 4.23. Again a cut of three times σ

above the noise was applied and the distribution then fitted with a Landau approximation. P2 is the fit parameter for the most probable peak.

In the case of the low gain channel (Figure 4.23), the Gaussian distributed noise and the signal are not distinguishable anymore. Therefore these distributions were fitted with a Landau+Gauss fit. It was also tested if cuts with different thresholds or a pure Landau approximation result in a better χ^2/ndf, but this was not the case. For very small signals in the low gain channel both fitting methods did not result in reasonable values. Therefore all further results are derived with a Landau fit only for the high gain channel and a Landau+Gauss fit for the corresponding low gain channel.

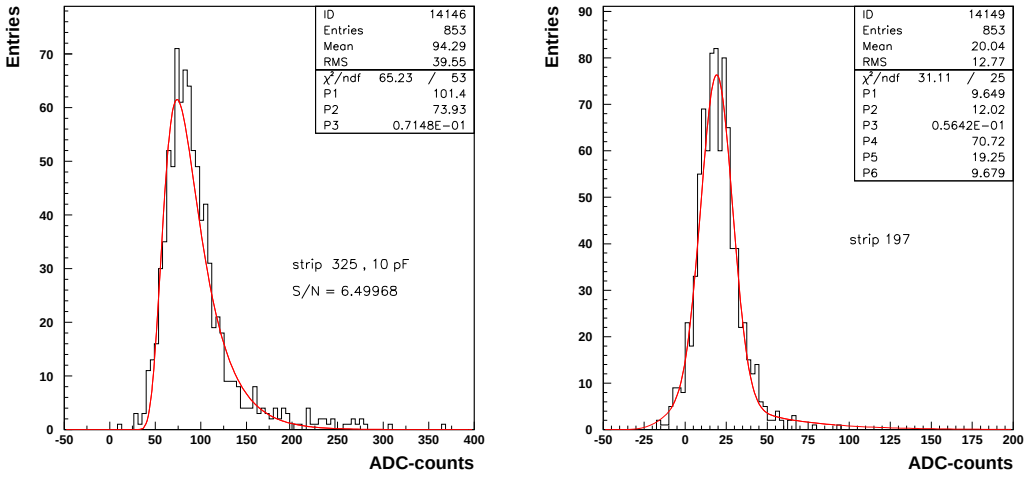

Figure 4.23: Left: ADC count distribution for one sample high gain channel. Right: ADC count distribution for the corresponding low gain channel. P1-P3 are the fit parameter for the Landau distribution, P3-P5 the fit parameter for the Gauss distribution.

Charge Injection for Cross Calibration

During the charge injection studies the unit "MIP" was defined as the charge equivalent to 24000 electrons ($2.4{\cdot}10^4 \cdot 1.6 \cdot 10^{-19}$ As = 4 fC) directly injected into the HELIX128 input, negative MIPs stands for negative charge. Figure 4.24 depicts the response of the high gain HELIX128 chip in ADC counts (charge injection into one channel). In this case the charge division with a 4.7 pF capacitor was used. Considering only the linear range of Figure 4.24, the dynamic range is estimated to be about ±70MIPs. It was decided later that the final setup would use 10 pF charge division capacitors, which has a charge injection dynamic range of ±40MIPs[52][53]. The work presented here uses the 4.7 pF capacitor charge division value.

In the case of the prototype with a sensor, the charge is generated within the silicon and transported via the fanout to the charge division and further on to the HELIX128. Because of the large total capacitance of the TIGRE and additional loss due to the stray capacitance of the fanout, about half of the electrons/holes generated by a MIP is lost. Therefore a calibration was performed.

The charge injection system was connected to the test beam setup and former measurements were repeated with this readout. Since the ADC in the test beam area was selected for the use with 1 MIP data, its dynamic range is limited to a few MIPs. Figure 4.25 depicts

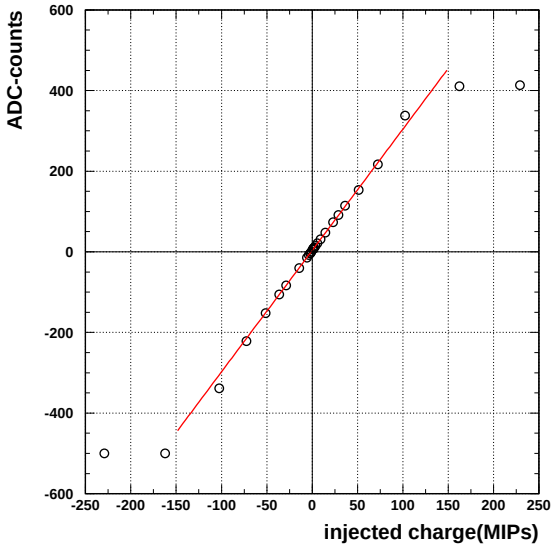

Figure 4.24: Response of the HELIX128 high gain channel to injected charge measured with the setup in Hall 1. One MIP is equivalent to 24000 electrons. The saturation in the negative range is due to saturation of the ADC.

the response of the HELIX128 to injected charge measured with the telescope readout. A charge equivalent to one MIP (24000 electrons) results in a signal of (196±6) ADC counts. Comparing this to (100±5) ADC counts measured with 1 GeV electrons (see Section 4.4.4) there is a factor of 1.95 between both measurements. This leads to a dynamic range of 70 MIPs×1.95=136.5 MIPs $\sim$ 135 MIPs for the 4.7 pF capacitor. Using calibration values determined for a 10 pF charge division capacitor [52], which is used in the final detector setup, a dynamic range of $\sim \pm$70MIPs was measured.

These values both appear to be sufficient for the necessary dynamic range of |70| MIPs for the Silicon Recoil Detector.

4.4.4 Experimental Results

Comparison p-Side with n-Side

The support structure of the TIGRE sensor was designed to be able to connect either the p- or the n-side of the sensor to the fanout. The frame within the box clamps the TIGRE sensor in a fixed position. This gives the possibility to test both sides of the sensor with the same hybrid with HELIX128 chips. For this purpose the wire bonds between fanout and sensor were removed, and the sensor was flipped and rebonded. The pads on the fanout are large enough to repeat such a procedure a couple of times. The readout for the n-side was exactly the same as for the p-side except the reversed sensor bias voltage and another fine delay adjustment (see Section 4.4.2). During the analysis the same programs were used. The ADC counts after pedestal and common mode subtraction were simply multiplied with (-1) to use the same fitting procedures.

Long runs (10000-15000 events) were taken for the p-side and for the n-side. By leaving the xyϕ-table in the same position for p- and n-side measurements (4.7 pF), the same channels detected signals during the runs.

Figure 4.26 depicts the most probable peaks extracted for a number of channels for the

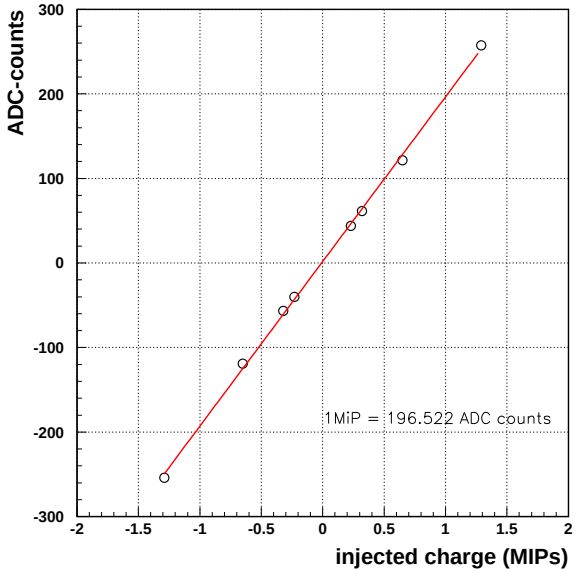

Figure 4.25: Response of the HELIX128 low gain channel to injected charge measured with the test beam setup in Hall 2. One MIP corresponds to 24000 electrons.

p-side and the n-side respectively. The peak values for either type are scattered within a ±5% band around the mean value. The ∼20% difference between the signal size of the p-side and that of the n-side can be explained by the difference in the total capacitance.

In Figure 4.27 a simplified network of the involved capacitances for three channels is shown. C_{STR} is the total capacitance of a strip and C_{int} the inter-strip capacitance. Both are different for p-side and n-side and are given in Table 4.2. The coupling capacitance C_C

	p-side	n-side
Strip capacitance C_{STR}	34 pF	54 pF
Interstrip capacitance C_{int}	9 pF	7 pF

Table 4.2: Total strip capacitance and inter-strip capacitance for the p-side and n-side of the TIGRE detector [55]

is 1 nF in the case of the TIGRE. C_{virt} is the total input capacitance of the electronics including the fanout, the low gain HELIX128, and the high gain HELIX128. C_{virt} has an estimated value of 45 pF. Using these numbers the signal height of the n-side is expected to be about 17 % less than the signal height of the p-side.

Signal to Noise Ratio S/N

The method described in Section 4.4.3 was also used to derive the signal to noise ratio S/N. Due to the large total capacitance of the TIGRE about half of the charge does not reach the HELIX128 and is lost. Furthermore, the test beam setup is noisy. This results in a S/N of 6 for a 22 pF coupling capacitor and about 6.5 for 10 pF and 4.7 pF. For the p-side the S/N is about 20% larger because of the larger signal height as described above. The noise of the system was comparable for both sensor sides. These numbers are for 1 MIP signals.

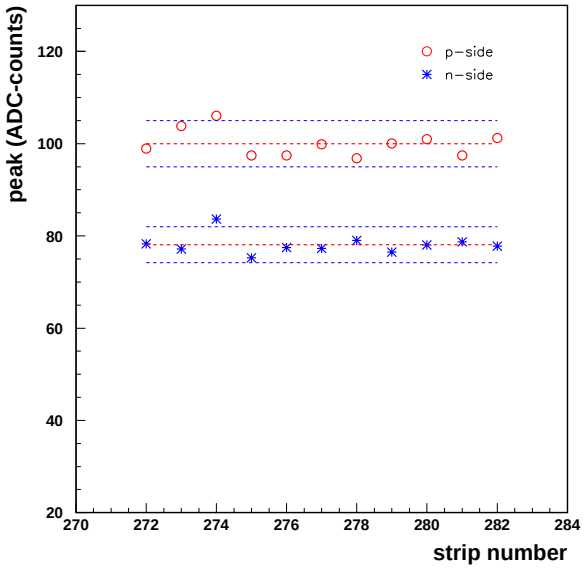

Figure 4.26: Comparison of the most probable peaks for the n-side and p-side. For both sides all values are within a ±5% band around the mean value. The difference between n-side and p-side signal size can be explained by the difference in the total capacitance of both strip types.

Charge Division

Laboratory measurements proved that the dynamic range of the HELIX128 can be increased significantly using charge division by capacitive coupling. These studies were performed with a ZEUS hybrid for a small number of channels using the laser test stand [50]. In the case of the prototype module with sensor each channel was equipped with charge division, using different capacitors (4.7 pF, 10 pF, 22 pF). During the beam test the module was moved between runs in order to collect data for all three types.

In order to compare both measurements the most probable peaks of the Landau distribution were extracted for single strips according the procedure described in Section 4.4.3. For very small signals in the low gain channel (4.7 pF–coupling), the fit didn't result in reasonable values. But since the low gain channel is designed for low momentum protons with large energy deposition, this is not necessary.

In Table 4.3 the expected fraction of charge flowing into the high and the low gain channels is given for all three capacitors and both types of measurements. The results agree within the uncertainties of roughly 10 %.

Coupling capacitor	charge q_{high}	charge q_{low}	1 MIP q_{high}	1 MIP q_{low}
22 pF	67 %	33 %	72 %	28 %
10 pF	78 %	22 %	82 %	18 %
4.7 pF	86 %	14 %	–	–

Table 4.3: Charge division for 22 pF, 10 pF and 4.7 pF capacitive coupling for charge injection [50] and real MIP data. In case of the 4.7 pF coupling capacitor the extraction of the low gain signal was impossible due to its small size.

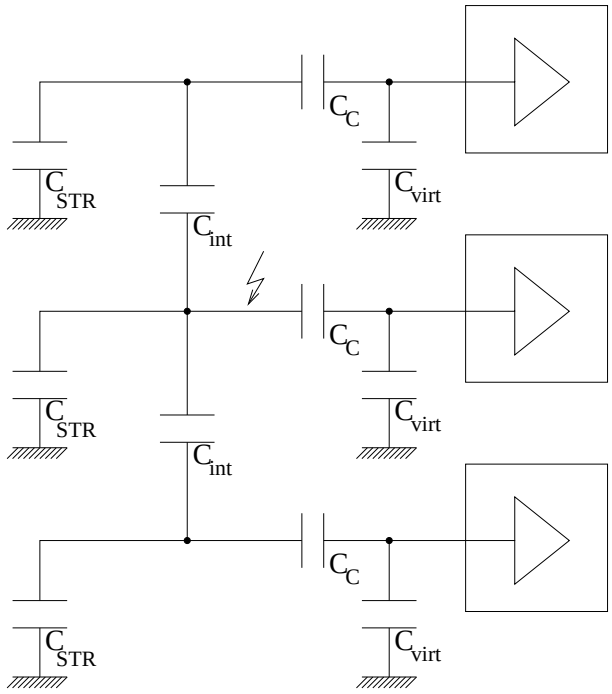

Figure 4.27: C_{STR} is the total capacitance of a strip and C_{int} the inter-strip capacitance. C_{virt} is the total input capacitance of the electronics. C_{TIGRE} the total capacitance of a sensor strip, is 38 pF for the p-side and 21 pF for the n-side. C_{FANOUT} is the capacitance of the fanout, assumed to be of the order of 15 pF. The effective capacitance C_{eff} of the HELIX128 is 31 pF [51] and the coupling capacitor C_C is 4.7 pF.

4.4.5 Conclusions

A first prototype module for the HERMES Silicon Recoil Detector was built and tested with 1 GeV electrons at DESY II. It was shown that the concept of charge division is working under realistic conditions. A comparison between direct charge injection measurements and 1 MIP data leads to a dynamic range of |100| MIPs for the 4.7 pF capacitor and |70| MIPs for the 10 pF capacitor which are both sufficient to satisfy the necessary dynamic range of |60| MIPs required by the Silicon Recoil Detector.

Because of the large total capacitance of the TIGRE about half of the electron/holes generated by a MIP is lost. This leads to the relatively small S/N, but at the same time increases the effective dynamic range.

Chapter 5

Recoil Detector Monte Carlo

In this section a detailed description of the integration of the Hermes Recoil Detector into the Hermes Monte Carlo software chain will be presented, first looking at the various software packages and then at a tracking procedure developed specifically for the Recoil Detector.

The Hermes software chain has a modular framework of separate programs which each serve a specific, individual function but which use the same database format for the information that allows them to be used together to form the overall Hermes Monte Carlo (HMC). The Monte Carlo scheme used at HERMES therefore consists of two distinct parts, Generator Monte Carlo, (GMC) and Hermes Monte Carlo, (HMC). A schematic overview is shown in Figure 5.1. The physics events generated in GMC are passed through the Monte Carlo simulation, HMC, and then the track reconstruction of the event is done in HRC, the Hermes Reconstruction Code.

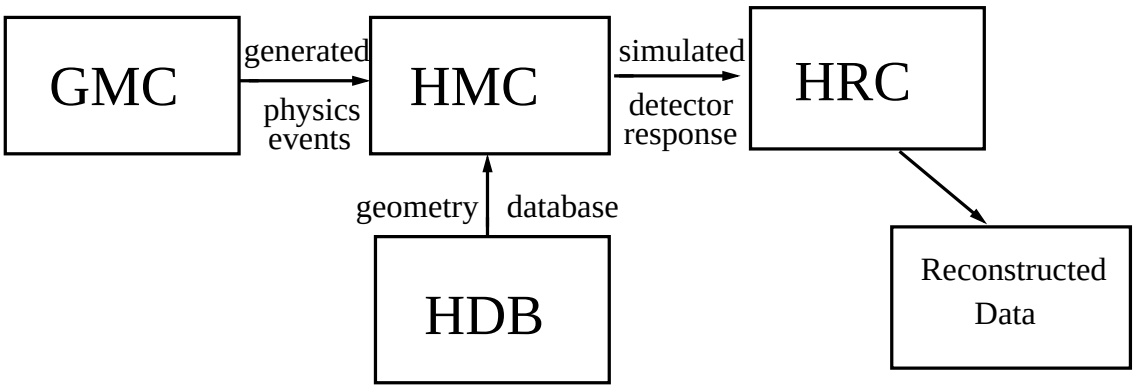

Figure 5.1: The Hermes Monte Carlo software chain

5.1 GMC - Generator Monte Carlo

In the Monte Carlo chain the first stage consists of a suite of physics generators that simulate different physical processes. The type of physics that is generated can be chosen by using the appropriate generator. For example, for the Recoil Detector an important physics generator will be the DVCS/BH (Deeply Virtual Compton Scattering/Bethe-Heitler) generator. The processes studied by the Recoil Detector will generally produce a low momentum proton at large laboratory angles. One such process is known as Deeply Virtual Compton Scattering

(DVCS) and has a competing process in which the same final state results from a different mechanism known as Bethe-Heitler (BH) or Brehmsstrahlung. The events generated by these programs have a standard output format which means that they can be used in the Hermes Monte Carlo (HMC). There is also the possibility of customising or creating a personalised generator for particular events if they are not available in one of the standard generators.

5.1.1 Cosmic RAY Generator - CRAYG

As part of the implementation of the Recoil Detector into the Hermes Monte Carlo a generator which produces cosmic ray muons had to be created and developed. This generator allows the path of cosmic rays incident on the Recoil Detector to be simulated. This provides us with the opportunity, for example, to investigate the viability of cosmic rays for alignment purposes.

Cosmic rays, apart from those associated with solar flares, come from outside of the solar system. The particles which are most numerous at sea level are muons. Most muons are produced high in the atmosphere (typically around 15km). The overall angular distribution of muons at the ground is $\propto \cos^2\theta$, which is characteristic of muons with $E_\mu \sim 3$ GeV. At lower energy the angular distribution becomes increasingly steep, while at higher energy it flattens, approaching a $\sec\theta$ distribution for $E_\mu \gg \epsilon_\pi$ and $\theta < 70°$[34].

The events produced by the Cosmic Generator assume that the average energy of the muons produced is 3 GeV and that the angular distribution of the cosmic rays follow a $\cos^2\theta$ dependence (Figure 5.2).

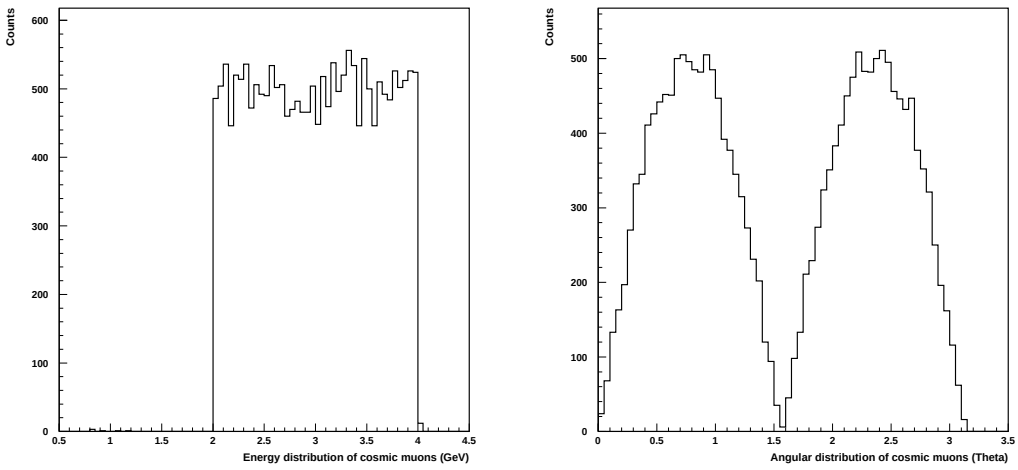

Figure 5.2: Left: Energy distribution of cosmic muons generated in CRAYG. Right: Angular distribution, θ of generated cosmic muons in CRAYG.

To simulate the straight line tracks of a cosmic ray passing through the Recoil Detector two back to back particles which originate from within the detector were produced. The reason for generating the cosmic rays from within the Recoil Detector is that in this way most of the generated particles will pass through the detector whereas if the production point of the vertex was outside the region of the detector then most of the generated cosmic rays would not intersect the Silicon Detector, and, therefore be a waste of computing time. The first step of this process is to define a plane which is the xz plane with regard to

the HERMES reference coordinate system. The program then generates a random point on the plane which is used as the vertex where the particles are produced. The plane in which the vertices lie is placed within the center of the Silicon Detector itself. A muon of the appropriate energy and angular distribution is then produced from this newly defined vertex. In order to produce a particle of the opposite direction with the same kinematics, the opposite momenta of the initial particle are taken and used to produce a second particle traveling in the opposite direction. This back to back particle, from a simulation point of view, appears to the detector as a muon traveling with a straight track through the detector (Figure 5.3). This cosmic generator was used to test the viability of using cosmic rays to align the Silicon Detector and also the Scintillating Fibre Detector. A picture of the Cosmic generator working within HMC is shown in Figure 5.4 (Figure 5.5 shows a Cosmic Muon being tracked as it passes through the Recoil Detector[56]).

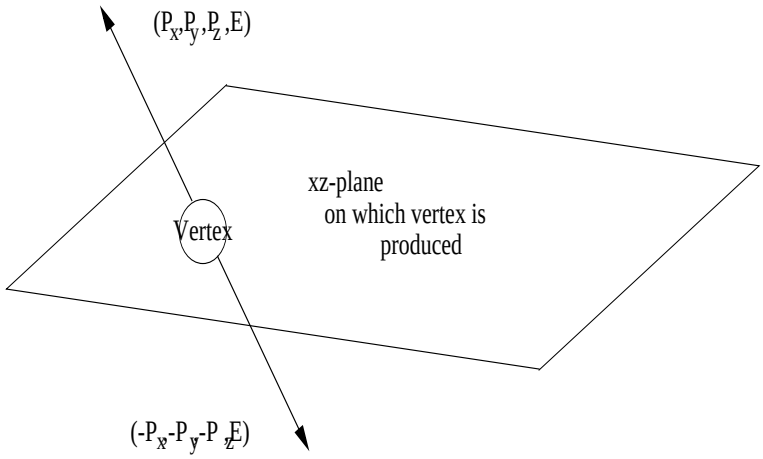

Figure 5.3: Back to back cosmic particle production in the xz plane

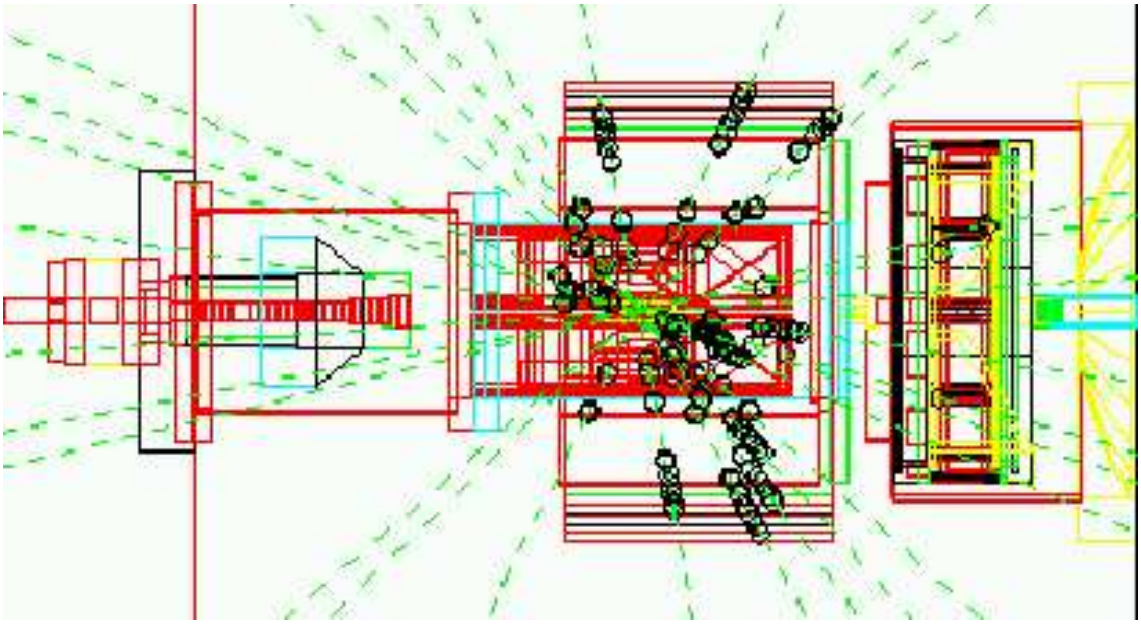

Figure 5.4: Cosmic muon events generated in HMC with Recoil Detector present

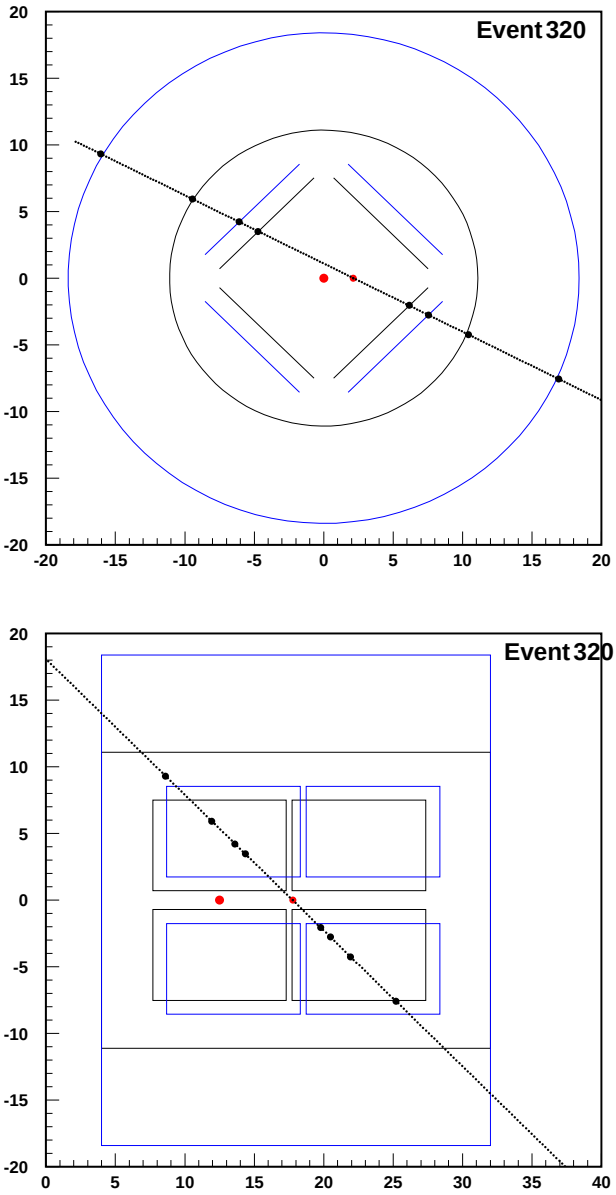

Figure 5.5: Reconstructed Cosmic track passing through the Recoil Detector

5.2 HMC - Hermes Monte Carlo

HMC is the generic name given to a suite of programs which make up the overall Monte Carlo for the HERMES experiment, however it also specifically refers to the code which simulates the detector response within the overall Monte Carlo suite. It consists of the first stage, GMC which are the physics generators and produce the events which are used within the actual Monte Carlo simulations. These events are then read into the HMC package where they are processed and then subsequently output to HRC where reconstructed tracks are found within the HERMES spectrometer. In order for the Recoil Detector to

be implemented into the Hermes Monte Carlo software chain the changes described below had to be implemented and the relevant files updated and modified.

For the results presented here the output from HMC is run through a private version of HRC where events in the HERMES spectrometer are reconstructed. The HMC events are also not piped to the μDST writer as will be done with the Recoil Detector as it is implemented into the latest production version of HMC.

5.2.1 Digitisation

In order to implement a new detector into the Hermes Monte Carlo (HMC) additions are required to be made to the software and subroutines on which it calls. One of the most important things that has to be done in order for a simulated detector response to be useful is what is known as digitisation. Digitisation simply converts the raw Monte Carlo information into the form which is analogous to the form that the actual detector will produce. For example the hit positions on the detector would be converted into a relevant hit strip or hit module, for example, in the Silicon Detector. The usual output information is typically a strip number hit and an energy deposition. It is therefore useful to have the same format coming out of the Monte Carlo. This enables software development to be done before the final detector is installed and commissioned which is, for example, necessary for the tracking code development currently under way for the Recoil Detector.

In the Hermes front region the Lambda Wheels have been commissioned and will compliment the Recoil Detector to give a much improved kinematical coverage for the front region of the Hermes Spectrometer once both upgrades are completed.

Much work has been done by the Lambda Wheel group with regards to software development both for the readout electronics and also with the Monte Carlo simulations for the detector[57][58][59]. The idea of using software that was already developed, although for a different detector, was appealing as it would enable tested methods and ideas to be used and developed for the Recoil Detector. The digitisation uses similar output table formats as the Lambda Wheels and ideas were adopted from the Lambda Wheel groups' approach.

The Recoil Detector itself will consist of three separate subdetectors; a Silicon Detector, a Scintillating Fibre Detector and a Photon Detector. At an early stage a well defined nomenclature was defined for each of the three subdetectors. For the Silicon Detector the format : S[12][IO][1-4] was decided upon. Where 1 or 2 refers to the upstream and downstream respectively. The 'I' refers to the inner detectors and 'O' refers to the outer detectors. The numbers 1 through 4 are defined to be one of the four quadrants of the Silicon Detector. The position of module 1 was arbitrarily chosen to be the lower left quadrant when viewing the detector looking downstream with y pointing upward and x pointing to the left (Figure 5.6). The other quadrants are then numbered in a clockwise direction 2 through 4. The iGType for the Silicon Detector is 44. A table showing the nomenclature for the three subdetectors is Table 5.1.

Detector name	Nomenclature	iGType
Silicon Detector	S[12][IO][1-4]	44
SciFi Detector	SF[IO][1-4]	42
Photon Detector	SGI[letter-number]	43
	Scintillating layer 1-3	
	Convertor layer A-C	

Table 5.1: Nomenclature for the Recoil Detectors' subdetectors

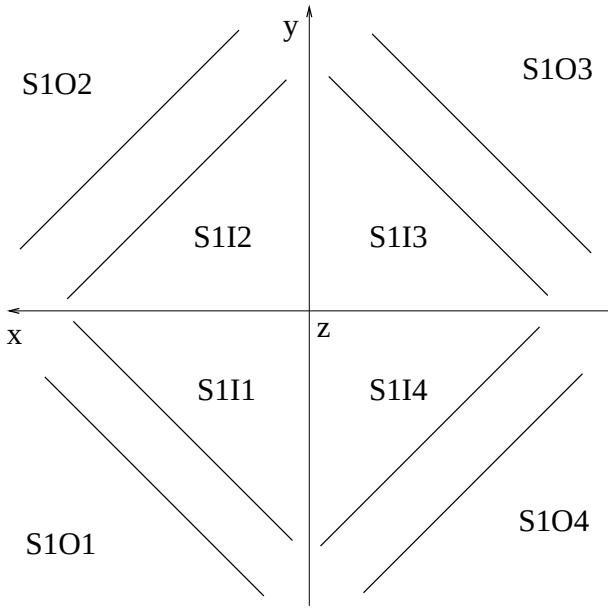

Figure 5.6: Diagram of Silicon nomenclature definition (looking downstream)

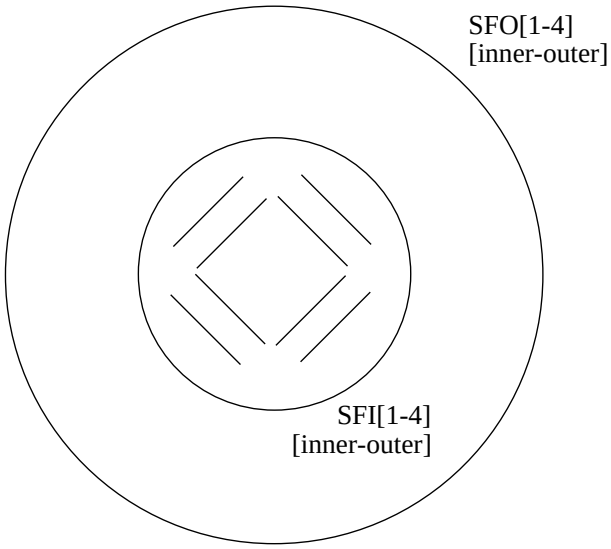

Figure 5.7: Diagram of SciFi Detector nomenclature definition (looking downstream)

The naming scheme for the SciFi detector followed the designation:SF[IO][1-4] (Figure 5.7).The 'I' refers to the inner Scifi detector layers and 'O' refers to the outer SciFi layers. The numbering from 1 to 4 is related simply to each of the four layers, going outward, for either the outer or inner SciFi Detector. The iGType for the SciFi detector is 42.

The Photon Detector naming scheme is: SG[IO][1-4] (Figure 5.8). When the nomenclature of the Photon Detector was originally decided upon it was still unclear as to what the exact geometry of the detector would be. The geometry has now been defined and consists of three layers of converting material (tungsten) and three layers of scintillating material. The nomenclature used in the Monte Carlo geometry is : SGI[letter—number], where the letter is used for the converter layers and is from A-C and the numerical value is associated

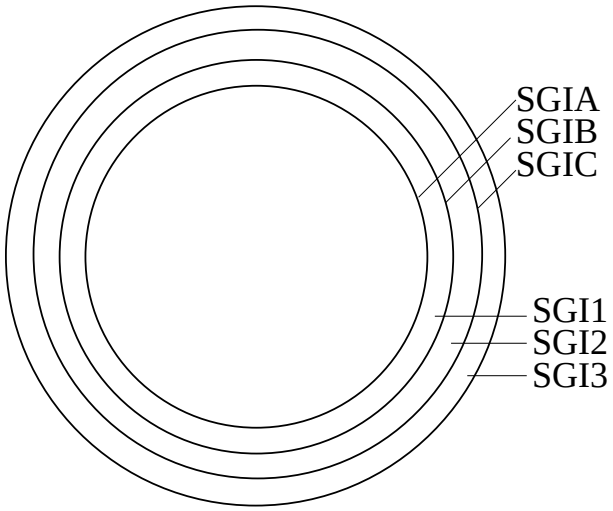

Figure 5.8: Diagram of Photon Detector nomenclature definition (looking downstream)

with the scintillator layers and runs from 1-3. The iGType for the Photon detector is 43.

The standard table format currently used in the Hermes Monte Carlo follows ADAMO (Aleph DAta MOdel)[60]. In order for the Recoil Detector to be implemented within the Hermes Monte Carlo a new ADAMO table has to be produced for each of the three subdetectors containing information relevant to each detector in turn. For the Silicon Detector the table is called dataSiliRec (relating to 'Sili'con 'Rec'oil) and it is filled with data from the Monte Carlo output for the Silicon Detector (Table 5.2). Table formats for both the SciFi and the Photon Detector were decided upon and the names given to the tables are 'dataSciRec' and 'dataPhotoRec' for the SciFi and Photon detectors respectively(Tables 5.3, 5.4)

dataSiliRec	
ID	ID number of the entry
iStrip	Strip number 1-128
iADCHigh	ADC value for high gain channel
iADCLow	ADC value for low gain channel
rPulsHigh	ionisation energy loss of particle
rPulsLow	ionisation energy loss of particle
iCMHigh	common mode noise high gain
iCMLow	common mode noise low gain
iTrailerHigh	trailer information high gain
iTrailerLow	trailer information low gain
iPlane	hit side of the module
dgDETS	identifies the struck module

Table 5.2: ADAMO table format for dataSiliRec

The digitisation for the SciFi and Photon Detectors was implemented by Wolfgang Sommer, of Giessen University, and Michael Tytgat, of Gent University, for the SciFi detector and the Photon detector respectively.

The Silicon Detector digitisation was the main area of the digitisation implementation on which my work was focused. A brief description of the way in which the digitisation

dataSciRec	
ID	ID number of the entry
iPMT	PMT channel number which is read out
iADC	ADC value for for the struck channel
rPuls	energy deposited in the SciFi detector
dgDETS	identifies the struck module

Table 5.3: ADAMO table format for dataSciRec

dataPhotoRec	
ID	ID number of the entry
iPMT	PMT channel number which is read out
iADC	ADC value for for the struck channel
rPuls	energy deposited in the Photon detector
dgDETS	identifies the struck module

Table 5.4: ADAMO table format for dataPhotoRec

operates for the Silicon Detector is given below.

When the Silicon Detector geometry was first implemented into a private version of HMC, the ability to have the Recoil Detector volumes as 'actual' detectors was not available and so the detector volumes were introduced into HMC as 'dummy' detectors. The only difference this makes to the digitisation is that the detector volumes are referenced by their 'mcHit_dgDETS' number rather than by the well defined 'dgDETINFO_cName' which was defined earlier. The main problem that this produces is that once the Recoil Detector geometry is moved into the final HMC version the numbers in the 'mcHit_dgDETS' table will change and the digitisation will no longer function. This problem will be solved once the Recoil Detector is able to use the 'actual' detector ability within HDB and HMC.

When an active detector is struck within HMC the digitisation subroutines are called. The subroutine which decides whether the detector hit is relevant or not and tries to call the appropriate digitisation code is called 'digi_sort.F' and is contained within the same directory as all the other digitisation code (Figure 5.9). The main job of 'digi.sort.F' is to determine whether the detector that was hit is one of the detectors that the digitisation has knowledge of. It does this by using two well defined values that each sensitive detector has, 'dgDETS_IType' and 'dgDETINFO_cName'. These values are unique for each detector within the Monte Carlo and for the Recoil Detector the definition for the Recoil subdetectors was explained earlier. Once 'digi_sort' decides that a given detector is valid it makes a call to the digitisation for that particular detector. In the case of the Silicon Detector the call would be made to the 'digi_silirec.*' digitisations.

For the silicon digitisation the first subroutine to be called is 'digi_silirec_modular.F'. The main function of this program is to determine from the HMC setting which digitisation type has been chosen by the user. There are four possible choices for digitisation in general, however for the Silicon Detector it has been decided to use the first of the four choices, namely 'NONE', which is the simplest choice of digitisation. Depending on the type of digitisation chosen the appropriate digitisation subroutines are then called. In the case of the Silicon Detector the next digitisation subroutine called is 'digi_silirec_none_modular.F' which contains the majority of the digitisation code and is explained below

The first thing that the digitisation in 'digi_silirec_none_modular.F' does is to define the centers of each of the four Silicon modules relative to the (0,0,0) of the Hermes

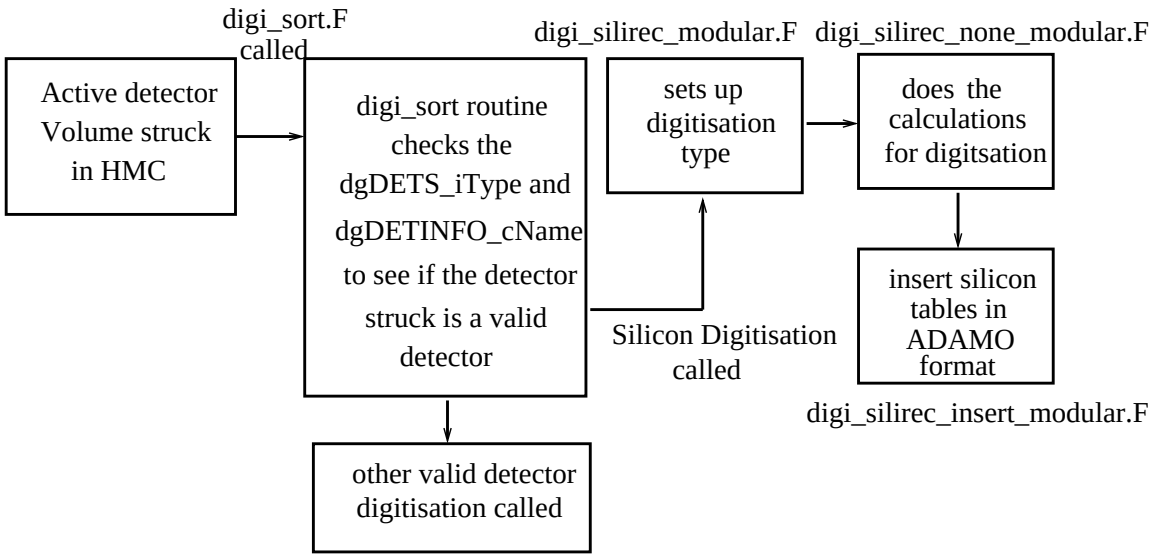

Figure 5.9: Flowchart showing how the Silicon Digitisation is called from HMC

Coordinate system.

Once this is done the relevant rotation necessary for each Silicon TIGRE detector is introduced so that each TIGRE will have the correct rotation. This is done for all 16 TIGREs individually.

The next step is to calculate the x, y and z coordinates for the center of each TIGRE detector. This is achieved by calculating the distance of each TIGRE from the center of the apparatus to which it belongs, and thereby obtain the x, y, z coordinates of the center of the TIGRE. This uses both the angle at which the TIGRE is orientated and the center coordinates of the apparatus which are known. This calculation is done separately for each of the 16 TIGREs belonging to the 4 modules. See equation (5.1).

$$\begin{aligned} &\text{y detector centre} = \text{y apparatus centre} + \\ &\sqrt{2}(\text{position of detector relative to apparatus centre}) \end{aligned} \tag{5.1}$$

Next the enter and exit coordinates are obtained. The enter and exit coordinates for the detector are calculated by using the mcHit_* values. For the front coordinate the mcHit_XEnter value is simply used to obtain the entry coordinate. For the exit coordinate, however, both the mcHit_XEnter and mcHit_X values are used. The mcHit_X value is the coordinate in the center of the struck module. Therefore using the difference between the mcHit_XEnter and mcHit_X to get a length in x between the entry coordinate and the exit coordinate (Figure 5.10). The length between the incoming, entry coordinate, and the outgoing, exit coordinate, can then be calculated. This method is used to calculate the enter and exit coordinates for x, y and z hit points. See equations (5.2), (5.3).

$$\text{Front Side Hit Coord} = (\text{mcHit Enter Coord}) - (\text{Detector Centre}) \tag{5.2}$$

$$\text{Back Side Hit Coord} = (\text{mcHit Central Coord}) - (\text{mcHit Enter Coord}) - (\text{Detector Centre}) \tag{5.3}$$

The hit coordinates obtained then have to be translated using the angle by which the TIGRE detector is rotated in order that all the detectors lie in the same plane before the

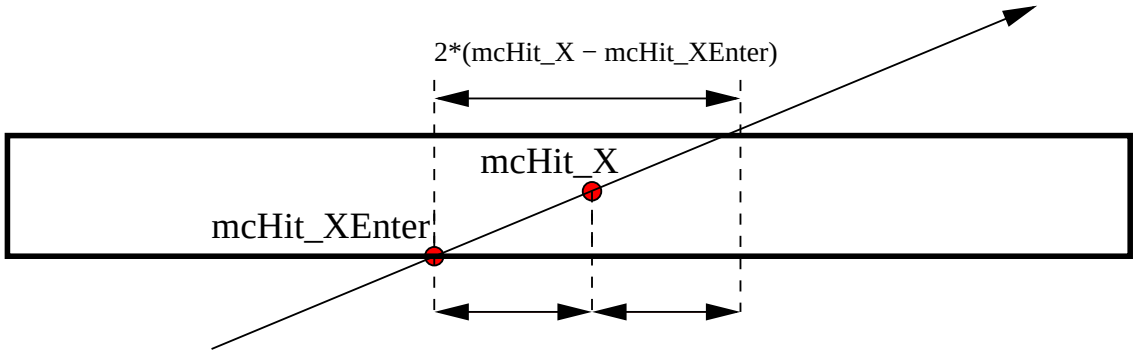

Figure 5.10: Diagram showing how exit coordinate calculated in the digitisation

strip calculations are made. The x and y strip coordinates are thereby compensated for the angle at which the TIGRE detector was struck due to its' angular orientation. See equations (5.4), (5.5).

$$\begin{aligned}&\text{X hit Coord front and back within detector frame} = \\ &(\text{ X Hit Coord front/back})*\sin(\text{Rotation Angle of TIGRE}) - \\ &(\text{X Hit Coord front/back})*\cos(\text{Rotation Angle of TIGRE})\end{aligned} \tag{5.4}$$

$$\begin{aligned}&\text{Y hit Coord front and back within detector frame} = \\ &(\text{ Y Hit Coord front/back})*\cos(\text{Rotation Angle of TIGRE}) + \\ &(\text{Y Hit Coord front/back})*\sin(\text{Rotation Angle of TIGRE})\end{aligned} \tag{5.5}$$

In the digitisation the next stage is to calculate from a given y and z 'hit' coordinates the strip numbers which would be struck in reality. The strip numbering runs 1 through 128 and the pitch of the strips is 758 μm. See equation (5.6)

$$\text{Y Strip Coord} = (\text{Y Hit Coord within Detector}) + 64*(\text{Strip Pitch}) \tag{5.6}$$

The next stage of the digitisation aims to reproduce the strip orientation that is present in the final Silicon Detector flexfoil design[61][62]. In the final flexfoil design there are two different strip orientations depending on whether the side of the detector is p-side or n-side. Also there is a difference between the outer and inner TIGREs as to which side (n or p) is presented towards the target. The strip numbering also had to be in the same order as it would be in the final design in order for tracking routines, for example, to have a realistic input for the reconstruction code (Figure 5.11). The way in which this was implemented was to treat each TIGRE detector separately and to find the correct calling routine which produces the correct strip orientation and n-side, p-side ordering. The calling subroutine calculated the strip numbering and order and so is important to be called for the correct TIGRE and side. The called subroutine is called 'digi_calc_strips' and calculated from the y and z coordinates the strip number that would have been struck and also the energy deposited in each hit strip. The method the digitisation employs was to find a range of strips that were struck from the coordinates that were hit and then calculated a strip number at that point. When only 1 strip is hit all of the energy is deposited within that single strip. The way in which the energy deposited is calculated is to use a multiplication factor already used by the Lambda Wheels digitisation which is called 'LWrDEToElecFactor' which relates the amount of energy deposited by the 'mcHit_rDE' table from the Monte Carlo to the number of electrons which would be deposited within the material. The value for 'SiliRecrDEToElecFactor' is 2.807E+08.This number converts the

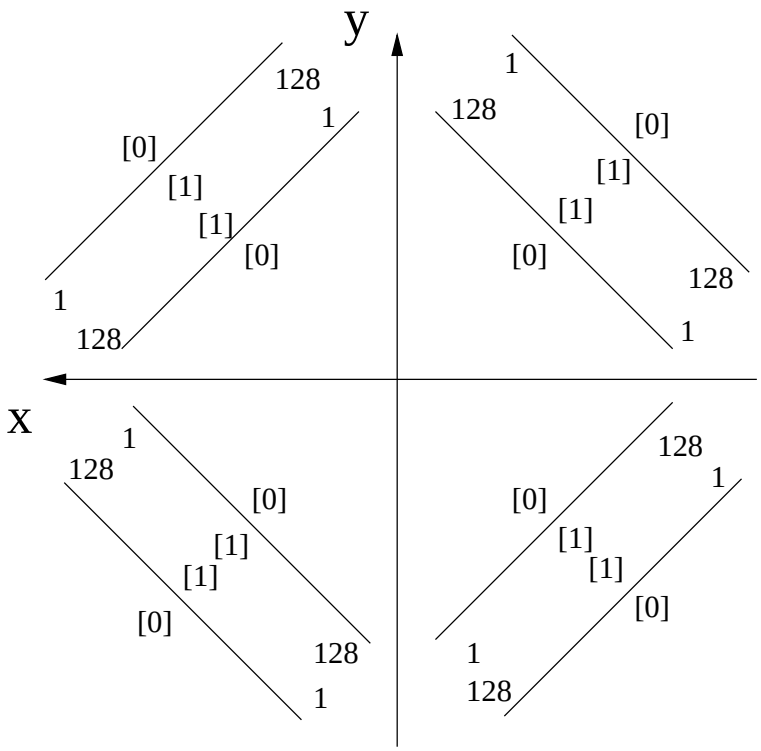

Figure 5.11: n-p side strip orientation and numbering for Silicon Detector flexfoils:[0] is the n-side of the Silicon, [1] the p-side of the Silicon. 1-128 indicate the strip numbering for each of the two sides. The view is looking downstream.

ionisation energy loss of a particle within the material to the number of induced electrons that are produced. The value 2.807E+08 comes from the division of 24,000 electrons/MIP (Minimum Ionising Particle) by the most probable energy loss per MIP which is 85.5 keV. The empirical value 24,000 electrons/MIP is the number of electrons induced by a MIP particle in 300 μm of Silicon. The value 85.5 keV, the most probable energy loss per MIP was calculated in [50] and was checked by a Monte Carlo simulation of MIP particles depositing energy in 300 μm Silicon. The 2.807E+08 electrons/GeV is the induced charge per ionisation energy loss. The 'mcHit_rDE' value is defined to be the ionisation energy loss by a particle as it passes through a given material. When more than a single strip is struck the digitisation finds the range of strips that are struck and finds out which fraction of the total path length of the passing particle lies within each strip. This fraction of the path length is then used to distribute a similar fraction of the total energy deposited to each of the hit strips. The output from this routine then passes on the numbers of the hit strips, the plane value (0 or 1 for n or p), the energy deposited within the given strip and the detector number struck onto the next part of the digitisation.

The subroutine 'digi_silirec_insert_modular.F' then takes the output from 'digi_silirec_none_modular.F' and prepares it for insertion into the ADAMO tables relevant to the Silicon Detector. The first modification to the input from the previous part of the digitisation is to take the energy calculated to be deposited within one strip and to divide it by 2. This takes into account that approximately half of the charge deposited within the Silicon Detector will be lost within the detector and not reach the HADC's. A multiplication factor of 0.78 and 0.22, corresponding to a choice of 10 pF for the divider capacitance, was introduced to account for the ratio of the shared charge for charge division

between the high and low gain channels of the Helix readout chip[63]. For the 'trailerhigh' , 'trailerlow', 'icmhigh', 'icmlow' dummy values are entered as they will only become relevant for the actual detector and test beam setups involving their readout. For consistency it was decided to attempt to keep the Monte Carlo output format analogous to the actual Silicon Detector output format.

The next stage is to fill the 'dataSiliRec' ADAMO tables with the relevant information. These tables can then be used to look at the detector information for the Silicon Detector after it has been produced in the Monte Carlo simulations. A flow diagram of the digitisation can be seen in Figure 5.12.

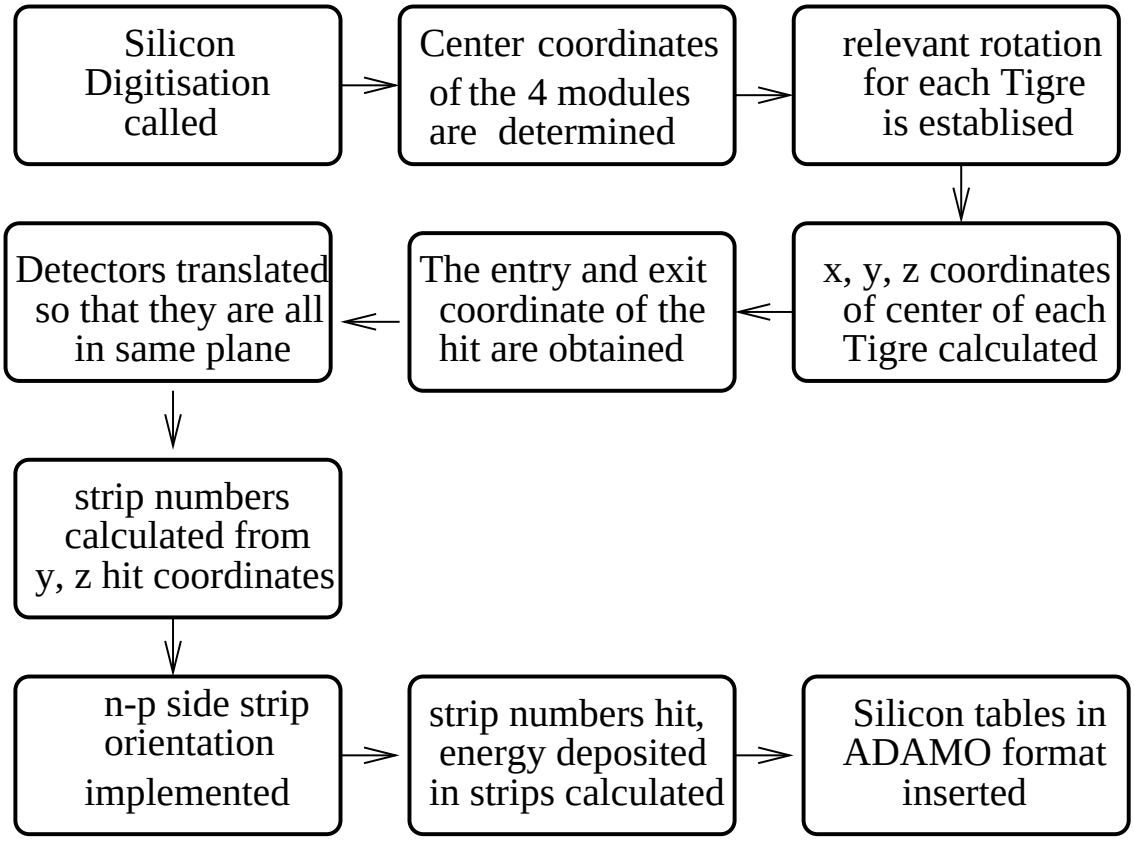

Figure 5.12: Schematic diagram of the digitisation program

5.2.2 Geometry

In order for HMC to accurately locate the positions and materials that compose the overall detector it requires a precise model of the spectrometer and its components. This information is provided by a file which is known as the geometry file.

At present the geometry for the Silicon Detector, SciFi Detector and Photon Detector have been implemented into the Hermes Monte Carlo (Figure 5.13). Chen Tao of DESY, Hamburg also implemented a collimator design into HMC and did studies on the optimal design for the collimator[64]. Each piece which is placed within the Monte Carlo using HDB via the geometry file has to be implemented such that all the information required by HDB is correctly written into the geometry file. There are many interconnecting relationships between the given piece and its material and position and many other factors. Each of

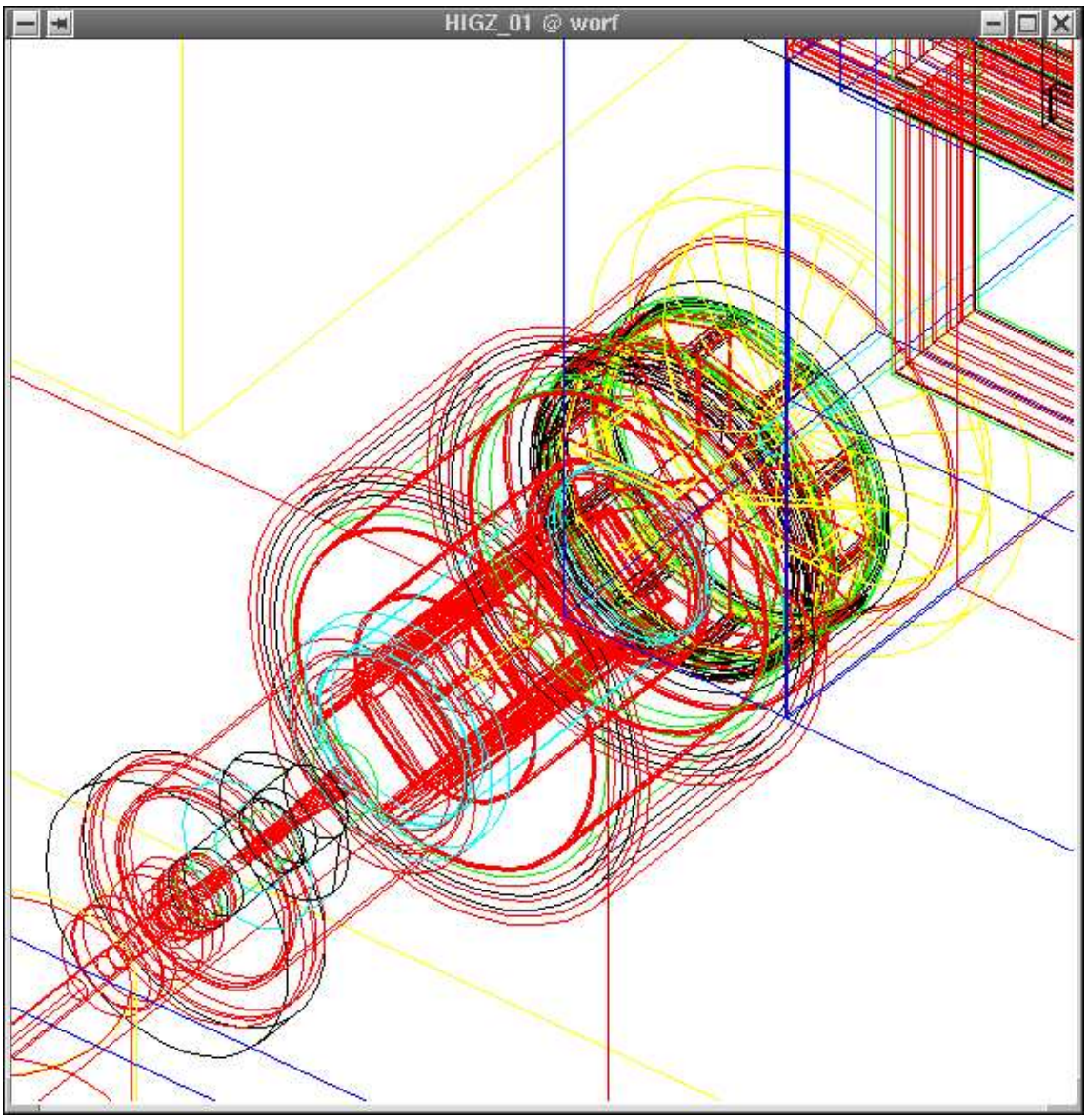

Figure 5.13: Recoil Detector Geometry in HMC looking downstream

these relationships must be put in correctly otherwise HDB will have difficulty to recognise what is meant or worse put in the piece incorrectly.

5.2.3 Magnet

In order for the updated Recoil Detector Monte Carlo to simulate the conditions that will occur in the final configuration a field map has to be implemented that reproduces the magnetic field which will be present in the final setup. The method employed to implement a new field map into HMC is described below.

The magnet used in the Recoil Detector Monte Carlo is the fieldmap 'Variant_1_2_field.dat' obtained from [65] with 1 cm resolution. The file in its original format takes the format shown below.

```
Field component.  Variant 1 (2cm).

 R    Z    bmod            bz          br
0.0 -2.0   0.0             0.0         0.0
0.0 -1.99  8.495621E-05   -8.49562E-05 0.0
0.0 -1.98  1.699124E-04   -1.69912E-04 0.0
0.0 -1.97  2.548686E-04   -2.54869E-04 0.0
0.0 -1.96  3.398248E-04   -3.39825E-04 0.0
0.0 -1.95  4.24781E-04    -4.24781E-04 0.0
...
```

In order for the fieldmap to be used within HMC it has to be converted from its original format into one that can be used with HMC. This is achieved by using a perl script, written by Maurice Bouwhuis [66], which reads in the 'Variant_1_2_field.dat' and outputs a fieldmap which is in a form directly usable by HMC once linked to the correct file. The format that this 'converted' fieldmap takes is shown below. The B_r and B_z components of the fieldmap implemented are shown in figure 5.14.

```
Converted from file fieldmaps/Variant_1_2_field.dat
Field scaled with factor 1
Values of -BZ

R position Zposition  Value
0.0        -1824.0    0.000000
0.0        -1814.0   -0.000085
0.0        -1804.0   -0.000170
...
OK

Converted from file fieldmaps/Variant_1_2_field.dat
Field scaled with factor 1
Values of -BR

R position Z position Value
0.0        -1824.0    0.000000
0.0        -1814.0    0.000000
0.0        -1804.0    0.000000
0.0        -1794.0    0.000000
...
OK
```

5.3 Tracking and Reconstruction

5.3.1 HRC - Hermes ReConstruction

At present as particles pass through the HERMES Spectrometer they pass through tracking detectors on either side of the dipole magnet. Using information from the detectors and the hit positions it is possible to reconstruct tracks of the particles. The name of the program that reconstructs the tracks is called the Hermes ReConstruction (HRC) program [67]. It essentially works by reconstructing partial tracks, one before the magnet and one after

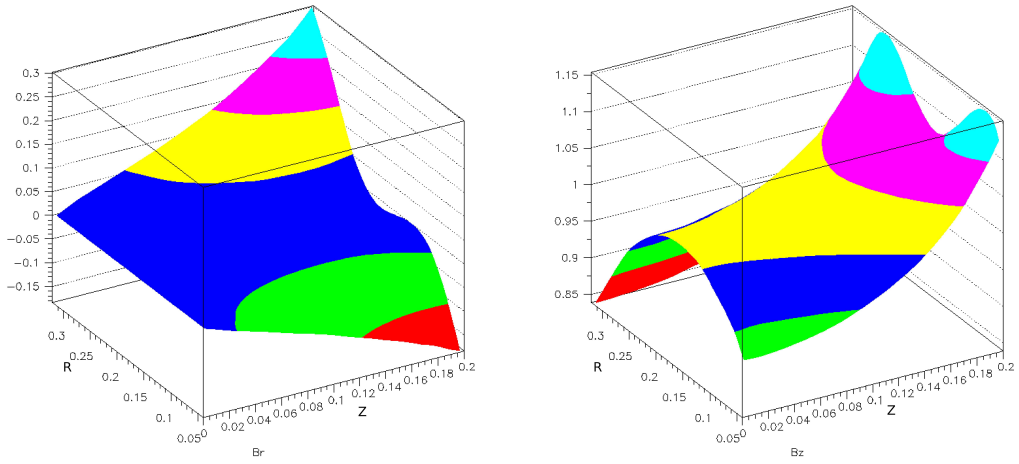

Figure 5.14: Left: The B_r component of the magnetic fieldmap. Right: The B_z component of the magnetic fieldmap.

and then tries to join them up in the middle of the magnet. If it finds a match then it concludes that a track was found. As mentioned HRC only reconstructs tracks within the spectrometer. This is useful for obtaining the information from the spectrometer which is currently available and using it with information obtained for the Recoil Detector. In order to use HRC with the Recoil Monte Carlo a private version of the code had to be installed so that the tables for the Silicon, SciFi and Photon Detectors were not removed during a pass of the Monte Carlo events through HRC.

In order for a new detector to use the HRC program for track reconstruction for the Recoil Detector alterations would have to be made to the HRC code itself. Therefore for the Silicon Detector it has been decided, as was decided for the Lambda Wheels, not to try to incorporate HRC for the task of doing the tracking for the Recoil Detector. Instead the tracking will be done in a separate program. The tracking program developed by the Lambda Wheel group is called XTC (eXternal Tracking Code). A similar scheme is used for the Recoil Detector track reconstruction. Although HRC will not be used directly for tracking in the Recoil Detectors sub-detectors the output from HRC will still be used for tracking in the HERMES Spectrometer and this information may be used in the Recoil Detector tracking code in some form. The tracking routines for the final Recoil Detector are in an advanced stage and use a variety of approaches, some of which were presented in [56]. The routines that are being developed are designed to be accessible to the standard Hermes ANalysis frame (HANNA) through library functions and a modular style of code writing that will allow the integration into the HERMES software chain to be straight forward.

5.3.2 Hanna Tracking

For the Silicon Detector much work has already been done by Bernhard Krauss in his stand-alone Monte Carlo[16][68]. As part of this work he has already developed a tracking routine for the Silicon Detector. The tracking algorithm described below adopts and takes over the tracking code ideas developed in the stand-alone Monte Carlo and makes it usable with the Hermes Monte Carlo software scheme. This has involved translating the code from

Fortran to C and also changes to the code to deal with the ADAMO table format that the Hermes Monte Carlo uses. A flow diagram of the program can be seen in Figure 5.15.

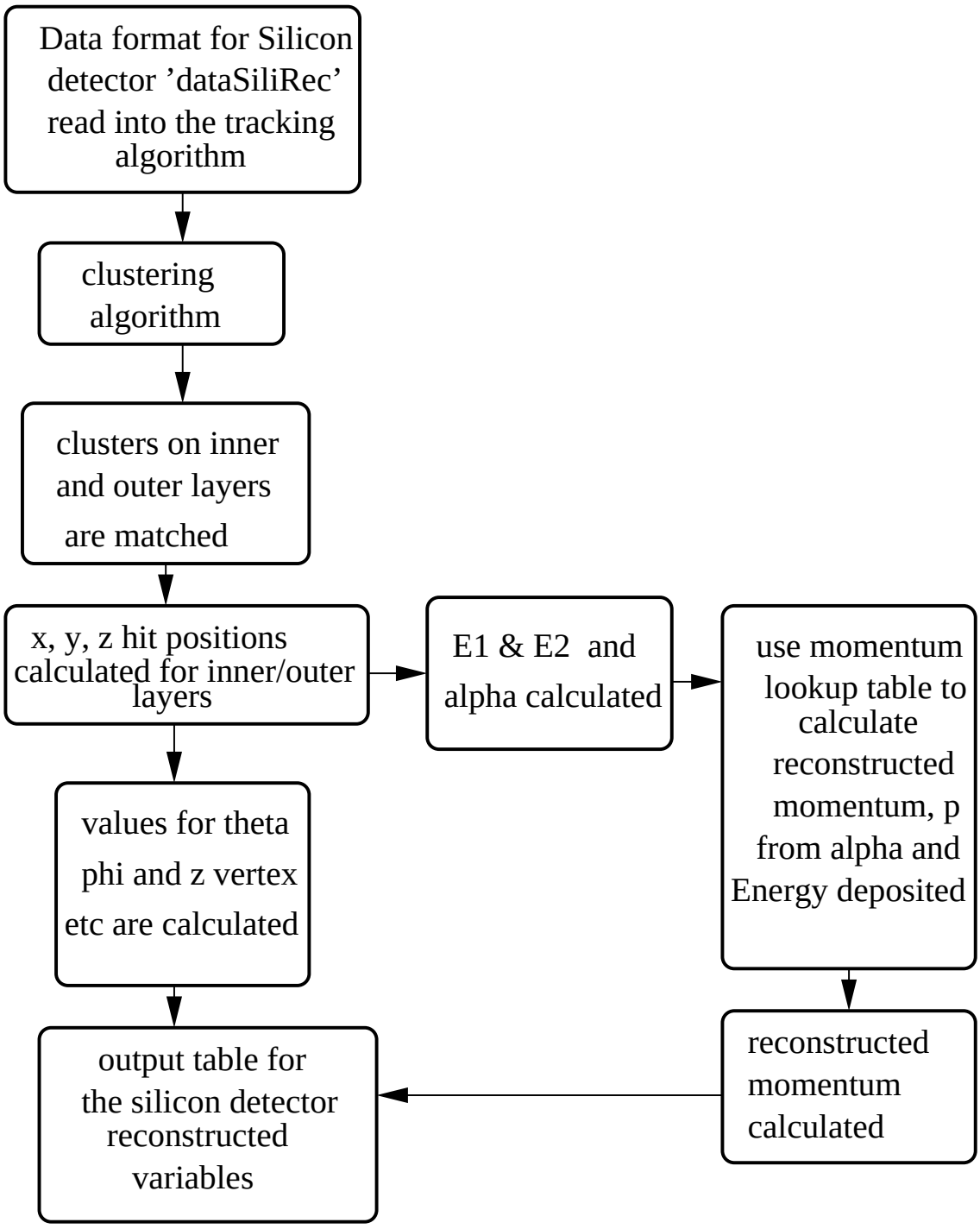

Figure 5.15: Flowchart of Tracking Program

The tracking code is written in C so that it is compatible with other tracking code that is being developed. At HERMES both C and Fortran is used for the software although for the tracking it was decided to move to C in order to have common ground with the other stand alone tracking routine mentioned earlier, XTC, used by the Lambda Wheels. The

code is written within a HANNA frame which is now a standard at HERMES. This allows the code to be easily portable between different tracking codes and also to implement easily into the software chain.

The high gain and low gain channels of the Helix readout have also been simulated taking values obtained in test beam experiments at the DESY II testbeam [63]. Once the table information for the Silicon Detector has been read into the HANNA frame all its information is available for use.

The program then loops over the strips that have been hit and groups them together in clusters of hit strips. If these strips satisfy a given energy cut and are above threshold then they are accepted as a member of a cluster. A look is then taken at the energy of the cluster itself to see if it is above the value chosen for a valid cluster. A flow diagram showing the clustering algorithm is shown in Figure 5.16. All the clusters in a given layer, for example the inner layer, are then found and compared to clusters in the other layer, the outer. If there are two clusters that are within a given energy cut of one another, ie the energies of both the clusters are within 0.5 MeV of one another then they are taken as a matching pair. Using the positions and energies of these clusters, each in a different layer, the values can be calculated for the kinematical variables which are required. In the case of this tracking program the values calculated are phi, which is the azimuthal angle and theta, the polar angle. Both of these values are obtained using the positions calculated within each of the given clusters. The value for the Z Vertex is also calculated which is the reconstructed position where the tracking program determines that the particle was generated from, the z axis being the beam axis, using the inner and outer Silicon Detectors' information only and linearly extending the resulting 'tracklet' to the xz plane at y=0. The energy deposited within each of the two silicon layers is also calculated from the energy deposition values that are given in the dataSiliRec ADAMO table from HMC. The reconstructed energy deposition value is corrected from the raw value given in the table by a correction factor, α, which takes the angle at which the particle strikes the material into account and hence the path length that the particle traverses as it passes through the silicon layer.

The other value that the tracking program reconstructs is the momentum of the given particle. At the moment the assumption is made that if the corrected energy in each of the two layers passes certain threshold criteria then the particle in question is assumed to be a proton. In order to reconstruct the momentum of the incident proton a lookup table was produced which contains the proton momentum associated with a given energy deposition and correction factor, α. This is available for both of the silicon layers. Therefore when a proton hits a layer with a given angle of incidence and energy deposition, the lookup table determines the momentum of that proton. A diagram showing the momentum reconstruction routine is shown in figure 5.17. The lookup table was produced using Monte Carlo events (300k) in HMC, using the reconstruction code to calculate the energies and correction factors used in the table. The events produced by the template generator were chosen to be protons generated with a flat distribution in momentum between 50 and 800 MeV. The polar angle (θ) distribution was chosen to have a large number of events with large values of polar angle (θ). The information from the second layer of the lookup table was used when the corrected energy deposited in the first layer fell below 2.4 MeV. This was used to give a more accurate momentum reconstruction than the one using only a single layer lookup value for momentum reconstruction. The lookup tables used within the reconstruction code are shown in figures 5.18.

The reconstructed values obtained in the tracking algorithm are then filled into an ADAMO table which contains the reconstructed information for the Silicon Detector, the table is called 'rcSiliRec'(Table 5.6).

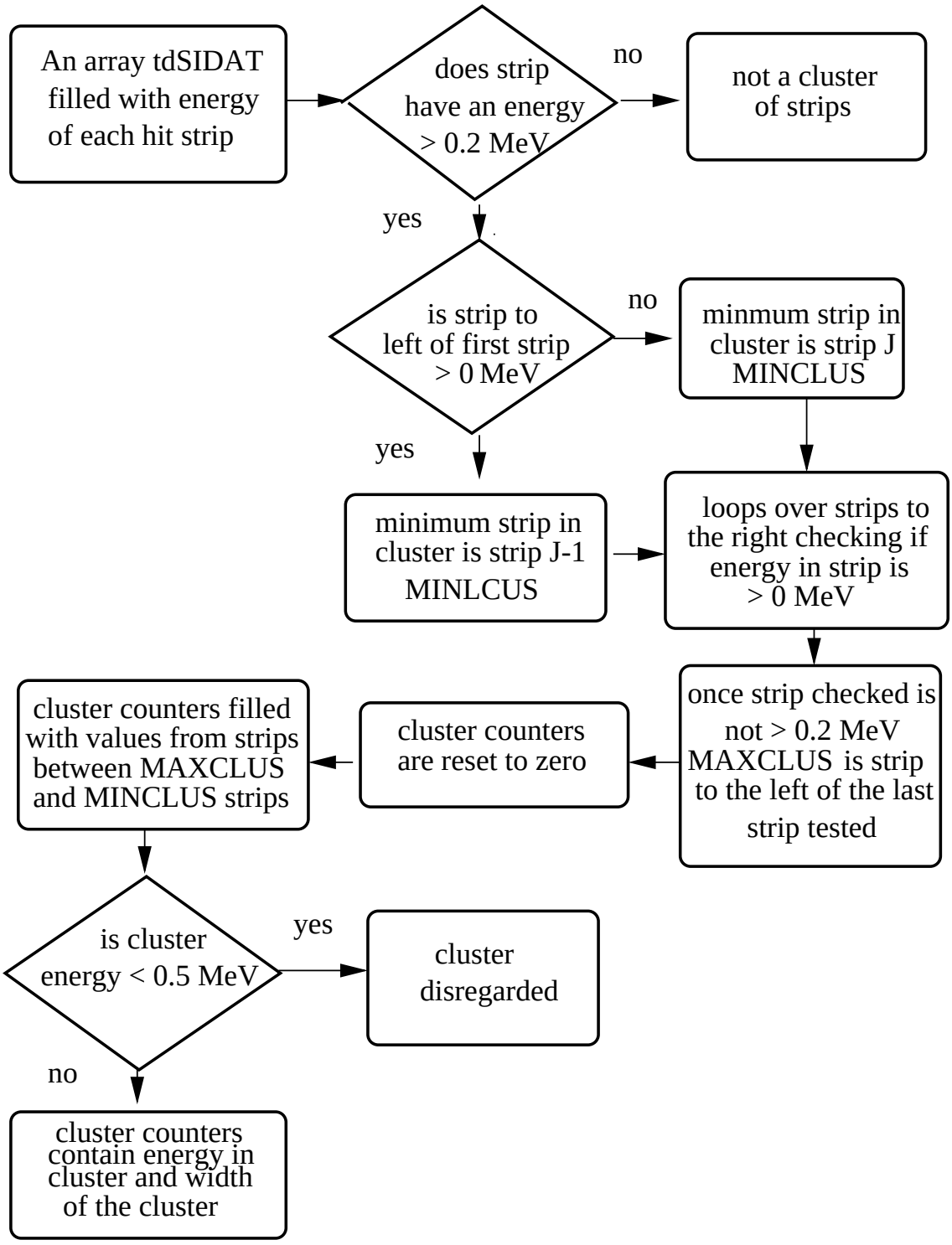

Figure 5.16: Flowchart of Clustering algorithm

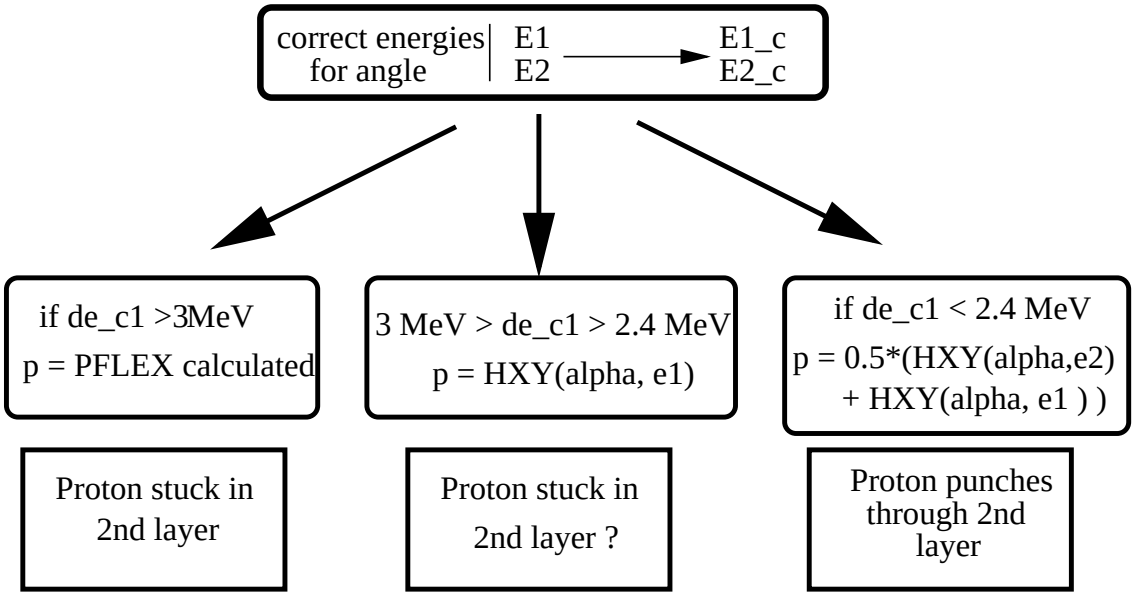

Figure 5.17: Schematic representation of the momentum reconstruction routine, with alpha related to the angle at which the proton is incident upon the Silicon. E1 and E2, the energies deposited in layer 1 and 2 respectively

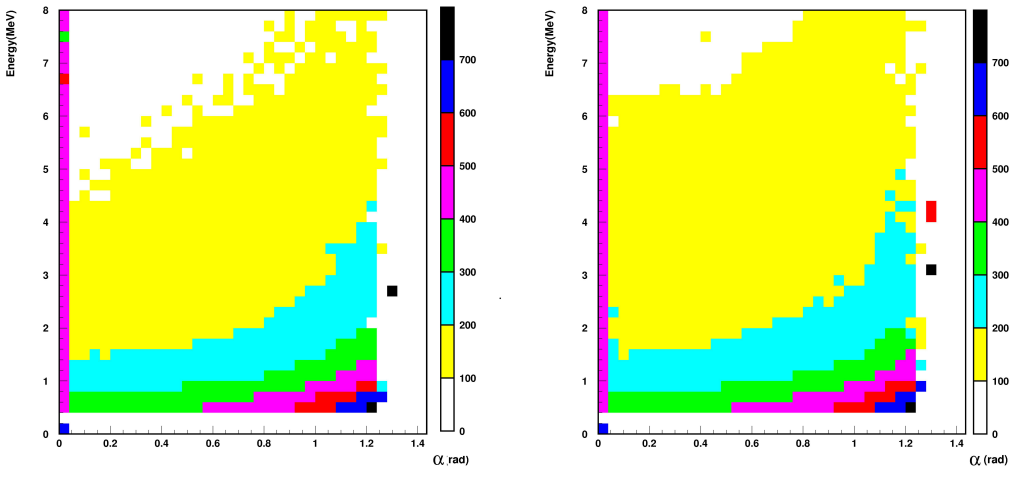

Figure 5.18: Lookup tables used within the tracking reconstruction code

5.3.3 Kinematical Cuts

In the tracking code a cut on the kinematical variables is introduced in order that the reconstructed protons in the Silicon Detector also correspond to a photon and a positron being detected within the acceptance of the HERMES spectrometer. To implement the cuts ideas were adopted from Bernhard Krauss' 'Pextra' program. The kinematical cuts shown in table 5.5 are applied to the positron detected in the spectrometer.

Kinematical cuts	
Q^2 Minimum	1 (GeV^2)
Q^2 Maximum	10 (GeV^2)
x Minimum	0
x Maximum	1
y Minimum	0
y Maximum	1
ν Minimum	0 (GeV)
ν Maximum	23 (GeV)
W^2 Minimum	4 (GeV^2)
W^2 Maximum	100 (GeV^2)
$\theta^{\gamma^*\gamma}$	< 0.07 rad

Table 5.5: Kinematical cuts applied to the DVCS events

The limit of $\theta^{\gamma^*\gamma} < 0.07$ rad was also used and is defined as the angle between the real and virtual photons.

Once these kinematical cuts are applied a further selection is done on the HRC tables. These cuts are made both on rcTrack values and also on rcCluster values. The satisfying condition being that there is more than a single cluster found in the calorimeter and that the energy of that cluster is greater than 1 GeV. A condition is also placed that the particles which are filled into the ntuples are in fact protons.

After these kinematical cuts, the table values are filled into ntuples which are then used within an analysis package, for example, PAW to look at the plots and distributions of the reconstructed values.

rcSiliRec	
rcSiliRec.P	reconstructed momentum
rcSiliRec.Theta	polar scattering angle
rcSiliRec.Phi	azimuthal scattering angle
rcSiliRec.ZVx	z point of closest approach to the beam axis
rcSiliRec.PID	assumption of PID 14 for proton
rcSiliRec.E1	energy deposited by a particle in the inner layer
rcSiliRec.E2	energy deposited by a particle in the outer layer

Table 5.6: ADAMO table format output from reconstruction code

5.3.4 Reconstructed Plots and TDR Comparison

The main method which is used to verify that the reconstructed events are comparable to the stand alone track reconstruction code developed by Bernhard Krauss and to look at the distributions of the reconstructed values is to make plots from the ntuples output from the reconstruction code. The plots from the reconstruction code are compared to the plots made for the Recoil Detector Technical Design Report (TDR)[31] which were made with the 'Pextra' standalone code.

DVCS P Versus θ Plots

The first plots are the θ versus momentum, p plot for protons produced by BH/DVCS events. The main qualification for a proton to be shown in the plot is that a photon and a positron must also have been detected in the HERMES spectrometer satisfying the kinematical cuts mentioned previously. Figure 5.19(Left) shows the plot from the Track Hanna reconstruction program. The comparison plot from the TDR is shown in figure 5.19(right)

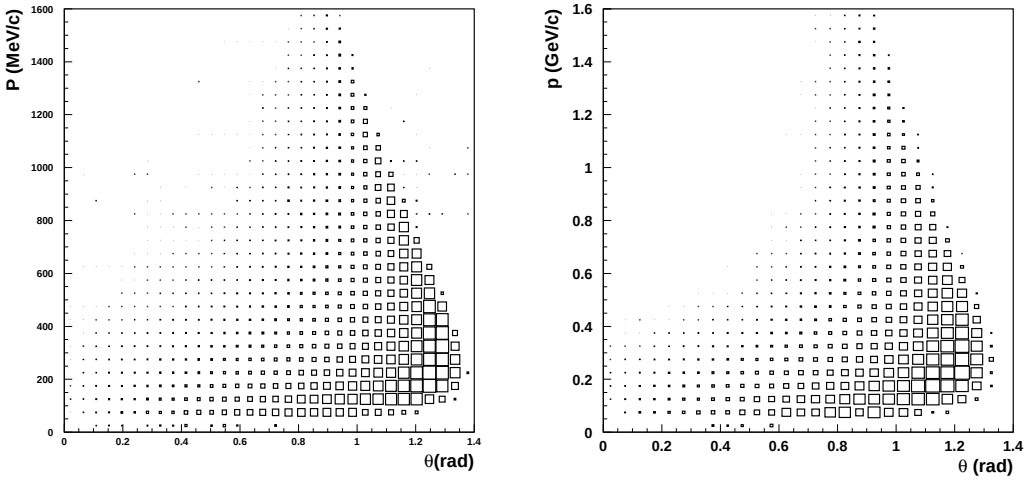

Figure 5.19: Left: Kinematic distribution of recoil protons from BH/DVCS in momentum p and polar angle θ in Track Hanna. Right: Kinematic distribution of recoil proton from BH/DVCS in momentum p and polar angle θ from TDR.

The two plots appear to show good agreement with each other. The slight difference in distributions can be explained by the fact that the cut made on mcTrack and rcCluster in the track Hanna reconstruction code is done at the HRC level whereas the cuts on accepted positron track and photon cluster in the TDR reconstruction code use μDST's to do the acceptance cut.

Kinematic Coverage and Detection Probability

In the TDR plots are shown which combine the detectors' geometric acceptance and detection efficiency, based on the detector thresholds, to form detection probability plots. The detection probability for recoil protons from BH/DVCS events as functions of proton momentum, p are shown below for both the Track Hanna plots and also for the TDR plots (Figure 5.20).

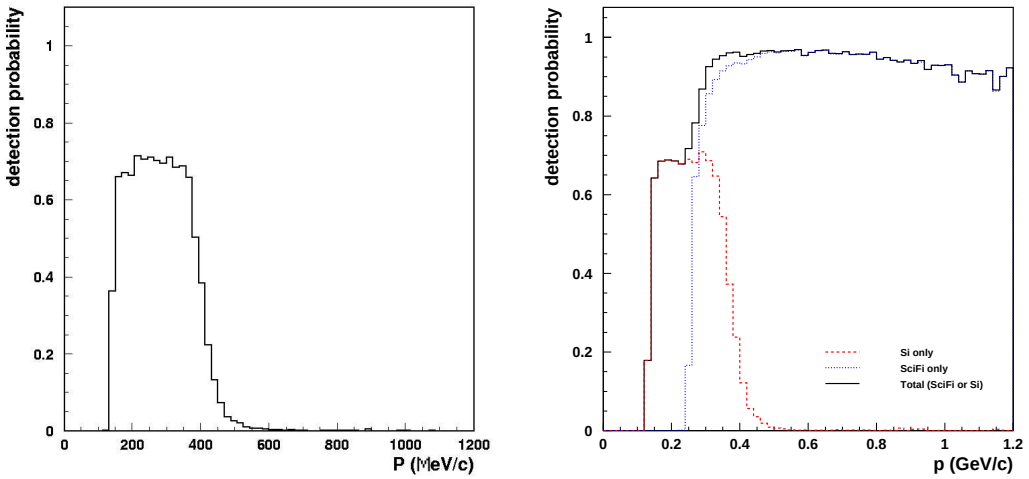

Figure 5.20: Left: Detection probability for Silicon Detector as a function of momentum, p in Track Hanna. Right: Detection probability for Silicon Detector as a function of momentum, p in TDR.

Again the plots appear to be in good agreement with the detection probability of approximately 0.7 for both the track Hanna reconstruction code and also the TDR reconstruction code. The thresholds where the Silicon Detector detects the proton momentum are also in good agreement with each other.

The detection probability for recoil protons from BH/DVCS events as functions of polar angle θ are shown below for both Track Hanna and TDR plots (Figure 5.21).

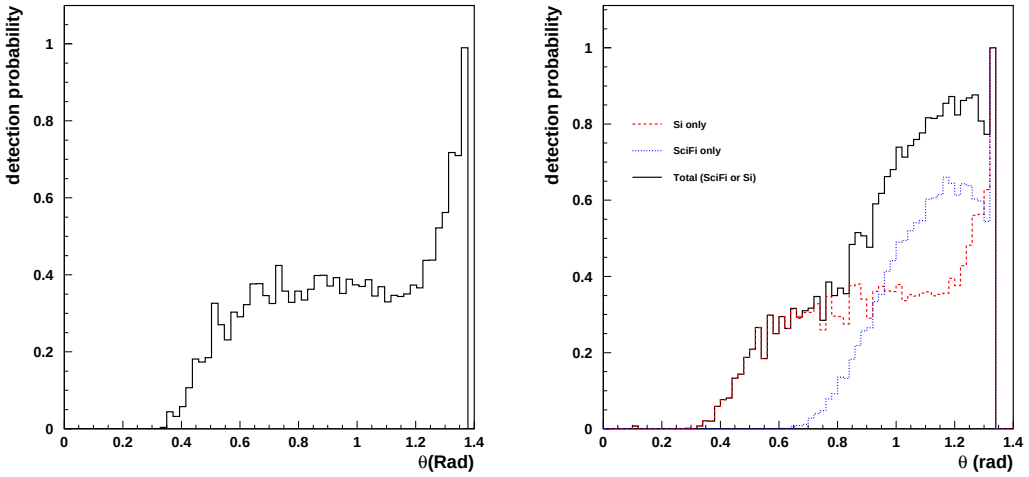

Figure 5.21: Left: Detection probability for Silicon Detector as a function of polar angle, θ in Track Hanna. Right: Detection probability for Silicon Detector as a function of polar angle, θ in TDR.

A comparison between the two plots shows the same detection probability of around 0.4 for both the Track Hanna plots and the TDR plots with a gentle rise to a detection

probability of around 1 at higher values of θ. Again, the two reconstructed plots appear to be in good agreement with each other.

Momentum Resolution Plots

The TDR plot (figure 5.22), below, shows the momentum resolution for the Silicon Detector over the range where the detector is efficient. The momentum resolution for the Silicon Detector is seen to rise from approximately 0.03 for BH/DVCS protons at around 150 MeV/c to roughly 0.8 for a proton momentum of around 500 MeV/c.

The momentum resolution plot produced by the Track Hanna program shows a good agreement with the momentum resolutions' behaviour. The resolution also rises from approximately around 0.03 for protons with a momentum on the order of 150 MeV/c. The resolution also rises steadily and reaches a value around 0.6 for a momentum of around 450 MeV/c. The difference in the values of momentum resolution at energies between around 350 MeV/c and 500 MeV/c can be explained by the lack of a noise simulation in the Track Hanna Monte Carlo sample, which results in a slightly improved momentum resolution at these values.

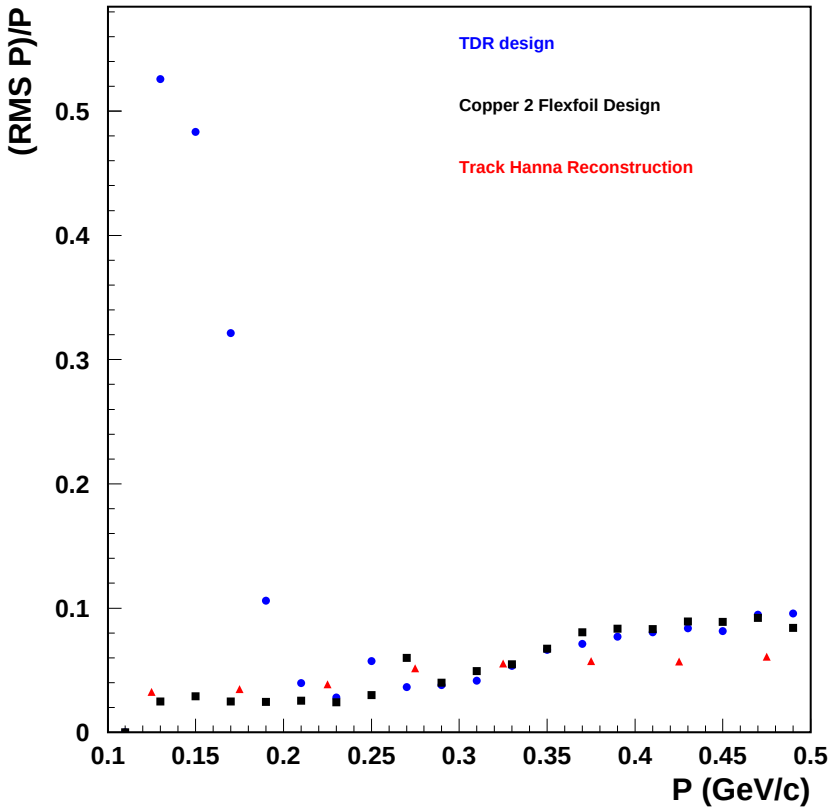

Figure 5.22: Momentum resolution for the Silicon Detector is shown. The momentum resolution with the TDR flexfoil design is shown. The momentum resolution for the updated flexfoil design for both reconstruction programs is also shown

Resolution in Φ

The angular resolution provided by the Silicon Detector for the azimuthal angle Φ is shown in figure 5.23 and shows the Φ resolution obtained both by the Track Hanna reconstruction program and also from the TDR reconstruction program.

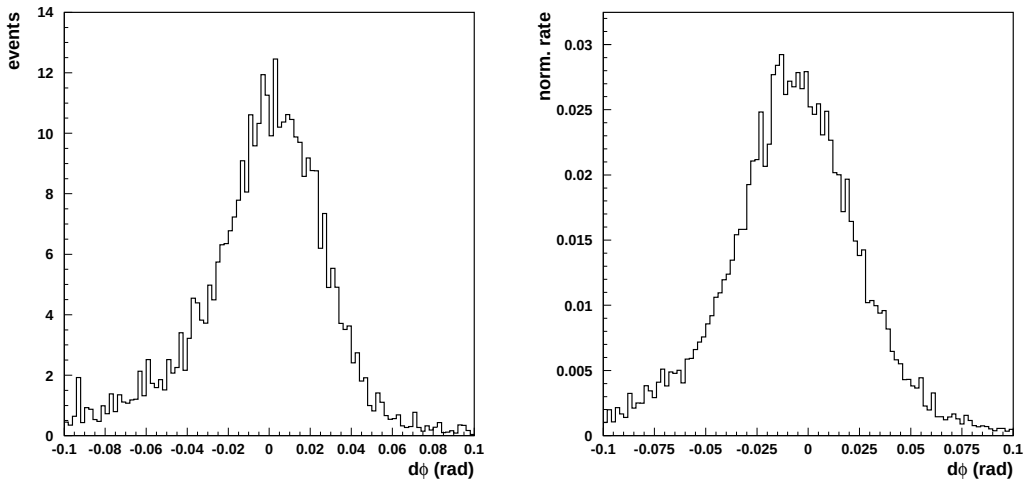

Figure 5.23: Left: Resolution dΦ in the azimuthal angle around the beam for the Silicon Detector. Right: TDR plot of resolution dΦ in the azimuthal angle around the beam for the Silicon Detector

Comparing the two Φ resolution plots it can be seen that there appears to be good agreement between the two distributions.

Energy Deposition in Silicon Detector

Using the energy deposited in each of the two layers and plotting the energy deposited in the 1^{st} silicon layer against that of the energy deposited in the 2^{nd} layer a plot is made which shows the energies at which the recoil proton has enough energy to 'punch through' from one layer to the next (See figure 5.25).

Also shown are the plots of the energy deposited in the 1^{st} and 2^{nd} Silicon layers plotted independently (See figure 5.24).

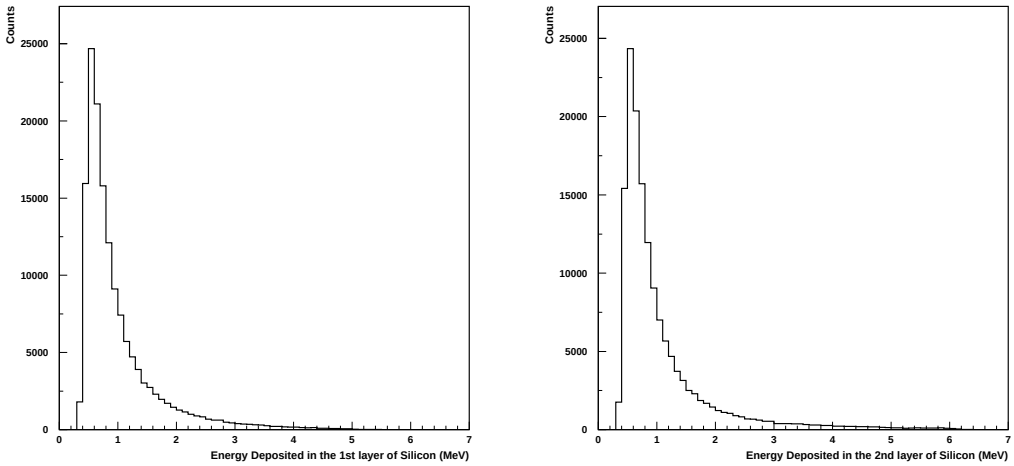

Figure 5.24: Left: Plot of energy deposited in 1^{st} Silicon layer. Right: Plot of energy deposited in 2^{nd} Silicon layer.

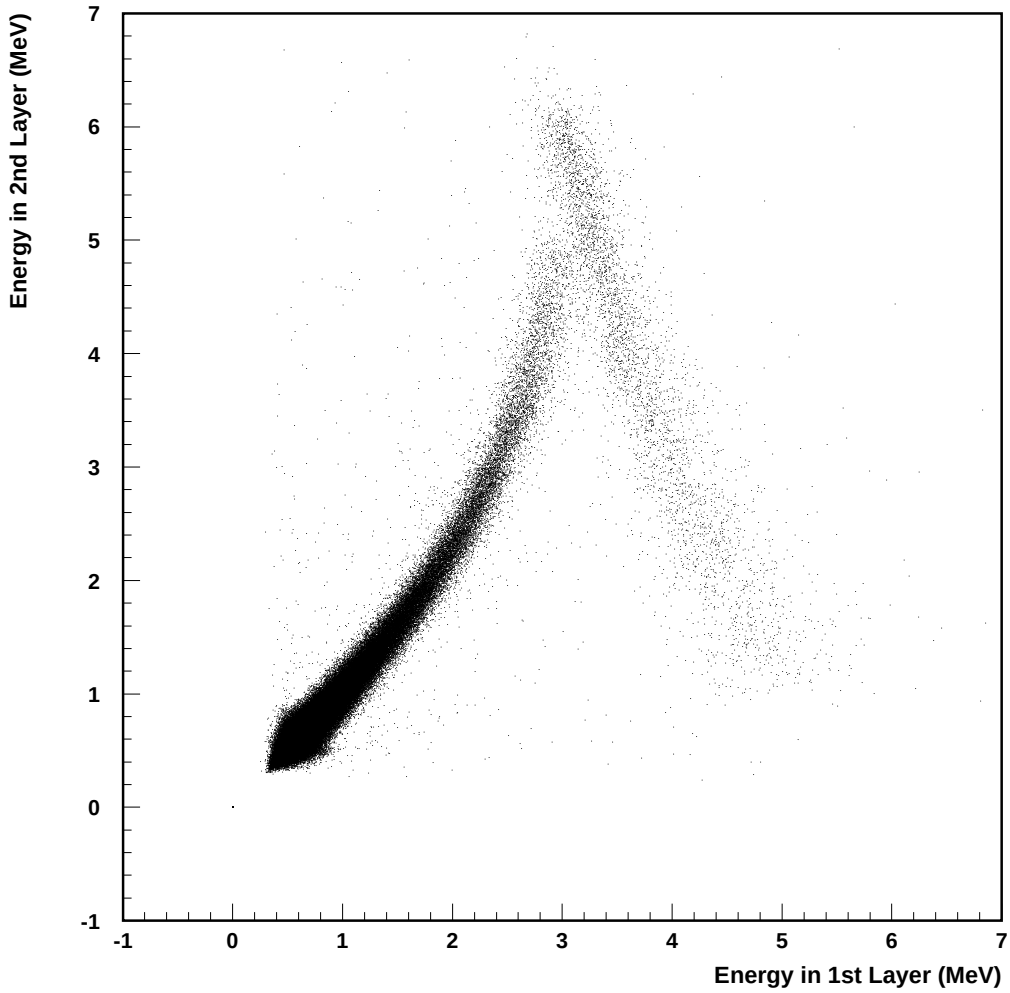

Figure 5.25: Plot of energy deposited in 1^{st} Silicon layer against energy deposited in the 2^{nd} Silicon layer.

Chapter 6

Physics of Vector Meson Production

In this chapter the theoretical and physical basis of this analysis will be described in some detail. First, an overview of the kinematical variables used in the analysis will be explained and presented. Then, in order to give a general overview of vector meson physics the theoretical models that are presented in the latter part of the analysis will also be explained in more detail with an emphasis given to those models which are relevant to the HERMES kinematical region.

6.1 Kinematics

The definition of the kinematical variables and definitions used is this analysis is given in this section. The four-momenta of the incoming and outgoing lepton are denoted as k and k' respectively. The target nucleon has a four-momentum p and a rest mass M. The four momentum and energy of the hadronic final state is p' and $E_{p'}$. In the HERMES laboratory frame (lab) the target is at rest and the energy of the initial and scattered lepton is denoted as E and E' respectively. The polar scattering angle between the incoming and outgoing lepton momentum is θ.

The four momentum of the exchanged virtual photon is then:

$$q \equiv k - k' \tag{6.1}$$

The negative of the four momentum of the virtual photon, or the photon virtuality is given by :

$$Q^2 \equiv -q^2 = -(k - k') \overset{lab}{\approx} 4EE' \sin^2(\frac{\theta}{2}) \tag{6.2}$$

which has positive values for a space-like photon. In this equation the electron rest mass is neglected with respect to the lepton momentum. The Bjorken scaling variable, x is defined as:

$$x \equiv \frac{Q^2}{2p.q} = \frac{Q^2}{2M\nu} \tag{6.3}$$

with:

$$\nu \equiv \frac{p.q}{M} \overset{lab}{=} E - E' \tag{6.4}$$

so that ν represents the energy transfer from the incoming lepton to the virtual photon in the laboratory frame. The Bjorken scaling variable y is given by:

$$y \equiv \frac{p.q}{p.k} \overset{lab}{=} \frac{\nu}{E} \tag{6.5}$$

which in the laboratory frame denotes the fractional energy of the virtual photon with respect to the beam energy.

The squared center of mass energy of the photon-proton system is given by:

$$W^2 = (q+p)^2 = M^2 + 2M\nu - Q^2 = M^2 + Q^2\frac{1-x}{x} \tag{6.6}$$

The last part of the equation shows that for $x = 1$, it becomes $W = M$, which corresponds to elastic scattering. The square of the lepton-proton center of mass energy is denoted as:

$$s \equiv (k+p)^2 \overset{lab}{\approx} M^2 + 2ME \tag{6.7}$$

which in the case of HERMES with a beam energy of 27.5 GeV gives $\sqrt{s} = 7.2$ GeV.

In the context of diffractive vector meson production as depicted in figure 6.1, one commonly uses the squared four momentum transfer to the hadronic vertex:

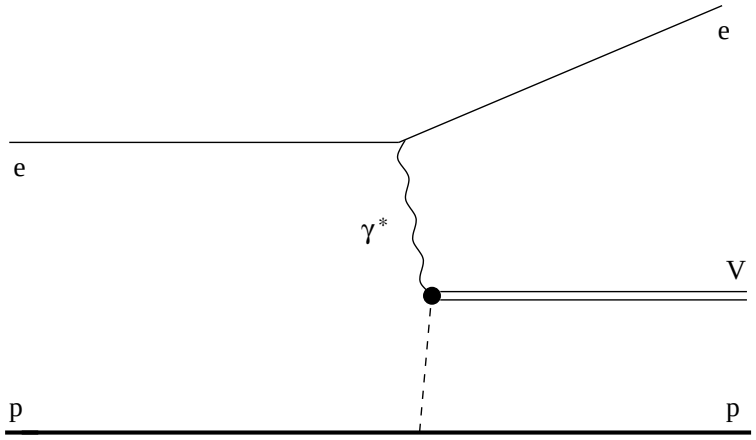

Figure 6.1: Schematic representation of exclusive vector meson production in electron scattering

$$t = (q-v)^2 = (p-p')^2 \tag{6.8}$$

where v is the four momentum of the vector meson. In the laboratory frame one obtains from the second part of the previous equation for exclusive scattering:

$$t = 2M(M - E_{p'}) \tag{6.9}$$

which gives a simple expression for the recoil target energy as a function of t.

Diffractive interactions have their main contribution at small values of t, their squared momentum transfer to the target, and their cross section in that region exhibits an exponential dependence on t. In the hadron center of mass frame one can derive from equation 6.8 that:

$$t = (\nu_{cm} - E_{\nu,cm})^2 - (\mid \vec{q}_{cm} \mid - \mid \vec{p}_{\nu,cm} \mid)^2 - 4 \mid \vec{q}_{cm} \mid\mid \vec{p}_{\nu,cm} \mid \sin^2(\theta_{cm}/2) \tag{6.10}$$

$$= t_0 - 4|\ \vec{q}_{cm}\ ||\ \vec{p}_{\nu,cm}\ |\sin^2(\theta_{cm}/2) \tag{6.11}$$

with θ_{cm} the angle between the vector meson and the virtual photon and t_0 the value t would attain if the vector meson was emitted along the direction of the virtual photon at fixed ν, Q^2, M_V and M_x. The variable t_0 is not Lorentz invariant and is calculated in the hadron center of mass frame using:

$$\nu_{cm} = \frac{W^2 - Q^2 - M_p^2}{2W} \tag{6.12}$$

$$E_{\nu,cm} = \frac{W^2 + M_V^2 - M_x^2}{2W} \tag{6.13}$$

$$|\ \vec{q}_{cm}\ | = \sqrt{\nu_{cm}^2 + Q^2} \tag{6.14}$$

$$|\ \vec{p}_{\nu,cm}\ | = \sqrt{E_{\nu,cm}^2 - M_V^2} \tag{6.15}$$

In the following analysis one often uses the quantity t' defined by:

$$t' = t - t_0 \tag{6.16}$$

In the relativistic scale used t, t_0 and $t' \leq 0$ GeV^2, which makes t_0 the maximum kinematically allowed value of t. Since the t_0 subtraction removes the longitudinal component of the momentum transfer, t' is a measure of the transverse momentum transfer. For exclusive, diffractive processes in the forward region t_0 is small and $t' \approx t$.

An often encountered variable is the polarisation parameter:

$$\epsilon = \frac{1-y}{1-y+y^2/2} \overset{lab}{=} \left(1 + 2(1 + \frac{\nu^2}{Q^2})\tan^2\frac{\theta}{2}\right)^{-1} \tag{6.17}$$

expressing the ratio of the longitudinal to transverse photon flux.

6.2 Deep Inelastic Scattering

The deep inelastic scattering process (DIS) of an electron or positron from a nucleon or nuclear target is depicted in lowest order in figure 6.2. Here we consider only the diagram where the exchanged boson is a virtual photon, as weak interactions mediated by the exchange of a heavy intermediate vector boson $W^{\pm}$ or Z^0 can be neglected for the energy and momentum transfers reachable in the HERMES experiment. Multi-photon exchange diagrams are suppressed by a factor of α_{em} and may be taken into account via so called radiative corrections.

The kinematics in an inclusive event are completely constrained by two independent variables, where often Q^2 and x are chosen. The DIS regime is usually defined via the kinematical constraints to have a large momentum transfer (e.g.$Q^2 > 1$ GeV^2) and a large photon-nucleon center of mass energy (e.g. $W^2 > 4$ GeV^2).

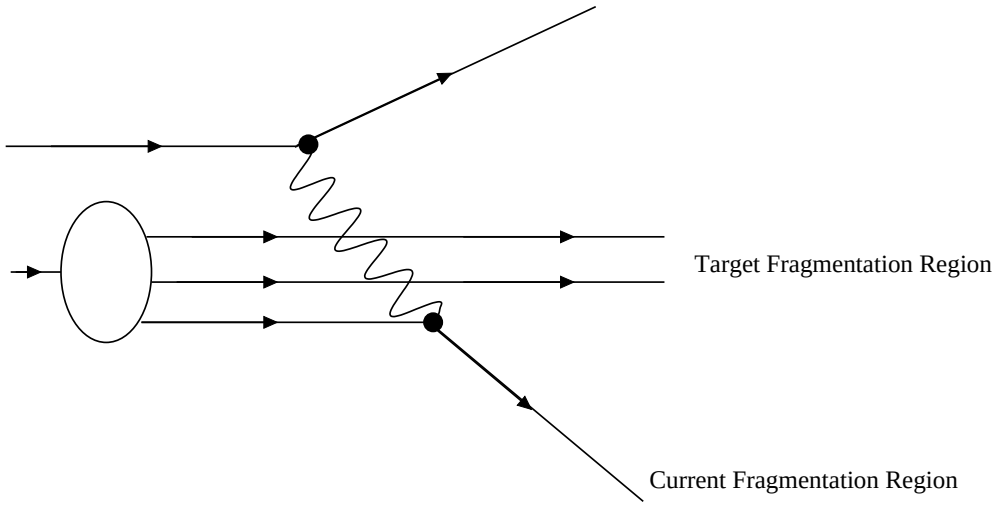

Figure 6.2: Schematic representation of the deep-inelastic scattering process in the quark parton model with the one-photon exchange approximation.

6.3 Diffraction

The term diffraction is derived from classical optics. In classical optics, diffraction is a process where a light wave is incident upon an obstacle and a resulting interference pattern is formed on the opposite side of the object due to its presence. This interfernce pattern results in maxima and minima being produced. Diffraction was first used in high energy physics as an analogy to explain the diffractive maxima and minima that were observed in the angular distribution spectra in elastic scattering on nuclear targets. It is also used to describe elastic elastic-hadron scattering where similar maxima and minima are observed.

An elastic reaction is one where the incident particles are left intact after the collision. In the case that one of the incident particles gives rises to either a resonance or a bunch of final outgoing states with the same quantum numbers as the initial particle while the other particle is unchanged then the process is refered to as single diffraction. In the case that both outgoing particles produce either a bunch of particles with the same quantum numbers as the initial particle or a resonance then the process is refered to as double diffraction. The different types of diffractive processes are shown in figure 6.3.

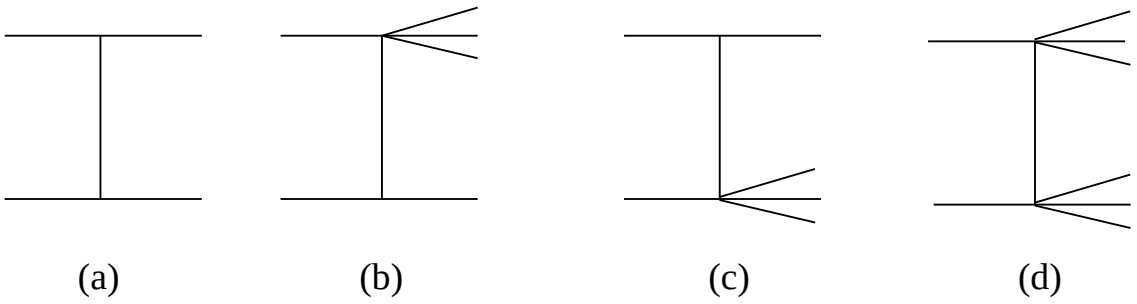

Figure 6.3: Different types of diffraction: (a) elastic scattering (b) and (c) single diffraction, (d) double diffraction

6.3.1 Optical Diffraction

The simplest model of diffraction is one in which an incident plane wave is scattered on a totally absorbing black disk, or sphere. of well defined radius R. The resulting angular distribution of the scattering process is the Fourier transfrom of the spatial distribution of the obstacle. The irradiance of the object is then given by:[69]

$$\frac{I(\theta)}{I(\theta=0)} = \Big(\frac{2J_1(x)}{x}\Big)^2 \approx 1 - \frac{R^2}{4}(k\theta)^2 \tag{6.18}$$

The distribution shows a strong peak in the forward direction at around $\theta = 0$ where the distributions maximum is formed at the centre of the formed pattern. with the Bessel function J_1, $k = 2\pi/\lambda$ the light wave number and $x = kR\sin\theta$. The pattern has maxima for $|x| = 3.83,\ 7.02..$ which are symmetrical around the optical axis through the centre of the aprerature.

In elastic-hadron scattering similar patterns are observed as those produced in the model above. The differential cross section depends mainly on the four momentum transfer squared between the two hadrons, $t = (p_1 - p_1')^2 = (p_2 - p_2')^2$. This can also be written as $-t = q^2 = (2p\sin\theta/2)^2$ where p is the momentum of the colliding particles and θ is the scattering angle in the centre of mass system. Therefore the differential cross section for elastic scattering depends mainly on q. In the impact parameter space the target particle is modelled by an opaque disk of radius R in the black disk model, with the impact parameter b being the distance of the two particles along the direction of the incoming particle. The absorption is total for $b \leq R$ and doesn't occur for $b > R$. The scattering is a function of both t and s, the centre of mass energy according to:[71]

$$T(s,t) \propto \frac{J_1(qR)}{qR} s \tag{6.19}$$

The elastic cross section exhibits diffractive maxima and minima, where minima occur for $qR = 3.83,\ 7.02...$ In figure 6.4 the diffractive forward peak at low $|t| \leq 1$ GeV^2 can be cleary obsrved. At $|t| \to 0$ the differential cross section depends only weakly on the energy and is roughly equivalent for all curves. It can also be seen that the first minimum in $|t|$ decreases slowly with increasing energy, which indicates a gradualy increasing in the effective size of the interaction radius. At high energy the first minimum occurs at around $|t| = 1.15$ GeV^2 which yields a value for the interaction of the radius of around 0.7 fm.

The simple model of scattering a plane wave can reproduce some of the basic properties of pp scattering. The model fails to predict however the ratio of elastic to the total cross section and also their energy dependence. The model suggests that $\sigma_{el}/\sigma_{tot} = 0.5$. In reality this ratio is well below 0.5 and decreases with increasing energy [72].

As nucleons do not have a sharply defined surface the optical model can be improved by having an absorbing disk which is not totally absorbing but is instead 'grey' with a Gaussian density distribution. The Gaussian shape leads to a cross section which falls off exponentially with t. The cross section in the forward region i.e $|t| \lesssim 0.5$ GeV^2 is normally written as:

$$\frac{d\sigma/dt}{(d\sigma/dt)_{t=0}} = e^{bt} \approx 1 - b(p\theta)^2 \tag{6.20}$$

with p the centre of mass momentum of the particles. Comparing this equation with 6.18 results in the relation between the radius of interation, R, and the slope parameter, b, which is:

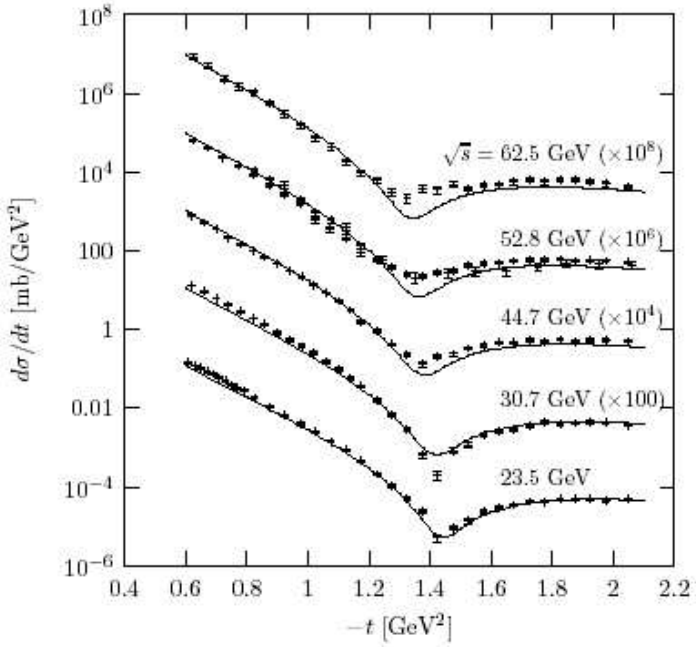

Figure 6.4: The elastic differential pp cross section $d\sigma/dt$ for different incident proton energies [70]

$$b = \frac{R^2}{4} \tag{6.21}$$

This implies that the slope of the forward elastic peak is related to the size of the scattering object on which the scattering occurs. The slope b can be obtained experimentally using pp scattering [73] at high energy. Typical values of b are between 5 to 13 GeV^{-2}.

6.4 Regge Theory

Regge theory shows that it is useful to treat the angular momentum l as a complex variable. Regge theory, which is used in particle physics, uses the idea of analytically continuing a scattering amplitude into the complex angular momentum plane [74]. Scattering amplitude singularities which are found in the complex plane are called Regge poles and correspond to either bound states or resonances depending on the value of the angular momentum.

Regge theory uses an approach called the crossing symmetry principle: an incoming particle of momentum p can be though of as being an outgoing antiparticle of momentum $-p$. The reaction $a(p_a) + b(p_b) \rightarrow c(p_c) + d(p_d)$ has squared centre of mass energy $s = (p_a+p_b)^2 > 0$ and the scattering angle is related to its momentum transfer $t = (p_a-p_c)^2 < 0$. In the crossed reaction $a(p_a) + \overline{c}(-p_c) \rightarrow \overline{b}(-p_b) + d(p_d)$ one has that the centre of mass energy squared is given by $(p_a - p_c)^2 > 0$ and the scattering angle is now related to the momentum transfer $(p_a + p_b)^2 < 0$. The positive region of t and the negative region of s of the first reaction play a role in the centre of mass energy squared and the momentum transfer respectively of the crossed process. The first reaction is called an s-channel reaction , while the second is referred to as the t-channel counterpart of the first one. Both reactions are described by the same amplitude, however they are in different and non-overlapping kinematical regions in s and t.

Hadronic states which have the same quantum numbers, for example, isospin, strangeness and baryon number appear to lie on a straight line which is called a Regge trajectory when the spin of the particle is plotted against the mass squared. These Regge trajectories can be parameterised as:

$$\alpha(t) = \alpha(0) + \alpha' t \tag{6.22}$$

where $\alpha(0)$ is the intercept and $\alpha' t$ the slope of the Regge trajectory. This can be done for particles whose quantum numbers differ only in their spin and mass and are plotted in what are known as Chew-Frautschi plots. Experimental results of diffractive scattering processes, which have a negative momentum transfer, can be added to such a plot and appear to align along extensions to $t < 0$ of the Regge trajectories, whose quantum numbers match possible resonances that could be exchanged in the crossed process.

An example is shown in figure 6.5 for the reaction $\pi^- p \to \pi^0 n$. The parity transfer in the reaction is positive and given by $\Delta P = (-1)^J P$ with J and P the angular momentum and parity of the object exchanged in the t-channel. In order to conserve all quantum numbers, the reaction can only proceed via the exchange of ρ, a_2 and ρ_3 with quantum numbers $J^P = 1^-, 2^+, 3^-$, which all lie on the Regge trajectory passing through the measured data points. This Regge trajectory is actually nearly identical to the ω/f trajectory also shown in the figure.

Regge theory is expected to work well for roughly $s > 10$ GeV^2, i.e energies above the resonance region. The optical theorem relates the imaginary part of the forward scattering amplitude to the total cross section:

$$\sigma_{tot} = \frac{1}{s}\mathrm{Im}(A|_{t=0}) \tag{6.23}$$

so that the forward differential cross section can be written as:

$$\frac{d\sigma}{dt}\Big|_{t=0} = \frac{1}{16\pi}(1+\eta^2)\sigma_{tot}^2 \tag{6.24}$$

with η the ratio of the real to the imaginary part of the forward scattering amplitude, which leads to:

$$\sigma_{tot} \propto s^{\alpha(t=0)-1} \tag{6.25}$$

This means that the high energy behaviour of the total cross section is dominated by the highest lying Regge trajectories, which in the Chew-Frautschi plot are the degenerate ρ/a_2 and ω/f trajectories with an intercept of about $\alpha_{\rho,\omega}(0) \approx 0.5$. One would therefore expect to find a total cross section going like $\sigma_{tot} \propto s^{-1/2}$. This behaviour however is not observed in hadron-proton scattering at high energy. Instead the cross sections appear to be rather constant with energy and even tend to rise slowly above about 10 GeV. To explain this observation in terms of Regge pole exchange a trajectory with $\alpha(0) \approx 1$ would be required, while all known particles have $\alpha(0) < 1$. The exchanged particle also needs to have the quantum numbers of the vacuum. This leads to the idea of a new linear trajectory called the Pomeron trajectory with $\alpha_{\mathbb{P}}(0) = 1 + \epsilon$ and $0 < \epsilon \ll 1$:

$$\alpha_{\mathbb{P}} = 1 + \epsilon + \alpha'_{\mathbb{P}} t \tag{6.26}$$

Assuming that the vector-meson cross section has the typical behaviour of hadron-hadron cross sections, the intercepts of the Regge and Pomeron trajectories can be described by a sum of two terms:

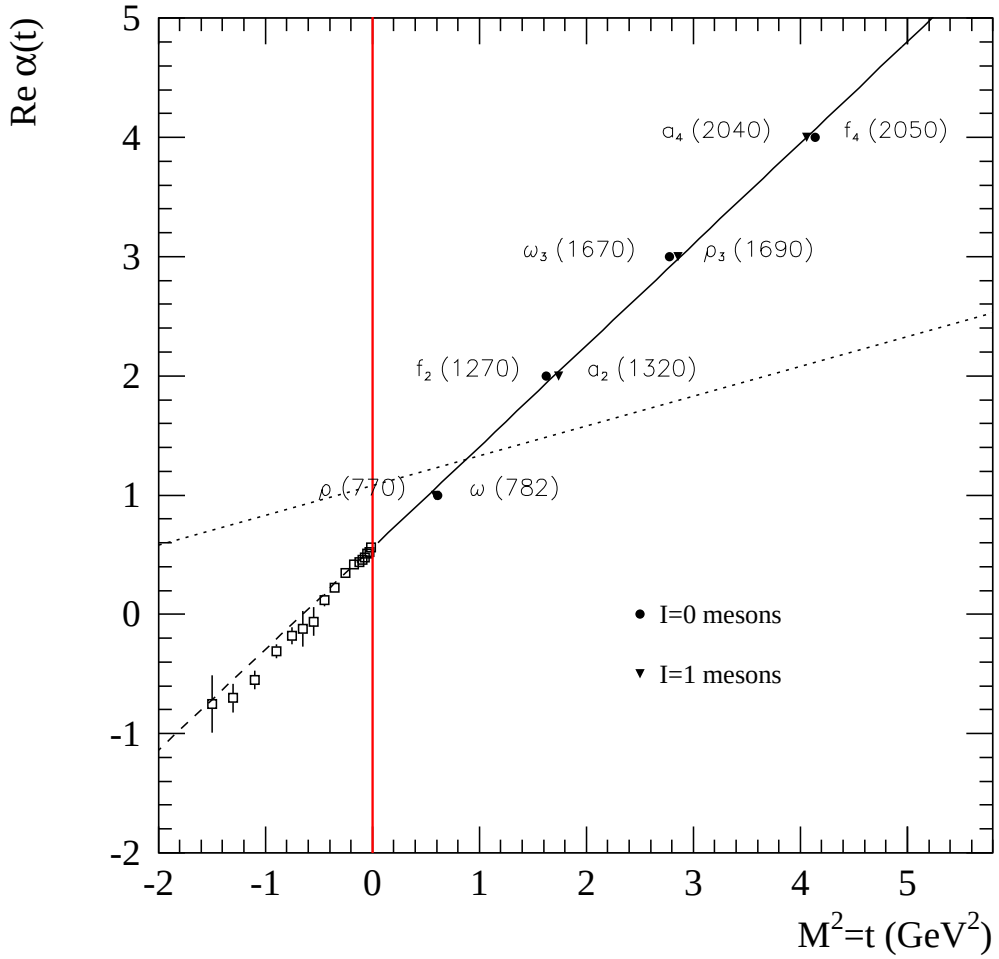

Figure 6.5: Chew-Frautschi plot for the two different (however almost identical) Regge trajectories corresponding to natural parity exchange. The full line shows a fit to the mesons according to equation 6.22, while the dashed line is the extension of the fit to $t < 0$. The points at $t < 0$ were derived from $\pi^- p \to \pi^0 n$ scattering data [75]. The dotted line represents the trajectory corresponding to Pomeron exchange.

$$\sigma_{tot} = X s^{\epsilon} + Y s^{-\eta} \tag{6.27}$$

In this case X and Y are arbitrary normalisations and $s = W^2$ is the hadron-hadron centre of mass energy. The first term corresponds to the Pomeron exchange and the second term to the exchange of the highest lying Regge trajectory $(\rho/a_2, \omega/f)$. The exponents ϵ and η for Pomeron and Reggeon exchange respectively, can be determined from fits to experimental data and are assumed to be independent of the interacting hadrons. The values obtained for X and Y depend on the specific process. Donnachie and Landshoff [76] applied the fit to pp and $p\overline{p}$ data with $\sqrt{s} > 10$ GeV and found values of $\epsilon = 0.0808$ and $\eta = 0.4525$ as displayed in figure 6.6.

6.5 Vector Meson Dominance Model

When quantum Electrodynamics was first introduced the photon was regarded as a massless, chargeless gauge boson with a pointlike coupling to elementary charged particles.

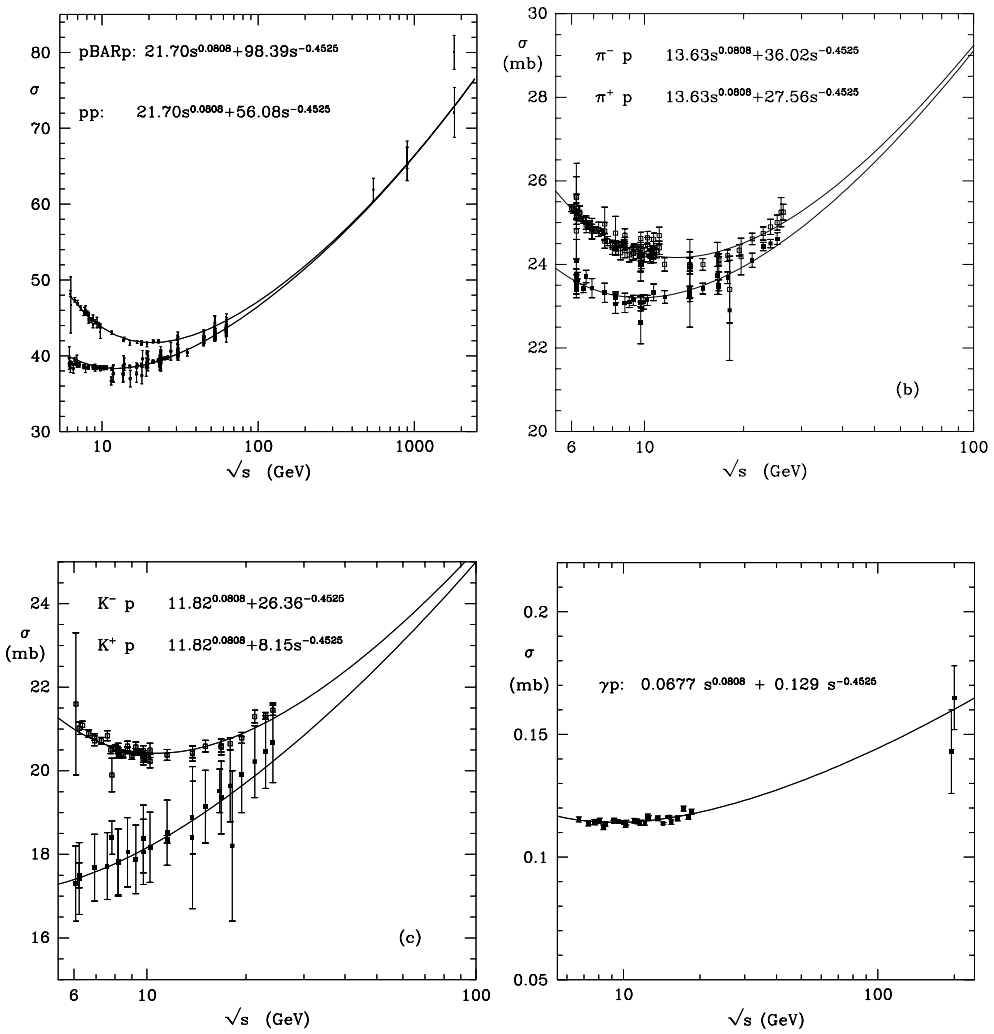

Figure 6.6: The total cross sections [76] for (a) pp and $p\overline{p}$, (b) $\pi^- p$ and $\pi^+ p$, (c) $K^- p$ and $K^+ p$ and (d) γp. The fitted curves correspond to equation 6.27. Note that the exponents ϵ and η were fixed at the values found in the pp and $p\overline{p}$ fit.

Later on, as the scale of the energy increased it was found that photons could actually fluctuate or materialise into electron-positron pairs ($\gamma \rightarrow e^+e^-$) through their interaction with a Coulomb field. This phenomenon was one of the first indications that the photon had a more sophisticated structure than was first thought. In quantum field theory the electromagnetic field couples to all particles carrying electromagnetic current enabling a photon to fluctuate into more complex virtual states. In this way the photon also acquires a hadronic internal structure, which occurs with a relative probability only on the order of $\alpha \sim 1/137$ as compared with the bare particle.

Scattering processes which involved scattering the photon onto a proton target were the first to show the hadronic properties of the photon. The reactions had many similarities with scattering processes which were purely hadronic.

The way in which these similarities were understood was to assume that the physical photon could be modeled as a superposition of a bare photon, $|\gamma_B >$ undergoing only purely electromagnetic interactions with the target and a small hadronic component, $|\gamma_h >$ which takes part in pure hadronic interactions:

$$|\gamma >\simeq \sqrt{Z_3}|\gamma_B > +\sqrt{\alpha}|\gamma_h > \tag{6.28}$$

where Z_3 assumes the proper normalisation of $|\gamma >$. Conservation laws indicate that $|\gamma_h >$ has the same quantum numbers as the bare photon, namely $J^{PC} = 1^{--}, Q = S = B = 0$. The contribution of the bare photon to the interaction can be neglected as it is several orders of magnitude smaller than the contribution of the hadronic part of the photon. The relatively large cross section for production of the light vector mesons ρ^0, ω and ϕ suggests that the latter constitute the dominant contribution to the hadronic photon component $|\gamma_h >$. The so called vector meson dominance model (VDM) is based on the assumption that these three mesons are the only hadronic constituents of the photon and that the bare photon component $|\gamma_B >$ does not interact with hadrons at all.

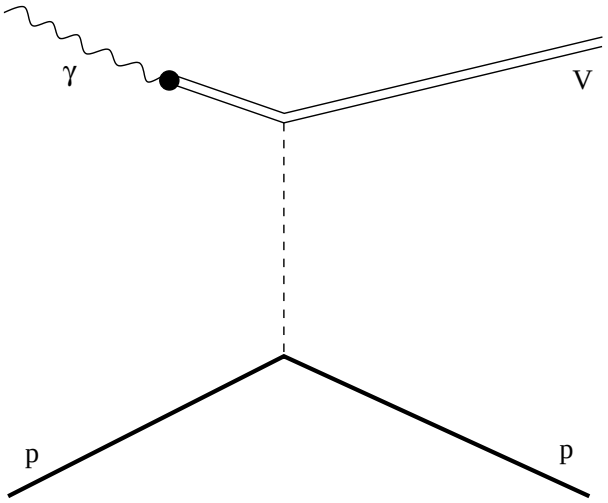

Figure 6.7: Photoproduction of vector mesons in the vector meson dominance model. The photon is assumed to virtually dissociate into a vector meson V, which subsequently scatters off a nucleon.

The photoproduction of vector mesons can be quite successfully described by this vector meson dominance model. The fluctuation of the formation time of a photon into a $q\overline{q}$ or virtual vector meson state is given by[77]:

$$t_f \approx \frac{2\nu}{Q^2 + M_V^2} \tag{6.29}$$

If t_f is long enough to allow the virtual vector meson to travel a distance much larger than the nucleon radius of about 1 fm, the photon fluctuates long before it hits the target and the interaction occurs between the virtual meson and the nucleon depicted in figure 6.7. Consequently photoproduction of vector mesons is closely related to elastic vector meson scattering off a nucleon.

The second term in equation 6.28 can be rewritten [77][78] as:

$$\sqrt{\alpha}|\gamma_h >= \sum_V \frac{e}{f_V}(1 + \frac{Q^2}{M_V^2})^{-1}|V > \tag{6.30}$$

where the vector meson states $|V >$ have momentum k and f_V denotes the $\gamma \leftrightarrow V$ coupling constant. The VDM coupling can be related to the mass of the vector meson and to its leptonic decay width Γ_{ee}^V according to[78]:

$$\frac{4\pi}{f_V^2} = \frac{3\Gamma_{ee}^V}{\alpha^2 M_V} \tag{6.31}$$

The Q^2 behaviour is determined by the propagation of single vector meson states only as expressed in equation 6.30. This leads to the VDM cross section predictions given separately for transversely and longitudinally polarised photons.

$$\sigma_T^{\gamma^* p}(Q^2, W) = \sum_V \frac{e}{f_V^2}(1 + \frac{Q^2}{M_V^2})^{-2}\sigma_T^{Vp}(W) \tag{6.32}$$

$$\sigma_L^{\gamma^* p}(Q^2, W) = \sum_V \frac{e}{f_V^2}(1 + \frac{Q^2}{M_V^2})^{-2}\xi_V^2\frac{Q^2}{M_V^2}\sigma_T^{Vp}(W) \tag{6.33}$$

where σ_T^{Vp} is the total cross section for the transversely polarised vector meson. The longitudinal Vp cross section need not be the same as the transverse one, which justifies the introduction of the factor ξ_V^2 representing the ration of the two. In VDM it is predicted to be $\mathcal{O}(1)$[79]. However experimental results on ρ^0 production indicate that this ratio is lower[80][81]. One also notices from equation 6.33 that the longitudinal cross section vanishes at Q^2 =0, i.e for real photons.

Using the VDM predictions one arrives at the relation between the total virtual photoproduction and the real photoproduction cross section:

$$\sigma^{\gamma^* p}(Q^2, W) = \big(1 + \epsilon\xi_V^2\frac{Q^2}{M_V^2}\big)\big(1 + \frac{Q^2}{M_V^2}\big)^{-2}\sigma^{\gamma p}(W) \tag{6.34}$$

where $\epsilon = \frac{\Gamma_L}{\Gamma_T}$ is the ratio between the longitudinal and transverse photon flux. The ratio of equations 6.32 and 6.33 gives us the important VDM prediction that for the ratio of the longitudinal and transverse photoproduction cross section:

$$R = \frac{\sigma_L}{\sigma_T} = \xi_V^2\frac{Q^2}{M_V^2} \tag{6.35}$$

6.6 Vector Meson Polarisation

This section deals with the formalism used to study vector meson polarisation states. The vector meson and the virtual photon have the same quantum numbers. The vector meson spin density matrix elements can be expressed in terms of helicity amplitudes describing the transfer of the virtual photon helicity to the vector meson. It is therefore useful to start with the derivation of the spin density matrix of the virtual photon to come to that of the vector meson itself. In the end the vector meson angular decay distribution is expressed as a function of these spin density matrix elements. A detailed and complete description of the formalism can be found in [82][83]. The relevant features of the theory will be explained in the paragraphs below. The nomenclature and format of the equations presented below is from [84].

6.6.1 The Photon Spin Density Matrix

The differential cross section for vector meson V production in eN scattering reads:

$$\frac{d\sigma_{eN\to eNV}}{dE'd\Omega'd\Phi dt} = \frac{1}{(2\pi)^5}\frac{E'}{E}\frac{m^2}{4\sqrt{\nu^2+Q^2}}\frac{1}{Q^4}\sum_{spins}|\mathcal{M}|^2 \tag{6.36}$$

where $d\Omega'$ is the volume element of the scattered lepton, Φ the angle between the scattering plane and the hadron production plane and $\mathcal{M}$ the matrix element describing the scattering process. The matrix element is given by:

$$\mathcal{M} = e^2 < l_2|j_\mu|l_1 > \cdot < n_2 v|j^\mu|n_1 > \tag{6.37}$$

where l_1, l_2, n_1, n_2 and v are the spinors for the incoming and outgoing lepton and nucleon and vector meson respectively, e the electric charge and j the electromagnetic current operator.

For an unpolarised lepton beam $|\mathcal{M}|^2$ can be rewritten in terms of known a lepton tensor $\widetilde{L}_{\mu\nu}$ and a hadronic tensor $\widetilde{T}^{\mu\nu}$:

$$\frac{1}{4}\sum_{spins}|\mathcal{M}^2| = \frac{1}{4}\,\widetilde{L}_{\mu\nu}\widetilde{T}^{\mu\nu} \tag{6.38}$$

where both tensors are defined as:

$$\widetilde{L}_{\mu\nu} = \sum_{spins} m^2 < l_2|j_\mu|l_1 > \cdot < l_2|j_\nu|l_1 >^* \tag{6.39}$$

$$\widetilde{T}^{\mu\nu} = \sum_{spins} < n_2 v|j_\mu|n_1 > \cdot < n_2 v|j_\nu|n_1 >^* \tag{6.40}$$

$\widetilde{L}_{\mu\nu}$ is the virtual photon spin density matrix describing the spin state of the photon. One can evaluate this tensor in a coordinate system with the z-axis of the virtual photon direction $q = l_2 - l_1$ and with l_1 and l_2 in the x, z plane where $\widetilde{L}_{\mu\nu}$ in general has the transverse (x, y), longitudinal (z) and scalar (0) components. A Lorentz transformation along $\overrightarrow{q}$ leaves the transverse components unchanged, but transforms the scalar and longitudinal components into each other. Just like the polarisation of a physical spin 1 particle is Lorentz invariant, one can show that this also holds for the spin density matrix. It can thus be evaluated in the Breit frame, resulting in a matrix $L_{\mu\nu}(\epsilon, \delta)$ with ϵ the polarisation parameter defined by $\frac{L_{11}}{L_{12}} = \frac{1-\epsilon}{1+\epsilon}$ and $\delta = \frac{2m^2}{Q^2}(1-\epsilon)$ the mass correction parameter. Finally $L_{\mu\nu}$ can be written in the hadron centre of mass helicity frame by rotating it around the z-axis over an angle Φ between the leptonic and hadronic production plane:

$$L_{\lambda\lambda'} = U_{\lambda\mu} L_{\mu\nu} U^{-1}_{\nu\lambda'} \tag{6.41}$$

where λ and λ' denote the photon helicity ($\lambda, \lambda' = +1, 0, -1$) and $U_{\lambda\mu}$ describes the rotation. The end result is a spin density matrix $L_{\lambda\lambda'}$, which is a function of ϵ, δ and Φ.

In the case of a polarised incident lepton beam with polarisation vector P_μ, $\widetilde{L}_{\mu\nu}$ has to be replaced by another matrix $\widetilde{\mathcal{L}}_{\mu\nu}$ given by:

$$\widetilde{\mathcal{L}}_{\mu\nu} = \widetilde{L}_{\mu\nu} + \widetilde{S}_{\mu\nu}\ . \tag{6.42}$$

Just like $\widetilde{L}_{\mu\nu}$, $\widetilde{S}_{\mu\nu}$ is Lorentz invariant under a boost along $\overrightarrow{q}$ and can be transformed into the helicity basis to $S_{\lambda\lambda'}$ which is a function of ϵ, Φ and the degree of polarisation P.

The photon density matrix, normalised to a unit flux of transverse photons, then becomes:

$$\rho(\gamma)_{\lambda\lambda'} = \frac{1-\epsilon}{Q^2}(L_{\lambda\lambda'} + S_{\lambda\lambda'}) \tag{6.43}$$

The spin density matrix can be decomposed into an orthogonal set of nine hermitian matrices $\sum^{\alpha}$:

$$\rho(\gamma) = \frac{1}{2}\sum_{\alpha=0}^{8} \widetilde{\Pi}_{\alpha} \sum^{\alpha} \tag{6.44}$$

where $\widetilde{\Pi}_{\alpha}$ is a known vector, function of ϵ, δ, Φ and the lepton polarisation vector. Each of the nine hermitian matrices describes a different photon polarisation state. The matrices $\sum^{0\ldots3}$ describe the transverse photons and correspond to the formalism used in the photoproduction formalism[82]: $\sum^{0}$ represents the unpolarised part, $\sum^{1-2}$ gives the linear polarisation and $\sum^{3}$ describes the circular polarisation. $\sum^{4}$ corresponds to longitudinal photons and $\sum^{5\ldots8}$ provide transverse/longitudinal interference terms.

6.6.2 The Vector Meson Spin Density Matrix

The paragraphs above dealt with the lepton vertex only, leading to the spin density matrix of the virtual photon. To come to the spin density matrix of the vector meson, we now consider the hadron vertex corresponding to the scattering reaction $\gamma^{*}N \rightarrow VN$. The cross section for this process looks like:

$$\frac{d\sigma_{\gamma^{*}N\rightarrow VN}}{dtd\Phi} = \frac{1}{32\pi^{2}(\nu^{2}+Q^{2})}\frac{2(1-\epsilon)}{Q^{2}}\frac{1}{4}\sum_{spins}|\mathcal{M}|^{2} \tag{6.45}$$

where the factor $2(1-\epsilon)/Q^{2}$ is introduced to normalise to unit transverse photon flux. The cross section can be rewritten in terms of the helicity amplitudes of Jacob and Wick, describing the transfer of the photon helicity to the vector meson after summing over the nucleon helicities:

$$T_{\lambda_{V}\lambda_{N'}\lambda_{\gamma}\lambda_{N}} = < \lambda_{V}\lambda_{N'}|j_{\lambda_{\gamma}}|\lambda_{N} > \tag{6.46}$$

with $j_{\lambda_{\gamma}=\pm1} = j_{x} \pm ij_{y}$ and $j_{\lambda_{\gamma}=0} = j_{z}$, resulting in:

$$\frac{d\sigma_{\gamma^{*}N\rightarrow VN}}{dtd\Phi} = \frac{1}{32\pi^{2}(\nu^{2}+Q^{2})}\frac{1}{2}Tr(T\rho(\gamma)T^{\dagger}) \tag{6.47}$$

The vector meson spin density matrix is then:

$$\rho(V) = \frac{1}{2}(T\rho(\gamma)T\dagger)/\int\frac{d\Phi}{2\pi}Tr(T\rho(\gamma)T\dagger) \tag{6.48}$$

where a summation over the nucleon helicities is understood and the integral is used to normalise the matrix. The density matrix can now be decomposed into hermitian matrices in a similar way as for the photon density matrix:

$$\rho(V) = \sum_{\alpha=0}^{8}\Pi_{\alpha}\rho^{\alpha} \tag{6.49}$$

with

$$\rho^{\alpha}_{\lambda_{V}\lambda'_{V}} = \frac{1}{2N_{\alpha}}\sum_{\lambda_{N'}\lambda_{N}\lambda_{\gamma}\lambda'_{\gamma}} T_{\lambda_{V}\lambda_{N'}\lambda_{\gamma}\lambda_{N}}\sum\nolimits^{\alpha}_{\lambda_{\gamma}\lambda'_{\gamma}} T^{*}_{\lambda'_{V}\lambda_{N'}\lambda'_{\gamma}\lambda_{N}} \tag{6.50}$$

where the N_{α} are normalisation constants and the vector Π_{α} is a known function of ϵ, δ, $R = \frac{\sigma_{L}}{\sigma_{T}}$, Φ and the lepton polarisation vector. Each of these nine hermitian matrices ρ^{α} again represent production by different virtual photon polarisation states. $\alpha = 0$

corresponds to unpolarised transverse photons, $\alpha = 1, 2$ to the two directions of linear polarisation, $\alpha = 3$ represents circular photons and $\alpha = 4$ gives longitudinally polarised photon production. $\alpha = 5...8$ provide the transverse/longitudinal interference part, where only $\alpha = 5, 6$ contribute for an unpolarised lepton beam, while a polarised lepton beam gives the additional $\alpha = 7, 8$ terms.

Due to parity conservation the following symmetry relation for the helicity amplitudes holds:

$$T_{-\lambda_V - \lambda_{N'} - \lambda_\gamma - \lambda_N} = (-1)^{(\lambda_V - \lambda_{N'}) - (\lambda_\gamma - \lambda_N)} T_{\lambda_V \lambda_{N'} \lambda_\gamma \lambda_N} \tag{6.51}$$

One can prove that as a consequence of the previous relation and symmetry properties of the $\sum^\alpha$ matrices, the vector meson spin density matrix elements defined by equation 6.50 obey the symmetry relation:

$$\rho^\alpha_{-\lambda-\lambda'} = \begin{cases} (-1)^{\lambda-\lambda'} \rho^\alpha_{\lambda\lambda'} & \alpha = 0,\ 1,\ 4,\ 5,\ 8, \\ -(-1)^{\lambda-\lambda'} \rho^\alpha_{\lambda\lambda'} & \alpha = 2,\ 3,\ 6,\ 7 \end{cases} \tag{6.52}$$

6.6.3 Vector Meson Decay Angular Distribution

The ρ^0 or ω vector mesons are spin-1 objects and therefore in their rest frame they carry a total angular momentum $J = L+S = 1$. Due to angular momentum conservation, the decay meson system also has $J = 1$. When looking at the most common decay modes, $\rho^0 \to 2\pi$ and $\omega \to 3\pi$, the decay particles have spin 0, meaning that the angular momentum L of the decay system must be 1. When a vector meson decays, its spin state will be reflected in the orbital angular momenta of its decay particles.

The decay distribution of the vector meson will be described in the vector meson rest frame using the so called s-channel helicity system, in which the quantisation axis (z-axis) is chosen opposite to the direction of the outgoing nucleon in the centre of mass frame (see figure 6.8). The decay angles θ and ϕ are, in the case of the ρ^0, defined as the polar and azimuthal angle of one of the decay pions, where usually the π^+ is taken. For a three particle decay one would take the polar and azimuthal angles of the unit vector along the normal to the decay plane.

In the vector meson rest frame the decay angle distribution for the decay into 2 or 3 pseudoscalar mesons is given by:

$$\frac{dN}{d\cos\theta d\phi} \equiv W(\cos\theta, \phi) = \sum_{\lambda_V \lambda'_V} < \theta, \phi | M | \lambda_V > \rho(V)_{\lambda_V \lambda'_V} < \lambda'_V | M^\dagger | \theta, \phi > \tag{6.53}$$

with M the decay amplitude. $< \theta, \phi | M | \lambda_V >$ can be expressed as a function of the general Wigner D-functions $D^j_{mm'}(R)$ which give the probability that the quantum state $|j, m >$ is transformed into the state $|j, m' >$ after the rotation R. Here the D-functions are to be taken as $D^{S_V}_{\lambda_V \lambda_\pi}(R)$ and they are given by:

$$D^1_{10}(\phi, \theta, -\phi) = -\frac{1}{\sqrt{2}} e^{-i\phi} \sin\theta \tag{6.54}$$

$$D^1_{00}(\phi, \theta, -\phi) = \cos\theta \tag{6.55}$$

$$D^1_{-10}(\phi, \theta, -\phi) = \frac{1}{\sqrt{2}} e^{i\phi} \sin\theta \tag{6.56}$$

The vector meson angular distribution in terms of the spin density matrix now reads:

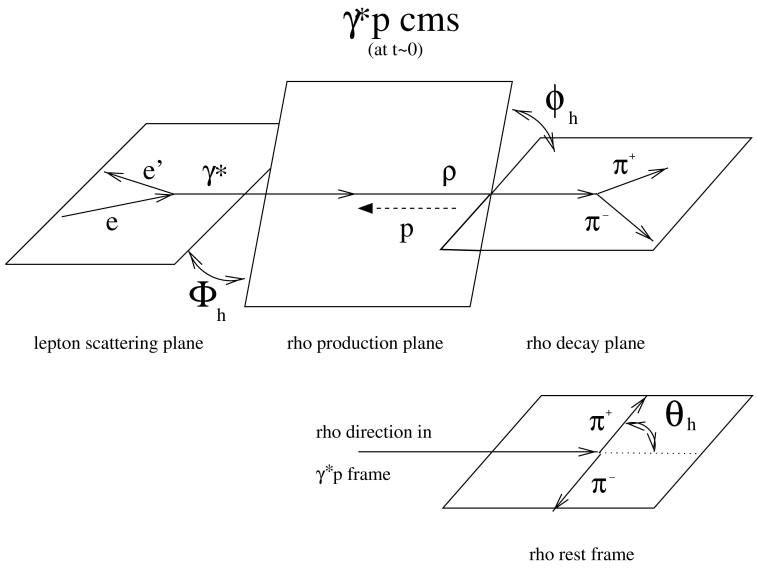

Figure 6.8: The definition of the angles used in the ρ^0 vector meson analysis. Φ is the angle between the scattering plane and the hadron production plane. θ, and ϕ are the polar and azimuthal angles of the decay π^+ in the vector meson rest frame in the s-channel helicity system.

$$W(\cos\theta,\phi,\Phi) = \frac{3}{4\pi}\sum_{\lambda_V\lambda'_V} D^1_{\lambda_V 0}(\phi,\theta,-\phi)^*\rho(V)_{\lambda_V\lambda'_V} D^1_{\lambda'_V 0}(\phi,\theta,-\phi) \tag{6.57}$$

where the Φ dependence comes from the vector meson density matrix which Φ dependence arises in turn from the virtual photon density matrix as can be seen from 6.48. Inserting equation 6.49 the above can then be written as:

$$\begin{aligned} W(\cos\theta,\phi,\Phi) &= \sum_{\alpha=0}^{8}\Pi_\alpha W^\alpha(\cos\theta,\phi,\Phi) \\ &= \sum_{\alpha=0}^{8}\Pi_\alpha\Big[\frac{3}{4\pi}\sum_{\lambda_V\lambda'_V} D^1_{\lambda_V 0}(\phi,\theta,-\phi)^*\rho^\alpha_{\lambda_V\lambda'_V} D^1_{\lambda'_V 0}(\phi,\theta,-\phi)\Big] \end{aligned} \tag{6.58}$$

The last equation can be split into an unpolarised part and a beam polarisation dependent term:

$$W(\cos\theta,\phi,\Phi) = W^{unpol.}(\cos\theta,\phi,\Phi) + W^{pol.}(\cos\theta,\phi,\Phi) \tag{6.59}$$

where the beam polarisation is either longitudinal or transverse.

With the symmetry relation 6.52 the total number of independent matrix elements appearing in equation 6.59 is 26. The unpolarised part turns out to be a function of 18 ρ^α_{ik} with $\alpha = 0....2, 4....6$. However, in order to separate the contributions of ρ^0_{ik} and ρ^4_{ik} the value for R has to be known and thus a separation of σ_L and σ_T is needed. For a longitudinal beam polarisation the polarised term in equation 6.59 provides us with 8 additional ρ^α_{ik} with $\alpha = 3, 7, 8$. It is therefore sufficient to measure with a longitudinally polarised lepton beam to completely determine the full set of matrix elements entering equation 6.52 given the fact that R is known. Measurements with a transversely polarised

lepton beam yield only the contributions of ρ^{α}_{ik} with $\alpha = 7, 8$ and hence do not provide any additional information as compared to the longitudinal beam polarisation case.

In the case no separation of σ_L and σ_T is done, the following combinations of the matrix elements ρ^{α}_{ik} can be determined:

$$r^{\alpha}_{ik} \equiv \frac{\rho^{0}_{ik} + \epsilon R \rho^{4}_{ik}}{1 + \epsilon R} \tag{6.60}$$

$$r^{\alpha}_{ik} \equiv \begin{cases} \frac{\rho^{\alpha}_{ik}}{1+\epsilon R} & \alpha = (1,\ 2,\ 3) \\ \sqrt{R}\frac{\rho^{\alpha}_{ik}}{1+\epsilon R} & \alpha = (5,\ 6,\ 7,\ 8). \end{cases} \tag{6.61}$$

With a longitudinally polarised lepton beam, as in HERMES, the decay angular distribution given by equation 6.59 becomes:

$$W(\cos\theta, \phi, \Phi) = W^{unpol.}(\cos\theta, \phi, \Phi) + W^{long.pol.}(\cos\theta, \phi, \Phi) \tag{6.62}$$

The polarisation independent term then reads:

$$\begin{aligned} W^{unpol.}(\cos\theta, \phi, \Phi) &= \frac{3}{4\pi}\big[\frac{1}{2}(1 - r^{04}_{00}) + \frac{1}{2}(3r^{04}_{00})\cos^2\theta \\ &= -\sqrt{2}\mathrm{Re}r^{04}_{00}\sin 2\theta\cos\phi - r^{04}_{1-1}\sin^2\theta\cos 2\phi \\ &= -\epsilon\cos 2\Phi(r^{1}_{11}\sin^2\theta + r^{1}_{00}\cos^2\theta - \sqrt{2}\mathrm{Re}r^{1}_{10}\sin 2\theta\cos\phi - r^{1}_{1-1}\sin^2\theta\cos 2\phi) \\ &= -\epsilon\sin 2\Phi(\sqrt{2}\mathrm{Im}r^{2}_{10}\sin 2\theta\sin\phi + \mathrm{Im}r^{2}_{1-1}\sin^2\theta\sin 2\phi) \\ &= \sqrt{2\epsilon(1+\epsilon)}\cos\Phi(r^{5}_{11}\sin\theta + r^{5}_{00}\cos^2\theta - \sqrt{2}\mathrm{Re}r^{5}_{10}\sin 2\theta\cos\phi - r^{5}_{1-1}\sin^2\theta\cos 2\phi) \\ &= \sqrt{2\epsilon(1+\epsilon)}\sin\Phi(\sqrt{2}\mathrm{Im}r^{6}_{10}\sin 2\theta\sin\phi + \mathrm{Im}r^{6}_{1-1}\sin^2\theta\sin 2\phi)\big] \end{aligned} \tag{6.63}$$

This contribution contains 15 independent matrix elements, which in this work will be referred to as the 'unpolarised' elements. The term depending on the longitudinal beam polarisation P_b is given by:

$$\begin{aligned} W^{long.pol.}(\cos\theta, \phi, \Phi) = \\ \frac{3}{4\pi}P_b[&\sqrt{1-\epsilon^2}(\sqrt{2}\mathrm{Im}r^{3}_{10}\sin 2\theta\sin\phi + \mathrm{Im}r^{3}_{1-1}\sin^2\theta\sin 2\phi) \\ &+ \sqrt{2\epsilon(1-\epsilon)}\cos\Phi(\sqrt{2}\mathrm{Im}r^{7}_{10}\sin 2\theta\sin\phi + \mathrm{Im}r^{7}_{1-1}\sin^2\theta\sin 2\phi) \\ &+ \sqrt{2\epsilon(1-\epsilon)}\sin\Phi(r^{8}_{11}\sin^2\theta + r^{8}_{00}\cos^2\theta - \sqrt{2}\mathrm{Re}r^{8}_{10}\sin 2\theta\cos\phi \\ &- r^{8}_{1-1}\sin^2\theta\cos 2\phi)] \end{aligned} \tag{6.64}$$

where P_b can be positive or negative depending on the helicity of the beam. The polarisation dependent term is seen to contain 8 independent matrix elements, which will be referred to as the 'polarised' elements.

6.6.4 S-Channel Helicity Conservation

An important assumption in vector meson production concerns the helicity conservation in the s-channel (SCHC) at the $\gamma^* p$ vertex in the hadronic centre of mass system, meaning that the helicity of the virtual photon would be retained by the vector meson. In terms of the helicity amplitudes this translates into:

$$T_{\lambda_V \lambda_{N'} \lambda_\gamma \lambda_N} = T_{\lambda_V \lambda_{N'} \lambda_\gamma \lambda_N}\delta_{\lambda_V \lambda_\gamma}\delta_{\lambda_{N'} \lambda_N} \tag{6.65}$$

In that case all the amplitudes corresponding to a helicity change become zero:

$$T_{01} = T_{10} = T_{0-1} = T_{-10} = T_{-11} = T_{1-1} = 0 \tag{6.66}$$

where the nucleon helicities were omitted. Taking equation 6.51 into account leaves only three independent amplitudes, T_{00}, T_{11} and T_{-1-1}. Using the relations between the helicity amplitudes and the matrix elements (see Appendix C) one finds that all matrix elements become zero except r^{04}_{00}, r^{1}_{1-1}, r^{2}_{1-1}, Re r^{5}_{10}, Im r^{6}_{10} , Im r^{7}_{10} and Re r^{8}_{10}.

The decay angle distribution $W(\cos\theta, \phi, \Phi)$ given in equation 6.62 can, in the case of SCHC, be expressed as a function of $\cos\theta$ and Ψ, where $\Psi = \phi - \Phi$ is called the polarisation angle and represents the angle between the vector meson decay plane and the lepton scattering plane:

$$\begin{aligned} W(\cos\theta, \Psi) = \frac{3}{4\pi}[&\frac{1}{2}(1 - r^{04}_{00}) + \frac{1}{2}(3r^{04}_{00} - 1)\cos^2\theta \\ &+ \epsilon r^{1}_{1-1}\sin^2\theta\cos 2\Psi - 2\sqrt{\epsilon(1+\epsilon)}\mathrm{Re}r^{5}_{10}\sin 2\theta\cos\Psi \\ &+ 2P_b\sqrt{\epsilon(1+\epsilon)}\mathrm{Im}r^{7}_{10}\sin 2\theta\sin\Psi]. \end{aligned} \tag{6.67}$$

The terms in r^{04}_{00} which denote the contribution to longitudinal vector mesons, depend only on $\cos\theta$. The term in r^{1}_{1-1} represents the contribution from transverse vector mesons. The last two terms correspond to an interference between the longitudinal and transverse contributions.

6.6.5 Natural and Unnatural Parity Exchange

As was explained in previous sections the exclusive, diffractive production of vector mesons can be seen to proceed via exchange of particles through the t-channel. The exchanged particle could have natural parity $P = (-1)^J$, or unnatural parity $P = -(-1)^J$. Using yet another symmetry property of the helicity amplitudes:

$$T_{-\lambda_V\lambda_{N'}-\lambda_\gamma\lambda_N} = \pm(-1)^{\lambda_V-\lambda_\gamma}T_{\lambda_V\lambda_{N'}\lambda_\gamma\lambda_N} \tag{6.68}$$

which is valid to leading order in s and where the $+(-)$ sign corresponds to natural (unnatural) parity exchange, one can show that both the helicity amplitudes and the spin density matrix elements can be split into a contribution from both natural and unnatural parity exchange. A complete measurement of the spin density matrices $\rho^{0\ldots8}$ even allows to separate both contributions and to determine the natural and unnatural parity exchange fractions of the transverse and longitudinal cross sections.

The Pomeron in diffractive interactions carries the quantum numbers of the vacuum and therefore has intrinsic parity equal to 1. Pomeron exchange thus corresponds to natural parity exchange (NPE) in the t-channel.

When assuming natural parity exchange in the t-channel together with SCHC, equation 6.68 leaves only two independent amplitudes, where usually T_{00} and T_{11} are chosen. The latter two denote the non-flip amplitudes for production by longitudinal and transverse photons respectively. A phase difference between these amplitudes is introduced according to:

$$T_{00}T^*_{11} = |T_{00}||T_{11}|e^{-i\delta}. \tag{6.69}$$

In that case equation 6.67 can be written as:

$$W(\cos\theta,\Psi) = \frac{1}{1+\epsilon R}\frac{3}{8\pi}[\sin^2\theta(1+\epsilon\cos 2\Psi) + 2\epsilon R\cos^2\theta$$
$$- \sqrt{2\epsilon(1+\epsilon)R}\cos\delta\sin 2\theta\cos\Psi + P_b\sqrt{2\epsilon(1-\epsilon)R}\sin\delta\sin 2\theta\sin\Psi] \quad (6.70)$$

where the decay angle distribution is now determined by the R ratio and δ only.

6.7 Non-Perturbative Models

6.7.1 The Donnachie and Landshoff Model

Donnachie and Landshoff [85] used their Regge type fits of hadron-hadron cross sections in combination with the additive quark model and vector meson dominance to predict the energy behaviour of the ρ^0 real photoproduction cross section. Combining expression 6.24 of the optical theorem with VDM yields:

$$\left.\frac{d\sigma^{\gamma p\to\rho^0 p}}{dt}\right|_{t=0} = \frac{e^2}{f_{\rho^0}^2}\left.\frac{d\sigma^{\gamma p\to\rho^0 p}}{dt}\right|_{t=0} = \frac{1}{16\pi}\frac{e^2}{f_{\rho^0}^2}(1+\eta^2)(\sigma_{tot}^{\rho^0 p})^2 \quad (6.71)$$

The total $\rho^0 p$ cross section can be related to those of the $\pi^{\pm}p$ interactions using the additive quark model:

$$\sigma_{tot}^{\rho^0 p} \approx \frac{1}{2}\left(\sigma_{tot}^{\pi^+ p} + \sigma_{tot}^{\pi^- p}\right) \quad (6.72)$$

Inserting their Regge type (see expression 6.27) cross section fits [76] to π^+p and π^-p scattering gave a total $\rho^0 p$ cross section in millibarns:

$$\sigma_{tot}^{\rho^0 p} = 13.6s^{0.008} + 31.8s^{-0.45} \quad (6.73)$$

This model provides a good description of the energy behaviour of the cross section, however the absolute magnitude is predicted to be about 15% above the measured values.

This over estimation of the cross section is explained by the $\gamma - V$ coupling constant f_{ρ^0} used in the model. The coupling was related to the e^+e^- decay via equation 6.31, while the vector meson photoproduction measurements yield a coupling which is larger [86]. Using the Donnachie and Landshoff fits together with a coupling constant derived from photoproduction measurements in the centre of mass energy region $9< W <18$ GeV, results in a much better agreement to the data [86].

6.7.2 The Manayenkov Model

Manayenkov [87] used an approach where the amplitude of the photon dissociation into a $q\overline{q}$ pair is described by a light-cone wave function. The scattering of the colourless $q\overline{q}$ pair off the nucleon is then calculated using Reggeon exchange phenomenology. The production of the final vector meson state from the scattered quark-antiquark pair is calculated with the aid of the parton-hadron duality concept.

The scattering of the quark-antiquark pair on the proton at high energies for large $(Q^2 + m_v^2)$ and small x can be described in the double-logarithmic approach of pQCD through two gluon exchange ladders[88]. In Manayenkov's approach, however Regge formalism for the amplitude of the $q\overline{q}$ pair scattering off the target is used, rather than the approach used in pQCD. In order to obtain the quark-reggeon vertices from the nucleon-reggeon vertices the nucleon was treated as a 3 quark system whose spin structure is described by

the non-relativistic quark model [89]. The parameters of the quark-reggeon vertices were obtained [90] with the aid of the parameters of the nucleon-reggeon vertices found by fitting to experimental data on hadron-nucleon scattering[91][92][93]. In Manayenkov's approach exchanges with the pomeron, P and secondary reggeons f, ρ, ω, A_2 are taken into account.

The final vector meson production from the scattered $q\overline{q}$ pair is the second step in the model calculation. Due to the fact there is no appropriate light-cone wave function of the ρ^0 meson available Manayenkov used an approach based on parton-hadron duality [94]. The final state of the colourless $q\overline{q}$ pair is projected onto the state with $J^P = 1^-$ and isospin, $I = 1$ in order to calculate the ρ^0 meson spin density matrix.

The model appears to work well at the total energy of the photon-nucleon scattering in the centre of mass system $W > 4$ GeV, where the Regge phenomenology is known to be applicable. The calculations performed in this approach appear to be in reasonable agreement with the world data on $R = \sigma_L/\sigma_T$ at $Q^2 < 4$ GeV^2, where perturbative QCD is, strictly speaking, inapplicable. The approach however fails to agree with the available data for $Q^2 > 4$ GeV^2, where pQCD describes the data well. The matrix elements in this model agree relatively well with the current world data up to the region where $Q^2 = 8$ GeV^2.

6.8 Perturbative QCD Models

Regge theory is a suitable way of describing vector meson production at low and high energies, but only at low momentum transfers. As soon as the hard scale in the scattering process sets in, one can turn to a perturbative quantum chromodynamics (pQCD) based model description of vector meson production. The hard scale can be introduced by going to higher values of momentum transfer Q^2 or $|t|$, or also by generating vector mesons containing heavy quarks (c or b quarks). The two collider experiments at HERA can access this kind of hard regime and provided a large amount of measurements allowing the testing of a variety of pQCD models.

When looking at exclusive vector meson production, one has to remember that the initial and final states in the scattering process cannot be described in a perturbative regime and therefore have to be separated from the short distance, hard interaction part. A general factorisation theorem proven by Collins, Frankfurt and Strikman [24] states that at large values of $Q^2 \gg \Lambda^2_{QCD}$, for small $|t|$ and assuming that the meson mass can be neglected $M_V^2 \ll s$, the leptoproduction cross section $\gamma^* p \to V p'$ can be expressed as a convolution of a generalised parton distribution function of a proton, a hard scattering function and a meson wave function.

In the proton rest frame vector meson production at high energy can be seen to occur in three distinct steps ordered in time: the virtual photon breaks up in a quark-antiquark pair;the quark-antiquark pair interacts hard with the target; the scattered quark-antiquark pair forms the final state vector meson. The scattering process on the proton occurs on a much shorter time scale than the fluctuation of the photon in the $q\overline{q}$ pair or the vector meson formation time, allowing the scattering to be treated as a perturbation.

The amplitude can thus be factorised in:

$$A = \Psi^*_{\gamma^* \to q\overline{q}} \otimes A_{q\overline{q}+p \to q\overline{q}+p} \otimes \Psi_{q\overline{q} \to V} \tag{6.74}$$

The first term represents the amplitude for the fluctuation of the virtual photon into a $q\overline{q}$ pair. The last term describes the recombination of the final, scattered hadronic state into the vector meson. The middle term corresponds to the short distance amplitude of the scattering of the hadronic state with the target. This latter term can be calculated in

pQCD models and the exchanged colour singlet system is at high energy (or small x) usually modeled as a gluon pair or a gluon Lipatov ladder. The obtained amplitude is proportional to the square of the gluon density in the proton $(xg(Q^2, x))^2$. This makes hard vector meson production more sensitive to variations in the gluon distribution than the inclusive process which depends linearly on $xg(Q^2, x)$. Significant theoretical uncertainties arise due to the choice of the scale at which the gluon density is probed, the parameterisation of the gluon distribution and the modeling of the vector meson wave function [95].

Some general features of pQCD like calculations are:

- The cross section for hard diffractive vector meson production is related to the square of the gluon density in the nucleon and therefore provides a sensitive probe of the gluon content in the target.
- The cross section should be dominated by production due to longitudinally polarised photons at high Q^2, meaning that $R = \sigma_L/\sigma_T$ should increase with Q^2 to values above unity.

6.8.1 The Model of Goloskokov *et. al*

In the approach of Goloskokov and Kroll [96] electroproduction of the light vector mesons at small x_{Bj} is analysed using a GPD based approach. In this kinematical domain the gluonic GPD H^g, which parameterises the response of the proton to the emission and reabsorption of gluons, controls the process. At present the gluonic GPD is not calculable, instead an ansatz using double distributions is assumed to construct the model for this GPD. A t dependence for the gluonic GPD H^g is difficult due to lack of a plausible parameterisation. The electroproduction amplitudes are therefore evaluated at $t \simeq 0$ and then multiplied by a factor which is exponential in t. The authors note that this approach must be improved once more detailed differential cross section data is released.

The GPD approach appears to reproduce all the main features of vector meson electroproduction at small x_{Bj}. The assumption of the dominance of the contribution from the GPD H^g over those from $\widetilde{H}^g$ and E^g leads to results which appear to be similar to those obtained assuming the dominance of natural parity exchange.

The numberical results obtained using this approach are in reasonable agreement with the small x_{Bj} data on cross sections and spin density matrix elements for electroproduction of ρ and ϕ mesons measured by H1 and ZEUS. The results appear to be in reasonable agreement for the region $Q^2 > 4$ GeV^2. The t dependence of vector meson production is not yet satisfactorily solved. The GPD approach has, in contrast to some other approaches, the potential to investigate the t dependence of electroproduction. However the lack of undestanding of the GPD's t dependence prevents this at this time.

6.8.2 The Model of Martin *et. al.*

It is suggested by Martin, Ryskin and Teubner in [94] that any description of vector meson production in terms of a convolution of the wave function of the $q\overline{q}$ pair (produced by the γ^*) with one of the vector mesons, yields a prediction for the longitudinal cross section consistent with the behaviour of the data, while the transverse cross section is predicted much too small and falls too rapidly with increasing Q^2.

The authors present an alternative pQCD approach to ρ electroproduction based on the production of open light $q\overline{q}$ pairs and the hadron-parton duality assumption, where the convolution of the ρ wave is omitted. The parton-hadron hypothesis states that the total hadron (ρ, ω,...) production cross section averaged over a mass interval of typically 1 GeV^2

is well represented by the partonic cross section. In the low mass region containing the ρ meson, complicated partonic states (with e.g additional gluon emission) are suppressed, while on the hadronic side one has mainly 2π and some 3π states. The cross section is therefore modeled according to:

$$\sigma(\gamma^* p \to \rho p) \approx 0.9 \sum_{q=u,d} \int_{M^2_{low}}^{M^2_{high}} dM^2 \frac{d\sigma(\gamma^* p \to (q\overline{q})p)}{dM^2} \tag{6.75}$$

where the integration limits are chosen to span the ρ invariant mass region (e.g 0.6< M <1.05 GeV) with $M^2_{high} - M^2_{low} \sim 1$ GeV^2 and where the factor 0.9 is introduced to allow for ω production. The basic diagram in their calculation is depicted in figure 6.9. The virtual photon fluctuates into a $u\overline{u}$ or $d\overline{d}$ pair, which then interacts hard with the proton via the exchange of the 2-gluon system or gluon ladder. A long time after the interaction the $q\overline{q}$ pair is distorted by confinement and has, due to phase space restrictions little alternative but to hadronise into a ρ meson.

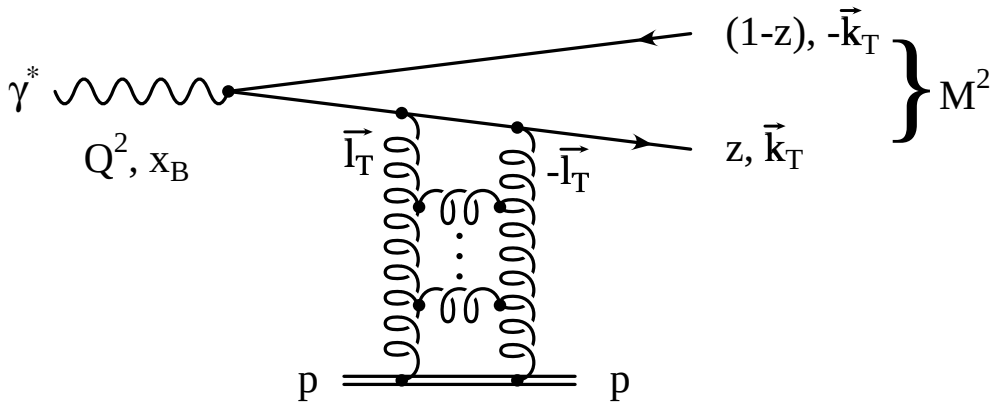

Figure 6.9: The diffractive production of an open light $q\overline{q}$ pair with an invariant mass M, as used in the model of Martin *et. al.*. z and $(1-z)$ are the momentum fractions of the quark and antiquark relative to the virtual photon momentum. $\pm k_T$ denotes the transverse momenta of the quark and antiquark.

Both the longitudinal and transverse part of the cross section are found to be proportional to the square of the gluon density which is probed at a scale:

$$K^2 = z(1-z)Q^2 + k_T^2 \tag{6.76}$$

where z and $1-z$ are the longitudinal momentum fractions of the quark and antiquark relative to the virtual photon momentum and $\pm k_T$ are the transverse momenta of the quark with respect to the virtual photon. The scale represents the typical transverse distance probed in the process by $b_T \approx 1/K$.

The calculations are done under the assumption of s-channel helicity conservation and for $t = 0$. The model has no explicit dependence on t and therefore an exponential behaviour $exp(-b|t|)$ is added to the cross section with $b = 5.5$ GeV^{-2} as seen in experimental data for large Q^2.

Their prediction for the R ratio may be written as:

$$\frac{\sigma_L}{\sigma_T} = \frac{Q^2}{M^2}\left(\frac{\gamma}{\gamma+1}\right)^2 \tag{6.77}$$

with M the invariant mass of the $q\overline{q}$ pair and γ the effective anomalous dimension of the gluon as defined by $\gamma \equiv \mathrm{d}\ \ln(xg(x,K^2)/\mathrm{d}\ \ln K^2$. This anomalous dimension is seen to decrease with increasing Q^2 and therefore slows down the strong increase with Q^2 of the R ratio at high Q^2.

The model suffers from large normalisation uncertainties on the predicted cross section. One problem is the choice of the width of the invariant mass interval over which the parton-hadron duality assumption has to be applied. Another is the effect of virtual gluon corrections to open $q\overline{q}$ production, which leads to the so-called K factor enhancement $exp(\alpha_s C_f \pi)$ with the colour factor $C_f = 4/3$. The major ambiguity here is the choice of the scale α_s. Nevertheless, the prediction of the R ratio is rather free of the above uncertainties and should therefore, according to the authors, provide a valuable probe of the gluon distribution $g(x,K^2)$ in the domain $x \approx Q^2/W$ and $K^2 \lesssim Q^2/4$.

Chapter 7

Data Analysis and Hermes Monte Carlo

In this chapter we discuss the way in which the raw data which the detector accumulates is converted into a form more suited for a physics analysis. We then review the organisation of the HERMES data stream and production chain. A look will then be taken at the tracking, clustering and particle identification algorithms which are used within the software chain to extract the physics information from the detector response. The last section of the chapter will focus on the HERMES Monte Carlo. Monte Carlo simulations are utilised within the analysis at HERMES in different ways and are an important tool. The software simulates different types of scattering processes and reproduces the geometry and response of the detector for these reactions.

7.1 Data Organisation and Production

The large amount of data collected in the experiment requires a simple organisation in order to be manageable in a physics analysis.

The data acquisition records all detector information when it receives an appropriate trigger, the data recorded at that point is referred to as a single event. Each event corresponds to a scattering process of the HERA lepton beam on the target.

The event stream from the DaQ is put into what are referred to as bursts, lasting typically 10 seconds. The bursts are grouped into runs where the amount of data collected is determined by the size of the tapes in the central storage.

Each run belongs to a given fill, defined as a beam fill of the HERA machine, which generally lasts for 8 hours. At the beginning of a fill, after the positrons has been injected and as soon as beam and detector conditions are appropriate, the HERMES spectrometer is switched on and the data taking for that run begins. The data taking continues until the lepton (positron) beam current reduces to around 12 mA, at which point the high density unpolarised gas is generally introduced into the target until the lepton beam current is further reduced to around 9 mA at which point the data taking is stopped and the subdetectors are put on stand by.

The HERMES data is also subdivided by the year in which the data was collected. This is due to the different spectrometer configuration and varied polarised targets for different years.

The software production chain used at HERMES is shown schematically in figure 7.1. The HERMES Decoder (HDC) reads the raw event run files, in what is called EPIO format, and converts the data for each subdetector into its specific quantities, for example hit

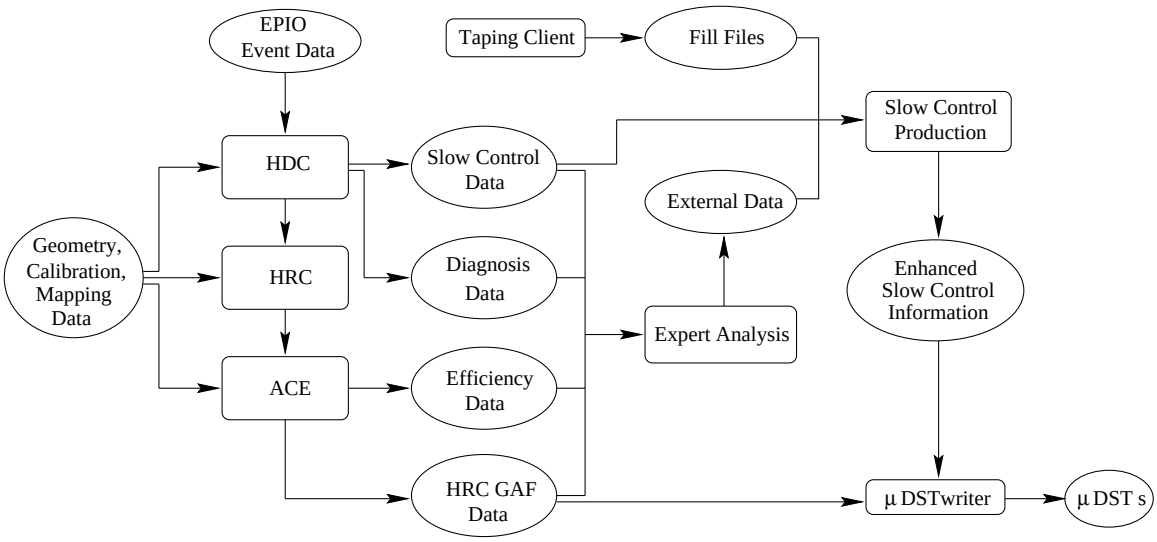

Figure 7.1: Diagram of the HERMES data production chain. Boxes represent software. Packages handling the data stored on disks or tape are depicted by ellipses [84].

positions in a given detector or energy deposition in a specific module. The output format is based on the tabular output of the ADAMO package and the data is written to GAF's (Generic Adamo Files). The HDC output is then fed into the HERMES Reconstruction Code (HRC) which in essence does the reconstruction of the particle trajectories that are recorded in the spectrometer and also takes care of the clustering in the calorimeter. Tracking chamber efficiencies are calculated from the HRC GAF output files by the ACE (Alignment, Calibration, Efficiency) program. The detector geometries, and mapping and calibrations of the various subdetectors used by the program described above are contained on several DAD (Distributed ADAMO Database) servers.

The slow control information is provided partially by 'fill files' of the taping client and also include some external data coming from offline studies performed by subsystem experts. This combined information is used to produce a time ordered slow control data file for each fill.

Finally a filter program extracts the relevant data for a physics analysis from the HRC output and combines it with the corresponding information from the slow control fill files to produce compact run files called μDSTs (Data Summary Tapes). These μDSTs form the basis for all further physics analysis.

7.2 Tracking and Clustering

Data coming from the HERMES decoder or from the HERMES Monte Carlo is analysed by the HERMES Reconstruction Code which uses a pattern recognition algorithm to reconstruct the charged particle trajectories from the information recorded by the tracking chambers.

The tracking algorithm starts by combining the detector hits in each of the three wire directions (U, X, V) to reconstruct track projections, called tree-lines, in each of these three planes. This is accomplished by a pattern recognition routine which matches the detector information against a database representing all possible tracks in the spectrometer. As depicted in figure 7.2 a recursive tree-search algorithm starts in a first step with an artificial detector resolution of two bins. The hit pattern obtained in this way is matched against a

first-level database pattern. In each successive step the resolution is doubled and the hit patterns are compared to all physically possible child patterns deduced from matching the parent pattern found in the previous step. This procedure is repeated until the bin size is on the order of the spatial resolution of the tracking chambers.

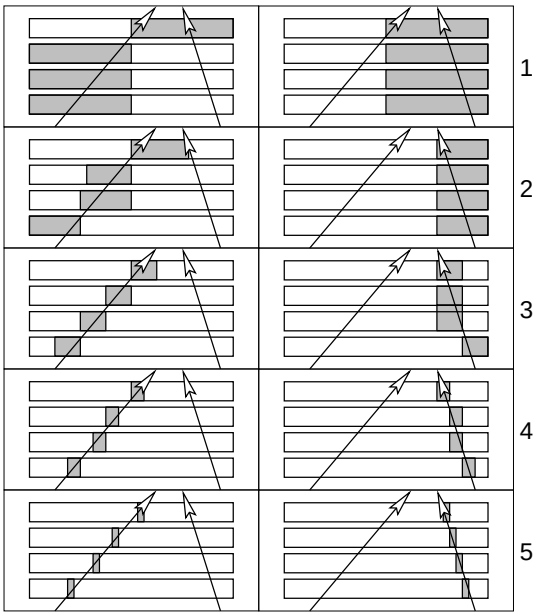

Figure 7.2: The tree-line search algorithm recursively matches the detected hit pattern against a database, with increasing resolution.

Once a full track is found the momentum of the particle is determined using a lookup table, generated beforehand by tracking a large amount of particles through a Monte Carlo model of the setup with a parameterisation of the accurately measured field map of the spectrometer. The momentum and angular resolution attained is better than $\Delta p/p = 0.5\%$ and 1 mrad respectively.

For each track the minimal distance of approach to the beamline is calculated, which provides a good indication whether the particle originates from an interaction with the target or not.

Particle showers in the calorimeter are usually larger than the cell size of the colorimeter, so that signals are produced not only in the block that was hit, but also in the surrounding blocks. This results in the formation of so called calorimeter clusters. Test beam measurements reported cluster widths of σ_{cl} =4.5 cm. The determination of the calorimeter energy of charged particles is important for the particle identification. Also neutrals, especially photons, produce calorimeter clusters whose energy and position represent the only source of information on these particles as they are not seen by the tracking chambers.

The cluster search algorithm in HRC is based on finding the local energy maxima in the calorimeter plane. A cluster is then defined as the group of 3×3 cells centred around the block with the largest energy signal. The energy of the cluster is calculated by summing over its member cells and the (x, y)-position of the cluster is defined as the energy weighted mean position of the center of the blocks in the cluster. Partial cluster overlap is taken into account by distributing the energy of overlapping cells proportional to the energy sums of the non-overlapping cells.

A detailed description of the HERMES reconstruction code and the tracking algorithms can be found in [97].

7.3 Particle Identification

The main aim of the HERMES PID system is to provide a reliable method to allow separation of leptons and hadrons.

One way to accomplish this is to use the responses of the individual detectors directly in the analysis and to impose hard cuts to select clean lepton or hadron samples.

Another way is to combine all four detector responses into a logarithmic likelihood ratio method. In this method the response of a detector D is converted into a conditional probability $\mathcal{L}_i^D$ that the observed signal is due to the passage of a particle of type i. This is achieved using the different responses of each PID detector to leptons and hadrons, determined from test beam measurements, Monte Carlo simulations or by using clean samples obtained with restrictive cuts on other PID detectors in the spectrometer. The detector responses for a certain particle type are actually momentum and angle dependent. The response distributions are used directly or are fitted with analytical functions. To obtain the conditional probabilities $\mathcal{L}_i^D$ (referred to as parent distributions), the response distributions to a certain type of particle are normalised to one. The combination of several detectors D yields the overall conditional probability for particle type i:

$$\mathcal{L}_i = \Pi_D \mathcal{L}_i^D \tag{7.1}$$

These conditional probability distributions can be converted into true probabilities $\mathcal{P}_i$ that the observed responses are due to a particle of type i, by taking into account the different particle fluxes ϕ_i. These fluxes are, in general, momentum and scattering angle dependent. Bayes' theorem shows that this probability is given by:

$$\mathcal{P}_i = \frac{\phi_i \mathcal{L}_i}{\sum_j \phi_j \mathcal{L}_j} \tag{7.2}$$

For positron-hadron separation this becomes:

$$\mathcal{P}_e = \frac{\mathcal{L}_e}{\Phi \mathcal{L}_h + \mathcal{L}_e} \tag{7.3}$$

$$\mathcal{P}_h = \frac{\Phi \mathcal{L}_h}{\Phi \mathcal{L}_h + \mathcal{L}_e} \tag{7.4}$$

where Φ is the flux ratio ϕ_h/ϕ_e. A PID parameter is defined in the analysis by taking the logarithm of the ratio of these positron and hadron probabilities.

$$PID = \log_{10}\left(\frac{\mathcal{P}_e}{\mathcal{P}_h}\right) = \log_{10}\left(\frac{\mathcal{L}_e}{\Phi \mathcal{L}_h}\right) = \log_{10}\left(\frac{\mathcal{L}_e}{\mathcal{L}_h}\right) - \log_{10}\Phi. \tag{7.5}$$

When a particle is equally likely to be a positron or a hadron the PID parameter are zero, while positive (negative) values indicate the particle is more likely to be a positron (hadron). Similarly, a PID parameter for each individual detector can be introduced as follows:

$$PID_D = \log_{10}\left(\frac{\mathcal{L}_e^D}{\mathcal{L}_h^D}\right) \tag{7.6}$$

such that equation 7.5 becomes:

$$PID = \sum_D PID_D - \log_{10}\Phi \tag{7.7}$$

The flux ratio Φ can be neglected provided it is not a strong function of momentum and angle. This simply shifts the PID distribution.

In the PID scheme before the responses of the calorimeter, preshower and Cerenkov are combined to form a log-likelihood quantity given by:

$$PID3 = PID_{cal} + PID_{pre} + PID_{Cer} = log_{10}\Big(\frac{\mathcal{L}_e^{Cal}\mathcal{L}_e^{pre}\mathcal{L}_e^{Cer}}{\mathcal{L}_h^{Cal}\mathcal{L}_h^{pre}\mathcal{L}_h^{Cer}}\Big) \tag{7.8}$$

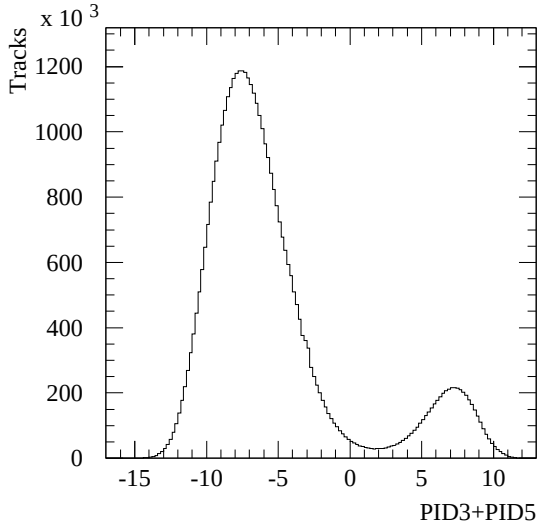

Figure 7.3: Distribution of PID3+PID5 used as the PID parameter for the 1996-97 data.

A similar quantity PID2 is defined using only the calorimeter and preshower. The TRD response of the six individual TRD modules is combined to form a quantity:

$$PID5 = PID_{TRD} = log_{10}\Big(\frac{\Pi_{m=1}^{6}\mathcal{L}_e^{TRD,m}}{\Pi_{m=1}^{6}\mathcal{L}_h^{TRD,m}}\Big) \tag{7.9}$$

The commonly used PID quantity used for this analysis is then simply:

$$PID_{96-97} = PID3 + PID5 \tag{7.10}$$

as shown in figure 7.3 where the PID3 quantity is based on information from the Cerenkov detector, and also:

$$PID_{98-00} = PID3 + PID5 \tag{7.11}$$

where in this expression the PID3 quantity is based on information from the RICH (Ring Imaging Cerenkov) detector.

7.4 The HERMES Monte Carlo

Monte Carlo simulations of a particle physics experiment are usually needed to study the influence of the experimental apparatus on the detected physics events. The spectrometer has a finite geometrical acceptance which allows detection of only a fraction of the induced physics events. Detection systems have a certain finite resolution and efficiency and can also influence measurements due to e.g. multiple scattering, energy losses, Brehmsstrahlung or

particle showering. This will lead to smearing effects in the reconstructed event quantities with respect to their real values. After the reconstruction each event has to pass through a certain software analysis chain, which also has a certain intrinsic efficiency. All these effects have to be estimated and corrected for using Monte Carlo simulations of the measurement. Apart from this use, Monte Carlo studies can also be used to estimate e.g background rates or physical processes.

The tracking and modeling of the detector responses is implemented using the GEANT (Generation of Events ANd Tracks) detector description and simulation tool [98]. Using experimental resolutions and detector efficiency functions, the generated detector signals are finally digitised into more realistic responses. The entire output of HMC is stored in ADAMO formatted GAF files which are readable by the HERMES reconstruction program, so that the Monte Carlo data can be treated just like actual measured data.

The Monte Carlo studies of vector meson production for this analysis are produced using the latest HERMES version of the RhoMC which was developed from stand alone codes and integrated into the HERMES software production [99].

Figure 7.4 shows a ρ^0 event produced by RhoMC passing through the HERMES detector.

7.5 The ρ^0 Monte Carlo Generator

The Monte Carlo simulations in this ρ^0 analysis are all performed using a generator based on the vector meson dominance model[100][101]. It applies the commonly used 'hit and miss' technique [102] to generate events according to a VDM based cross section with the free variables being Q^2, the energy of the scattered lepton E', and the azimuthal scattering angle ϕ. The cross section for exclusive diffractive ρ^0 electroproduction is modeled as:

$$\frac{d\sigma}{dQ^2 dE' d\phi} = \frac{1}{2EE'}\Gamma_T(\cos\theta, \phi, E')\sigma_{\gamma^* p}(Q^2) \tag{7.12}$$

where $\sigma_{\gamma^* p}(Q^2)$ represents the virtual photoproduction cross section $\gamma^* p \to \rho^0 p$ and Γ_T the transverse photon flux factor given by:

$$\Gamma_T(\cos\theta, \phi, E') = \frac{\alpha}{4\pi^2}\frac{W^2 - M^2}{2M}\frac{1}{Q^2}\frac{E'}{E}\frac{2}{1-\epsilon} \tag{7.13}$$

The virtual photoproduction cross section is modeled with a VDM-like Q^2 dependence:

$$\sigma_{\gamma^* p}(Q^2) = \frac{1}{(1 + Q^2/M^2)^2}\sigma_{\gamma p} \tag{7.14}$$

where the real photoproduction cross section $\sigma_{\gamma p} = \sigma_{\gamma^* p}(Q^2 = 0)$ is given by:

$$\sigma_{\gamma p}(Q^2 = 0) = A_\gamma \frac{2M}{W^2 - M^2} + B_\gamma \tag{7.15}$$

with $A_\gamma = 29.4\mu b\cdot$ GeV and $B_\gamma = 9.5\mu b$ as determined from a fit given in reference [103]. To speed up the sample and reject method, the sampling of high Q^2 events, where the cross section becomes relatively low, is somewhat suppressed by generating events uniformly in a variable K given by e.g. $K \propto (1/Q^2)^2$, rather than in Q^2 itself.

The invariant mass is generated according to a skewed Breit-Wigner distribution [100] :

$$\frac{dN}{dM_{2\pi}} \propto \frac{M_{2\pi}\Gamma_\rho M_\rho}{(M_{2\pi}^2 - M_\rho^2)^2 + M_\rho^2\Gamma_\rho^2}\Big(\frac{M_\rho}{M_{2\pi}}\Big)^{n_{skew}} \tag{7.16}$$

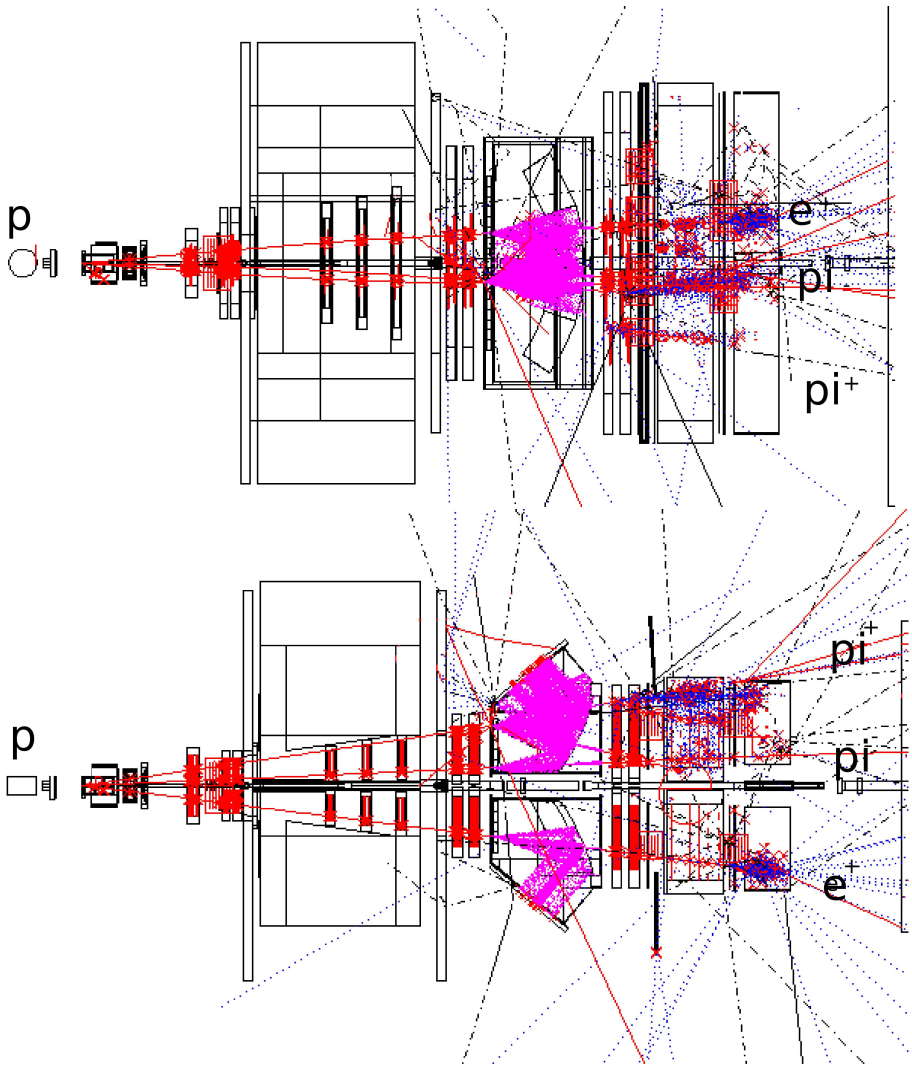

Figure 7.4: A picture of a simulated $e^+p \to e^+\rho^0 p$ event from the RhoMC generator used within HMC. The plot on top shows the detector view from the top. The plot on bottom shows the side view of the detector. The recoiling proton which is currently undetected is seen to be within the acceptance of the simulated HERMES Recoil Detector. The tracks of the scattered lepton and the two charged pions can also be seen in the picture.

where the skewing parameter $n_{skew} = 2$ and $\Gamma(M_{2\pi})$ is given by:

$$\Gamma(M_{2\pi}) = \Gamma_0 \Big(\sqrt{\frac{M_{2\pi}^2 - 4M_\pi^2}{M_\rho^2 - 4M_\pi^2}} \Big)^3 \frac{M_\rho}{M_{2\pi}} \tag{7.17}$$

with $\Gamma_0 = 0.1507$ GeV and $M_\rho = 0.7700$ GeV, the ρ^0 width and mass [104].

The forward diffractive peak of the cross section as a function of t' was modeled according to:

$$\frac{dN}{dt'} \propto e^{-b|t'|} \tag{7.18}$$

with $b = 6.0$ GeV^{-2} following the data in [103].

The generation of the decay angular distributions is implemented in several ways allowing the user to choose the preferred method. One model assumes s-channel helicity conservation and natural parity exchange in the t-channel. The decay angles are then generated according to:

$$\frac{dN}{d\cos\theta d\Psi} \propto 2\epsilon R\cos^2\theta + \sin^2\theta(1+\epsilon\cos 2\Psi) - \sqrt{2\epsilon R(1+\epsilon)}\cos\delta\sin 2\theta\cos\Psi \qquad (7.19)$$

The ratio $R = \sigma_L/\sigma_T$ is computed according to $R = \frac{1}{\epsilon}\frac{r_{00}^{04}}{1-r_{00}^{04}}$, where the matrix element is given by $r_{00}^{04} = 0.28015(Q^2)^{0.45080}$ as taken from [105]. In another scenario, one can generate the decay angle according to the full blown equation 6.59. In that case all 23 SDMEs and the beam polarisation have to be given by the user as input. A third possibility exists where the decay angles are simply isotropically generated. Additional information on the generator can be found in [106].

Chapter 8

Analysis Results

In this chapter the data quality requirements required for the data samples used in this analysis are presented. The selection procedure used to extract the ρ^0 events from the data sample will also be described, with an emphasis being placed on the selection of exclusive, diffractive ρ^0s. The analysis of the Spin Density Matrix Elements (SDME's) extraction will then be shown the results of the analysis and conclusions drawn will be presented.

8.1 Data Quality

In order to ensure that the data obtained in the analysis was stable and reliable in the context of high quality performance of the HERMES experiment, a detailed selection process on the data was carried out. The selection process involved looking to each of the various subdetectors that combine to make the overall HERMES detector, in order to determine whether each of the subdetectors was performing optimally. Certain criteria specific to the given subdetector were required in order for the data to be considered for the final analysis.

Data quality selection was applied on the fill, run and burst level. In order to obtain reliable, clean data samples various data quality cuts were applied to the data runs coming from HERMES. The data quality selection criteria used in this analysis are adopted from [84] which in turn were derived from the HERMES inclusive g_1 analysis [107]. Table 8.1 shows the data quality selection criteria applied in this analysis for both the 1996/1997 (96d0,97d0) and also for the 1998, 1999 and 2000 (98d0, 99c0, 00d0) data samples.

8.1.1 Data Acquisition

As the data acquisition is responsible for recording the data collected by the experiment it is essential that this system is operating properly.

If a trigger occurs while the previous event is still being read out then it cannot be accepted by the DAQ system and the corresponding event is lost. The fraction of time where the event cannot be accepted by the DAQ is referred to as the dead time. The corresponding live time τ_{live} can be estimated from the total number of triggers generated and accepted by the DAQ per burst:

$$\tau_{live} = \frac{T_{acc}}{T_{gen}} \tag{8.1}$$

A quantity is also calculated separately for trigger 21, τ_{21}. Trigger 21 is the main physics trigger at HERMES and uses scintillator hodoscopes H0 and H1, the preshower detector H2, and the electromagnetic calorimeter in combination to provide the trigger for the experiment. Also, a correction factor for the total live time was computed to account

Quantity	Criterion	1996	1997	1998	1999	2000
Beam Polarisation	$30 < P_{beam} < 80\%$	■	■	■	■	■
Live Time	$50 \leq \tau_{live} < 100\%$	■	■	■	■	■
	$0 < \tau_{r21} \leq 100\%$	■	■	■	■	■
	$95 \leq \tau_{Art} \leq 100\%$	■	■	■	■	■
Burst Length	$0 < t_{burst} \leq 11s$	■	■	■	■	■
Beam Current	$8 \leq I_e \leq 50mA$	■	■	■	■	■
Luminosity Rate	$5 \leq N_{lumi} \leq 50Bq$	■	■	■	■	■
First Burst	reject first burst in run	■	■	■	■	■
Last Burst	reject last burst in run	■	■	■	■	■
μDST Problems	reject bad timing burst records	■	■	■	■	■
Logbook data quality	reject bad logbook bursts	■	■	■	■	■
GMS - Calorimeter data quality	check for dead calorimeter blocks	■	■	■	■	■
GMS - H2 and luminosity monitor	check for zero bad blocks	■	■	■	■	■
TRD data quality	reject bad TRD bursts	■	■	■	■	■
High Voltage trips	reject FC and BC trips	■	■	■	■	■
RICH High Voltage trips	reject RICH HV trips			■	■	■
Cerenkov data quality	reject bad Cerenkov bursts	■	■			
RICH data quality	reject bad RICH bursts			■	■	■
Beam Polarisation Fit	regular polarimeter update	■	■	■	■	■

Table 8.1: The 1996, 97 and the 1998, 1999, 2000 data quality cuts.

for missing events in the data stream, resulting in an artificial live time τ_{Art}. Cuts were imposed in this analysis on τ_{21} and τ_{Art} as well as τ_{live}.

At the beginning and end of a run the DAQ has to perform clean-up and initialisation tasks. To avoid problems the first and last burst from each run were removed from the data samples. Also, bursts which showed timing problems or problems synchronising with the slow control were removed from the data set.

8.1.2 Beam Performance

In order to select periods where the beam conditions were stable, selection cuts are applied on the beam current and on the performance of the luminosity monitor. The cut on the lower limit of the beam current removes periods where the polarisation was low and in which the polarimeter measurements were unreliable. The upper limit cuts on the beam polarisation also removes periods where there is an unphysically high polarisation measurement. The luminosity monitor is sensitive to fluctuations in the beam orbit, therefore the cut on its count rate ensures a stable beam and removes spikes from the luminosity monitor readout.

8.1.3 Tracking Chambers

In order to ensure that the particles detected and reconstructed in the experiment are reliable and accurate a check had to be implemented on the stability and efficiency of the tracking detectors to ensure that they were performing properly.

When the current drawn by a drift chamber exceeds a certain limit the high voltage is switched off. This is referred to as a 'trip' of the high voltage. This 'trip' prevents damage to the thin drift chamber wires. Trips are normally caused by a high background or by particles showering, due to an unstable beam. Once a chamber trips and for a short time, afterwards the efficiency of the detector plane is lower and doesn't contribute reliably to the tracking. A selection cut is applied to ensure that the tracking efficiency for the data sample is sufficient.

8.1.4 Trigger and Particle Identification Detectors

The performance of the H1 hodoscope, the preshower and the Calorimeter detectors is monitored as these detectors influence both the trigger efficiency and the particle identification performance of the experiment. All detectors which are read out by photo multipliers use a gain monitoring system (GMS) which is used to monitor detector performance during data taking. In the 1996-97 and 1998, 1999, 2000 data analysis a data quality selection check was applied to the GMS to ensure that no dead blocks are detected during the data taking period for each of the relevant detectors. The TRD and Cerenkov (RICH for 1998, 1999, 2000) also affect the particle identification performance and are therefore monitored to ensure that they experience no high voltage trips and that their performance is stable over time.

8.2 Selection of ρ^0 Events

After the data quality selection cuts have been applied to the data, a data sample that is suitable for a further analysis is available. The data quality cuts are in the main part designed to produce a reliable, stable data sample which can be used by the analyser as the initial starting point for an analysis. The initial sample can then be further refined by removing events which are not desirable with additional cuts in order to extract the information which is needed for the given analysis.

The analysis covered in this thesis covers the data taking years 1996, 1997 and also 1998, 1999 and 2000. The data analysed in 1996 and 1997 was on both ^{1}H and ^{2}H targets. Polarised ^{1}H data was available in 1996-97 data sample. In the years 1998, 1999 and 2000 the data that was analysed was again taken on ^{1}H and ^{2}H targets. In these years however the polarised gas target was ^{2}H. The results in this analysis were obtained by looking at the scattered positron in the HERMES detector and (a fraction of) the particles produced in the scattering process.

The HERMES detector, in the period when the data for this analysis was taken, had no method to detect recoil particles from the scattering processes. The detection of the recoiling proton will in future be possible due to the development and installation of the HERMES Recoil Detector which will surround the target region with a large-acceptance multiple-layered detector[31].

The event information for this analysis was obtained by the detection of the scattered positron and the vector meson decay products in the HERMES acceptance. The ρ^0 is a short lived, unstable particle that decays immediately after formation. The decay mode

and width of the ρ^0 vector meson can be seen in table 8.4. The expected lifetime of the ρ^0 can be estimated by:

$$\tau = \frac{\hbar}{\Gamma} \tag{8.2}$$

resulting in $\tau_{\rho^0} = 4.4 \cdot 10^{-24}$s. The distance the ρ^0 travels before it decays can be approximated by $c\tau$, with c being the speed of light. Therefore $c\tau_{\rho^0} = 1.3$ fm which is roughly the scale of the nucleon. The ρ^0s main decay channel is $\rho^0 \rightarrow \pi^+\pi^-$.

8.2.1 Selection of Scattered Positrons and Hadrons

In order to identify the scattered positrons and charged pions detetcted in the HERMES experiment the PID parameters which are defined for the different data samples were used. For the PID cuts used in this analysis the misidentfication of leptons and hadrons is negligible.

Additional cuts were also applied to the track parameters for both the hadrons and lepton in order to more cleanly analyse the data samples. The selection criteria applied to positrons and charged hadron tracks are shown in table 8.2.

Charged Track Selection	
Particle Identification Cuts	
positron identification	charge=+1 PID3+PID5 $>$ 1 (98/99/2000) PID3+PID5 $>$ 1 (96/97)
hadron identification	PID3+PID5 $<$ 0 (98/99/2000) PID3+PID5 $<$ 0 (96/97)
Geometry Criteria	
horizontal fiducial cut (positron) vertical fiducial cut (positron) magnet septum plate	$\lvert x_{calo}\rvert < 175$ cm 108 cm $> \lvert y_{calo}\rvert > 30$ cm $40 < \lvert\theta_y\rvert < 140$ mrad $\lvert\theta_x\rvert < 170$ mrad
Target Region(positron and hadrons)	
reconstructed vertex inside target transverse vertex offset	$\lvert z_{vertex}\rvert < 20$ cm $r_{vertex} < 0.75$ cm
Kinematics	
non resonance region small radiative corrections	W $>$ 2.0 GeV y $<$ 0.85

Table 8.2: The hadron and lepton track selection criteria

A cut was imposed on the reconstructed positron vertex postions z_{vertex} and r_{vertex}. With z_{vertex} being the position along the z-axis and r_{vertex} being the perpendicular distance from the z-axis of the vertex. This cut was applied to ensure that only tracks originating from the target cell are selected, and hence that the selected positron interacted with the target gas in the interaction region.

A fiducial cut is also placed on the tracks using the position of the track at the calorimeter. This cut ensures that the positron deposits all of its energy in the calorimeter. In this way the tracks at the edges of the spectrometer where the positron identification efficiency goes down are removed from the final data sample.

In order to avoid the region of the septum plate in the magnet, a cut is applied to the vertical scattering angle of the positron and hadrons.

In order to ensure that the positron had enough energy to generate a trigger a kinematical cut on y was applied. This cut also limits the events in the data sample to be in a region where the radiative corrections are not too high. A kinematical cut was also applied to W to remove the events in the data sample in the nucleon resonance region.

8.2.2 Selection of Exclusive, Diffractive ρ^0 Events

In this analysis we are interested in the ρ^0 vector meson. In analysing the ρ^0 we disregard all additional tracks and trackless clusters other than the 3 track process, where one track corresponds to the scattered positron and the other two correspond to the two charged hadrons, which in the case of the ρ^0 are the π^+ and π^- pions. The signature of the ρ^0 in the spectrometer is the detection of two oppositely charged pions and a lepton without additional tracked particles.

The production of vector mesons can be identified as a peak in the invariant mass distribution M_V of the reconstructed candidate vector mesons. The vector meson candidates are formed by combining the measured, assumed decay particles ($\pi^+\pi^-$ in the ρ^0 case) which in four-vector language translates into adding up the four-momenta.

As non-exclusive events could also exhibit the same event topology as an exclusive event when a fraction of the produced particles escape the detector acceptance, another measure of the events exclusivity was needed. The following quantity:

$$\Delta E = \frac{M_x^2 - M_{targ}^2}{2M_{targ}} = \nu - E_V + \frac{t}{2M_{targ}} \tag{8.3}$$

was therefore introduced. With the rest mass of the recoiling baryonic system $M_x^2 = p'^2$ in semi-inclusive $A(e, e'V)$ is given by:

$$M_x = \sqrt{(p + q - p_V)^2}. \tag{8.4}$$

For exclusive events, M_x will be equal to the initial target rest mass, resulting in $\Delta E = 0$ GeV, while for non-exclusive events M_x will be larger and result in $\Delta E > 0$ GeV. For scattering on ^{1}H we have $M_{targ} = M_p$, the mass of the proton. For scattering on composite nuclei one can have either incoherent scattering from individual nucleons inside the target nucleus or coherent scattering from the entire nucleus. In the first case one can assume $M_{targ} = M_p$, while for the second case one would take $M_{targ} = M_A$ where M_A is the target mass. However, due to the limited experimental resolution it was not possible to distinguish between coherent and incoherent scattering processes. For this reason M_{targ} was chosen to be the proton mass throughout this analysis. For this reason, exclusive coherent events occur at slightly negative values of ΔE as can be seen from the second part of equation 8.3. As a quantity, ΔE is useful as it has the advantage that it includes the recoil energy correction $-t/2M_p$ and the threshold value for inelastic scattering $\Delta E = M_\pi + M_\pi^2/2M_p$ is independent of kinematics.

As was shown in detail in equations 6.8-6.16, for exclusive, diffractive processes in the forward region t_0 is small and $t' \sim t$. The following sections will explain in detail the specific selection cuts which were applied to the data samples in order to select only exclusive, diffractive ρ^0 events. The cuts used are summarised in table 8.3.

Parameter	Selection Criteria
Invariant mass	0.6 GeV $< M_{2\pi} <$ 1.0 GeV
Exclusive Events	$\Delta E <$ 0.6 GeV
Diffractive Events	$-t' <$ 0.4 GeV^2
2-Kaon mass	$M_{2K} >$ 1.06 GeV

Table 8.3: The selection cuts for exclusive, diffractive ρ^0 candidate events

8.2.3 ρ^0 Event Selection

In the analysis of ρ^0 the assumption is made that the hadrons which are detected are pions. It is expected that when the 2-pion invariant mass distribution is plotted a peak corresponding to ρ^0 production events should appear at :

$$M_{2\pi} = \sqrt{(p_{\pi^+} + p_{\pi^-})^2} \tag{8.5}$$

where p_π is the four-momentum of the hadrons assumed to be pions. The 2-pion invariant mass distribution is shown in figure 8.1. The ρ^0 peak shows up at the expected mass value ($\sim$ 770 MeV). The narrow peak in the lower mass region corresponds to K^0_S mesons which have an expected mass of 497.672 $\pm$ 0.031 MeV and also decay into $\pi^+\pi^-$ with a branching ratio of 68.61 $\pm$ 0.28 % [104]. The first step to filter the ρ^0 events was to impose a mass window of $0.6 < M_{2\pi} < 1.0$ GeV on the event sample. As can be seen in figure 8.1 the majority of the events within the selected mass window did not correspond to resonant ρ^0 production but rather to processes such as, for example, production of other particles decaying into hadrons or exclusive $\pi^+\pi^-$ production without resonant formation of an intermediate ρ^0 meson.

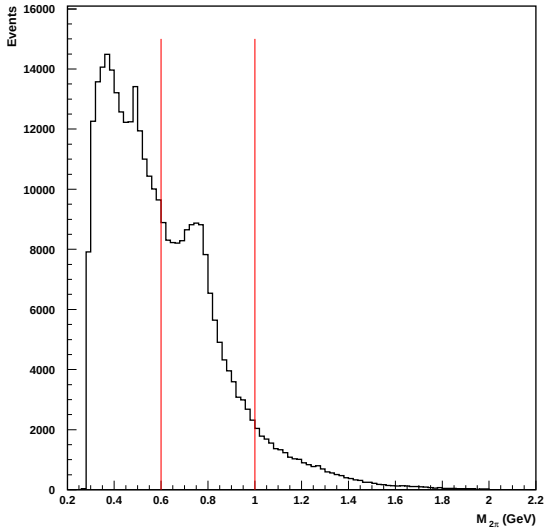

Figure 8.1: The reconstructed $M_{2\pi}$ distribution without any additional cuts. The ρ^0 event peak shows up at correct mass value. The narrow peak in the lower mass region corresponds to K^0_S production. The lines indicate the cut on the invariant mass window which selects on ρ^0 events.

In order to further restrict the event sample to exclusive, diffractive production in the forward region cuts on ΔE and t' were used. Figure 8.2 shows the ΔE distribution of the sample within the ρ^0 mass window. The majority of events in the event sample are non-exclusive and are contained at higher ΔE. Exclusive event candidates were selected using the cut $\Delta E < 0.6$ GeV. The correlation of ΔE versus $-t'$ is plotted in figure 8.3. A large number of exclusive events appear to be concentrated around values of very low $-t'$. This is a clear sign of a diffractive production mechanism. In this analysis the diffractive events were selected using the cut $-t' < 0.4$ GeV^2.

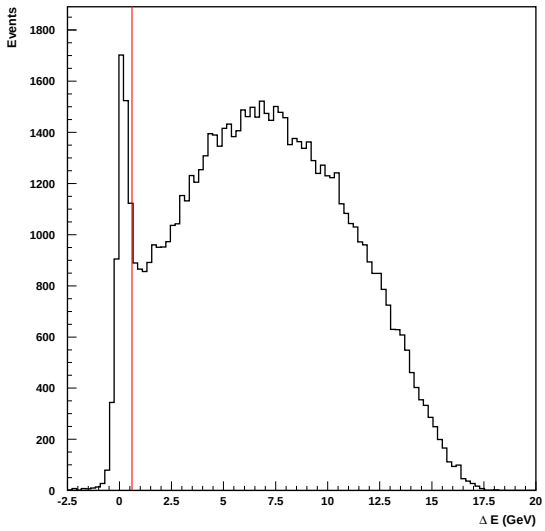

Figure 8.2: The ΔE distribution of the event sample within the ρ^0 mass window. The peak at $\Delta E \approx 0$ GeV corresponds to exclusive events.

The ρ^0 event candidates were reconstructed under the assumption that both charged hadrons were pions. As the pion identification capability of the threshold Cerenkov counter was limited to a certain momentum range, this information was not used in the ρ^0 analysis to avoid loss of event statistics. The sample of hadron pairs was therefore contaminated with, for example, protons and kaons. An important source of background events may come from the production of ϕ mesons which have a mass of 1019.413 $\pm$ 0.008 MeV and decay into K^+K^- pairs with a branching ratio of 49.1 $\pm$ 0.8 % [104]. To look for ϕ production events in the sample, one must examine the 2-kaon invariant mass distribution, given by:

$$M_{2K} = \sqrt{(p_{K^+} + p_{K^-})^2} \tag{8.6}$$

where p_K is the four-momenta of the hadrons assumed to be kaons. The 2-kaon invariant mass spectrum is plotted in figure 8.4 , where the distribution is shown using the cuts mentioned previously on ΔE and $-t'$. A narrow peak at the expected mass can be seen, corresponding to exclusive, diffractive ϕ production. The correlation between $M_{2\pi}$ and M_{2K} is shown in figure 8.5, where the lines correspond to the cuts described previously.

As the plot demonstrates, all ϕ events were outside the ρ^0 event sample when the 2-pion invariant mass window was imposed. However to clean up the invariant mass spectrum of the ρ^0 event candidates (see figure 8.6), all ϕ production events were removed from the sample by the additional requirement the $M_{2K} > 1.06$ GeV.

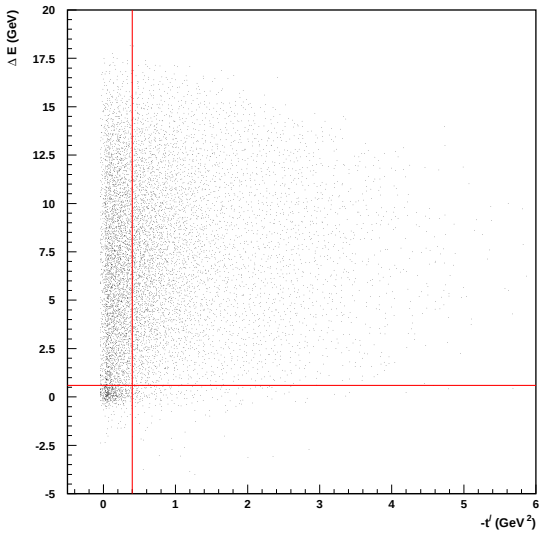

Figure 8.3: The correlation between ΔE and $-t'$ for the event sample. The exclusive events at very low $-t'$ correspond to diffractive production. The lines indicate the cuts used in the analysis.

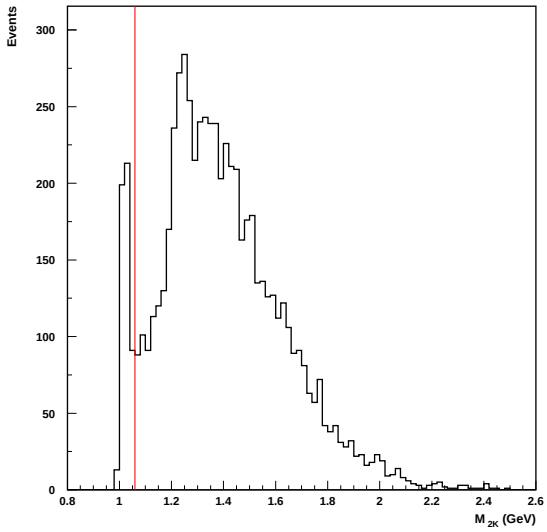

Figure 8.4: The 2-kaon invariant mass distribution, where a signal of exclusive, diffractive ϕ production is present at the expected mass value. The lines indicate the cuts used in the analysis.

All other sources of background in the event sample defined above, were not handled on the event selection level but will be discussed and corrected for further on in the analysis.

The influence of the cuts given above on the invariant mass distribution of the ρ^0 event sample is shown in figure 8.6.

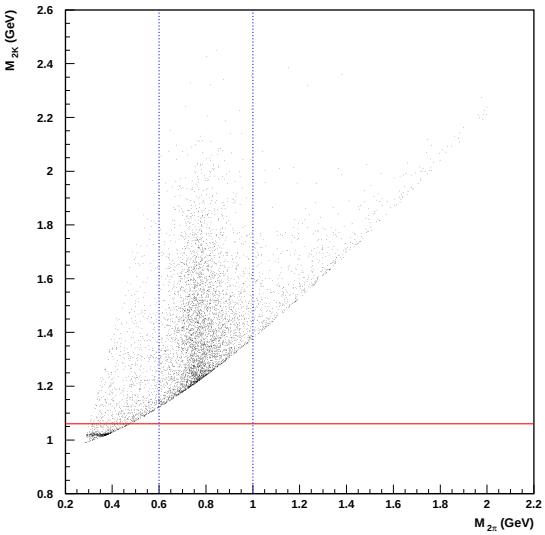

Figure 8.5: The correlation between $M_{2\pi}$ and M_{2K}, where the lines indicate the cuts as explained in the text. The plot demonstrates that all ϕ events were outside the ρ^0 event candidate sample when the 2-pion invariant mass window was imposed.

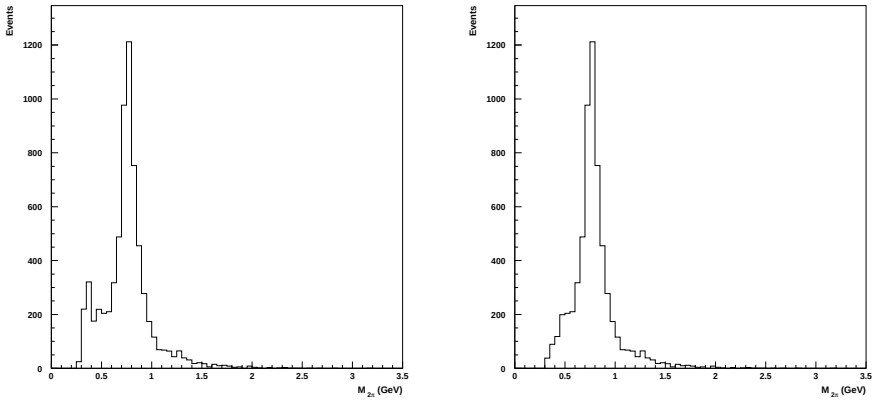

Figure 8.6: The effect of the cuts described in the text on the 2-pion invariant mass spectrum for exclusive, diffractive ρ^0 event candidate sample.

In figure 8.7 a fit to the ρ^0 peak is executed using a non-relativistic Breit-Wigner function given by:

$$\frac{dN}{dM_{2\pi}} = \frac{\Gamma_\rho}{4(M_\rho - M_{2\pi})^2 + \Gamma_\rho^2} \tag{8.7}$$

where M_ρ and Γ_ρ represent the mass and the width of the ρ^0 resonance. Table 8.4 gives the results of the Breit-Wigner fit compared to the accepted values for the ρ^0.

The values obtained using a non-relativistic Breit-Wigner fit appear to differ slightly from those from the PDG (Particle Data Group). The mass of the ρ^0 is underestimated and the width seems to be slightly overestimated. In general, however the comparison between

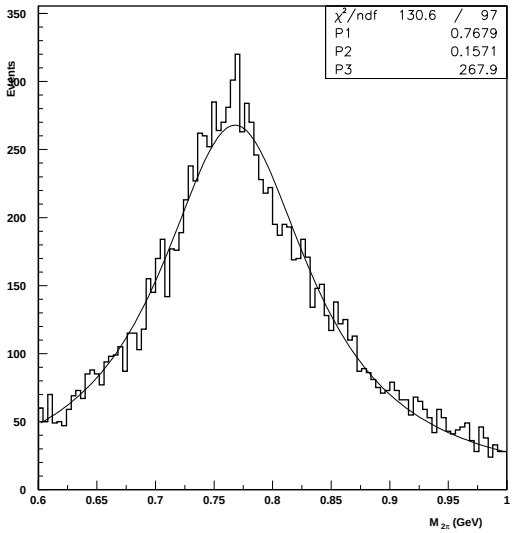

Figure 8.7: A non-relativistic Breit-Wigner fit on the 2-pion invariant mass spectrum for an exclusive, diffractive ρ^0 event candidate sample.

Particle Type	Mass(MeV)	Full Width(MeV)
$\rho^0(770)$	775.9 $\pm$0.5	150.4$\pm$1.3
ρ^0(BW fit)	767.9 $\pm$0.000886	157.1$\pm$0.002658

Table 8.4: The ρ^0 particle properties [108] compared to a non-relativistic Breit-Wigner fit result.

the two sets of values shows there to be an approximate agreement. The small errors shown in the non-relativistic Breit-Wigner fit are those arising from the fitting procedure alone and are not directly comparable with the errors presented by the PDG. It is expected that there will be additional, larger, systematic errors for this analysis which are not examined here, bringing the agreement between the fit results and the PDG values closer. The measurements used by the PDG to compile the value given in [108] vary depending on the process used to obtain and fit the value. The measurement value given in the particle data group for photoproduced, neutral only reaction is 768.5 $\pm$ 1.1 for the mass and 150.7 $\pm$ 2.9 for the width [108]. This is in better agreement with the value obtained in this analysis than the value given for the overall average of measured results, given in table 8.4.

8.3 ρ^0 Decay Angle Distribution Analysis

In this analysis we investigate the helicity transfer in exclusive ρ^0 production on both hydrogen and deuterium. The results for 23 spin density matrix elements (SDME's) are obtained for a single, average Q^2 value. The Q^2 dependence for the 15 unpolarised matrix elements are also extracted and considered. Using the matrix elements obtained in the analysis, the hypotheses of SCHC (s-Channel Helicity Conservation)and NPE (Neutral Parity Exchange) are investigated. The results obtained for the spin density matrix elements are then compared to predictions from different theoretical models.

8.3.1 The Maximum Likelihood Method

The maximum likelihood method is the preferred method to extract the spin density matrix elements for the ρ^0 vector meson [84][109]. The method used to extract the SDME's was essentially executed by maximising the log likelihood function for the 3-dimensional ($\cos\theta$, ϕ, Φ)(figure 6.8) decay angle matrix of the data sample and a sample of fully reconstructed Monte Carlo events. Using this method the SDME's are computed directly from the measured data sample.

The isotropically generated Monte Carlo events(figure 8.8) were generated with uniform angular distributions and were then iteratively reweighed with equation 6.59, with the matrix elements treated as free parameters in the fit (figure 8.9). In both figures 8.8 and 8.9 the same data event sample is shown in black behind the Monte Carlo and reweighed angular distributions.

The best fit parameters were determined with a binned maximum log-likelihood method. The number of events d_i in each bin i were assumed to be Poisson distributed:

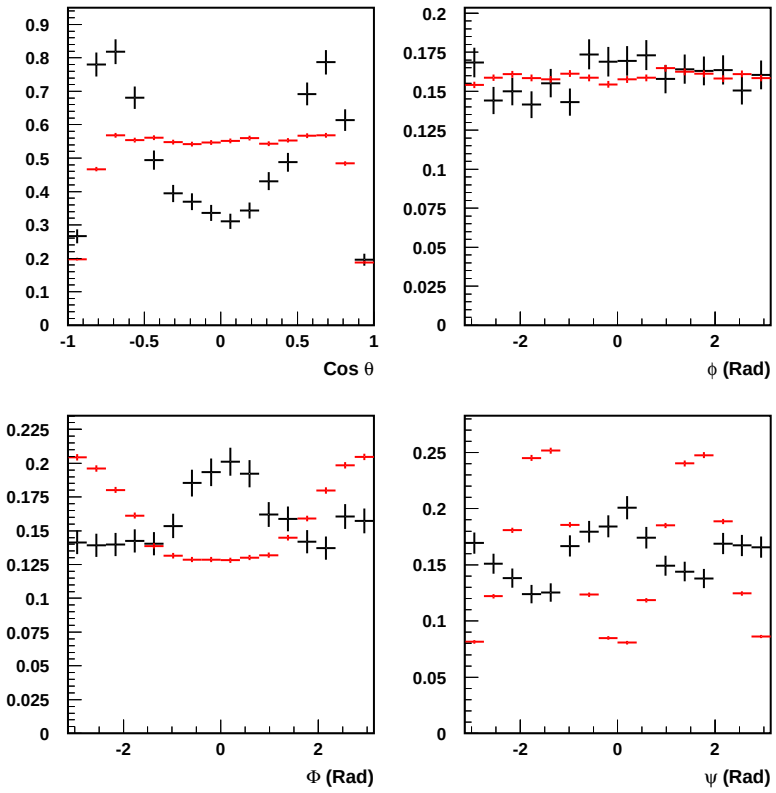

Figure 8.8: The distributions for $\cos\theta$, ϕ, Φ and Ψ. The Data event sample is marked by the black points. The red lines correspond to the isotropic Monte Carlo sample used in the fitting procedure.

$$P(d_i, c_N m_i') = \frac{(c_N m_i')^{d_i}}{d_i!} e^{-c_N m_i'} \tag{8.8}$$

with mean value $c_N m_i'$, where m_i' is the reweighed number of Monte Carlo events in

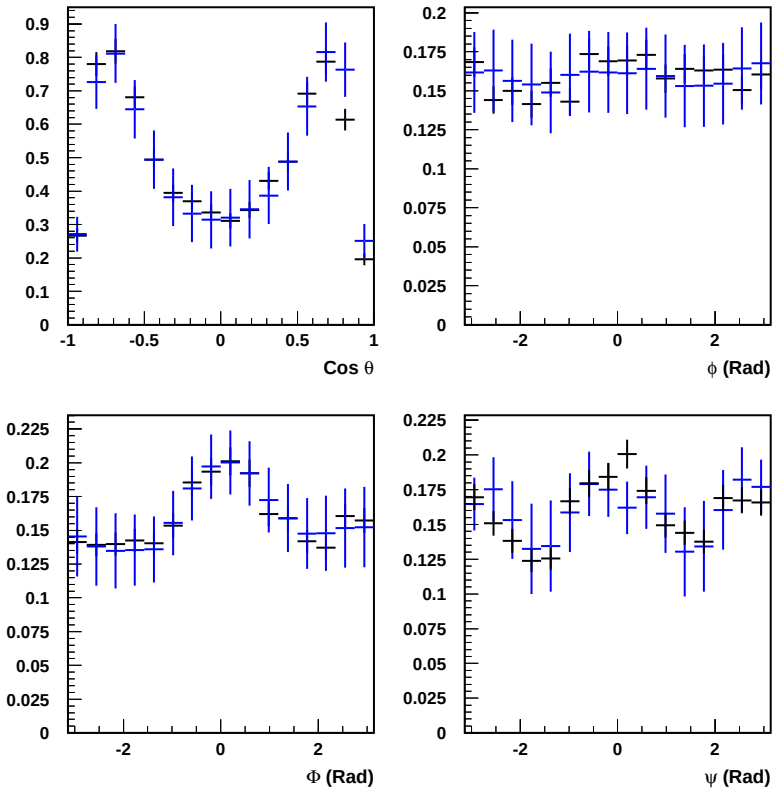

Figure 8.9: The distributions for $\cos\theta$, ϕ, Φ and Ψ. The Data event sample is marked by the black points. The blue lines correspond to the fit results obtained in the fitting procedure.

bin i and $c_N = \left(\sum_j d_j\right)/\left(\sum_j m'_j\right)$ is a normalisation factor to account for the difference in the total number of events in the data and Monte Carlo samples. A likelihood function was then defined as [110]:

$$L(\lambda) = \Pi_i^{bins} P(d_i, c_N(\lambda) m'_i(\lambda)) \tag{8.9}$$

where λ represents the 23 fit parameters being the 23 SDME's. The best fit parameters were determined by maximising the logarithm of the likelihood function:

$$\ln L(\lambda) = \sum_i [d_i \ln(c_N(\lambda) m'_i(\lambda)) - c_N(\lambda) m'_i] + constant \tag{8.10}$$

or equivalently by minimising $-\ln L(\lambda)$. The minimisation itself and error calculations were performed using the MINUIT package [111].

8.3.2 Radiative Corrections

The radiative corrections for exclusive vector mesons depend on the angle Φ between the lepton scattering and the hadron production plane [112]. The angle is determined by the direction of the vector meson and of the virtual photon momentum, where the virtual photon momentum is determined experimentally from the difference between the incoming and

the scattered lepton momentum. The emission of a real photon will alter the virtual photon direction with respect to the non-radiative case and thus also the Φ angle. Therefore the hard photon radiation contribution to the radiative corrections can be a strong function of Φ. This effect however, only becomes significant for high $|t|$ where the hard photon radiation contribution to the total radiative correction becomes relatively large. The remaining contributions to the radiative corrections depend only weakly on this angle. The total radiative corrections are also found to have no influence on the vector meson decay angles $\cos\theta$ and ϕ.

It was previously determined that in a SDME analysis at HERMES kinematics radiative corrections could be neglected [84]. The affect of a radiative correction applied to the sample resulted in a minimal change in the SDME's, on the order of 1%. Therefore in this analysis no radiative corrections were taken into account in the extraction of the final results.

8.3.3 DIS Background Subtraction

The ρ^0 data sample that is obtained up to this point in this analysis still has a background contribution coming from DIS fragmentation events that appear in the sample. In order to remove this contribution to leave a sample containing only exclusive ρ^0 events the DIS contribution to the event sample has to be estimated and then removed. In order to reproduce the shape of the background, a Monte Carlo simulation which generates fragmentation events consistent with those in the DIS region is used. The simulated events are produced by the LEPTO generator. This simulated data is then normalised to experimental data at ΔE >2 GeV, that is, in the fragmentation region where no signal from exclusive events is assumed to be present. This method is one adopted from a previous analysis[113]. The background contributions for the data samples used in this analysis are shown in Appendix B, tables B.1 and B.2.

The normalisation of the DIS Monte Carlo background contribution to the data sample is shown in figure 8.10.

Using this method the background contribution to the data sample is calculated and then subsequently subtracted to produce a subsequent data sample that is used as the input for the fitting program in which the SDME's are determined.

8.3.4 Spin Density Matrix Element Extraction Analysis

In this analysis the SDME's were extracted using the maximum likelihood method. The SDME's were extracted in the kinematic region 0.7< Q^2 <5.0 GeV^2 and $W > 2$ GeV. The number of internal bins used for the 3-dimensional matrix in ($\cos\theta$, ϕ, Φ) was chosen to be $8 \times 8 \times 8$. The results for both the hydrogen and deuterium data samples will be presented separately and then a conclusion given.

The beam polarisation is determined for each data sample separately. This is due to the fact that the sign of the beam polarisation enters directly into equation 6.59, which is used to reweight the Monte Carlo events in the likelihood method. To deal with this different weighting the extraction of the matrix elements is undertaken separately for the positive and negative beam helicity data samples. It should be noted that this is equivalent to running the fitting procedure on the two helicity event samples together with one set of SDME parameters.

As mentioned previously the radiative corrections to the SDME's analysis are negligible and are therefore not taken into account. The results are also not corrected for the presence of double-diffraction dissociation background in the sample. As the main physics studied here is driven by the $\gamma^* \rightarrow V$ vertex in the scattering region , the effect from DD background is expected to be negligible. The decay angle distributions for the proton dissociative

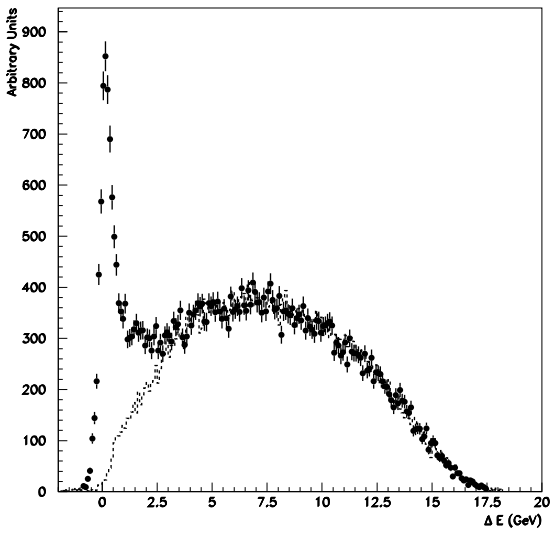

Figure 8.10: Plot showing the normalisation of the DIS background to a given data sample.

reaction were measured by ZEUS [114] and found to be consistent with those of exclusive events, supporting our assumption.

The amount of DIS fragmentation background in the exclusive data sample can be estimated using a DIS Monte Carlo sample. After the proper normalisation of the Monte Carlo background to the data, the 3-dimensional decay angle matrix of the background events are subtracted from the corresponding matrix for the data sample. The new background-subtracted data sample is then used as the input to the likelihood procedure.

Throughout this analysis the results are compared with a previous analysis performed at HERMES by Michael Tytgat[84], based on an earlier data production of the 1996/97 hydrogen data sample. The analysis of the 1996/97 data in this thesis is based on a more advanced data production, therefore perfect agreement with M. Tytgats analysis is not expected.

8.3.5 Systematic Error Approach

In order to determine the systematic error for the maximum likelihood procedure the number of bins used internally by the fitting procedure was changed. The number of internal bins was changed from $8 \times 8 \times 8$ to $5 \times 5 \times 5$. This procedure allows a guide for a systematic error which would arise from analysing a data set with an incorrect number of internal bins. Another aspect of the systematic error was the background subtraction method and the value which was subtracted from the data sample. In order to account for this the maximum likelihood procedure was run with and without background subtracted from the data sample to study the fitting procedures sensitivity.

It was determined in [84] that the dominant contributions to the systematic error come from the number of internal bins used in the fitting procedure and the background subtraction method used.

8.4 1996-97 Hydrogen Data Sample

The data sample analysed in this section is from the HERMES 1996-97 data taking period taken on a ^{1}H target. During 1996 HERA utilised a lepton beam with a positive beam helicity. During the 1997 data taking period both negative and positive beam helicities were used. The beam polarisation for 1996-97 is shown in figure 8.11.

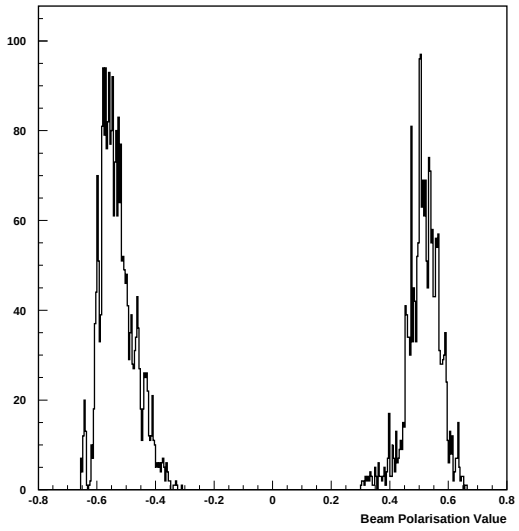

Figure 8.11: The beam polarisation of the data sample for 1996-97. Positive (negative) values correspond to positive (negative) beam helicity

The results for the 23 SDME's extracted from the two beam helicities are shown in figure 8.12. The error bars correspond to the statistical uncertainties obtained by MINUIT. The 15 SDME's shown above the horizontal dotted line are independent of the beam polarisation, whereas the 8 SDME's below the horizontal line require a longitudinal beam polarisation to be measured. The uncertainties in these 8 polarised SDME's are much larger than those of the 15 unpolarised SDME's. This is due to the fact that the beam is not fully polarised but only around 50 % polarised. The two sets of SDME's extracted from the two helicity samples are compatible within the statistical uncertainties.

The results show clearly that the matrix elements not restricted to zero in the case of SCHC are indeed non zero, for example, r^{04}_{00}, r^{1}_{1-1}, Im r^{2}_{1-1}, Re r^{5}_{10} and Im r^{6}_{10}. The two polarised matrix elements allowed to be non zero by SCHC, Im r^{7}_{10} and Re r^{8}_{10}, are found to have non-zero value, however they both have large uncertainties associated with them. For the SDME's extracted there also appear to be some matrix elements which are expected to be zero in the case of SCHC but are in fact non zero, for example, r^{5}_{00} is seen to be significantly different from zero.

The combined SDME values are compared to those obtained in a previous HERMES analysis on an earlier data sample [84] in figure 8.13. The analysis presented in this section is applied to the 1996-97 hydrogen data sample as was the previous analysis, however the data production used here is the most recent available and differs slightly from the production used in the previous analysis. The values obtained in both analysis appear to be in very good agreement. The results for the 23 SDME's are compared to theoretical predictions which is shown in figure 8.14.

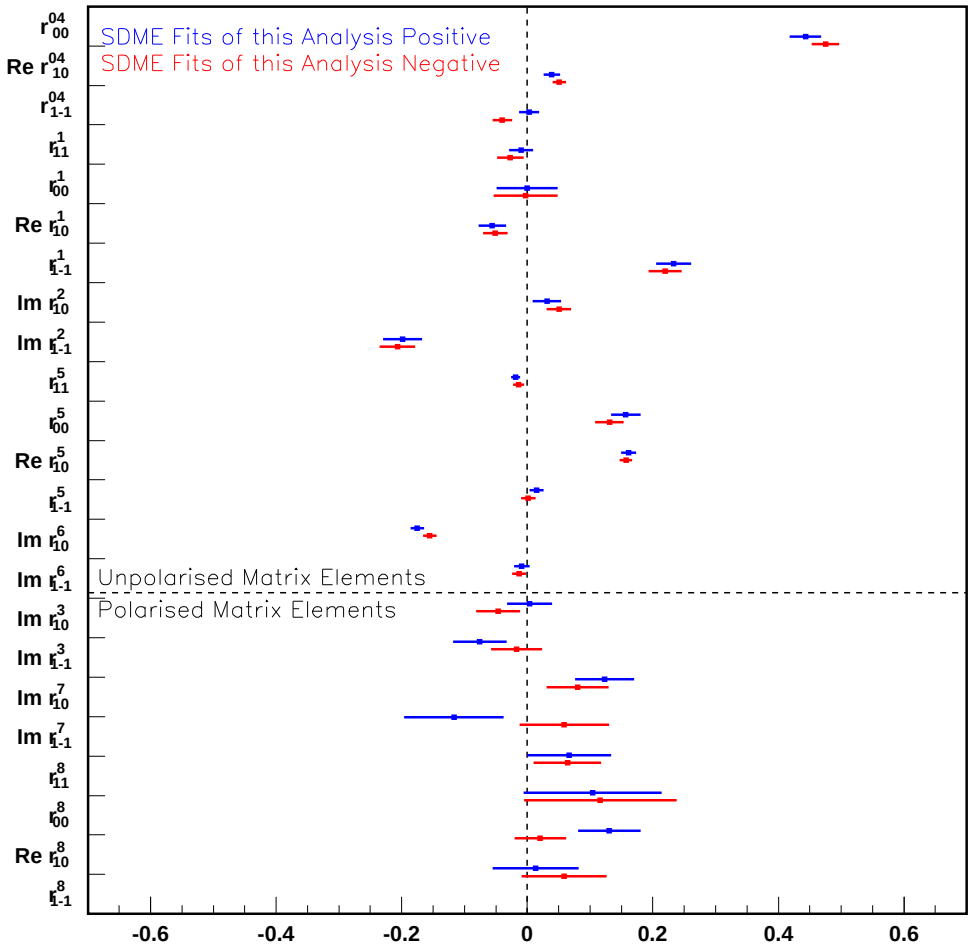

Figure 8.12: The 23 SDME's extracted separately from the positive and negative helicity samples for the 1996-97 Data Sample. The error bars indicate statistical uncertainty only.

The Q^2 dependence of the SDME's was studied by repeating the analysis in four Q^2 bins ($0.7 < 1.0 < 1.4 < 2.0 < 5.0$ GeV^2). As the event statistics is a crucial point in this kind of analysis, the binning was chosen to obtain a more uniform distribution of events in the different bins. In order to increase the overall statistics the data samples for the positive and negative helicities are added together, resulting in an average polarisation of only a few percent. The correlation matrix calculated by MINUIT for the 23 SDME's indicates that the correlations between the unpolarised and polarised SDME's are of minor importance. It is therefore safe to treat the combined sample as belonging to an unpolarised beam sample and to extract only the 15 unpolarised SDME's from the sample in 4 Q^2 bins. The results of the 4 Q^2 bin analysis are shown in figure 8.15. The approach used in this data sample is repeated throughout the analysis presented in this thesis in subsequent sections.

The results of the Q^2-dependence analysis show significant non zero values for the SCHC violating matrix element r^5_{00}.

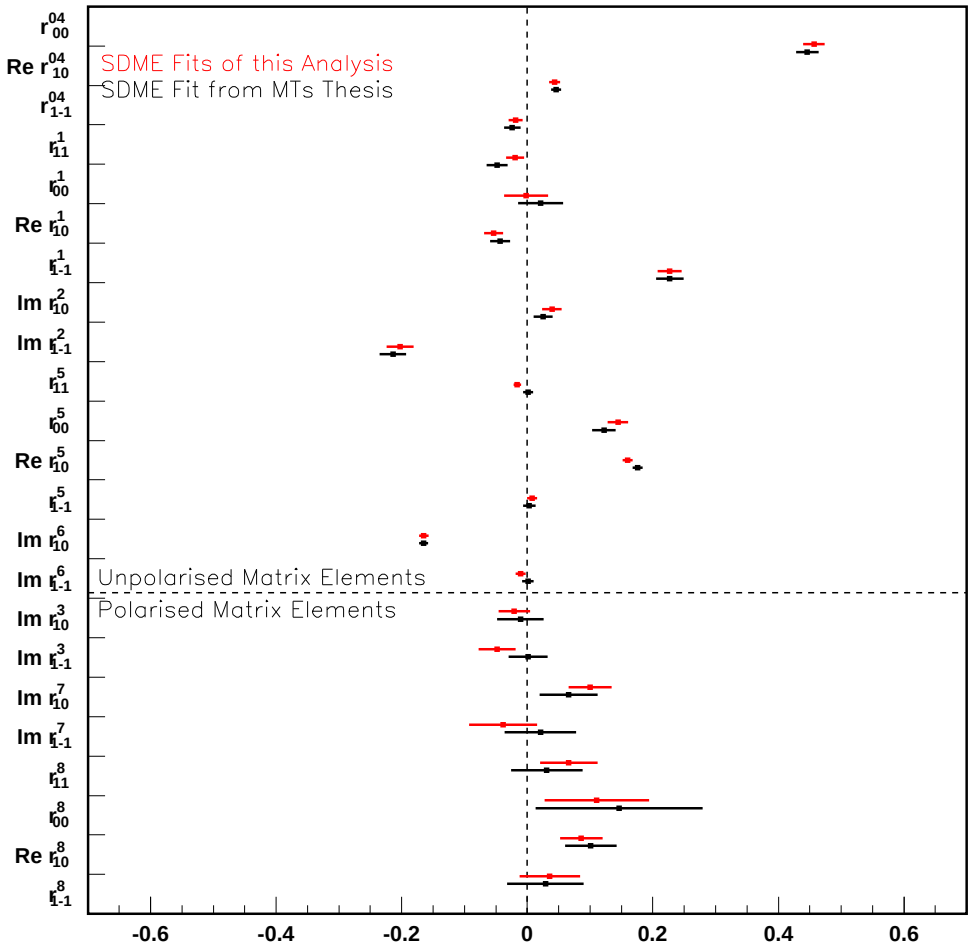

Figure 8.13: The combined values for the 23 SDME's extracted for the 1996-97 Data Sample. The error bars indicate statistical uncertainty only. They are compared to results obtained in a previous analysis at HERMES [84].

8.4.1 Natural Parity Exchange

Without assuming SCHC, the hypothesis of natural parity exchange in the t-channel alone leads to the following sum rule [114]:

$$1 - r^{04}_{00} + 2r^{04}_{1-1} - 2r^{1}_{11} - 2r^{1}_{1-1} = 0 \tag{8.11}$$

Using the results from table D.1, the left side of this equation equals 0.094 ± 0.055(stat) $\pm$ 0.073(syst), which is compatible with zero within the large uncertainties.

The Q^2-dependence of the left hand side of equation 8.11 is shown in figure 8.16. Within the large uncertainties, no clear indication for the non-validity of the NPE hypothesis can be seen.

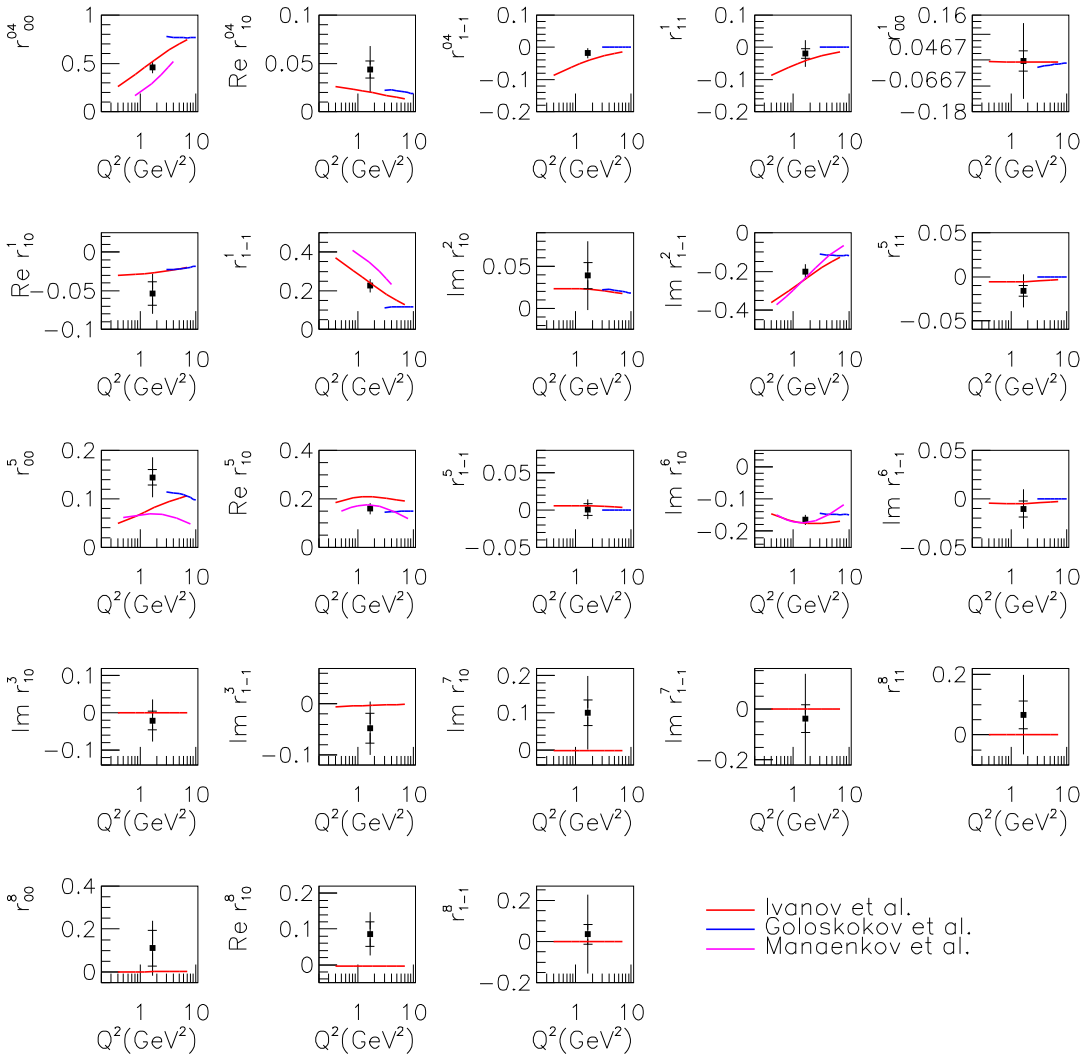

Figure 8.14: The 23 SDME's compared to theoretical model predictions for the 1996-97 data sample. The inner error bars represent the statistical error and the outer bars the systematic error.

8.4.2 s-Channel Helicity Conservation

Under the hypothesis of s-channel helicity conservation all matrix elements except, r^{04}_{00}, r^{1}_{1-1}, Im r^{2}_{1-1}, Re r^{5}_{10} and Im r^{6}_{10}, Im r^{7}_{10} and Re r^{8}_{10}, are expected to be zero. Also, the following relations are expected to hold between the non vanishing SDME's:

$$r^{1}_{1-1} = -\mathrm{Im}\ r^{2}_{1-1}, \mathrm{Re}\ r^{5}_{10} = -\mathrm{Im}\ r^{6}_{10}, \mathrm{Im}\ r^{7}_{10} = \mathrm{Re}\ r^{8}_{10} \tag{8.12}$$

Under the combined assumption of SCHC and NPE one also obtains another sum rule[114]:

$$1 - r^{04}_{00} - 2r^{1}_{1-1} = 0 \tag{8.13}$$

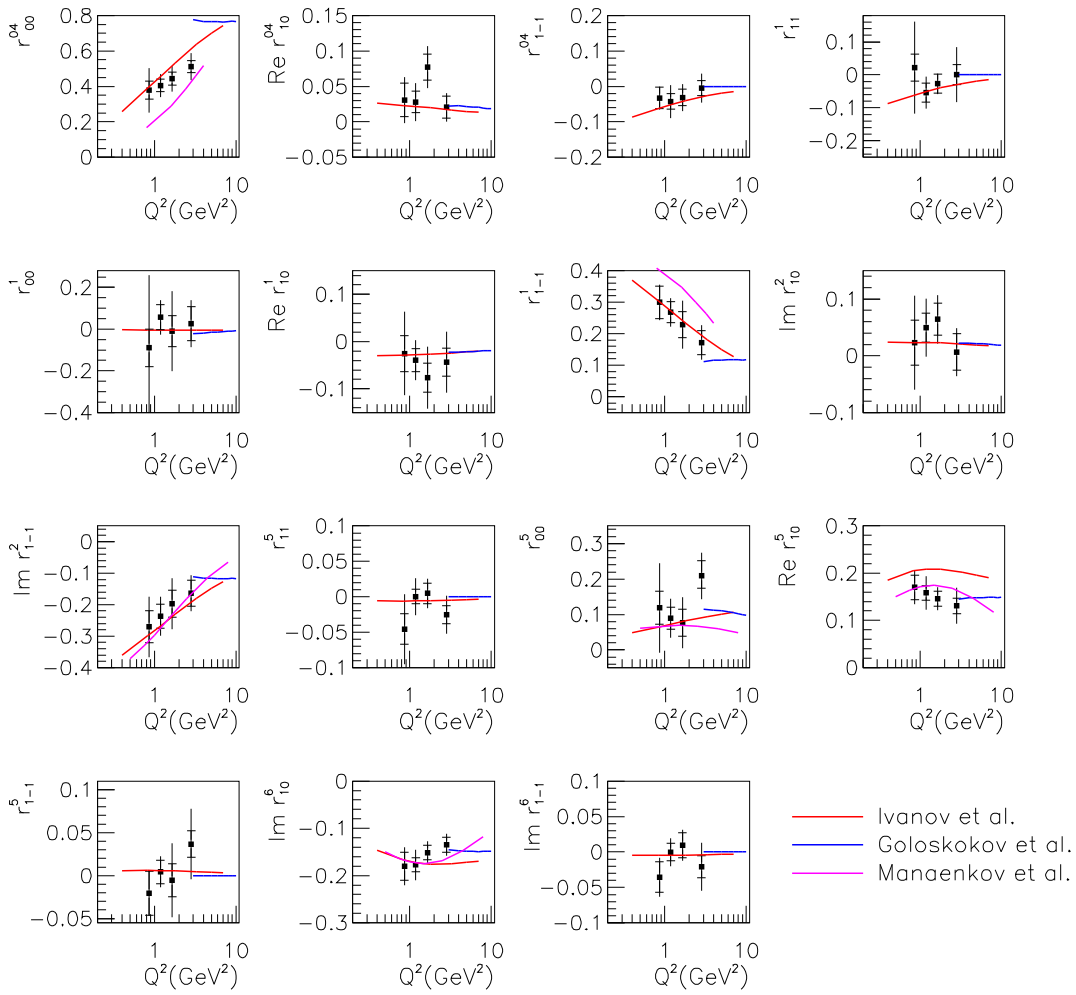

Figure 8.15: The 15 Unpolarised SDME's compared to theoretical model predictions for the 1996-97 data sample. The inner error bars represent the statistical error and the outer bars the systematic error.

Figures 8.17, 8.18 and 8.19 show the verification of these relations as a function of Q^2 using the results for the 15 unpolarised SDME's. The data supports the validity of the relations in equation 8.12. The sum rule in equation 8.13 also appears to be satisfied for the data results obtained.

As was mentioned previously there is a significant deviation from zero for the matrix element r^5_{00}. This matrix element is proportional to the interference between the helicity conserving longitudinal amplitude T_{00} and the single flip amplitude T_{01}. The latter amplitude corresponds to the the production of longitudinal polarised ρ^0 mesons from transverse photons. This is actually predicted to be the leading s-channel helicity violating effect[115][116]. The fact that the relations in equations 8.12 and 8.13 appear to be satisfied by the data, indicates that the helicity violating effect cannot be large.

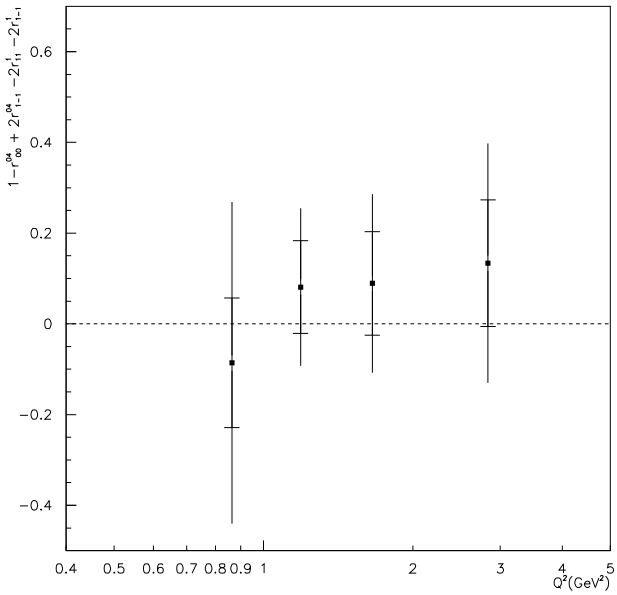

Figure 8.16: The verification of the natural parity exchange hypothesis by examining the validity of equation 8.11 as a function of Q^2 for the 1996-97 data sample. The inner error bars represent the statistical error and the outer bars the systematic error.

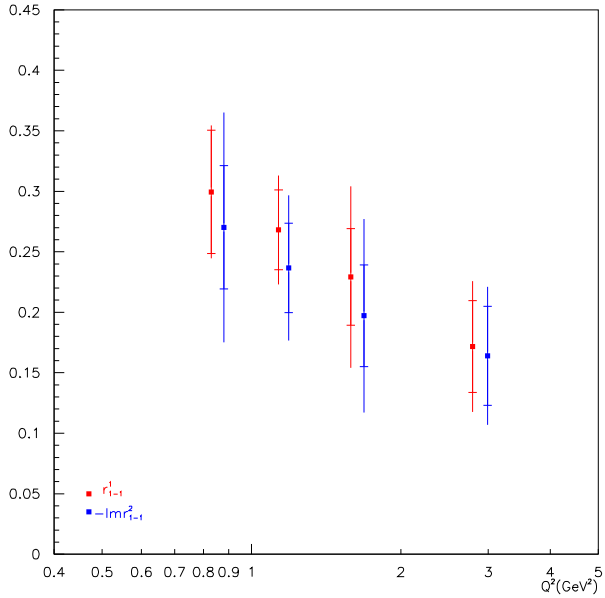

Figure 8.17: The verification of s-channel helicity by examining the relation $r^1_{1-1} = -r^2_{1-1}$ assumed in equation 8.12. 1996-97 data sample. The inner error bars represent the statistical error and the outer bars the systematic error.

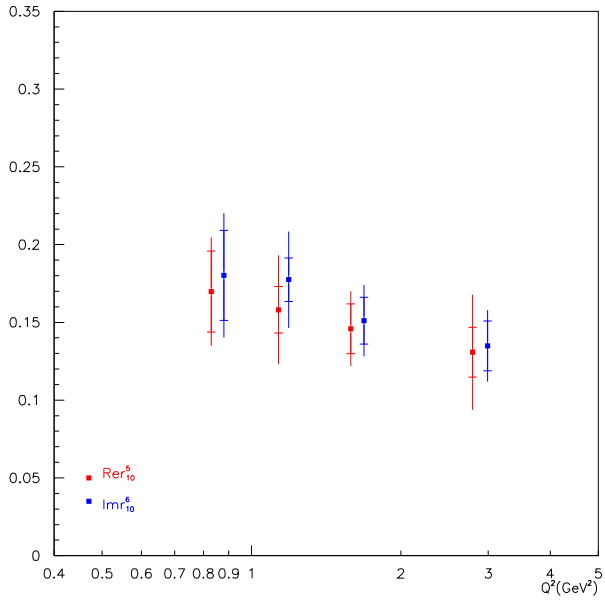

Figure 8.18: The verification of s-channel helicity by examining the relation Re r^5_{10} = $-$Im r^6_{10} assumed in equation 8.12. 1996-97 data sample. The inner error bars represent the statistical error and the outer bars the systematic error.

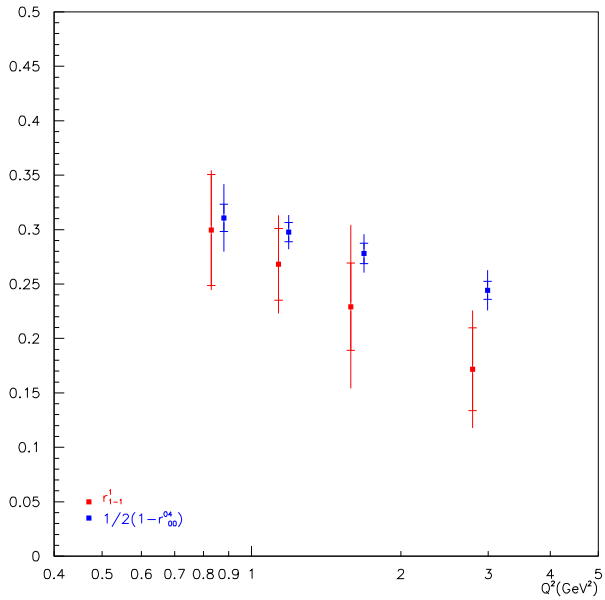

Figure 8.19: The verification of s-channel helicity assumed in equation 8.12 is examined. Note that for this relation equation 8.13 and NPE are assumed. 1996-97 data sample. The inner error bars represent the statistical error and the outer bars the systematic error.

8.4.3 Extraction of R_ρ

Under the assumption of SCHC the R_ρ ratio can be determined from:

$$R_\rho = \frac{\sigma_L}{\sigma_T} = \frac{1}{\epsilon}\frac{r_{00}^{04}}{1 - r_{00}^{04}} \tag{8.14}$$

The results for R_ρ as a function of Q^2 is shown in figure 8.20. Here the results are shown alongside the results obtained in a previous HERMES analysis on the 1996-97 hydrogen data sample [84]. The values presented from this analysis appear to be in good agreement with those obtained previously.

It has been shown that the assumption of SCHC in the determination of the R_ρ ratio is valid and that the results obtained are not significantly influenced by the assumption of SCHC [84][114].

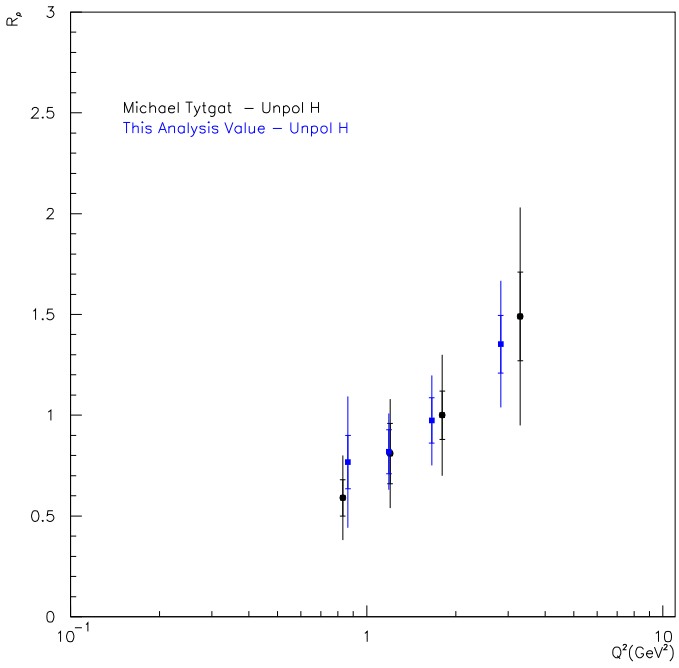

Figure 8.20: The measured values for R_ρ for the 1996-97 data sample. The inner error bars represent the statistical error and the outer bars the systematic error.

8.5 1998-2000 Hydrogen Data Sample

The data sample analysed in this section is from the HERMES 1998-2000 data taking period taken on a ^{1}H target. The analysis of this data sample is applied in exactly the same way as in the previous section. The beam polarisation for the 1998-2000 hydrogen sample is shown in figure 8.21.

The results for the 23 SDME's extracted from the two beam helicities are shown in figure 8.22.

The combined SDME values are compared to those obtained in a previous HERMES analysis on an different data sample [84] in figure 8.23. The previous analysis was applied

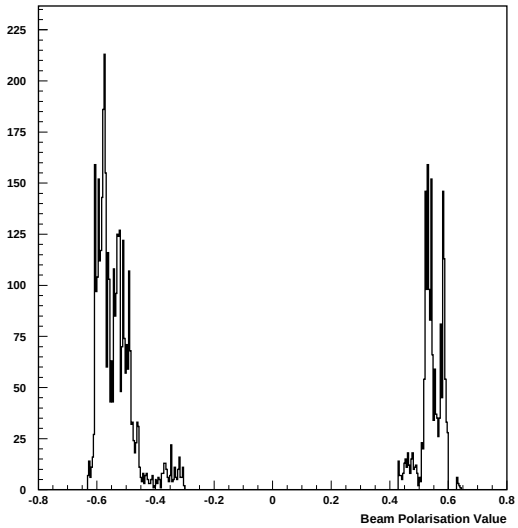

Figure 8.21: The beam polarisation of the data sample for 1998-2000. Positive (negative) values correspond to positive (negative) beam helicity

to the 1996-97 hydrogen data sample, and is shown here simply to have a frame of reference for the 1998-2000 hydrogen data sample.

The results for the 23 SDME's are compared to theoretical predictions which is shown in figure 8.24.

A Q^2 dependence of the SDME's was studied by doing the analysis in four Q^2 bins ($0.7 < 1.0 < 1.4 < 2.0 < 5.0$ GeV^2). The results of the 4 Q^2 bin analysis are shown in figure 8.25.

8.5.1 Natural Parity Exchange

Using the results from table D.3, the left side of this equation equals 0.210 ± 0.080(stat) ± 0.164(syst), which is compatible with zero within the large uncertainties.

The Q^2-dependence of the left hand side of equation 8.11 is shown in figure 8.26. Within the large uncertainties, no clear indication for the non-validity of the NPE hypothesis can be seen.

8.5.2 s-Channel Helicity Conservation

Figures 8.27, 8.28 and 8.29 show the verification of the relations presented in 8.12 as a function of Q^2 using the results for the 15 unpolarised SDME's. The data supports the validity of the relations in equation 8.12. The sum rule in equation 8.13 also appears to be satisfied for the data results obtained.

8.5.3 Extraction of R_ρ

The results for R_ρ as a function of Q^2 is shown in figure 8.30. Here they are shown alongside results obtained in a previous HERMES analysis [84].

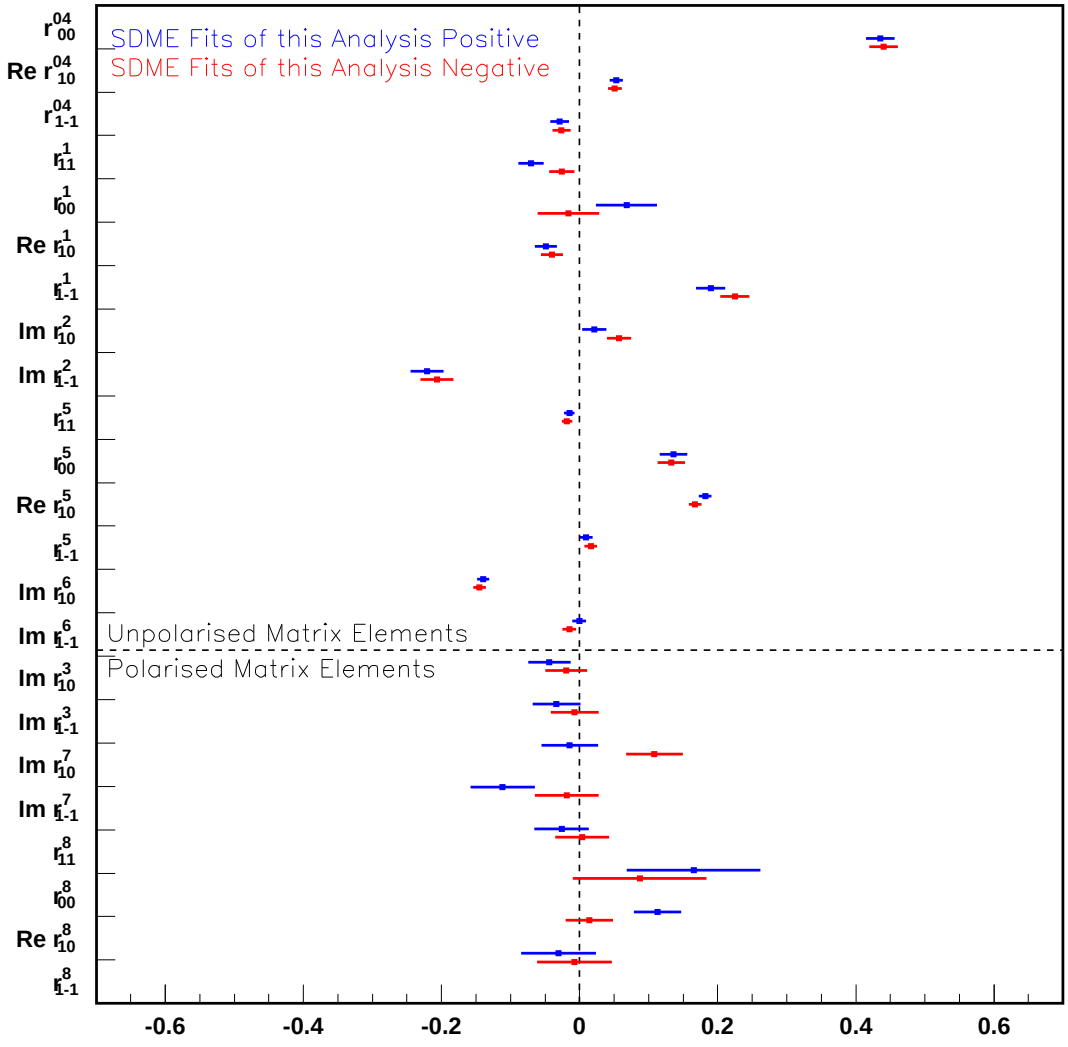

Figure 8.22: The 23 SDME's extracted separately from the positive and negative helicity samples for the 1998-2000 Data Sample. The error bars indicate statistical uncertainty only.

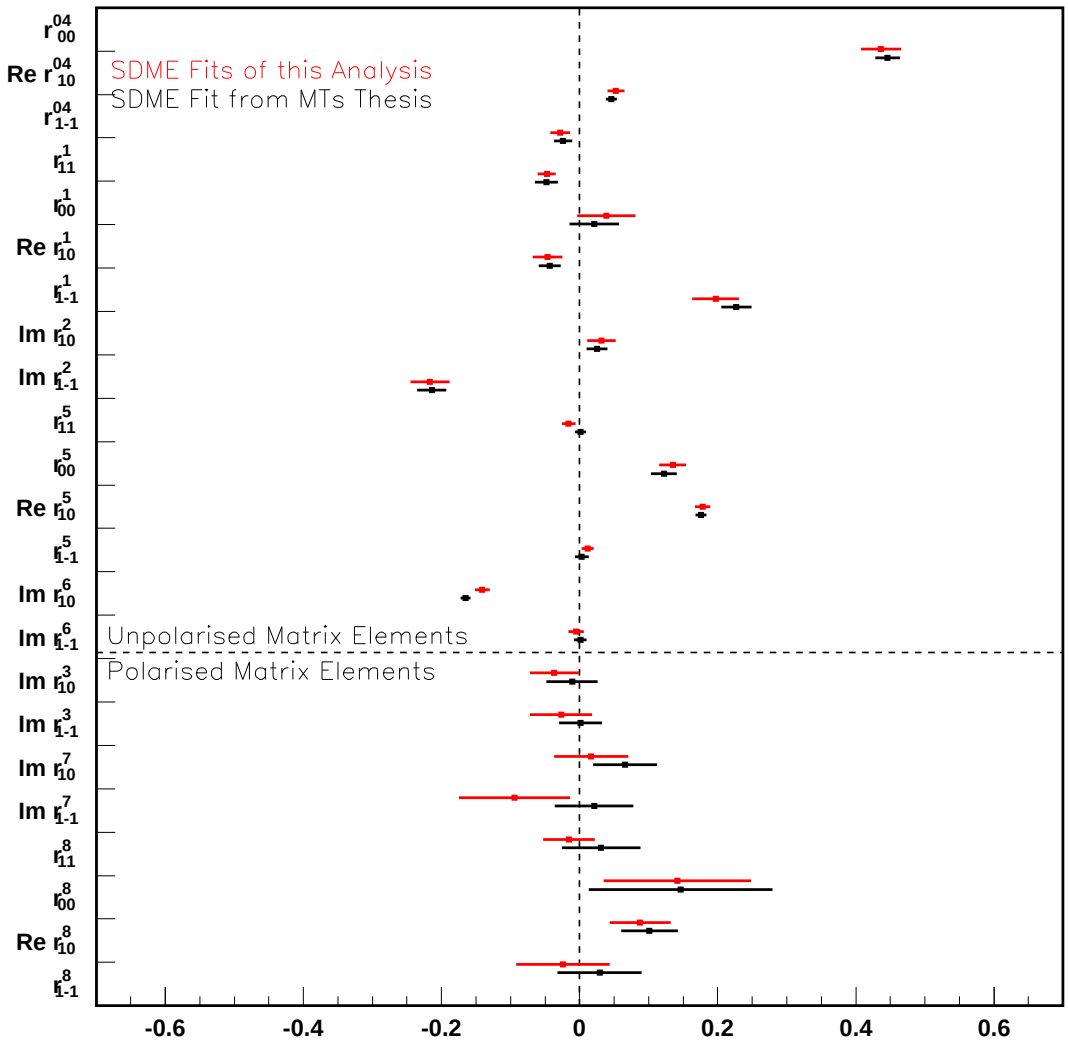

Figure 8.23: The combined values for the 23 SDME's extracted for the 1998-2000 Data Sample. The error bars indicate statistical uncertainty only. They are compared to results obtained in a previous analysis at HERMES [84].

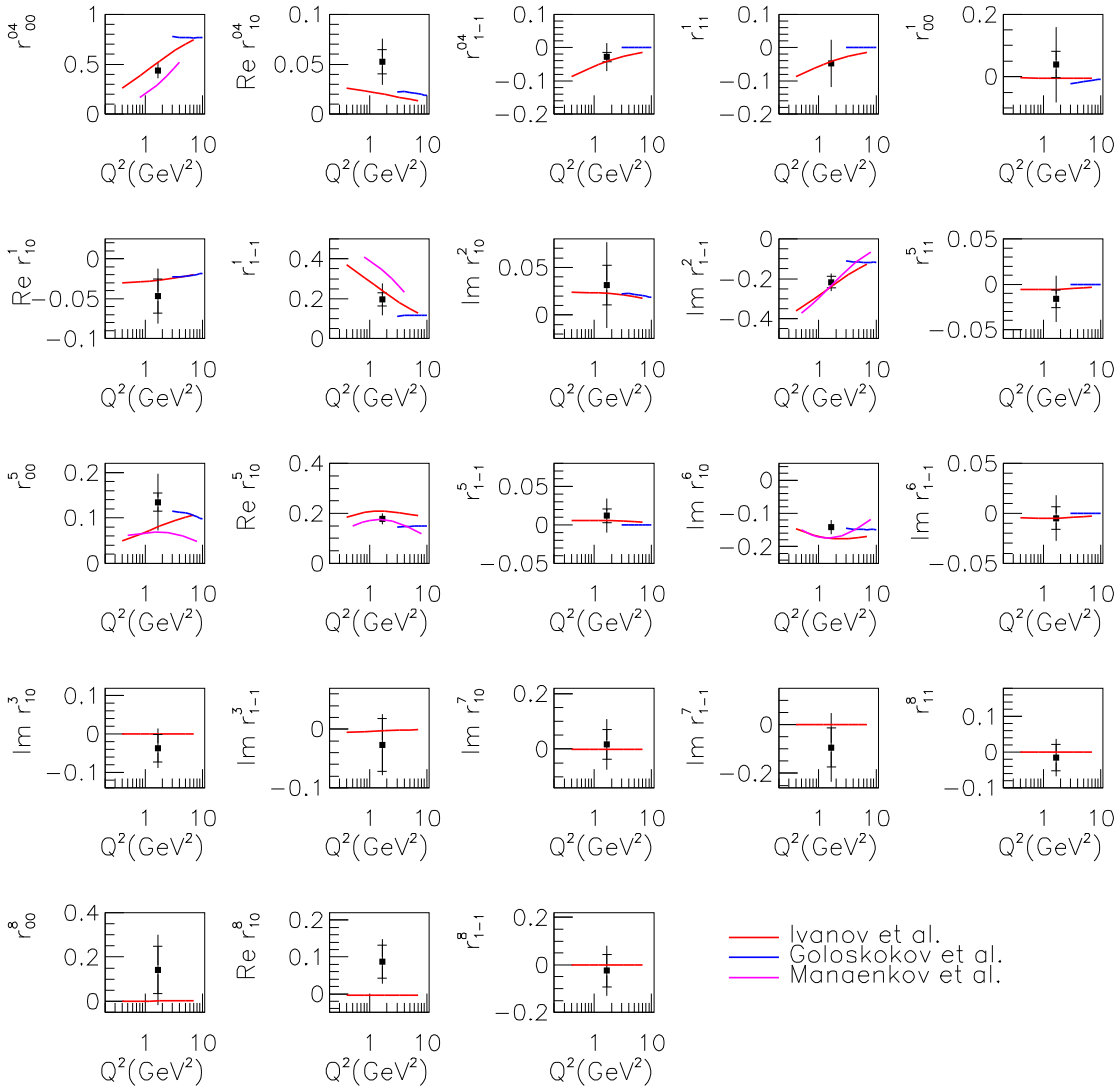

Figure 8.24: The 23 SDME's compared to theoretical model predictions for the 1998-2000 data sample. The inner error bars represent the statistical error and the outer bars the systematic error.

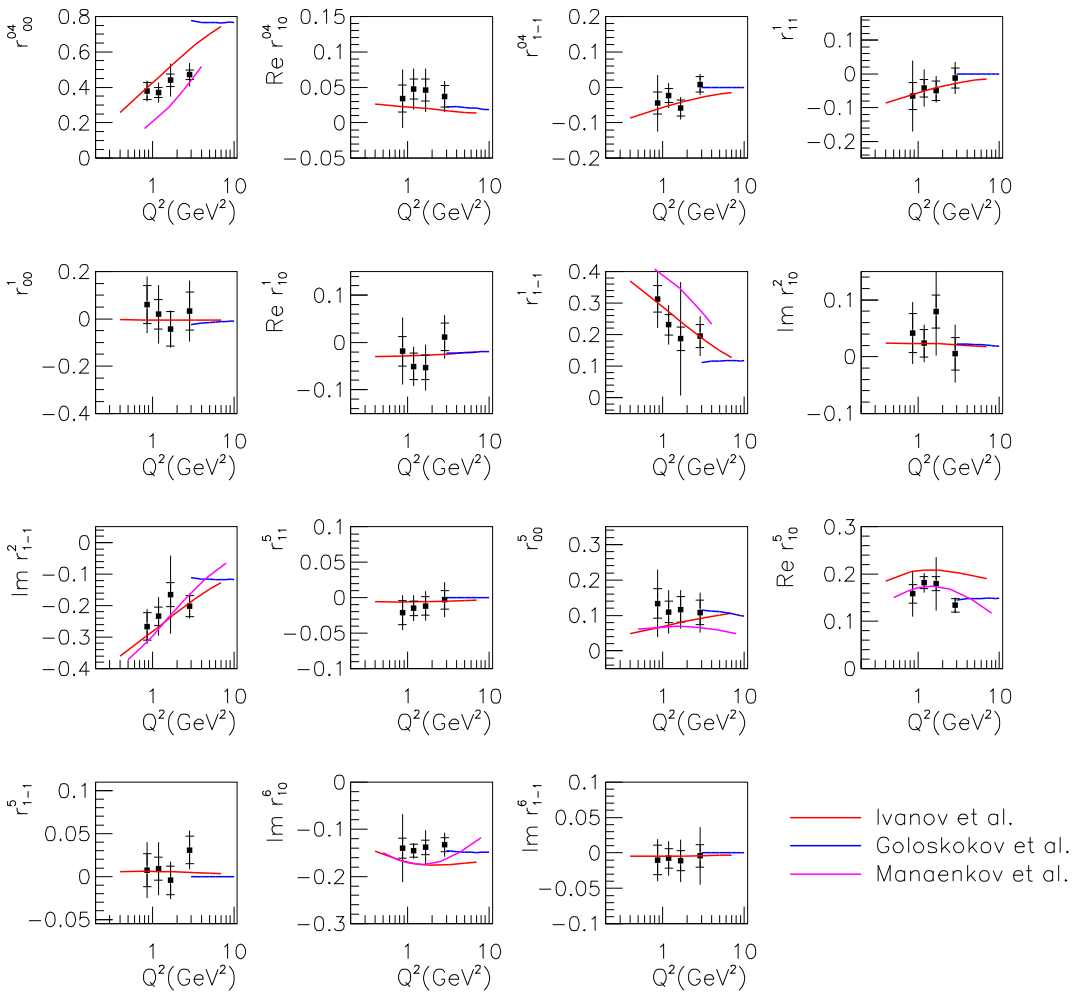

Figure 8.25: The 15 Unpolarised SDME's compared to theoretical model predictions for the 1998-2000 data sample. The inner error bars represent the statistical error and the outer bars the systematic error.

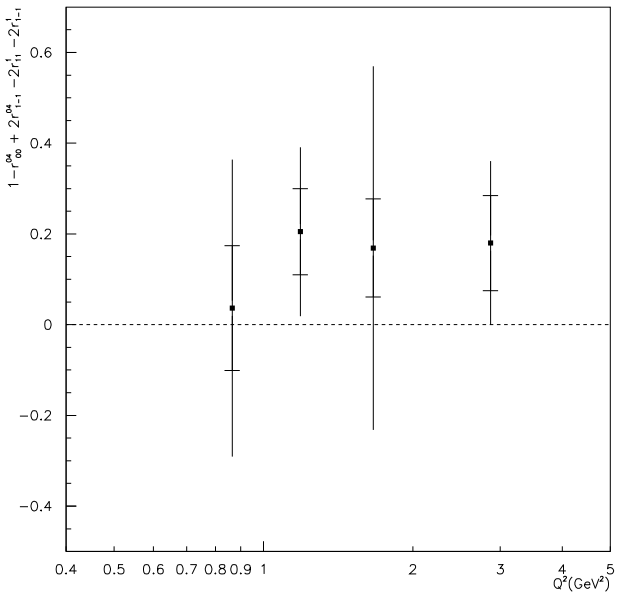

Figure 8.26: The verification of the natural parity exchange hypothesis by examining the validity of equation 8.11 as a function of Q^2 for the 1998-2000 data sample. The inner error bars represent the statistical error and the outer bars the systematic error.

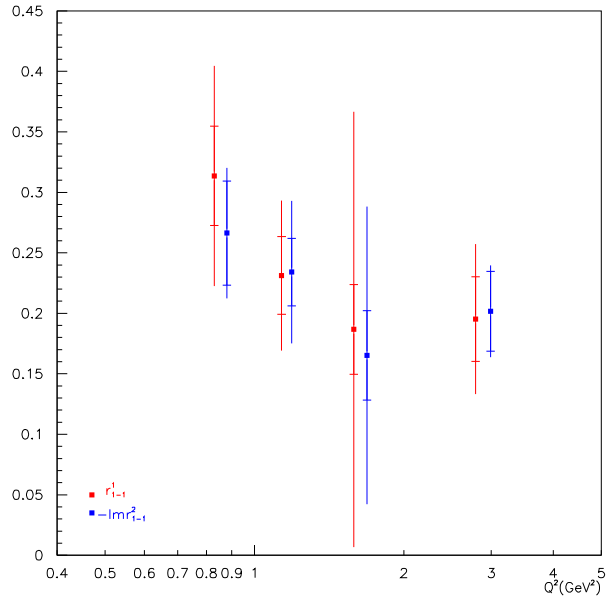

Figure 8.27: The verification of s-channel helicity by examining the relation $r^1_{1-1} = -r^2_{1-1}$ assumed in equation 8.12. 1998-2000 data sample. The inner error bars represent the statistical error and the outer bars the systematic error.

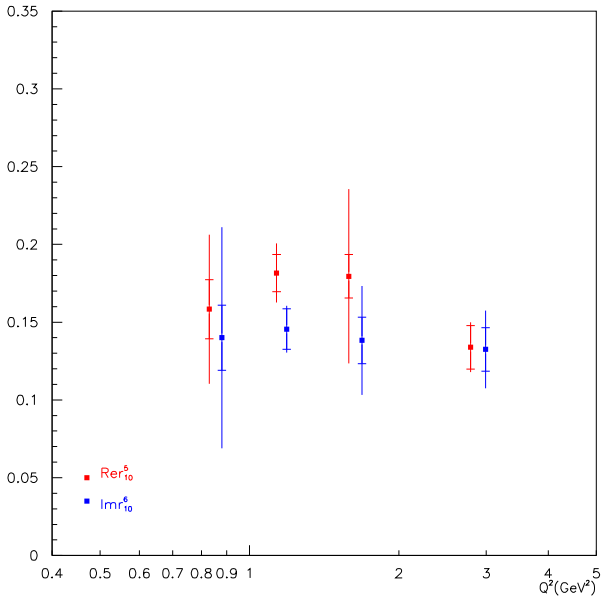

Figure 8.28: The verification of s-channel helicity by examining the relation Re r^5_{10} = $-$Im r^6_{10} assumed in equation 8.12. 1998-2000 data sample. The inner error bars represent the statistical error and the outer bars the systematic error.

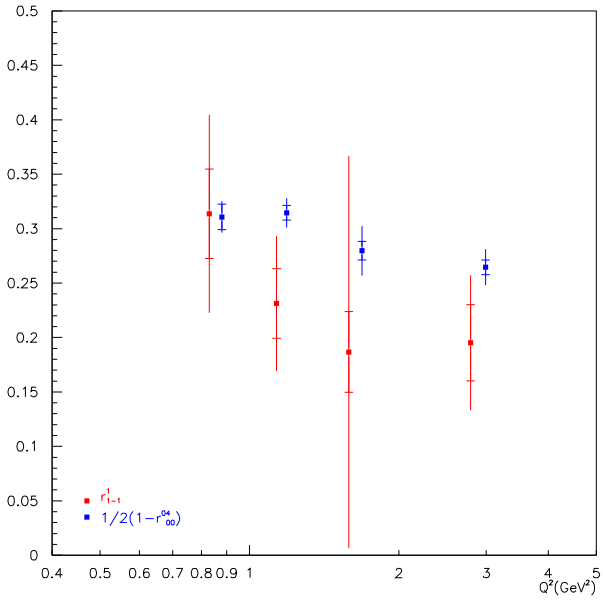

Figure 8.29: The verification of s-channel helicity assumed in equation 8.12 is examined. Note that for this relation equation 8.13 and NPE are assumed. 1998-2000 data sample. The inner error bars represent the statistical error and the outer bars the systematic error.

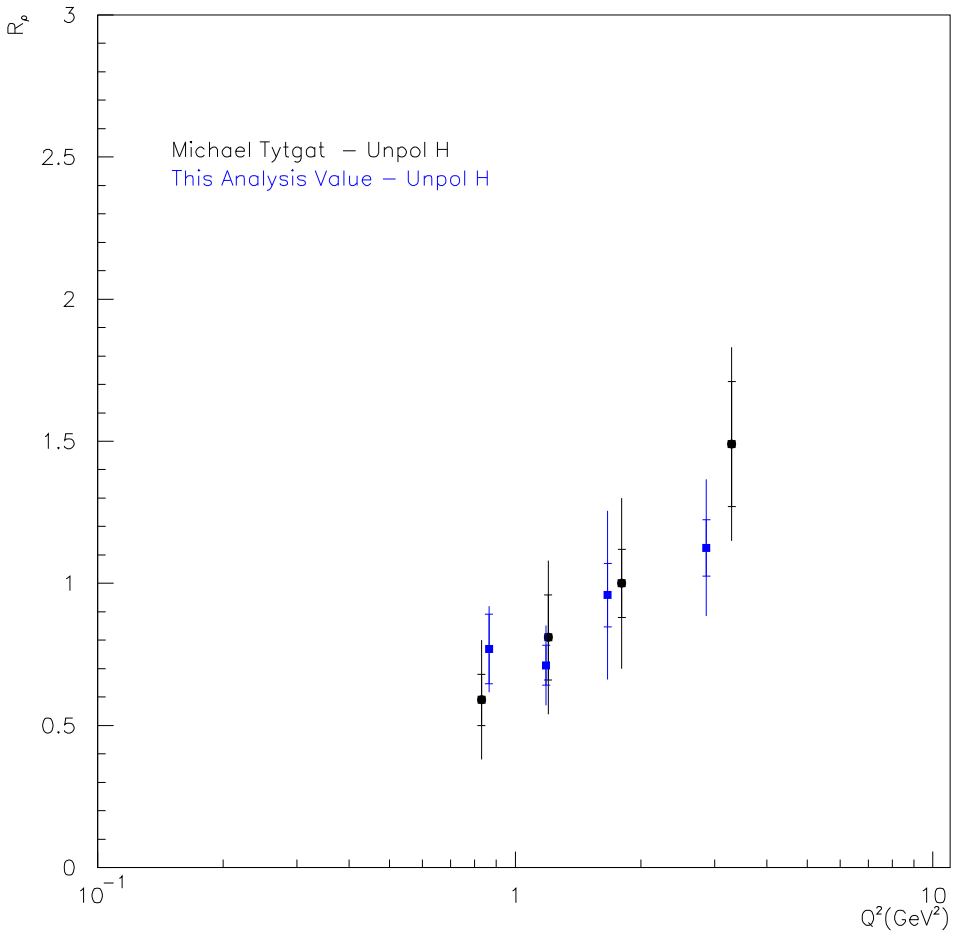

Figure 8.30: The measured values for R_ρ for the 1998-2000 data sample. The inner error bars represent the statistical error and the outer bars the systematic error.

8.6 1996-2000 Hydrogen Data Sample

The data sample analysed in this section is from the HERMES 1996-2000 data taking period taken on a ^{1}H target. The 1996-2000 hydrogen data sample is the combination of the 1996-97 and 1998-2000 hydrogen data samples which were analysed and presented separately in the previous two sections. Again, the analysis procedure used to analyse this data set is the same as used in the previous sections.

The beam polarisation for the 1996-2000 hydrogen sample is shown in figure 8.31.

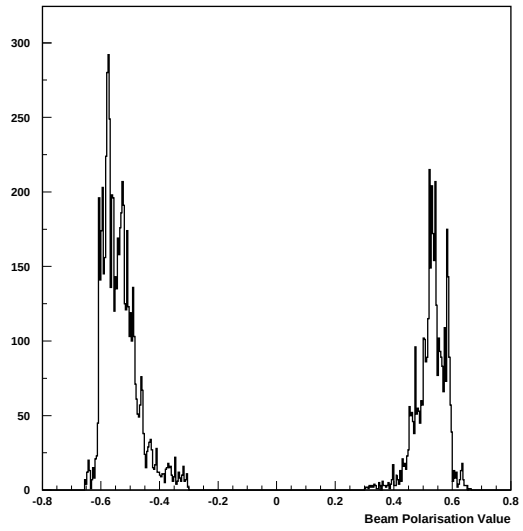

Figure 8.31: The beam polarisation of the data sample for 1996-2000. Positive (negative) values correspond to positive (negative) beam helicity

The results for the 23 SDME's extracted from the two beam helicities are shown in figure 8.32.

The combined SDME values are compared to those obtained in a previous HERMES analysis on an smaller data sample [84] in figure 8.33. The larger statistics contained within the 1996-2000 hydrogen data sample results in a decrease in the size of the statistical error bars shown in figure 8.33.

The results for the 23 SDME's are compared to theoretical predictions which is shown in figure 8.34.

The Q^2 dependence of the SDME's was studied by doing the analysis in four Q^2 bins ($0.7 < 1.0 < 1.4 < 2.0 < 5.0$ GeV^2) for the combined 1996-2000 hydrogen data sample. The results of the 4 Q^2 bin analysis are shown in figure 8.35.

8.6.1 Natural Parity Exchange

Using the results from table D.5, the left side of equation 8.11 equals 0.148 $\pm$ 0.047(stat) $\pm$ 0.096(syst), which is comparable with zero within the large uncertainties.

The Q^2-dependence of the left hand side of equation 8.11 is shown in figure 8.36. Within the large uncertainties, no clear indication for the non-validity of the NPE hypothesis can be seen.

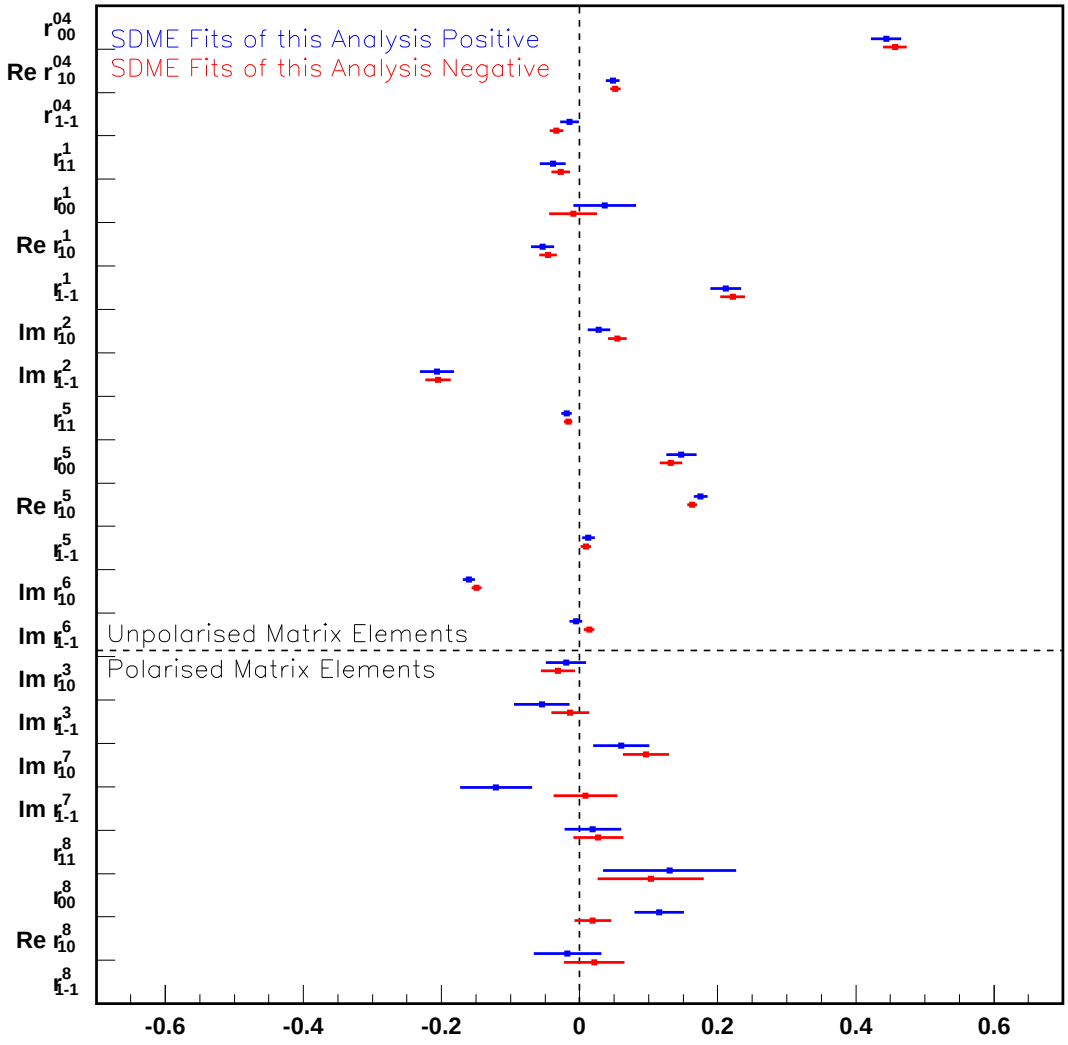

Figure 8.32: The 23 SDME's extracted separately from the positive and negative helicity samples for the 1996-2000 Data Sample. The error bars indicate statistical uncertainty only.

8.6.2 *s*-Channel Helicity Conservation

Figures 8.37, 8.38 and 8.39 show the verification of the relations 8.12 as a function of Q^2 using the results for the 15 unpolarised SDME's. The data supports the validity of the relations in equation 8.12. The sum rule in equation 8.13 also appears to be satisfied for the data results obtained.

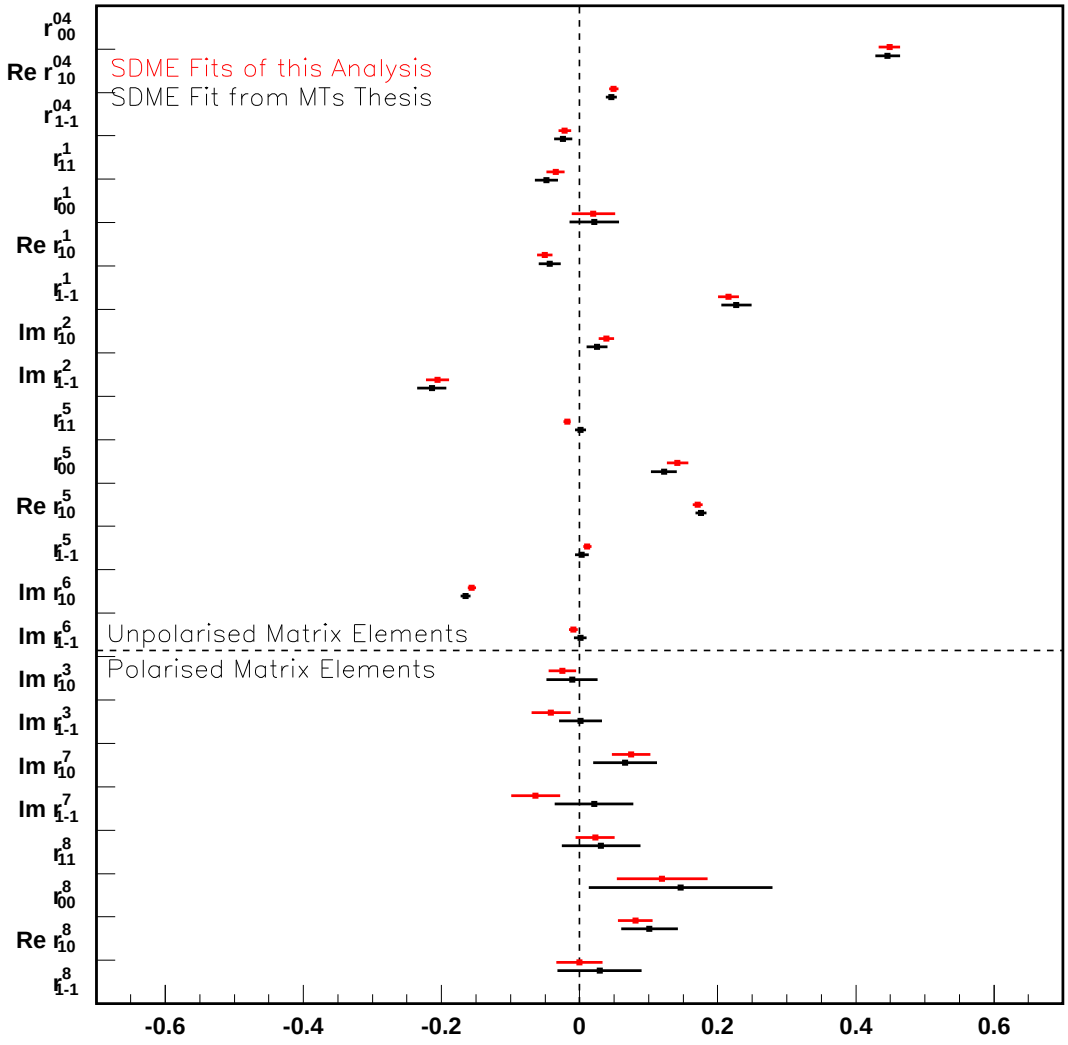

Figure 8.33: The combined values for the 23 SDME's extracted for the 1996-2000 Data Sample. The error bars indicate statistical uncertainty only. They are compared to results obtained in a previous analysis at HERMES [84].

8.6.3 Extraction of R_ρ

The results for R_ρ as a function of Q^2 is shown in figure 8.40. Here they are shown alongside those obtained in a previous HERMES analysis [84].

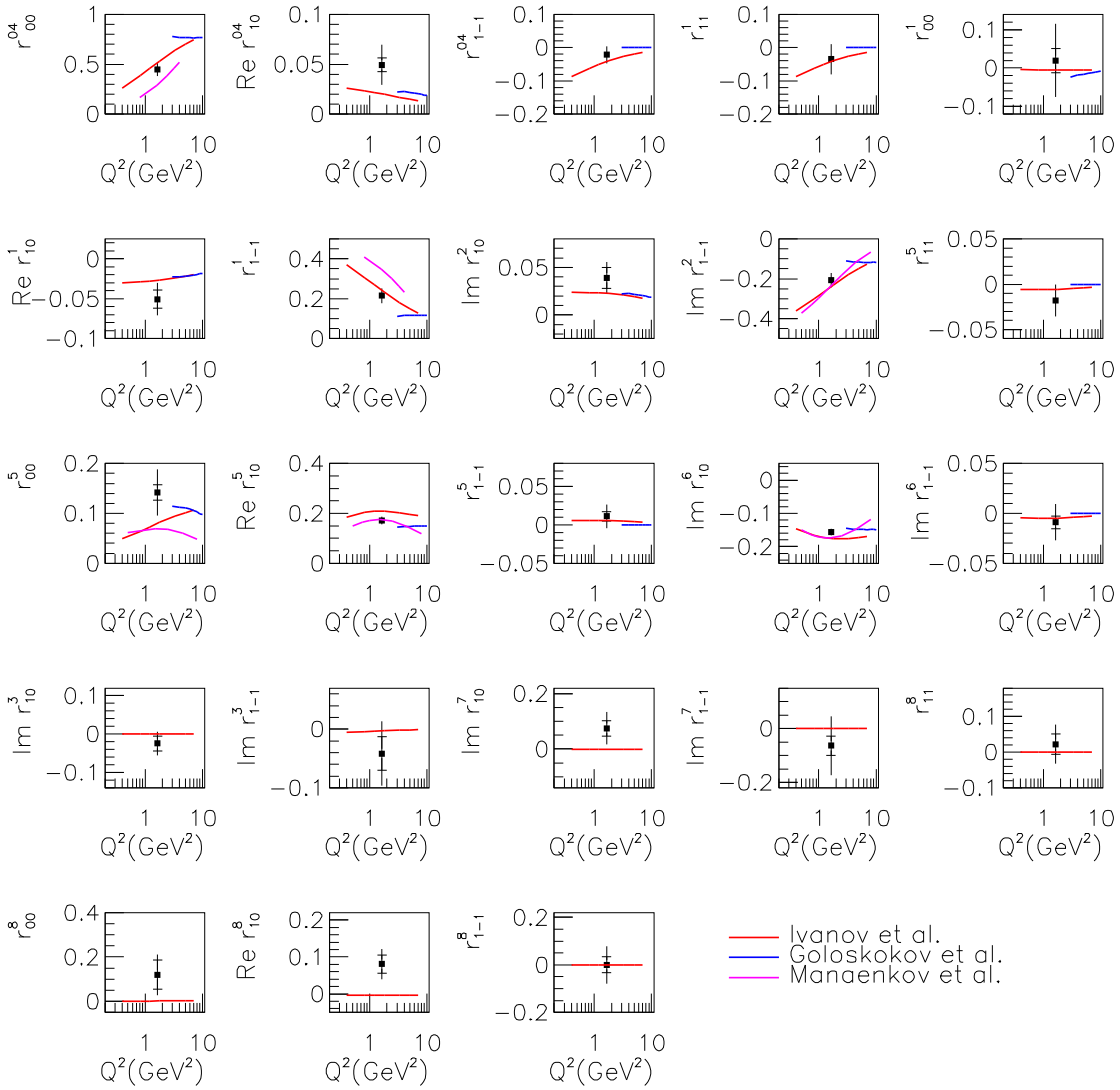

Figure 8.34: The 23 SDME's compared to theoretical model predictions for the combined 1996-2000 data sample. The inner error bars represent the statistical error and the outer bars the systematic error.

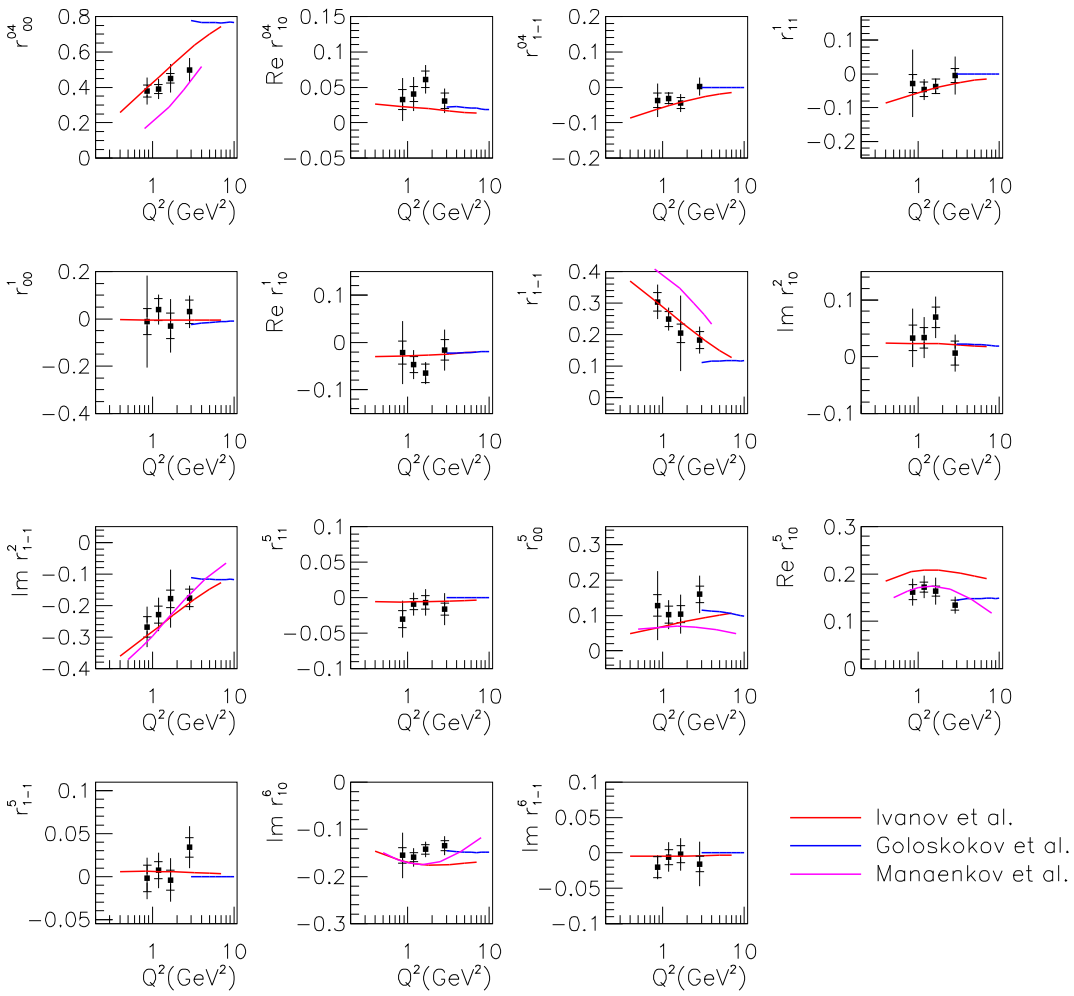

Figure 8.35: The 15 Unpolarised SDME's compared to theoretical model predictions for the 1996-2000 data sample. The inner error bars represent the statistical error and the outer bars the systematic error.

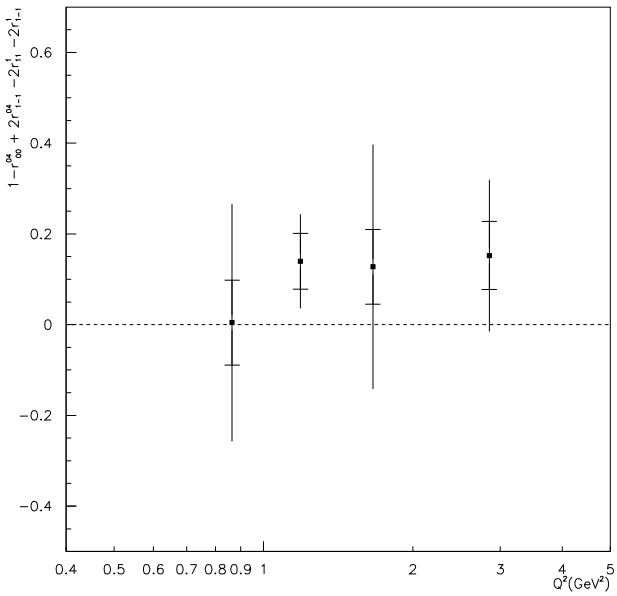

Figure 8.36: The verification of the natural parity exchange hypothesis by examining the validity of equation 8.11 as a function of Q^2 for the combined 1996-2000 data sample. The inner error bars represent the statistical error and the outer bars the systematic error.

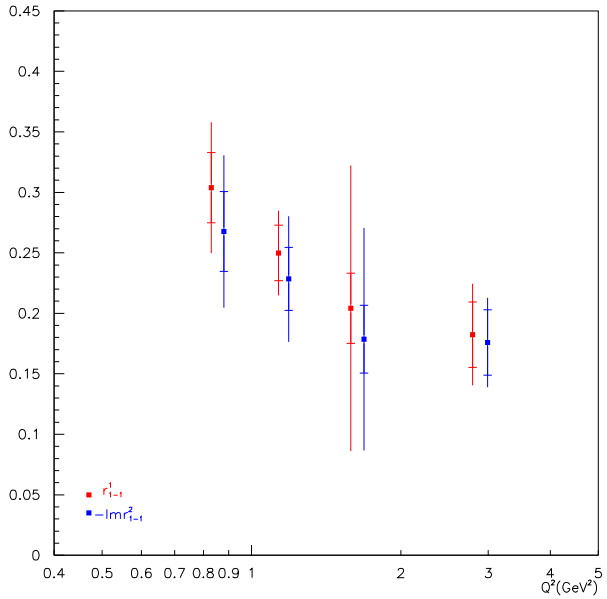

Figure 8.37: The verification of s-channel helicity by examining the relation $r^1_{1-1} = -r^2_{1-1}$ assumed in equation 8.12. Combined 1996-2000 data sample. The inner error bars represent the statistical error and the outer bars the systematic error.

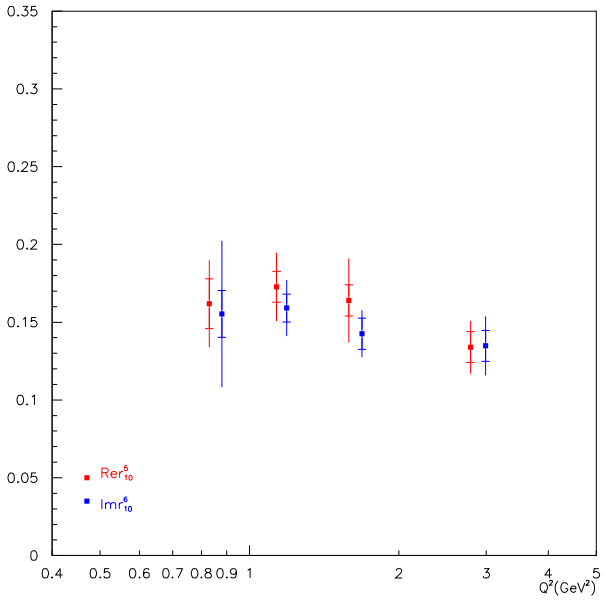

Figure 8.38: The verification of s-channel helicity by examining the relation Re $r^5_{10} = -$Im r^6_{10} assumed in equation 8.12. Combined 1996-2000 data sample. The inner error bars represent the statistical error and the outer bars the systematic error.

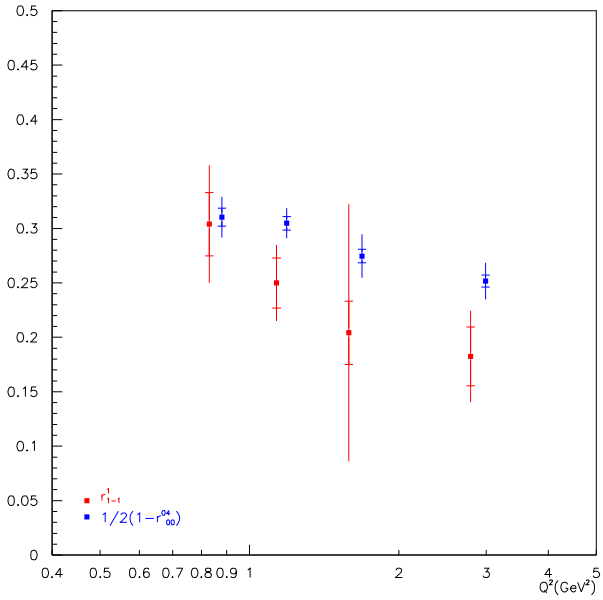

Figure 8.39: The verification of s-channel helicity assumed in equation 8.12 is examined. Note that for this relation equation 8.13 and NPE are assumed. Combined 1996-2000 data sample. The inner error bars represent the statistical error and the outer bars the systematic error.

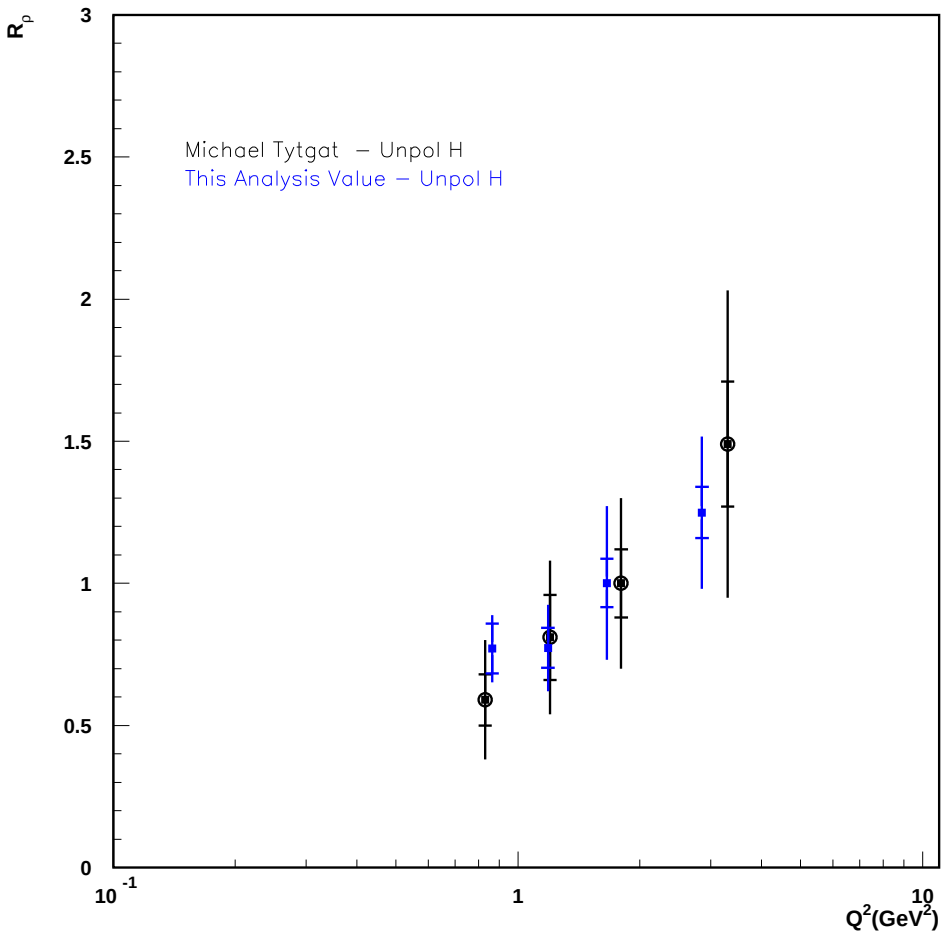

Figure 8.40: The measured values for R_ρ for the combined 1996-2000 data sample. The inner error bars represent the statistical error and the outer bars the systematic error.

8.7 1996-2000 Deuterium Data Sample

The data sample analysed in this section is from the HERMES 1996-2000 data taking period taken on a ^{2}H target. The beam polarisation for the 1996-2000 deuterium sample is shown in figure 8.41.

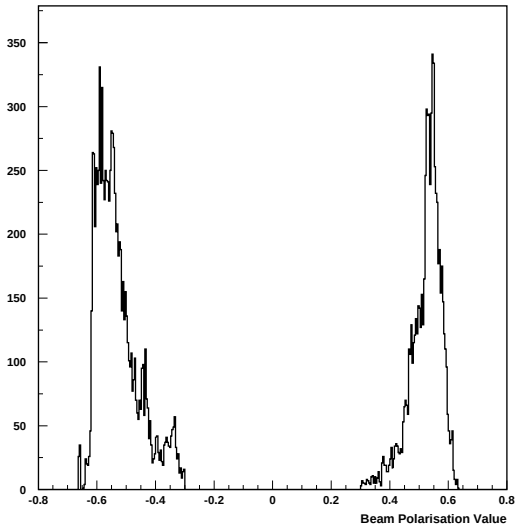

Figure 8.41: The beam polarisation of the data sample for 1996-2000. Positive (negative) values correspond to positive (negative) beam helicity

The results for the 23 SDME's extracted from the two beam helicities are shown in figure 8.42.

The combined SDME values are compared to those obtained in a previous HERMES analysis on a hydrogen data sample [84] in figure 8.43. The results for the 23 SDME's are compared to theoretical predictions for hydrogen which is shown in figure 8.44.

The Q^2 dependence of the SDME's was studied by doing the analysis in four Q^2 bins ($0.7 < 1.0 < 1.4 < 2.0 < 5.0$ GeV^2). The results of the 4 Q^2 bin analysis are shown in figure 8.45.

8.7.1 Natural Parity Exchange

Using the results from table D.7, the left side of equation 8.11 equals 0.099 ± 0.031(stat) $\pm$ 0.065(syst), which is comparable with zero within the large uncertainties.

The Q^2-dependence of the left hand side of equation 8.11 is shown in figure 8.46. Within the large uncertainties, no clear indication for the non-validity of the NPE hypothesis can be seen.

8.7.2 s-Channel Helicity Conservation

Figures 8.47, 8.48 and 8.49 show the verification of relations 8.12 as a function of Q^2 using the results for the 15 unpolarised SDME's. The data supports the validity of the relations in equation 8.12. The sum rule in equation 8.13 also appears to be satisfied for the data results obtained.

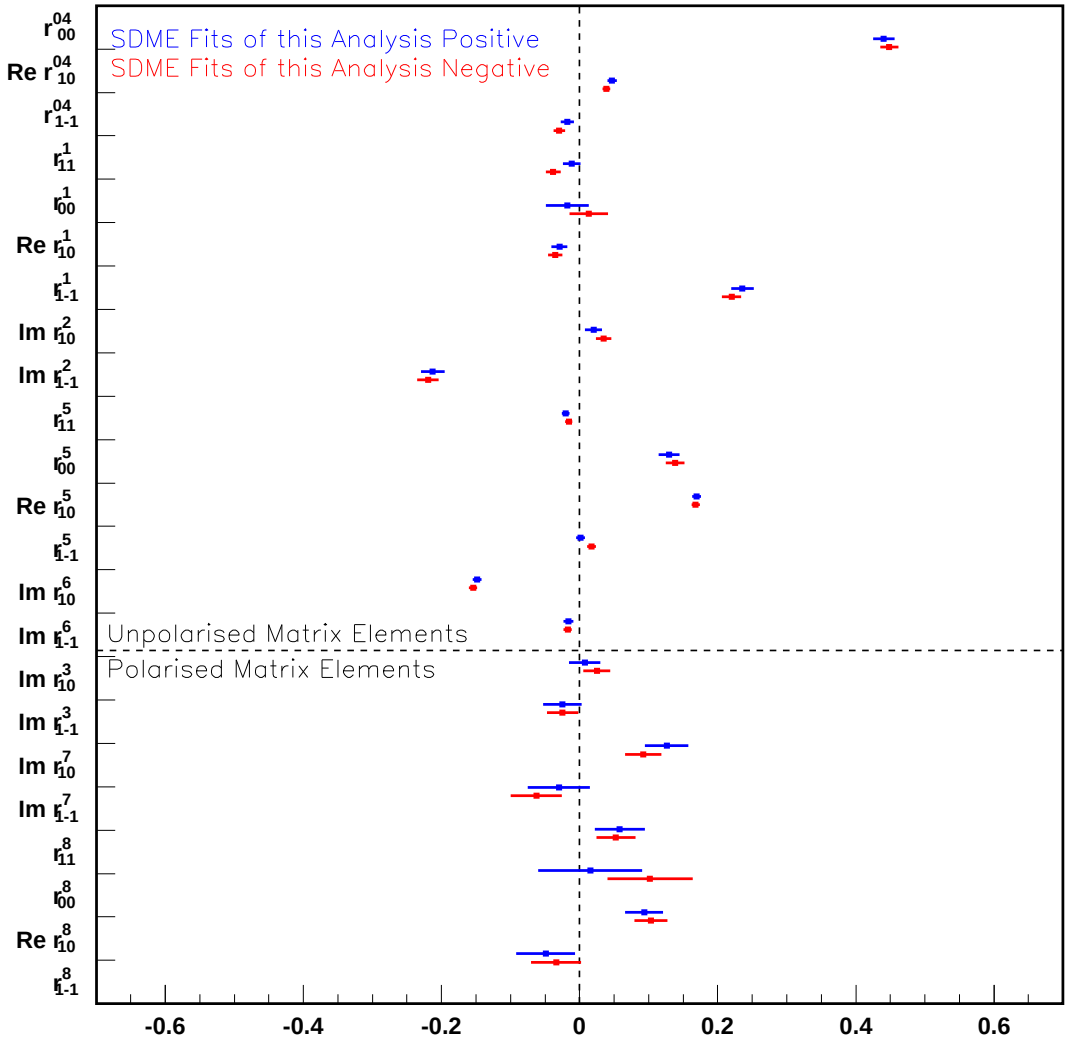

Figure 8.42: The 23 SDME's extracted separately from the positive and negative helicity samples for the 1996-2000 Data Sample. The error bars indicate statistical uncertainty only.

8.7.3 Extraction of R_ρ

The results for R_ρ as a function of Q^2 is shown in figure 8.50. Here they are shown alongside those obtained in a previous HERMES analysis on hydrogen [84].

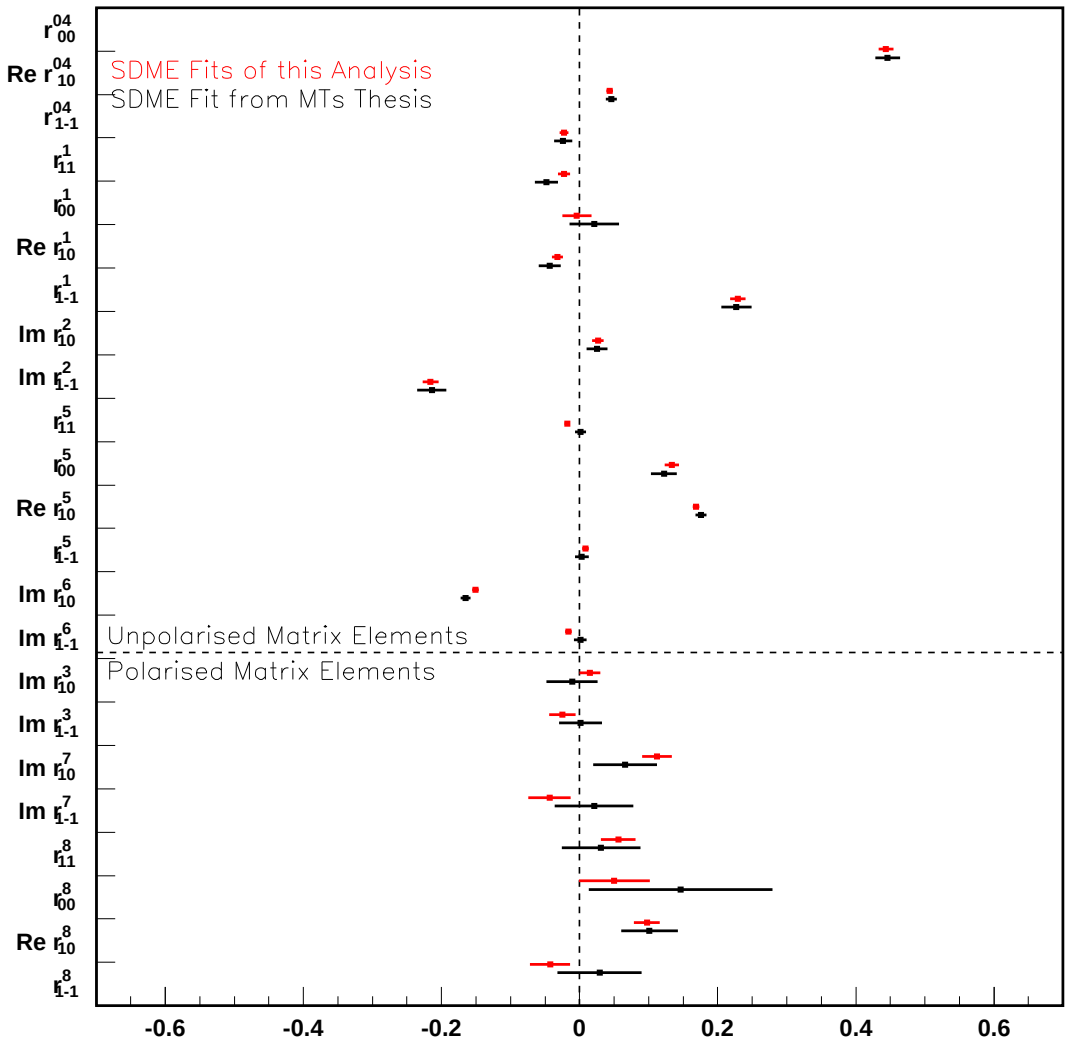

Figure 8.43: The combined values for the 23 SDME's extracted for the 1996-2000 Data Sample. The error bars indicate statistical uncertainty only. They are compared to results obtained in a previous analysis at HERMES on hydrogen [84].

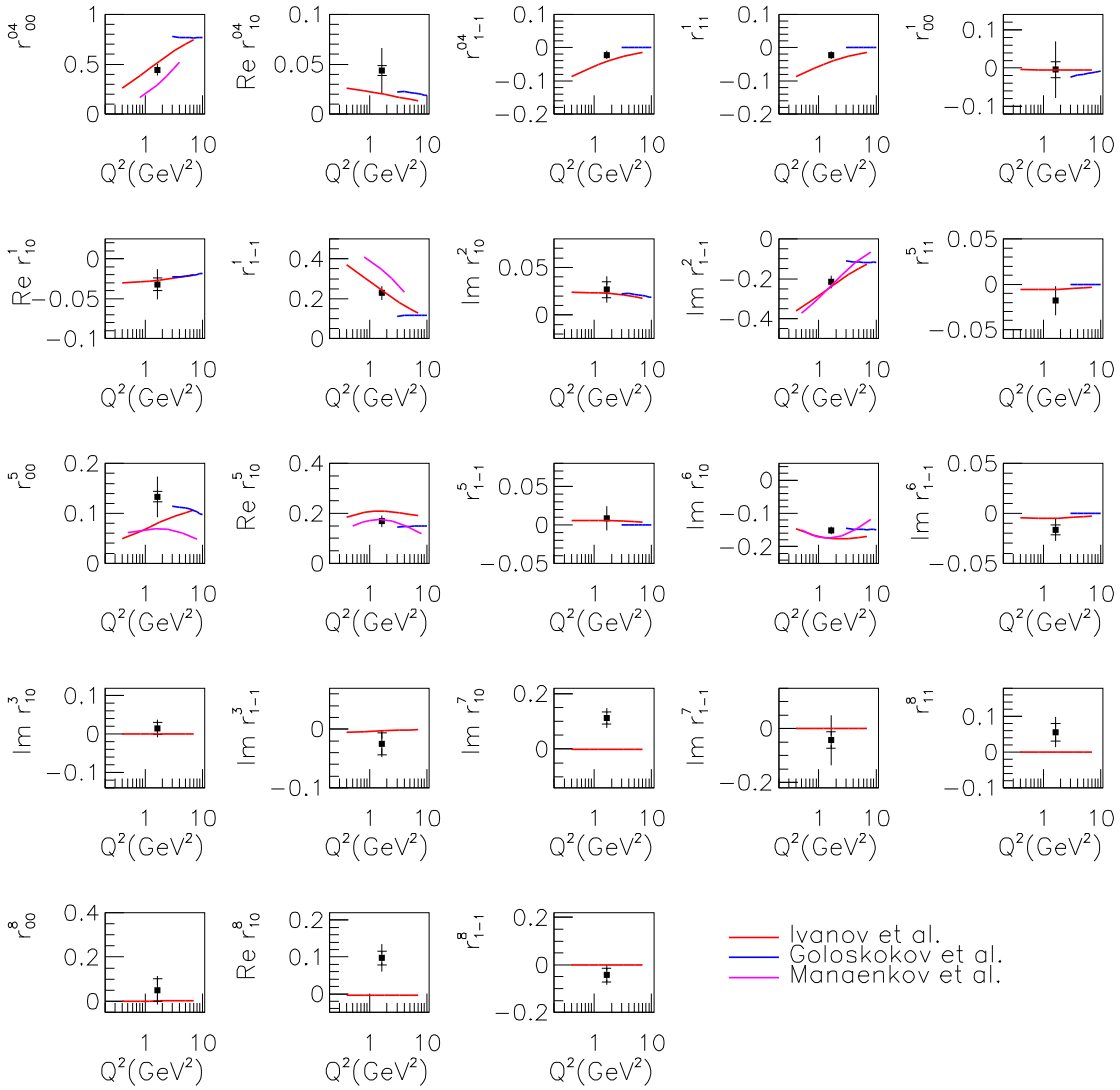

Figure 8.44: The 23 SDME's compared to theoretical model predictions for hydrogen for the combined 1996-2000 data sample. The inner error bars represent the statistical error and the outer bars the systematic error.

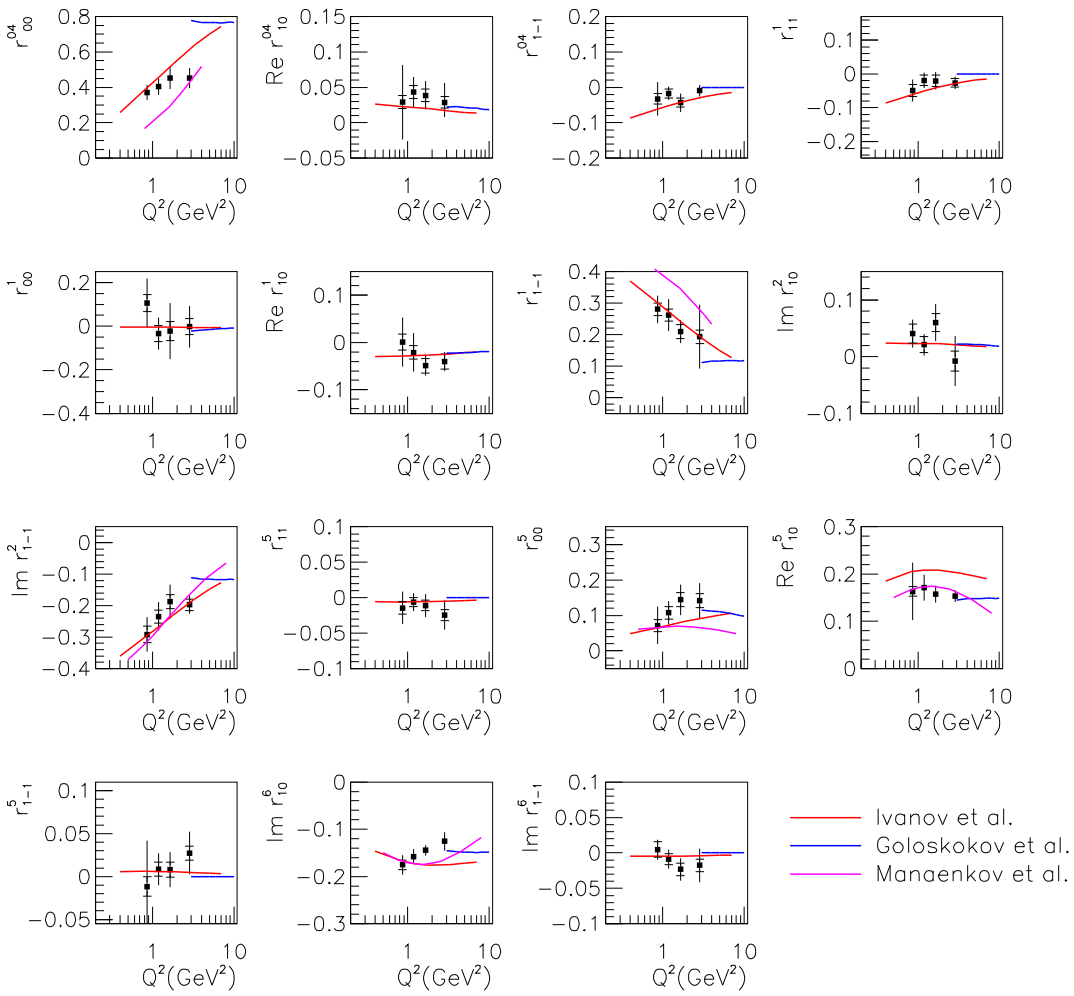

Figure 8.45: The 15 Unpolarised SDME's compared to theoretical model predictions for hydrogen for the 1996-2000 data sample. The inner error bars represent the statistical error and the outer bars the systematic error.

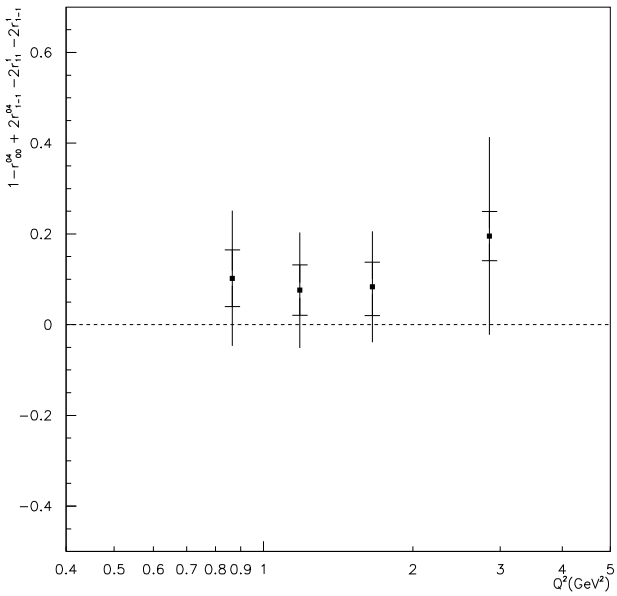

Figure 8.46: The verification of the natural parity exchange hypothesis by examining the validity of equation 8.11 as a function of Q^2 for the combined 1996-2000 data sample. The inner error bars represent the statistical error and the outer bars the systematic error.

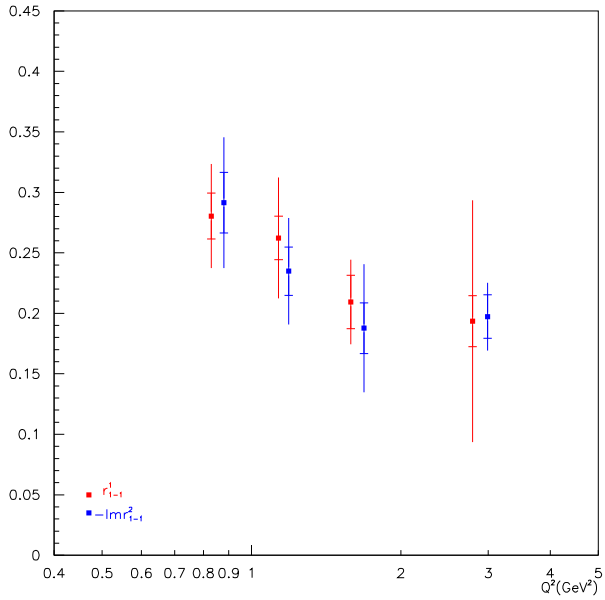

Figure 8.47: The verification of s-channel helicity by examining the relation $r^1_{1-1} = -r^2_{1-1}$ assumed in equation 8.12. Combined 1996-2000 data sample. The inner error bars represent the statistical error and the outer bars the systematic error.

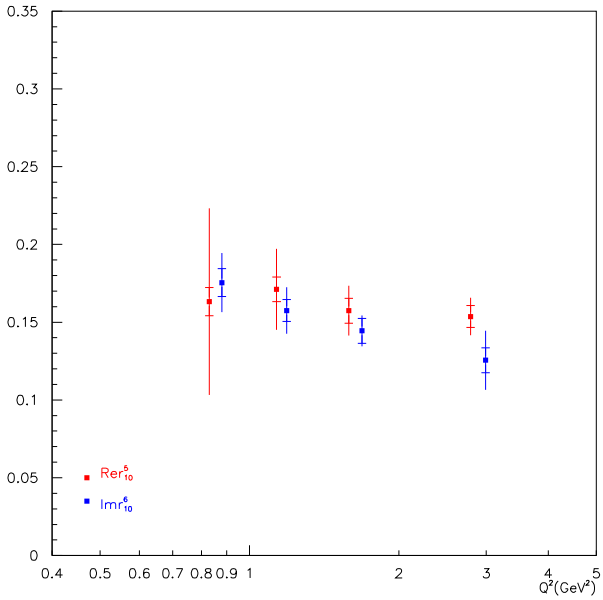

Figure 8.48: The verification of s-channel helicity by examining the relation Re $r^5_{10} = -$Im r^6_{10} assumed in equation 8.12. Combined 1996-2000 data sample. The inner error bars represent the statistical error and the outer bars the systematic error.

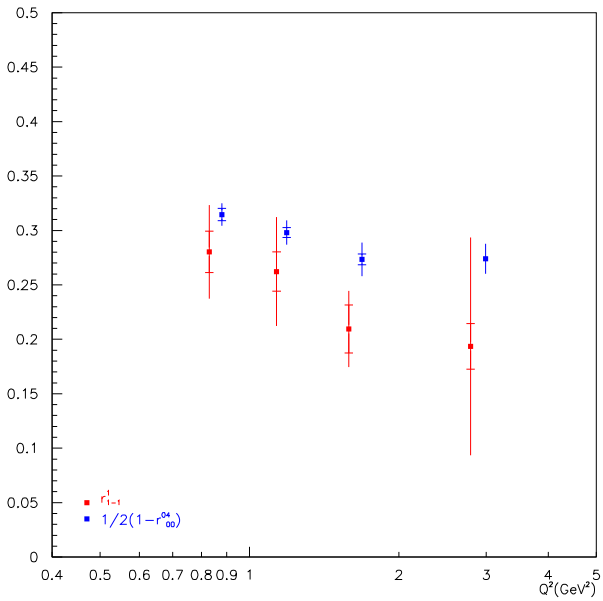

Figure 8.49: The verification of s-channel helicity assumed in equation 8.12 is examined. Note that for this relation equation 8.13 and NPE are assumed. Combined 1996-2000 data sample. The inner error bars represent the statistical error and the outer bars the systematic error.

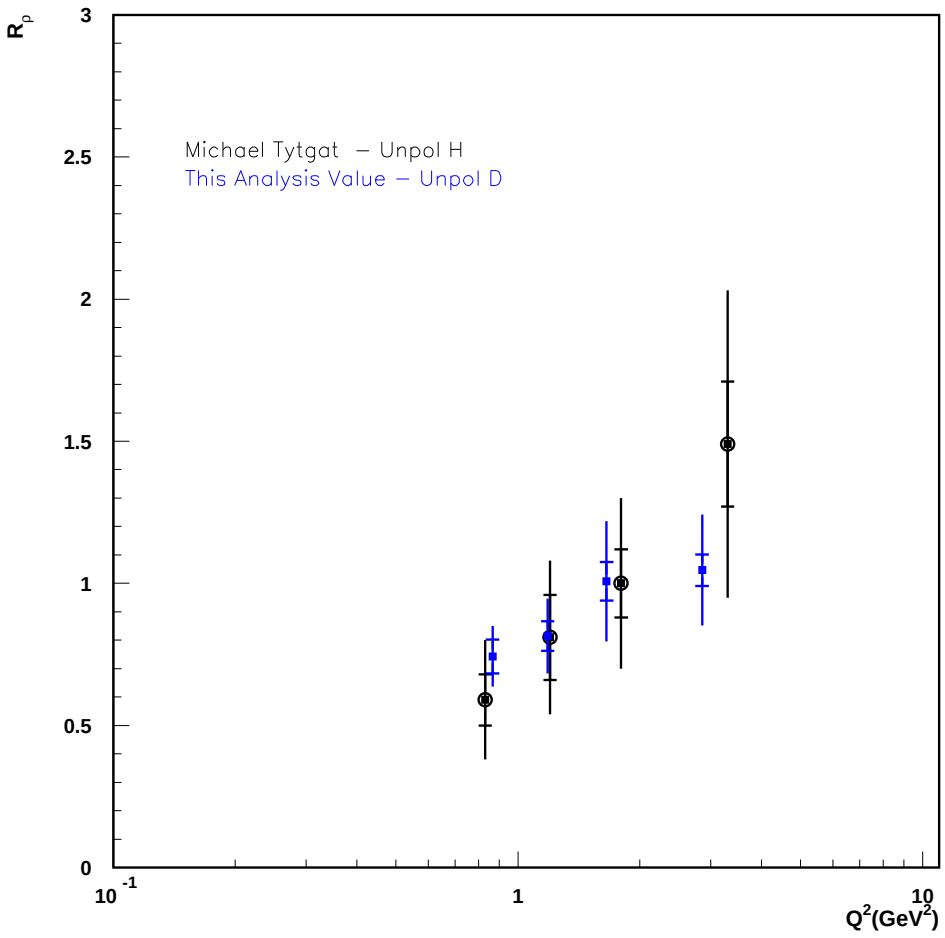

Figure 8.50: The measured values for R_ρ for the combined 1996-2000 data sample. The inner error bars represent the statistical error and the outer bars the systematic error.

8.8 1996-2000 Incoherent Deuterium Data Sample

The data sample analysed in this section is from the HERMES 1996-2000 data taking period taken on a ^{2}H target. The analysis in the section is the incoherent region, i.e $0.1 < t' < 0.4$ GeV^2 where the scattering occurs on individual nucleons within the nucleus, rather than on the nucleus as a whole. In figure 8.51 a fit applied to the t' distributions for both the hydrogen and deuterium data samples. In the region between $0.1 < t' < 0.4$ GeV^2 the slopes of the hydrogen and deuterium samples appear to be similar as is shown in table 8.5. The selection cut between $0.1 < t' < 0.4$ GeV^2 to select only incoherent events appears to be reasonable. The contribution from coherent events, where the scattering occurs on the nucleus as a whole, can be seen in the region below $t' < 0.1$ GeV^2 in the deuterium sample.

The beam polarisation for the 1996-2000 incoherent deuterium sample is shown in figure 8.52. In the comparisons between hydrogen and deuterium in this section of the analysis both the hydrogen and deuterium samples are analysed in the range between $0.1 < t' < 0.4$ GeV^2 to allow comparison between the two samples.

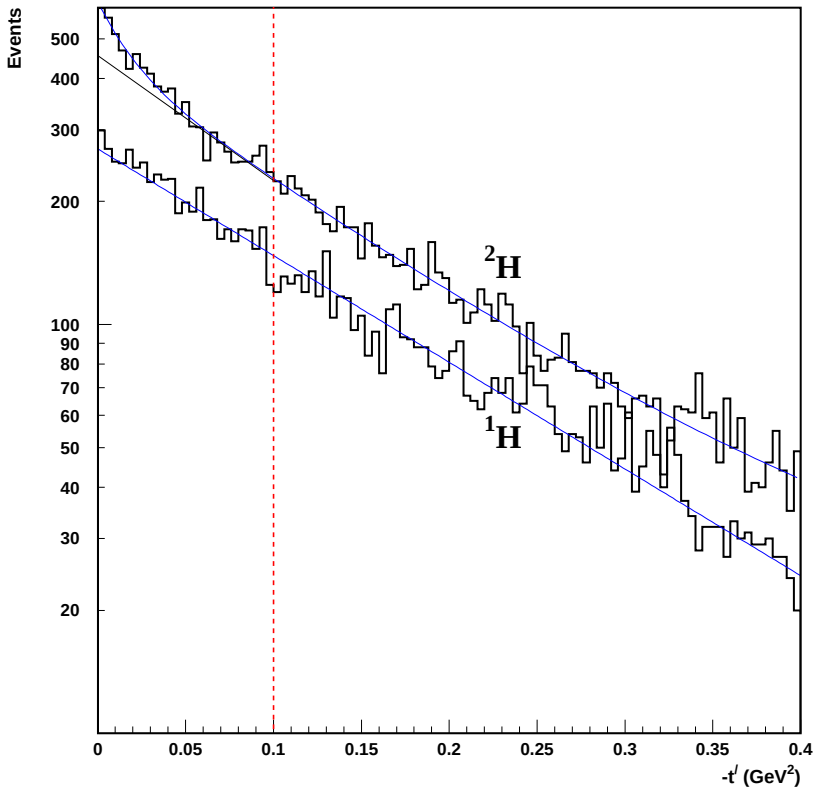

Figure 8.51: The t' distributions for exclusive ρ^0 production on ^{1}H and ^{2}H targets for the combined 1996-2000 data taking period. The blue lines show fits to the data samples. The red line shows the cut applied to select events in the incoherent region between $0.1 < t' < 0.4$ GeV^2. The black line in the region $t' < 0.1$ GeV^2 is drawn to show more clearly the contribution from coherent events in the ^{2}H sample.

The results for the 23 SDME's extracted from the two beam helicities are shown in figure 8.53.

Target	Slope Paramter (GeV^{-2}) Incoherent Region ($0.1 < t' < 0.4$ GeV^2)
^{1}H	5.816 ± 0.1869
^{2}H	5.475 ± 0.2135

Table 8.5: The fitted ρ^0 slope parameters in the incoherent region for hydrogen and deuterium targets for the combined 1996-2000 data taking period.

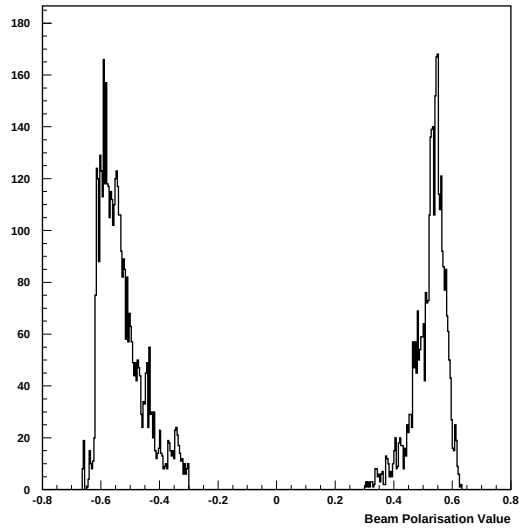

Figure 8.52: The beam polarisation of the incoherent deuterium data sample for 1996-2000. Positive (negative) values correspond to positive (negative) beam helicity.

The value of r^5_{00} in this incoherent t' range appears to be larger than it was previously when analysed over the entire $t < 0.4$ GeV^2 range. This could be a sign of the increasing tendency of r^5_{00} with increasing t'. This effect is observed for both the hydrogen and deuterium samples in this chosen t' range in plot 8.54. Plot 8.55 shows the incoherent deuterium results plotted on their own.

The results for the 23 SDME's are compared to theoretical predictions for hydrogen which is shown in figure 8.56.

The Q^2 dependence of the SDME's was studied by doing the analysis in four Q^2 bins ($0.7 < 1.0 < 1.4 < 2.0 < 5.0$ GeV^2). The results of the 4 Q^2 bin analysis are shown in figure 8.57.

8.8.1 Natural Parity Exchange

Using the results from table D.9, the left side of equation 8.11 equals 0.159 ± 0.047(stat) $\pm$ 0.073(syst), which is comparable with zero within the large uncertainties.

The Q^2-dependence of the left hand side of equation 8.11 is shown in figure 8.58. Within the large uncertainties, no clear indication for the non validity of the NPE hypothesis can be seen.

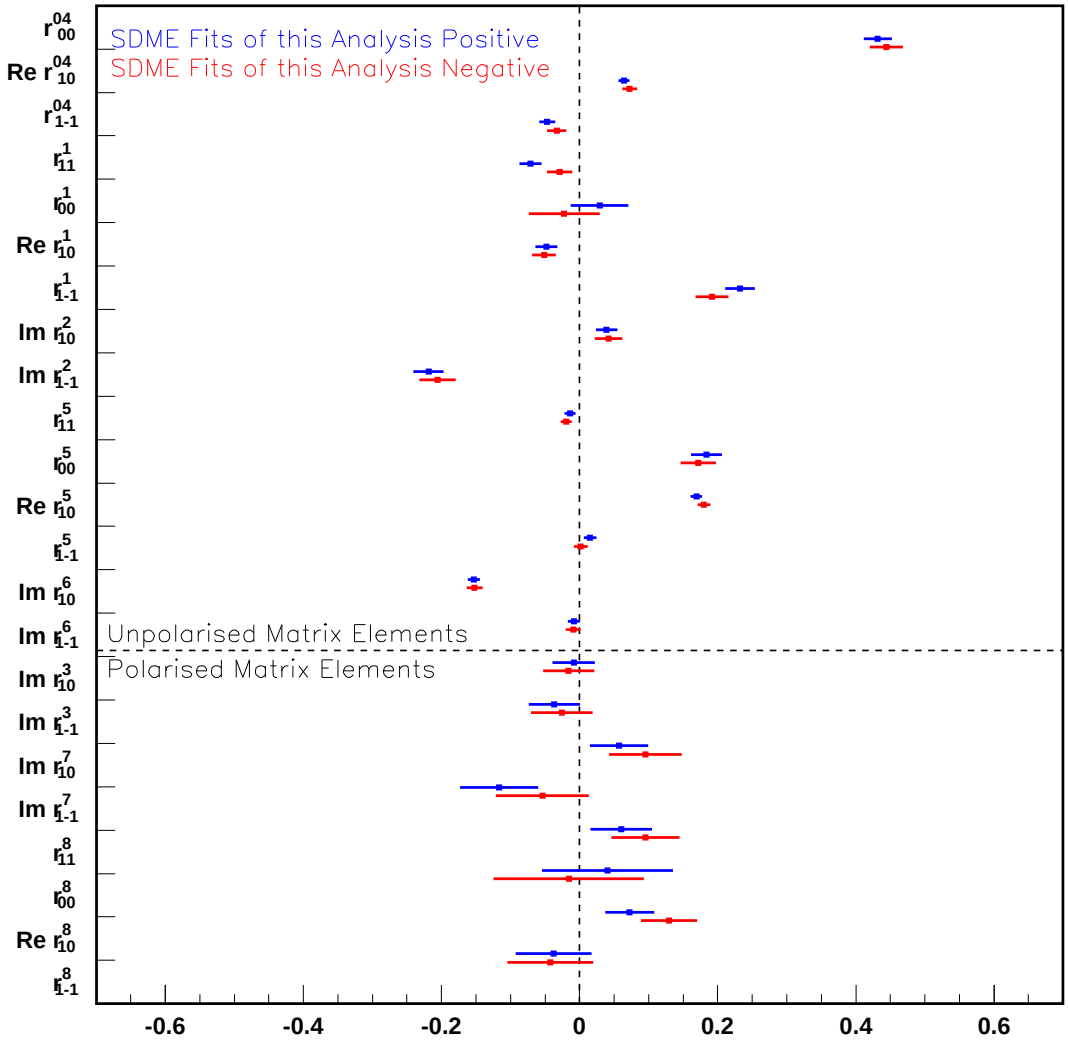

Figure 8.53: The 23 SDME's extracted separately from the positive and negative helicity samples for the incoherent deuterium 1996-2000 Data Sample. The error bars indicate statistical uncertainty only.

8.8.2 *s*-Channel Helicity Conservation

Figures 8.59, 8.60 and 8.61 show the verification of relations 8.12 as a function of Q^2 using the results for the 15 unpolarised SDME's. The data supports the validity of the relations in equation 8.12. The sum rule in equation 8.13 also appears reasonable for the data results obtained.

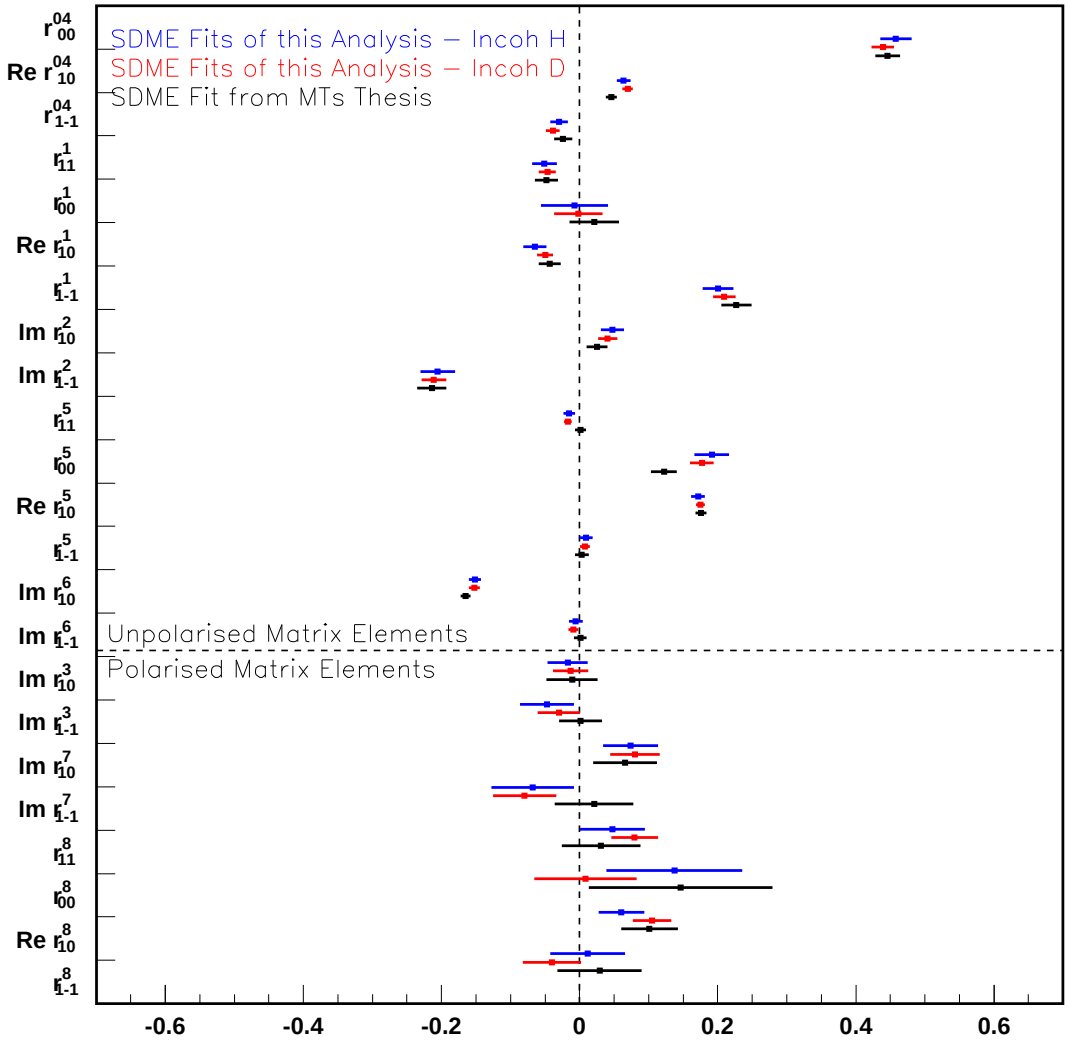

Figure 8.54: The combined values for the 23 SDME's extracted for the incoherent deuterium 1996-2000 Data Sample are compared here to the incoherent hydrogen 1996-2000 sample. The error bars indicate statistical uncertainty only. They are compared to results obtained in a previous analysis at HERMES on hydrogen [84].

8.8.3 Extraction of R_ρ

The results for R_ρ as a function of Q^2 is shown in figure 8.62. Here they are shown alongside those obtained in a previous HERMES analysis on hydrogen [84].

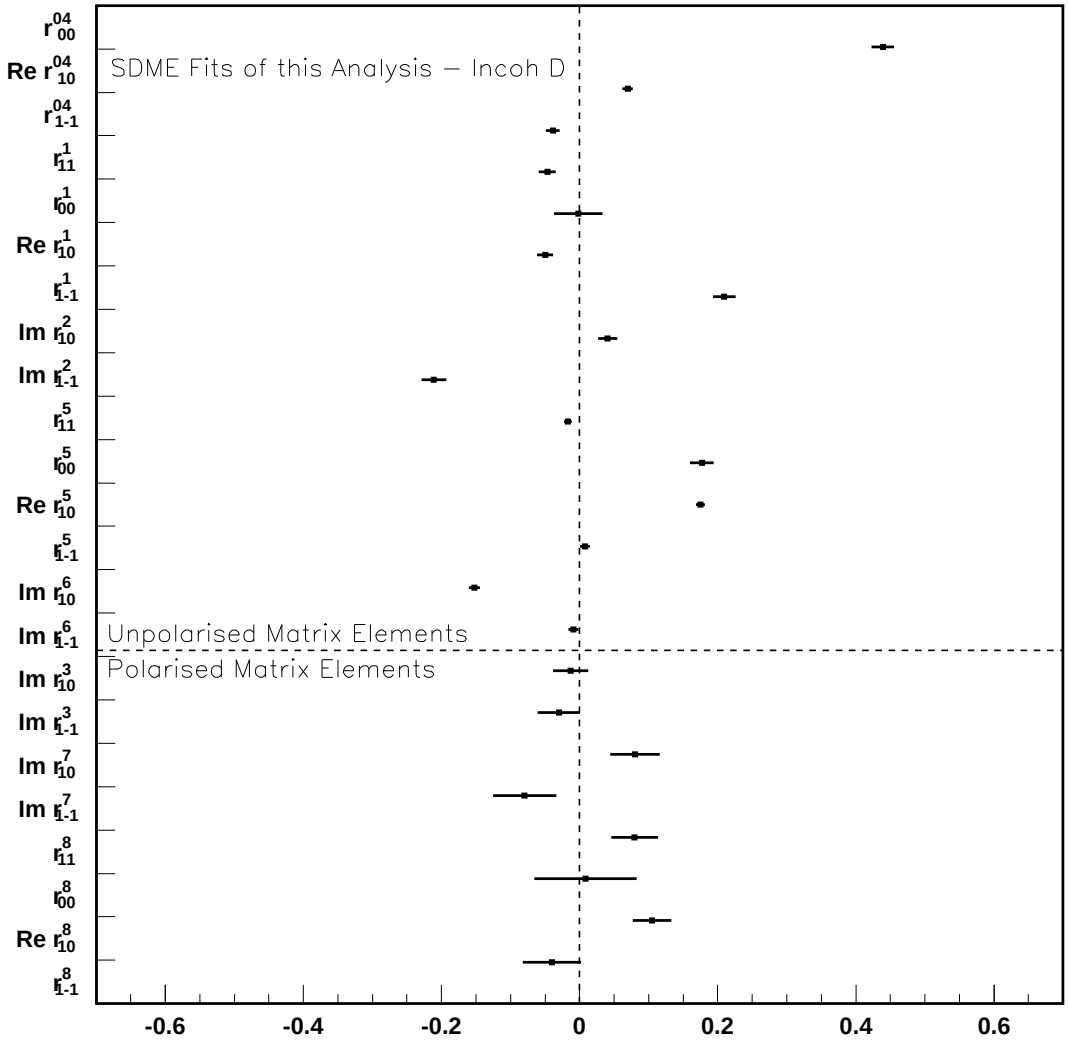

Figure 8.55: The combined values for the 23 SDME's extracted for the incoherent deuterium 1996-2000 Data Sample are shown here. The error bars indicate statistical uncertainty only.

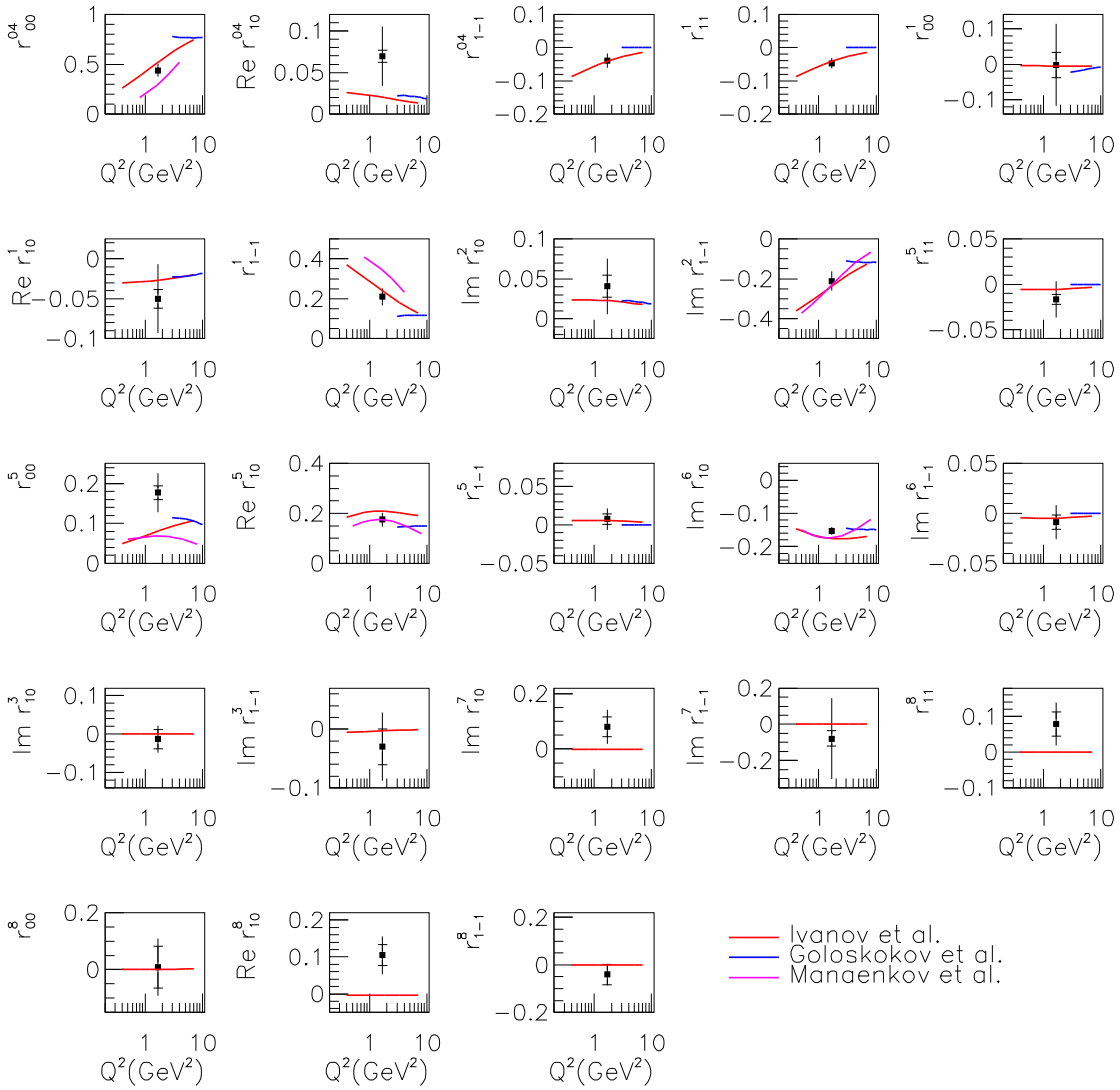

Figure 8.56: The 23 SDME's compared to theoretical model predictions for hydrogen for the combined incoherent deuterium 1996-2000 data sample. The inner error bars represent the statistical error and the outer bars the systematic error.

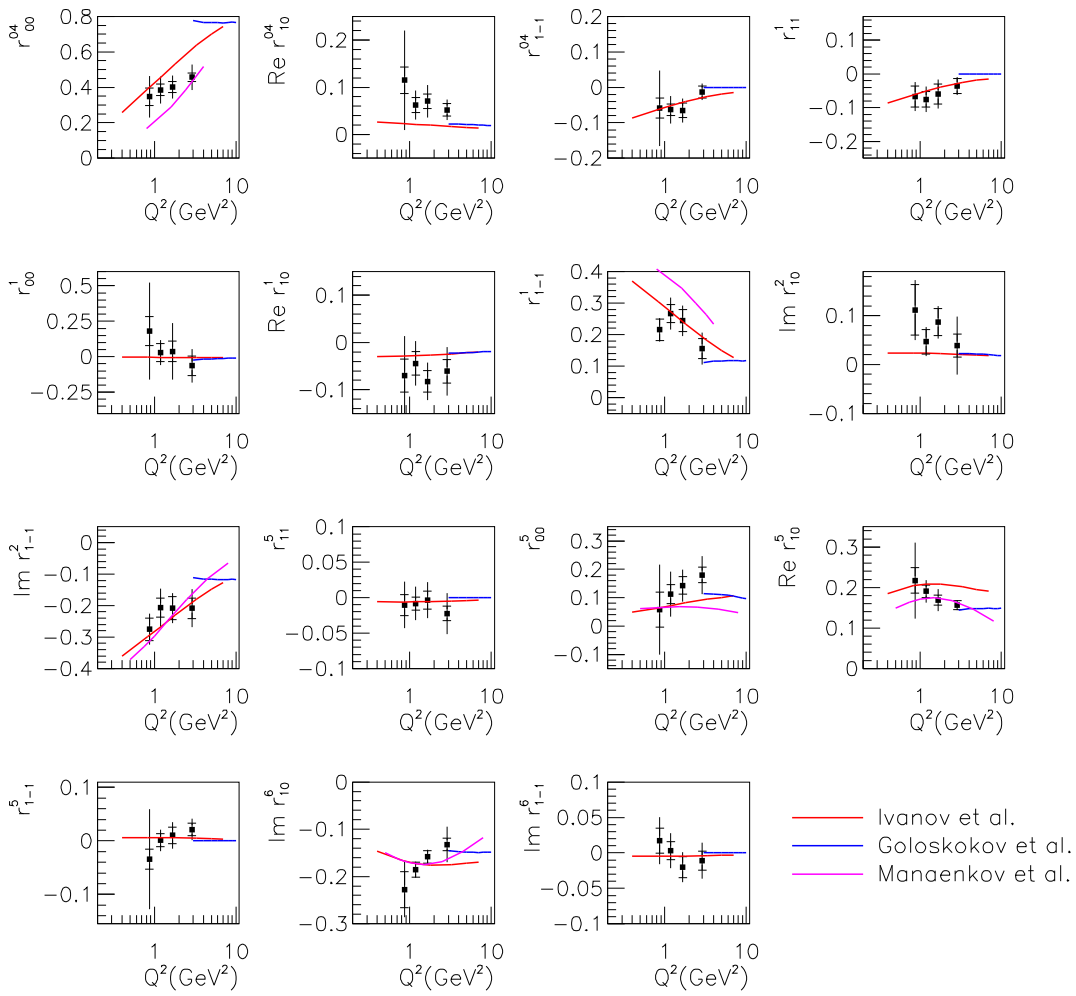

Figure 8.57: The 15 Unpolarised SDME's compared to theoretical model predictions for hydrogen for the incoherent deuterium 1996-2000 data sample. The inner error bars represent the statistical error and the outer bars the systematic error.

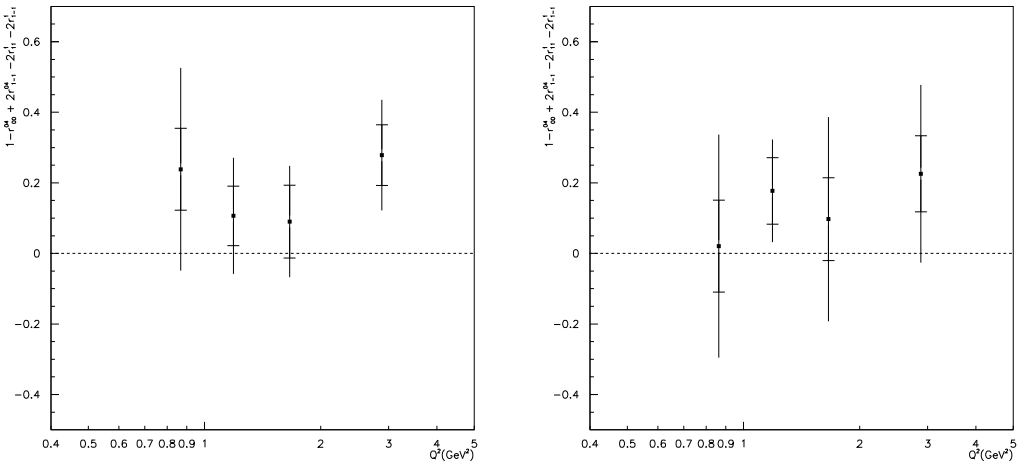

Figure 8.58: The verification of the natural parity exchange hypothesis by examining the validity of equation 8.11 as a function of Q^2 for the combined incoherent deuterium 1996-2000 data sample (left) and incoherent hydrogen 1996-2000 data sample (right). The inner error bars represent the statistical error and the outer bars the systematic error.

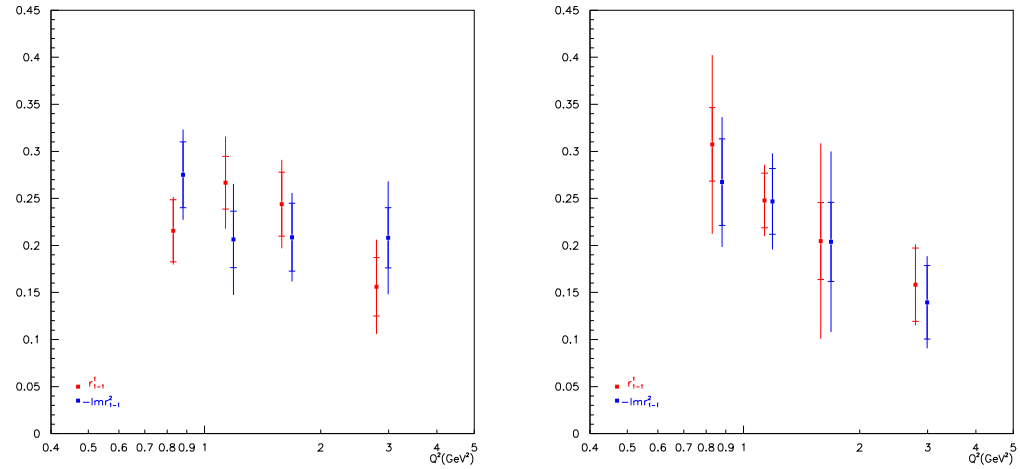

Figure 8.59: The verification of s-channel helicity by examining the relation $r^1_{1-1} = -r^2_{1-1}$ assumed in equation 8.12. Combined incoherent deuterium 1996-2000 data sample (left) and incoherent hydrogen 1996-2000 data sample (right). The inner error bars represent the statistical error and the outer bars the systematic error.

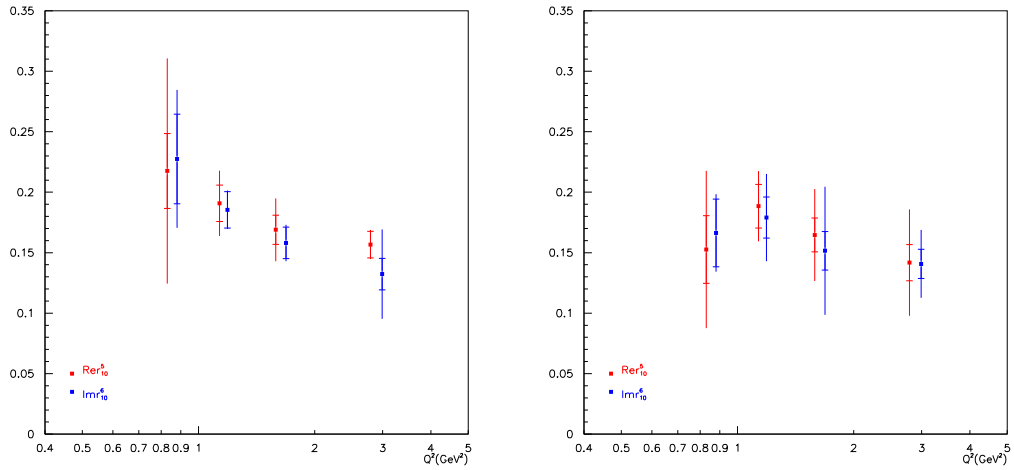

Figure 8.60: The verification of s-channel helicity by examining the relation Re r^5_{10} = $-$Im r^6_{10} assumed in equation 8.12. Combined incoherent deuterium 1996-2000 data sample (left) and incoherent hydrogen 1996-2000 data sample (right). The inner error bars represent the statistical error and the outer bars the systematic error.

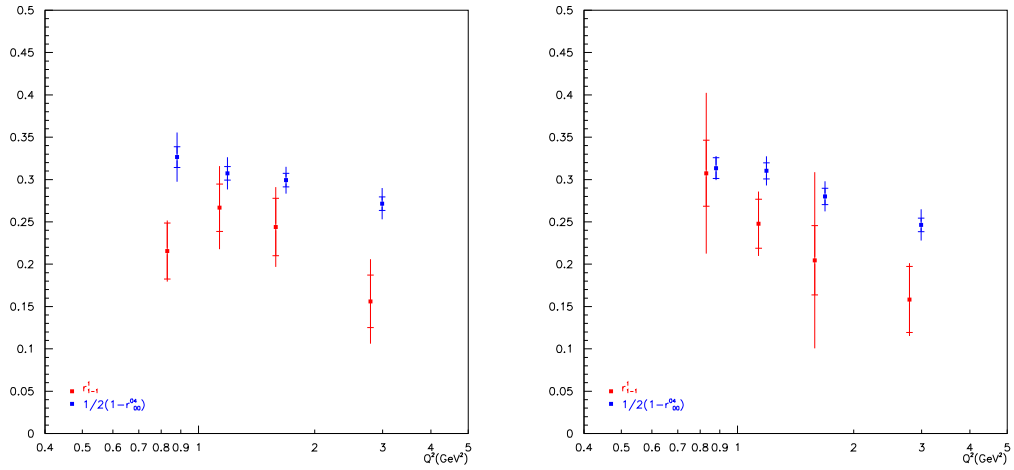

Figure 8.61: The verification of s-channel helicity assumed in equation 8.12 is examined. Note that for this relation equation 8.13 and NPE are assumed. combined incoherent deuterium 1996-2000 data sample (left) and incoherent hydrogen 1996-2000 data sample (right). The inner error bars represent the statistical error and the outer bars the systematic error.

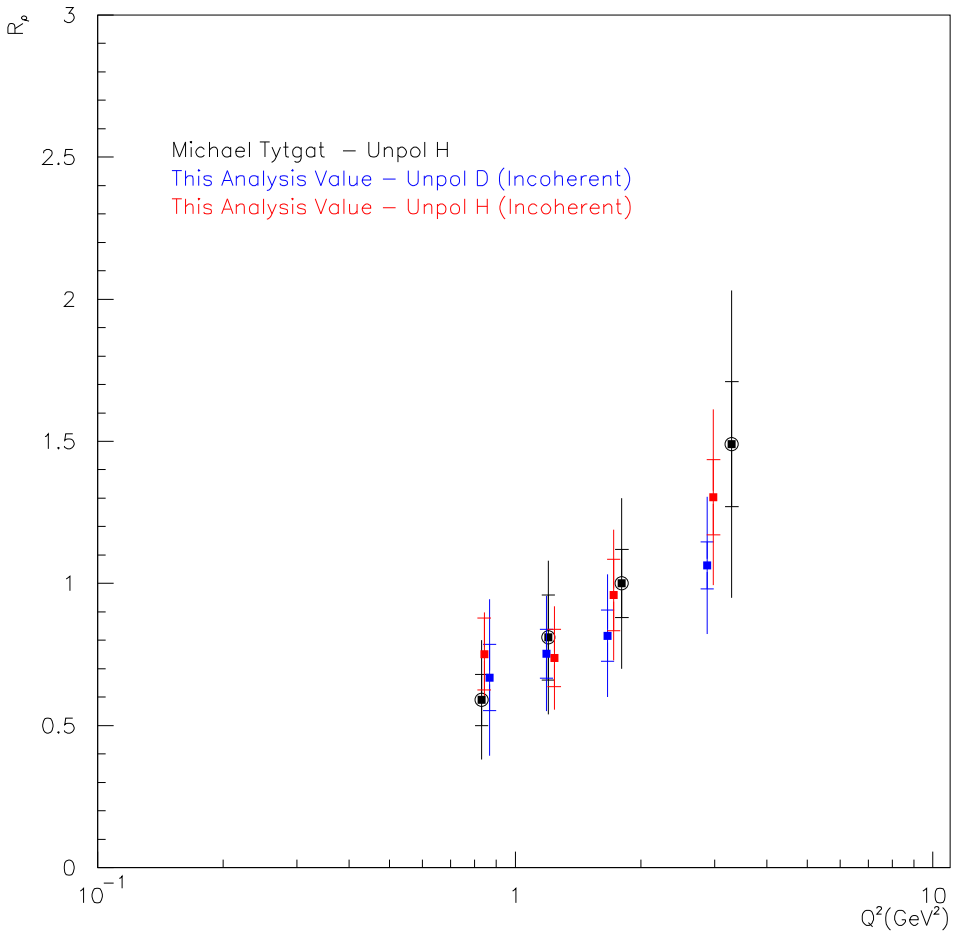

Figure 8.62: The measured values for R_ρ for the combined incoherent deuterium 1996-2000 data sample and the incoherent hydrogen 1996-2000 data sample are shown. The inner error bars represent the statistical error and the outer bars the systematic error.

8.9 World Data Comparison - $R_{\rho^0}(Q^2)$

In this section the results obtained for the 1996-2000 data samples for both hydrogen and deuterium are compared to data accumulated by other experiments around the world. The results plotted as a function of Q^2 for R_{ρ^0} are presented in figure 8.63 for the 1996-2000 hydrogen data sample and figure 8.64 for the 1996-2000 deuterium data sample. The values obtained in this analysis appear to be in very good agreement with results from other experiments and fit within the measured range of the other measurements.

The results for the hydrogen and deuterium samples also appear to be in good agreement with each other as a function of Q^2.

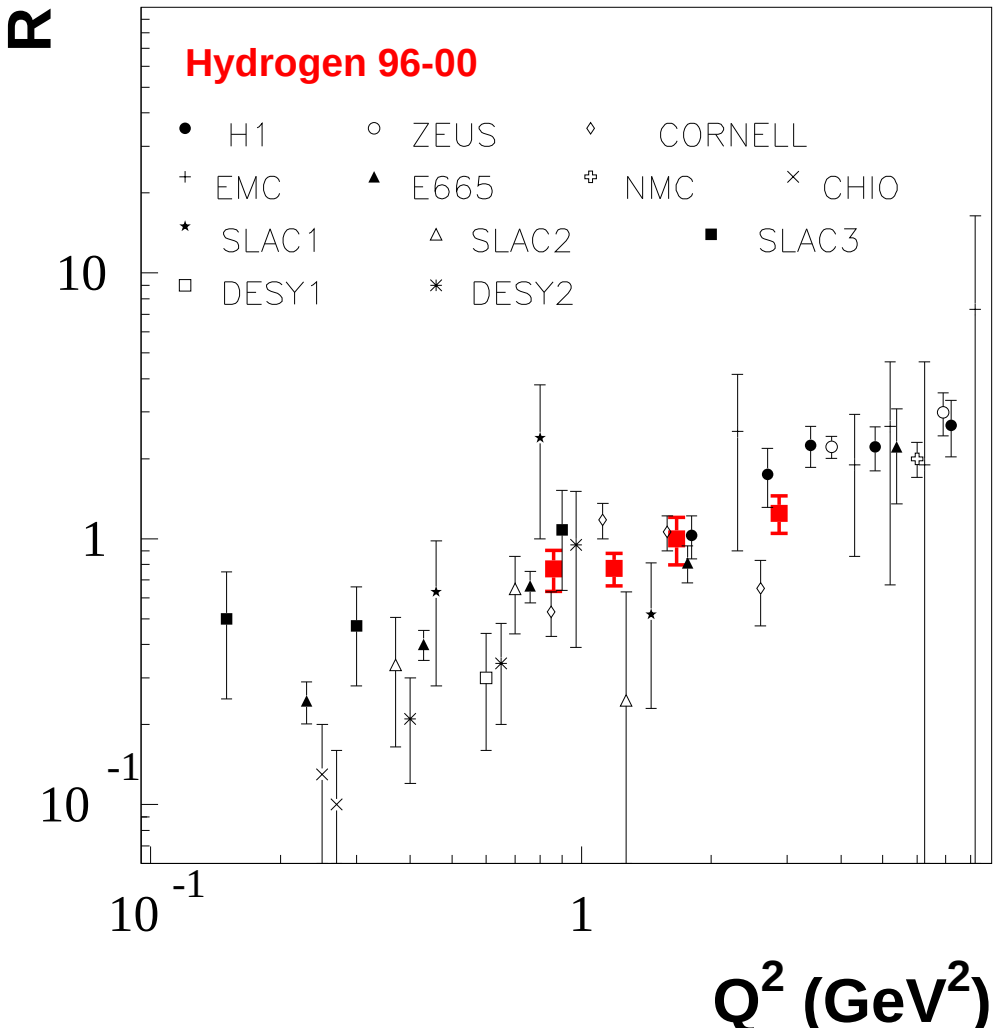

Figure 8.63: The longitudinal to transverse total ρ^0 production cross section ratio for the combined 1996-2000 hydrogen data sample plotted as a function of Q^2 with world data. Data are obtained at DESY (H1 -[117], ZEUS -[114], DESY1 -[118], DESY2 -[119]), at Cornell [103] and at SLAC (SLAC1 -[80], SLAC2 -[120], SLAC3 -[121]) in ep scattering and also in μp collision by E665 [122], NMC [123], EMC [124] and CHIO [125] collaborations. Total errors are depicted in this plot.

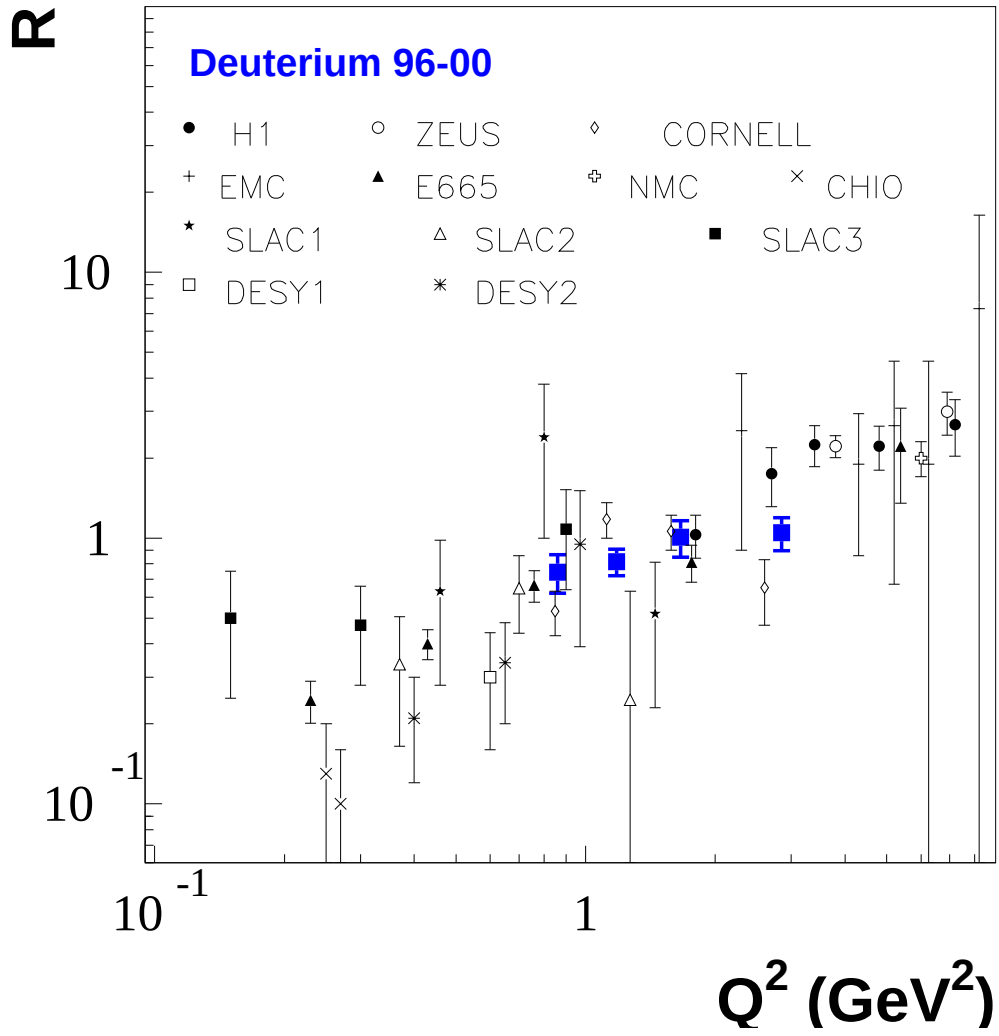

Figure 8.64: The longitudinal to transverse total ρ^0 production cross section ratio for the combined 1996-2000 deuterium data sample plotted as a function of Q^2 with world data. Data are obtained at DESY (H1 -[117], ZEUS -[114], DESY1 -[118], DESY2 -[119]), at Cornell [103] and at SLAC (SLAC1 -[80], SLAC2 -[120], SLAC3 -[121]) in ep scattering and also in μp collision by E665 [122], NMC [123], EMC [124] and CHIO [125] collaborations. Total errors are depicted in this plot.

Chapter 9

Conclusions

In this analysis the Spin Density Matrix Elements for the ρ^0 vector meson were extracted from both hydrogen and deuterium data samples. Initally a comparison was made with the 1996-97 hydrogen analysis [84] by M. Tytgat to ensure that the extraction method was reliable. Once this was achieved the analysis was extended to the 1998-2000 and the combined 1996-2000 hydrogen data samples. The 1996-2000 deuterium data sample was then analysed, first in the same t range as the 1996-2000 hydrogen data sample, and then in a modified t range to observe any t-dependence of the SDME's.

The 23 polarised SDME's were extracted for each of the data samples and compared to the theoretical model calculation by I.P Ivanov *et. al.* [126][116] which were tuned for HERMES kinematics [127]. Comparison was also made to the model of S.V Goloskokov *et. al.* [96] which were also tuned to be close to HERMES kinematics [128]. A third theoretical model was also used in the comparison and is by S.I Manayenkov *et. al.* [87] calculated for HERMES [129] for the 15 unpolarised SDME's only using a Regge based approach.

The calculations from Ivanov were originally performed for the H1 and ZEUS experiments and are based on the Pomeron (2-gluon) exchange. The theory lines presented for comparison here are calculated for the HERMES experiment at $< |t| >= 0.15$ GeV^2. Although the calculations are based on 2-gluon exchange, which is not expected to be valid at the HERMES experimental energy transfer region, the prediction appears to be in reasonable agreement with the results presented in this analysis. The SCHC violating matrix element r^5_{00} appears however to be underestimated by the model which may be due to neglected quark exchange [127]. The r^5_{00} matrix element violates SCHC and is non-zero. This is consistent with previous results from H1, ZEUS and HERMES and is predicted by both Ivanov and Manayenkovs' model predictions.

Under the hypothesis of SCHC all matrix elements except, r^{04}_{00}, r^1_{1-1}, Im r^2_{1-1}, Re r^5_{10} and Im r^6_{10}, Im r^7_{10} and Re r^8_{10}, are expected to be zero. These non-zero SDME's were observed in the data samples analysed for both hydrogen and deuterium targets.

The 15 unpolarised SDME's were extracted in 4 Q^2 bins which allowed the Q^2 dependence of the SDME's to be compared to the theoretical models described previously. In general there is good agreement between the behaviour of the matrix elements in Q^2 and the predictions of both Ivanov and Manayenkov. The predicted Q^2-dependence of the SCHC violating matrix element r^5_{00} also appears to be reproduced in this analysis.

The validity of the assumption of s-channel helity conservtion (SCHC) was also investigated in this analysis by comfirming that the relations assumed by SCHC, 8.11, are valid. This relation was analysed as a function of Q^2 for each data sample and appeared to confirm the assumption.

The assumption of Neutral Parity Exchange (NPE) was also investigated as a function of Q^2 and again, no clear indication for the non-validity of this assumption was found in

this analysis.

The ratio of longitudinal to transverse cross sections for the ρ^0, R_ρ was obtained in this analysis with good agreement to a previous analysis at HERMES [84]. A comparson with the value for R_ρ obtained in this analysis for both hydrogen and deuterium target agreed well with world data measured previously.

The SDME's obtained in the hydrogen and deuterium analysis appear to be in good agreement, with both samples producing similar results. This may be an indication that the coherent contribution ($t < 0.1$ GeV^2) of the deuterium data sample does not greatly alter the values extracted for the SDME's when analysed over the t-range used in this analysis.

The deuterium 1996-2000 data sample was analysed in a modified t-range to investigate any t-dependence of the SDME's. There appears to be a dependence in t for some of the matrix elements, in particular r^5_{00} seems to increase with increasing average t. Again the observed t-dependence of the matrix elements appears to be similar for both the hydrogen and deuterium data samples analysed.

The Recoil Detector which is soon to be commisioned in the HERMES front region is expected to bring improvements to the vector meson analysis presented in this thesis. The improved t-resolution of the Recoil Detector will be useful in examining, for example, the t-dependence of the SDME's more accurately than is currently possible. The increased statistics will also allow the accuracy of the measured SDME's to be improved which may allow for a more rigorous testing of theoretical models and hypotheses. Another possibility that the Recoil Detector may offer is the removal of the currently used ΔE cut which is used to remove the DIS background from the exclusive ρ^0 peak.

Appendix A

Data Sample Events

Year(helicity)	No. of Events.
96d0(+ve)	2082
97d0(+ve)	457
97d0(-ve)	3258
98d0(-ve)	323
00d0(+ve)	2290
00d0(-ve)	4249
96-00	12659

Table A.1: Number of ρ^0 events for hydrogen data samples used in this analysis.

Year(helicity)	No. of Events
96d0(+ve)	2333
97d0(+ve)	0
97d0(-ve)	2757
98d0(-ve)	2262
99c0(+ve)	1325
99c0(-ve)	1112
00d0(+ve)	5110
00d0(-ve)	5632
96-00	20531

Table A.2: Number of ρ^0 events for deuterium data samples used in this analysis.

Appendix B

DIS Background Contributions

Year	Pos. Hel. (%)	Neg. Hel. (%)	Q^2bin1 (%)	Q^2bin2 (%)	Q^2bin3 (%)	Q^2bin4 (%)
96/97	7.2±0.5	6.4±0.5	1.5±0.3	3.9±0.5	5.6±0.6	9.1±0.8
98/00	6.7±0.4	6.5±0.5	1.6±0.3	3.6±0.4	5.5±0.6	8.9±0.7
96-00	6.9±0.3	6.5±0.4	1.5±0.2	3.8±0.3	5.6±0.4	9.1±0.5

Table B.1: Contribution to the hydrogen data samples from DIS background calculated from the SIDIS Monte Carlo method.

Year	Pos. Hel. (%)	Neg. Hel. (%)	Q^2bin1 (%)	Q^2bin2 (%)	Q^2bin3 (%)	Q^2bin4 (%)
96-00	6.2±0.2	6.2±0.2	1.5±0.2	3.6±0.2	5.3±0.3	8.1±0.4

Table B.2: Contribution to the deuterium data sample from DIS background calculated from the SIDIS Monte Carlo method.

Appendix C

Vector Meson Spin Density Matrix Elements

Here the 23 vector meson spin density matrix elements are given in terms of the helicity amplitudes $T_{\lambda_V \lambda_\gamma}$. The expressions are derived from the equations listed in Appendix A in reference [82]. The nucleon helicities are omitted and we assume an implicit summation over them. The presentation of the elements shown below is adopted from [84].

$$r^{04}_{00} = \frac{1}{1+\epsilon R}\Big[\frac{1}{2N_T}(|T_{01}|^2 + |T_{0-1}|^2) + \frac{\epsilon R}{N_L}|T_{00}|^2\Big] \tag{C.1}$$

$$\text{Re } r^{04}_{10} = \frac{1}{1+\epsilon R}\text{Re}\Big[\frac{1}{2N_T}(T_{11}T^*_{01} + T_{1-1}T^*_{0-1}) + \frac{\epsilon R}{N_L}T_{10}T^*_{00}\Big] \tag{C.2}$$

$$r^{04}_{1-1} = \frac{1}{1+\epsilon R}\text{Re}\Big[\frac{1}{2N_T}(T_{11}T^*_{-11} + T_{1-1}T^*_{-1-1}) + \frac{\epsilon R}{N_L}T_{10}T^*_{-10}\Big] \tag{C.3}$$

$$r^{1}_{00} = \frac{1}{1+\epsilon R}\frac{1}{2N_T}(T_{0-1}T^*_{01} + T_{01}T^*_{0-1}) \tag{C.4}$$

$$r^{1}_{11} = \frac{1}{1+\epsilon R}\frac{1}{2N_T}(T_{1-1}T^*_{11} + T_{11}T^*_{1-1}) \tag{C.5}$$

$$\text{Re } r^{1}_{10} = \frac{1}{1+\epsilon R}\frac{1}{2N_T}\text{Re}(T_{1-1}T^*_{01} + T_{11}T^*_{0-1}) \tag{C.6}$$

$$r^{1}_{1-1} = \frac{1}{1+\epsilon R}\frac{1}{2N_T}\text{Re}(T_{1-1}T^*_{-11} + T_{11}T^*_{-1-1}) \tag{C.7}$$

$$\text{Im } r^{2}_{10} = \frac{1}{1+\epsilon R}\frac{1}{2N_T}\text{Re}(T_{1-1}T^*_{01} - T_{11}T^*_{0-1}) \tag{C.8}$$

$$\text{Im } r^{2}_{1-1} = \frac{1}{1+\epsilon R}\frac{1}{2N_T}\text{Re}(T_{1-1}T^*_{-11} - T_{11}T^*_{-1-1}) \tag{C.9}$$

$$\text{Im } r^{3}_{10} = \frac{1}{1+\epsilon R}\frac{1}{2N_T}\text{Im}(T_{11}T^*_{01} - T_{1-1}T^*_{0-1}) \tag{C.10}$$

$$\text{Im } r^{3}_{1-1} = \frac{1}{1+\epsilon R}\frac{1}{2N_T}\text{Im}(T_{11}T^*_{-11} - T_{1-1}T^*_{-1-1}) \tag{C.11}$$

$$r^{5}_{00} = \frac{\sqrt{R}}{1+\epsilon R}\frac{1}{\sqrt{2N_T N_L}}\frac{1}{2}(T_{00}T^*_{01} + T_{01}T^*_{00} - T_{00}T^*_{0-1} - T_{0-1}T^*_{00}) \tag{C.12}$$

$$r_{11}^{5} = \frac{\sqrt{R}}{1+\epsilon R}\frac{1}{\sqrt{2N_T N_L}}\frac{1}{2}(T_{10}T_{11}^{*} + T_{11}T_{10}^{*} - T_{10}T_{1-1}^{*} - T_{1-1}T_{10}^{*}) \tag{C.13}$$

$$\text{Re } r_{10}^{5} = \frac{\sqrt{R}}{1+\epsilon R}\frac{1}{\sqrt{2N_T N_L}}\frac{1}{2}\text{Re}(T_{10}T_{01}^{*} + T_{11}T_{00}^{*} - T_{10}T_{0-1}^{*} - T_{1-1}T_{00}^{*}) \tag{C.14}$$

$$r_{1-1}^{5} = \frac{\sqrt{R}}{1+\epsilon R}\frac{1}{\sqrt{2N_T N_L}}\frac{1}{2}(T_{10}T_{-11}^{*} + T_{11}T_{-10}^{*} - T_{10}T_{-1-1}^{*} - T_{1-1}T_{-10}^{*}) \tag{C.15}$$

$$\text{Im } r_{10}^{6} = \frac{\sqrt{R}}{1+\epsilon R}\frac{1}{\sqrt{2N_T N_L}}\frac{1}{2}\text{Re}(T_{10}T_{01}^{*} - T_{11}T_{00}^{*} + T_{10}T_{0-1}^{*} - T_{1-1}T_{00}^{*}) \tag{C.16}$$

$$\text{Im } r_{1-1}^{6} = \frac{\sqrt{R}}{1+\epsilon R}\frac{1}{\sqrt{2N_T N_L}}\frac{1}{2}\text{Re}(T_{10}T_{-11}^{*} - T_{11}T_{-10}^{*} + T_{10}T_{-1-1}^{*} - T_{1-1}T_{-10}^{*}) \tag{C.17}$$

$$\text{Im } r_{10}^{7} = \frac{\sqrt{R}}{1+\epsilon R}\frac{1}{\sqrt{2N_T N_L}}\frac{1}{2}\text{Im}(T_{10}T_{01}^{*} + T_{11}T_{00}^{*} + T_{10}T_{0-1}^{*} + T_{1-1}T_{00}^{*}) \tag{C.18}$$

$$\text{Im } r_{1-1}^{7} = \frac{\sqrt{R}}{1+\epsilon R}\frac{1}{\sqrt{2N_T N_L}}\frac{1}{2}\text{Im}(T_{10}T_{-11}^{*} + T_{11}T_{-10}^{*} + T_{10}T_{-1-1}^{*} + T_{1-1}T_{-10}^{*}) \tag{C.19}$$

$$r_{00}^{8} = \frac{\sqrt{R}}{1+\epsilon R}\frac{i}{\sqrt{2N_T N_L}}\frac{1}{2}(T_{00}T_{01}^{*} - T_{01}T_{00}^{*} - T_{00}T_{0-1}^{*} + T_{0-1}T_{00}^{*}) \tag{C.20}$$

$$r_{11}^{8} = \frac{\sqrt{R}}{1+\epsilon R}\frac{i}{\sqrt{2N_T N_L}}\frac{1}{2}(T_{10}T_{11}^{*} - T_{11}T_{10}^{*} - T_{10}T_{1-1}^{*} + T_{1-1}T_{10}^{*}) \tag{C.21}$$

$$\text{Re } r_{10}^{8} = -\frac{\sqrt{R}}{1+\epsilon R}\frac{1}{\sqrt{2N_T N_L}}\frac{1}{2}\text{Im}(T_{10}T_{01}^{*} - T_{11}T_{00}^{*} - T_{10}T_{0-1}^{*} + T_{1-1}T_{00}^{*}) \tag{C.22}$$

$$r_{1-1}^{8} = \frac{\sqrt{R}}{1+\epsilon R}\frac{i}{\sqrt{2N_T N_L}}\frac{1}{2}(T_{10}T_{-11}^{*} - T_{11}T_{-10}^{*} - T_{10}T_{-1-1}^{*} + T_{1-1}T_{-10}^{*}) \tag{C.23}$$

The ratio R of the longitudinal to transverse $\gamma^{*}p$ cross section and the two normalisation factors N_L and N_T are given by:

$$R = \frac{N_L}{N_T}, \tag{C.24}$$

$$N_L = |T_{00}|^2 + |T_{10}|^2 + |T_{-10}|^2, \tag{C.25}$$

$$N_T = \frac{1}{2}\big(|T_{11}|^2 + |T_{-1-1}|^2 + |T_{01}|^2 + |T_{0-1}|^2 + |T_{1-1}|^2 + |T_{-11}|^2\big). \tag{C.26}$$

Appendix D

Tabulated Results

Element	$< Q^2 > = 1.66$ GeV^2
r^{04}_{00}	0.456 ± 0.017 ± 0.039
Re r^{04}_{10}	0.043 ± 0.008 ± 0.015
r^{04}_{1-1}	-0.018 ± 0.011 ± 0.004
r^{1}_{11}	-0.019 ± 0.014 ± 0.027
r^{1}_{00}	-0.001 ± 0.035 ± 0.098
Re r^{1}_{10}	-0.053 ± 0.015 ± 0.010
r^{1}_{1-1}	0.226 ± 0.019 ± 0.014
Im r^{2}_{10}	0.039 ± 0.015 ± 0.025
Im r^{2}_{1-1}	-0.202 ± 0.021 ± 0.018
r^{5}_{11}	-0.015 ± 0.006 ± 0.012
r^{5}_{00}	0.144 ± 0.016 ± 0.025
Re r^{5}_{10}	0.159 ± 0.008 ± 0.014
r^{5}_{1-1}	0.007 ± 0.008 ± 0.005
Im r^{6}_{10}	-0.165 ± 0.007 ± 0.007
Im r^{6}_{1-1}	-0.010 ± 0.008 ± 0.012
Im r^{3}_{10}	-0.020 ± 0.025 ± 0.031
Im r^{3}_{1-1}	-0.047 ± 0.029 ± 0.023
Im r^{7}_{10}	0.100 ± 0.034 ± 0.064
Im r^{7}_{1-1}	-0.038 ± 0.054 ± 0.122
r^{8}_{11}	0.065 ± 0.045 ± 0.085
r^{8}_{00}	0.110 ± 0.083 ± 0.044
Re r^{8}_{10}	0.086 ± 0.033 ± 0.026
r^{8}_{1-1}	0.035 ± 0.048 ± 0.143

Table D.1: The 23 ρ^0 spin density matrix elements for the 1996/97 hydrogen data sample. The first errors are statistical, the second are systematic.

Element	$< Q^2 > = 0.86$ GeV^2	$< Q^2 > = 1.19$ GeV^2	$< Q^2 > = 1.66$ GeV^2	$< Q^2 > = 2.83$ GeV^2
r^{04}_{00}	0.378 ± 0.050 ± 0.074	0.404 ± 0.035 ± 0.028	0.443 ± 0.037 ± 0.034	0.511 ± 0.033 ± 0.041
Re r^{04}_{10}	0.030 ± 0.023 ± 0.008	0.027 ± 0.015 ± 0.011	0.077 ± 0.018 ± 0.011	0.020 ± 0.015 ± 0.004
r^{04}_{1-1}	-0.032 ± 0.030 ± 0.002	-0.042 ± 0.021 ± 0.024	-0.031 ± 0.023 ± 0.014	-0.004 ± 0.020 ± 0.019
r^{1}_{11}	0.021 ± 0.040 ± 0.099	-0.053 ± 0.028 ± 0.019	-0.027 ± 0.028 ± 0.001	0.0007 ± 0.029 ± 0.053
r^{1}_{00}	-0.090 ± 0.089 ± 0.258	0.056 ± 0.060 ± 0.021	-0.009 ± 0.073 ± 0.117	0.025 ± 0.081 ± 0.031
Re r^{1}_{10}	-0.025 ± 0.038 ± 0.050	-0.039 ± 0.024 ± 0.017	-0.076 ± 0.030 ± 0.034	-0.043 ± 0.029 ± 0.035
r^{1}_{1-1}	0.299 ± 0.051 ± 0.004	0.268 ± 0.033 ± 0.012	0.229 ± 0.040 ± 0.035	0.171 ± 0.038 ± 0.016
Im r^{2}_{10}	0.023 ± 0.039 ± 0.043	0.049 ± 0.025 ± 0.025	0.064 ± 0.028 ± 0.014	0.006 ± 0.032 ± 0.010
Im r^{2}_{1-1}	-0.270 ± 0.051 ± 0.044	-0.236 ± 0.037 ± 0.023	-0.197 ± 0.042 ± 0.038	-0.163 ± 0.041 ± 0.016
r^{5}_{11}	-0.045 ± 0.021 ± 0.027	0.0003 ± 0.010 ± 0.015	0.004 ± 0.014 ± 0.006	-0.025 ± 0.012 ± 0.013
r^{5}_{00}	0.118 ± 0.046 ± 0.080	0.089 ± 0.030 ± 0.024	0.076 ± 0.038 ± 0.033	0.209 ± 0.034 ± 0.031
Re r^{5}_{10}	0.169 ± 0.026 ± 0.009	0.158 ± 0.015 ± 0.020	0.145 ± 0.016 ± 0.008	0.130 ± 0.016 ± 0.021
r^{5}_{1-1}	-0.020 ± 0.025 ± 0.0003	0.004 ± 0.013 ± 0.004	-0.005 ± 0.019 ± 0.024	0.036 ± 0.015 ± 0.025
Im r^{6}_{10}	-0.180 ± 0.029 ± 0.011	-0.177 ± 0.014 ± 0.017	-0.151 ± 0.015 ± 0.008	-0.134 ± 0.016 ± 0.007
Im r^{6}_{1-1}	-0.035 ± 0.021 ± 0.005	-0.0001 ± 0.012 ± 0.007	0.009 ± 0.017 ± 0.004	-0.020 ± 0.015 ± 0.017

Table D.2: The 15 unpolarised SDME for different bins in Q^2 for the 1996/97 hydrogen data sample. The first errors are statistical the second systematic.

Element	$< Q^2 > = 1.66$ GeV^2
r^{04}_{00}	0.436 ± 0.029 ± 0.048
Re r^{04}_{10}	0.052 ± 0.012 ± 0.010
r^{04}_{1-1}	-0.028 ± 0.014 ± 0.028
r^{1}_{11}	-0.047 ± 0.012 ± 0.058
r^{1}_{00}	0.038 ± 0.042 ± 0.078
Re r^{1}_{10}	-0.046 ± 0.021 ± 0.012
r^{1}_{1-1}	0.196 ± 0.033 ± 0.045
Im r^{2}_{10}	0.031 ± 0.020 ± 0.024
Im r^{2}_{1-1}	-0.216 ± 0.028 ± 0.016
r^{5}_{11}	-0.015 ± 0.009 ± 0.015
r^{5}_{00}	0.134 ± 0.019 ± 0.042
Re r^{5}_{10}	0.177 ± 0.011 ± 0.010
r^{5}_{1-1}	0.011 ± 0.008 ± 0.013
Im r^{6}_{10}	-0.141 ± 0.010 ± 0.010
Im r^{6}_{1-1}	-0.004 ± 0.011 ± 0.011
Im r^{3}_{10}	-0.036 ± 0.035 ± 0.016
Im r^{3}_{1-1}	-0.026 ± 0.045 ± 0.007
Im r^{7}_{10}	0.016 ± 0.053 ± 0.036
Im r^{7}_{1-1}	-0.094 ± 0.080 ± 0.061
r^{8}_{11}	-0.015 ± 0.037 ± 0.015
r^{8}_{00}	0.141 ± 0.106 ± 0.052
Re r^{8}_{10}	0.087 ± 0.044 ± 0.015
r^{8}_{1-1}	-0.024 ± 0.067 ± 0.038

Table D.3: The 23 ρ^0 spin density matrix elements for the 1998-00 hydrogen data sample. The first errors are statistical, the second are systematic.

Element	$< Q^2 > = 0.86$ GeV^2	$< Q^2 > = 1.19$ GeV^2	$< Q^2 > = 1.66$ GeV^2	$< Q^2 > = 2.87$ GeV^2
r^{04}_{00}	0.378 ± 0.047 ± 0.011	0.370 ± 0.027 ± 0.027	0.440 ± 0.034 ± 0.057	0.470 ± 0.027 ± 0.039
Re r^{04}_{10}	0.034 ± 0.019 ± 0.022	0.047 ± 0.014 ± 0.014	0.045 ± 0.015 ± 0.015	0.037 ± 0.015 ± 0.006
r^{04}_{1-1}	-0.044 ± 0.031 ± 0.048	-0.023 ± 0.019 ± 0.015	-0.058 ± 0.022 ± 0.009	0.008 ± 0.021 ± 0.008
r^{1}_{11}	-0.065 ± 0.039 ± 0.065	-0.042 ± 0.026 ± 0.028	-0.050 ± 0.028 ± 0.006	-0.012 ± 0.030 ± 0.016
r^{1}_{00}	0.059 ± 0.080 ± 0.039	0.019 ± 0.062 ± 0.061	-0.042 ± 0.073 ± 0.005	0.033 ± 0.079 ± 0.049
Re r^{1}_{10}	-0.018 ± 0.031 ± 0.039	-0.050 ± 0.028 ± 0.013	-0.052 ± 0.025 ± 0.022	0.011 ± 0.029 ± 0.016
r^{1}_{1-1}	0.313 ± 0.041 ± 0.050	0.231 ± 0.032 ± 0.030	0.186 ± 0.037 ± 0.143	0.195 ± 0.035 ± 0.027
Im r^{2}_{10}	0.041 ± 0.034 ± 0.020	0.023 ± 0.024 ± 0.008	0.079 ± 0.029 ± 0.048	0.005 ± 0.028 ± 0.022
Im r^{2}_{1-1}	-0.266 ± 0.043 ± 0.011	-0.234 ± 0.028 ± 0.031	-0.165 ± 0.037 ± 0.086	-0.201 ± 0.033 ± 0.005
r^{5}_{11}	-0.021 ± 0.016 ± 0.007	-0.014 ± 0.010 ± 0.008	-0.011 ± 0.012 ± 0.008	-0.002 ± 0.013 ± 0.011
r^{5}_{00}	0.133 ± 0.041 ± 0.054	0.109 ± 0.030 ± 0.030	0.116 ± 0.035 ± 0.018	0.108 ± 0.034 ± 0.021
Re r^{5}_{10}	0.158 ± 0.019 ± 0.029	0.181 ± 0.012 ± 0.007	0.179 ± 0.014 ± 0.042	0.133 ± 0.014 ± 0.002
r^{5}_{1-1}	0.007 ± 0.019 ± 0.013	0.009 ± 0.013 ± 0.017	-0.004 ± 0.016 ± 0.005	0.030 ± 0.015 ± 0.006
Im r^{6}_{10}	-0.139 ± 0.021 ± 0.050	-0.145 ± 0.013 ± 0.002	-0.138 ± 0.015 ± 0.020	-0.132 ± 0.014 ± 0.011
Im r^{6}_{1-1}	-0.010 ± 0.020 ± 0.009	-0.007 ± 0.013 ± 0.011	-0.011 ± 0.014 ± 0.015	-0.004 ± 0.015 ± 0.024

Table D.4: The 15 unpolarised SDME for different bins in Q^2 for the 1998-00 hydrogen data sample. The first errors are statistical the second systematic.

Element	$< Q^2 > = 1.64$ GeV^2
r^{04}_{00}	0.448 ± 0.015 ± 0.049
Re r^{04}_{10}	0.049 ± 0.006 ± 0.013
r^{04}_{1-1}	-0.021 ± 0.009 ± 0.016
r^{1}_{11}	-0.034 ± 0.013 ± 0.032
r^{1}_{00}	0.019 ± 0.031 ± 0.063
Re r^{1}_{10}	-0.050 ± 0.011 ± 0.008
r^{1}_{1-1}	0.215 ± 0.015 ± 0.021
Im r^{2}_{10}	0.038 ± 0.011 ± 0.005
Im r^{2}_{1-1}	-0.205 ± 0.016 ± 0.019
r^{5}_{11}	-0.018 ± 0.005 ± 0.012
r^{5}_{00}	0.141 ± 0.015 ± 0.031
Re r^{5}_{10}	0.171 ± 0.007 ± 0.008
r^{5}_{1-1}	0.011 ± 0.006 ± 0.009
Im r^{6}_{10}	-0.156 ± 0.006 ± 0.003
Im r^{6}_{1-1}	-0.008 ± 0.006 ± 0.011
Im r^{3}_{10}	-0.024 ± 0.019 ± 0.011
Im r^{3}_{1-1}	-0.041 ± 0.028 ± 0.026
Im r^{7}_{10}	0.074 ± 0.027 ± 0.030
Im r^{7}_{1-1}	-0.063 ± 0.035 ± 0.074
r^{8}_{11}	0.022 ± 0.027 ± 0.026
r^{8}_{00}	0.119 ± 0.065 ± 0.026
Re r^{8}_{10}	0.080 ± 0.024 ± 0.015
r^{8}_{1-1}	-0.0002 ± 0.033 ± 0.045

Table D.5: The 23 ρ^0 spin density matrix elements for the 1996-2000 hydrogen data sample. The first errors are statistical, the second are systematic.

Element	$< Q^2 > = 0.86$ GeV^2	$< Q^2 > = 1.19$ GeV^2	$< Q^2 > = 1.66$ GeV^2	$< Q^2 > = 2.85$ GeV^2
r^{04}_{00}	0.379 ± 0.033 ± 0.042	0.390 ± 0.025 ± 0.030	0.450 ± 0.025 ± 0.055	0.496 ± 0.022 ± 0.045
Re r^{04}_{10}	0.032 ± 0.013 ± 0.016	0.040 ± 0.010 ± 0.013	0.061 ± 0.011 ± 0.008	0.030 ± 0.010 ± 0.006
r^{04}_{1-1}	-0.036 ± 0.020 ± 0.026	-0.031 ± 0.014 ± 0.002	-0.044 ± 0.016 ± 0.009	0.001 ± 0.011 ± 0.013
r^{1}_{11}	-0.028 ± 0.026 ± 0.073	-0.046 ± 0.021 ± 0.009	-0.037 ± 0.021 ± 0.001	-0.005 ± 0.021 ± 0.035
r^{1}_{00}	-0.011 ± 0.055 ± 0.139	0.039 ± 0.047 ± 0.016	-0.029 ± 0.054 ± 0.058	0.030 ± 0.050 ± 0.018
Re r^{1}_{10}	-0.021 ± 0.024 ± 0.042	-0.046 ± 0.016 ± 0.013	-0.065 ± 0.019 ± 0.003	-0.015 ± 0.021 ± 0.021
r^{1}_{1-1}	0.303 ± 0.029 ± 0.025	0.249 ± 0.023 ± 0.012	0.204 ± 0.029 ± 0.089	0.182 ± 0.027 ± 0.015
Im r^{2}_{10}	0.033 ± 0.022 ± 0.029	0.033 ± 0.017 ± 0.018	0.069 ± 0.018 ± 0.017	0.006 ± 0.021 ± 0.011
Im r^{2}_{1-1}	-0.267 ± 0.033 ± 0.030	-0.228 ± 0.026 ± 0.026	-0.178 ± 0.028 ± 0.064	-0.175 ± 0.027 ± 0.010
r^{5}_{11}	-0.030 ± 0.012 ± 0.014	-0.009 ± 0.008 ± 0.008	-0.006 ± 0.009 ± 0.009	-0.016 ± 0.008 ± 0.014
r^{5}_{00}	0.127 ± 0.030 ± 0.066	0.102 ± 0.023 ± 0.017	0.103 ± 0.024 ± 0.030	0.159 ± 0.022 ± 0.030
Re r^{5}_{10}	0.161 ± 0.016 ± 0.012	0.172 ± 0.010 ± 0.012	0.163 ± 0.010 ± 0.017	0.133 ± 0.010 ± 0.007
r^{5}_{1-1}	-0.002 ± 0.015 ± 0.008	0.007 ± 0.009 ± 0.010	-0.004 ± 0.011 ± 0.013	0.034 ± 0.011 ± 0.013
Im r^{6}_{10}	-0.155 ± 0.015 ± 0.032	-0.159 ± 0.009 ± 0.009	-0.142 ± 0.010 ± 0.005	-0.134 ± 0.010 ± 0.009
Im r^{6}_{1-1}	-0.020 ± 0.015 ± 0.001	-0.005 ± 0.010 ± 0.010	-0.002 ± 0.011 ± 0.010	-0.015 ± 0.011 ± 0.020

Table D.6: The 15 unpolarised SDME for different bins in Q^2 for the 1996-2000 hydrogen data sample. The first errors are statistical the second systematic.

Element	$< Q^2 > = 1.64$ GeV^2
r^{04}_{00}	0.443 ± 0.010 ± 0.046
Re r^{04}_{10}	0.043 ± 0.004 ± 0.017
r^{04}_{1-1}	-0.022 ± 0.006 ± 0.005
r^{1}_{11}	-0.022 ± 0.008 ± 0.002
r^{1}_{00}	-0.004 ± 0.021 ± 0.053
Re r^{1}_{10}	-0.031 ± 0.008 ± 0.010
r^{1}_{1-1}	0.229 ± 0.011 ± 0.022
Im r^{2}_{10}	0.026 ± 0.008 ± 0.005
Im r^{2}_{1-1}	-0.215 ± 0.011 ± 0.019
r^{5}_{11}	-0.018 ± 0.003 ± 0.012
r^{5}_{00}	0.133 ± 0.010 ± 0.030
Re r^{5}_{10}	0.168 ± 0.004 ± 0.018
r^{5}_{1-1}	0.008 ± 0.004 ± 0.011
Im r^{6}_{10}	-0.150 ± 0.004 ± 0.006
Im r^{6}_{1-1}	-0.016 ± 0.004 ± 0.006
Im r^{3}_{10}	0.014 ± 0.015 ± 0.007
Im r^{3}_{1-1}	-0.024 ± 0.019 ± 0.003
Im r^{7}_{10}	0.111 ± 0.021 ± 0.015
Im r^{7}_{1-1}	-0.043 ± 0.030 ± 0.062
r^{8}_{11}	0.056 ± 0.025 ± 0.017
r^{8}_{00}	0.050 ± 0.051 ± 0.012
Re r^{8}_{10}	0.097 ± 0.018 ± 0.018
r^{8}_{1-1}	-0.042 ± 0.029 ± 0.012

Table D.7: The 23 ρ^0 spin density matrix elements for the 1996-2000 deuterium data sample. The first errors are statistical, the second are systematic.

Element	$< Q^2 > = 0.86$ GeV^2	$< Q^2 > = 1.18$ GeV^2	$< Q^2 > = 1.66$ GeV^2	$< Q^2 > = 2.85$ GeV^2
r^{04}_{00}	0.370 ± 0.023 ± 0.018	0.403 ± 0.018 ± 0.027	0.453 ± 0.020 ± 0.042	0.451 ± 0.014 ± 0.041
Re r^{04}_{10}	0.028 ± 0.009 ± 0.043	0.043 ± 0.009 ± 0.012	0.038 ± 0.008 ± 0.011	0.028 ± 0.008 ± 0.012
r^{04}_{1-1}	-0.032 ± 0.014 ± 0.032	-0.017 ± 0.012 ± 0.006	-0.043 ± 0.012 ± 0.013	-0.009 ± 0.010 ± 0.006
r^{1}_{11}	-0.049 ± 0.017 ± 0.014	-0.019 ± 0.015 ± 0.007	-0.020 ± 0.017 ± 0.009	-0.026 ± 0.012 ± 0.005
r^{1}_{00}	0.105 ± 0.038 ± 0.073	-0.034 ± 0.036 ± 0.037	-0.023 ± 0.043 ± 0.085	-0.002 ± 0.036 ± 0.057
Re r^{1}_{10}	0.001 ± 0.016 ± 0.035	-0.020 ± 0.013 ± 0.026	-0.048 ± 0.015 ± 0.005	-0.040 ± 0.015 ± 0.004
r^{1}_{1-1}	0.280 ± 0.019 ± 0.024	0.262 ± 0.018 ± 0.032	0.209 ± 0.022 ± 0.013	0.193 ± 0.021 ± 0.079
Im r^{2}_{10}	0.040 ± 0.016 ± 0.007	0.021 ± 0.014 ± 0.004	0.060 ± 0.015 ± 0.017	-0.007 ± 0.017 ± 0.026
Im r^{2}_{1-1}	-0.291 ± 0.025 ± 0.029	-0.234 ± 0.020 ± 0.024	-0.187 ± 0.021 ± 0.032	-0.197 ± 0.018 ± 0.010
r^{5}_{11}	-0.014 ± 0.009 ± 0.013	-0.006 ± 0.006 ± 0.006	-0.011 ± 0.007 ± 0.008	-0.024 ± 0.007 ± 0.013
r^{5}_{00}	0.071 ± 0.016 ± 0.035	0.107 ± 0.017 ± 0.015	0.144 ± 0.019 ± 0.023	0.141 ± 0.019 ± 0.029
Re r^{5}_{10}	0.163 ± 0.009 ± 0.051	0.171 ± 0.008 ± 0.018	0.157 ± 0.008 ± 0.008	0.153 ± 0.007 ± 0.005
r^{5}_{1-1}	-0.011 ± 0.011 ± 0.042	0.008 ± 0.008 ± 0.010	0.008 ± 0.008 ± 0.011	0.027 ± 0.008 ± 0.016
Im r^{6}_{10}	-0.175 ± 0.009 ± 0.010	-0.157 ± 0.007 ± 0.008	-0.144 ± 0.008 ± 0.002	-0.125 ± 0.008 ± 0.011
Im r^{6}_{1-1}	0.004 ± 0.010 ± 0.003	-0.008 ± 0.007 ± 0.005	-0.023 ± 0.008 ± 0.006	-0.017 ± 0.008 ± 0.014

Table D.8: The 15 unpolarised SDME for different bins in Q^2 for the 1996-2000 deuterium data sample. The first errors are statistical the second systematic.

Element	$< Q^2 > = 1.68$ GeV^2
r^{04}_{00}	0.439 ± 0.016 ± 0.046
Re r^{04}_{10}	0.069 ± 0.007 ± 0.028
r^{04}_{1-1}	-0.038 ± 0.009 ± 0.011
r^{1}_{11}	-0.046 ± 0.012 ± 0.003
r^{1}_{00}	-0.001 ± 0.035 ± 0.079
Re r^{1}_{10}	-0.049 ± 0.011 ± 0.031
r^{1}_{1-1}	0.209 ± 0.016 ± 0.026
Im r^{2}_{10}	0.040 ± 0.013 ± 0.021
Im r^{2}_{1-1}	-0.211 ± 0.017 ± 0.031
r^{5}_{11}	-0.016 ± 0.005 ± 0.014
r^{5}_{00}	0.176 ± 0.017 ± 0.031
Re r^{5}_{10}	0.175 ± 0.006 ± 0.021
r^{5}_{1-1}	0.007 ± 0.006 ± 0.007
Im r^{6}_{10}	-0.152 ± 0.007 ± 0.004
Im r^{6}_{1-1}	-0.008 ± 0.007 ± 0.009
Im r^{3}_{10}	-0.013 ± 0.025 ± 0.009
Im r^{3}_{1-1}	-0.030 ± 0.030 ± 0.027
Im r^{7}_{10}	0.080 ± 0.035 ± 0.026
Im r^{7}_{1-1}	-0.079 ± 0.046 ± 0.176
r^{8}_{11}	0.079 ± 0.033 ± 0.026
r^{8}_{00}	0.008 ± 0.073 ± 0.026
Re r^{8}_{10}	0.104 ± 0.027 ± 0.023
r^{8}_{1-1}	-0.040 ± 0.042 ± 0.002

Table D.9: The 23 ρ^0 spin density matrix elements for the 1996-2000 incoherent deuterium data sample. The first errors are statistical, the second are systematic.

Element	$< Q^2 > = 0.87$ GeV^2	$< Q^2 > = 1.19$ GeV^2	$< Q^2 > = 1.66$ GeV^2	$< Q^2 > = 2.88$ GeV^2
r^{04}_{00}	0.347 ± 0.049 ± 0.067	0.385 ± 0.032 ± 0.044	0.401 ± 0.032 ± 0.031	0.457 ± 0.024 ± 0.046
Re r^{04}_{10}	0.115 ± 0.028 ± 0.076	0.062 ± 0.015 ± 0.014	0.070 ± 0.014 ± 0.019	0.052 ± 0.012 ± 0.009
r^{04}_{1-1}	-0.058 ± 0.027 ± 0.078	-0.063 ± 0.016 ± 0.022	-0.065 ± 0.020 ± 0.013	-0.012 ± 0.016 ± 0.006
r^{1}_{11}	-0.067 ± 0.031 ± 0.011	-0.075 ± 0.022 ± 0.014	-0.060 ± 0.029 ± 0.013	-0.036 ± 0.022 ± 0.004
r^{1}_{00}	0.180 ± 0.102 ± 0.240	0.028 ± 0.064 ± 0.023	0.037 ± 0.070 ± 0.129	-0.064 ± 0.068 ± 0.051
Re r^{1}_{10}	-0.070 ± 0.034 ± 0.049	-0.044 ± 0.024 ± 0.022	-0.082 ± 0.022 ± 0.016	-0.061 ± 0.024 ± 0.026
r^{1}_{1-1}	0.215 ± 0.033 ± 0.003	0.266 ± 0.028 ± 0.021	0.243 ± 0.034 ± 0.013	0.156 ± 0.031 ± 0.019
Im r^{2}_{10}	0.111 ± 0.051 ± 0.009	0.046 ± 0.024 ± 0.004	0.086 ± 0.027 ± 0.005	0.038 ± 0.023 ± 0.035
Im r^{2}_{1-1}	-0.275 ± 0.035 ± 0.013	-0.206 ± 0.030 ± 0.029	-0.208 ± 0.036 ± 0.011	-0.208 ± 0.032 ± 0.028
r^{5}_{11}	-0.010 ± 0.014 ± 0.017	-0.008 ± 0.009 ± 0.014	-0.003 ± 0.012 ± 0.012	-0.022 ± 0.010 ± 0.018
r^{5}_{00}	0.057 ± 0.062 ± 0.097	0.113 ± 0.033 ± 0.045	0.143 ± 0.030 ± 0.025	0.180 ± 0.027 ± 0.040
Re r^{5}_{10}	0.217 ± 0.031 ± 0.062	0.190 ± 0.015 ± 0.012	0.168 ± 0.012 ± 0.014	0.156 ± 0.011 ± 0.001
r^{5}_{1-1}	-0.030 ± 0.018 ± 0.074	0.0008 ± 0.012 ± 0.008	0.010 ± 0.015 ± 0.009	0.021 ± 0.011 ± 0.008
Im r^{6}_{10}	-0.227 ± 0.037 ± 0.020	-0.185 ± 0.015 ± 0.0009	-0.158 ± 0.013 ± 0.002	-0.132 ± 0.013 ± 0.024
Im r^{6}_{1-1}	0.017 ± 0.017 ± 0.015	0.003 ± 0.012 ± 0.012	-0.019 ± 0.014 ± 0.006	-0.010 ± 0.013 ± 0.011

Table D.10: The 15 unpolarised SDME for different bins in Q^2 for the 1996-2000 incoherent deuterium data sample. The first errors are statistical the second systematic.

Element	$< Q^2 > = 1.68$ GeV^2
r^{04}_{00}	0.457 ± 0.022 ± 0.048
Re r^{04}_{10}	0.063 ± 0.009 ± 0.021
r^{04}_{1-1}	-0.029 ± 0.012 ± 0.024
r^{1}_{11}	-0.051 ± 0.018 ± 0.046
r^{1}_{00}	-0.007 ± 0.048 ± 0.072
Re r^{1}_{10}	-0.064 ± 0.016 ± 0.026
r^{1}_{1-1}	0.200 ± 0.022 ± 0.016
Im r^{2}_{10}	0.047 ± 0.016 ± 0.008
Im r^{2}_{1-1}	-0.205 ± 0.024 ± 0.018
r^{5}_{11}	-0.015 ± 0.008 ± 0.013
r^{5}_{00}	0.191 ± 0.025 ± 0.049
Re r^{5}_{10}	0.171 ± 0.009 ± 0.014
r^{5}_{1-1}	0.009 ± 0.009 ± 0.003
Im r^{6}_{10}	-0.151 ± 0.008 ± 0.001
Im r^{6}_{1-1}	-0.005 ± 0.009 ± 0.016
Im r^{3}_{10}	-0.017 ± 0.028 ± 0.005
Im r^{3}_{1-1}	-0.047 ± 0.038 ± 0.084
Im r^{7}_{10}	0.074 ± 0.039 ± 0.027
Im r^{7}_{1-1}	-0.068 ± 0.059 ± 0.077
r^{8}_{11}	0.047 ± 0.046 ± 0.097
r^{8}_{00}	0.137 ± 0.098 ± 0.054
Re r^{8}_{10}	0.060 ± 0.033 ± 0.029
r^{8}_{1-1}	0.011 ± 0.054 ± 0.104

Table D.11: The 23 ρ^0 spin density matrix elements for the 1996-2000 'incoherent' hydrogen data sample. The first errors are statistical, the second are systematic.

Element	$< Q^2 > = 0.87$ GeV^2	$< Q^2 > = 1.19$ GeV^2	$< Q^2 > = 1.66$ GeV^2	$< Q^2 > = 2.88$ GeV^2
r^{04}_{00}	0.373 ± 0.049 ± 0.008	0.379 ± 0.038 ± 0.031	0.439 ± 0.039 ± 0.032	0.507 ± 0.032 ± 0.042
Re r^{04}_{10}	0.034 ± 0.024 ± 0.029	0.051 ± 0.019 ± 0.008	0.076 ± 0.017 ± 0.009	0.052 ± 0.014 ± 0.013
r^{04}_{1-1}	-0.064 ± 0.029 ± 0.027	-0.069 ± 0.022 ± 0.013	-0.073 ± 0.019 ± 0.035	0.003 ± 0.020 ± 0.016
r^{1}_{11}	-0.068 ± 0.036 ± 0.069	-0.095 ± 0.023 ± 0.013	-0.046 ± 0.032 ± 0.044	-0.021 ± 0.027 ± 0.067
r^{1}_{00}	0.010 ± 0.102 ± 0.008	0.083 ± 0.074 ± 0.141	-0.054 ± 0.074 ± 0.028	-0.063 ± 0.085 ± 0.088
Re r^{1}_{10}	-0.021 ± 0.040 ± 0.082	-0.060 ± 0.029 ± 0.015	-0.105 ± 0.026 ± 0.007	-0.035 ± 0.028 ± 0.079
r^{1}_{1-1}	0.307 ± 0.039 ± 0.056	0.247 ± 0.029 ± 0.009	0.204 ± 0.041 ± 0.063	0.158 ± 0.039 ± 0.004
Im r^{2}_{10}	0.049 ± 0.038 ± 0.004	0.075 ± 0.029 ± 0.024	0.110 ± 0.029 ± 0.062	0.021 ± 0.029 ± 0.010
Im r^{2}_{1-1}	-0.267 ± 0.046 ± 0.023	-0.246 ± 0.035 ± 0.016	-0.203 ± 0.042 ± 0.054	-0.139 ± 0.039 ± 0.010
r^{5}_{11}	-0.018 ± 0.017 ± 0.011	0.001 ± 0.010 ± 0.016	-0.007 ± 0.014 ± 0.016	-0.006 ± 0.012 ± 0.013
r^{5}_{00}	0.138 ± 0.058 ± 0.026	0.097 ± 0.049 ± 0.052	0.156 ± 0.036 ± 0.029	0.193 ± 0.034 ± 0.038
Re r^{5}_{10}	0.152 ± 0.028 ± 0.037	0.188 ± 0.018 ± 0.011	0.164 ± 0.014 ± 0.024	0.141 ± 0.015 ± 0.029
r^{5}_{1-1}	-0.016 ± 0.023 ± 0.003	0.004 ± 0.012 ± 0.009	-0.016 ± 0.015 ± 0.041	0.033 ± 0.016 ± 0.008
Im r^{6}_{10}	-0.166 ± 0.028 ± 0.004	-0.179 ± 0.017 ± 0.019	-0.151 ± 0.016 ± 0.037	-0.140 ± 0.012 ± 0.016
Im r^{6}_{1-1}	0.006 ± 0.021 ± 0.004	0.025 ± 0.015 ± 0.024	-0.004 ± 0.015 ± 0.033	-0.016 ± 0.015 ± 0.028

Table D.12: The 15 unpolarised SDME for different bins in Q^2 for the 1996-2000 'incoherent' hydrogen data sample. The first errors are statistical the second systematic.

	$< Q^2 >$=0.83 GeV^2	$< Q^2 >$=1.20 GeV^2	$< Q^2 >$=1.80 GeV^2	$< Q^2 >$=3.30 GeV^2
R_{ρ^0}	0.59±0.09±0.12	0.81±0.15±0.12	1.00±0.12±0.18	1.49±0.22±0.32

Table D.13: The results of R_{ρ^0} of Michael Tytgat [84]. The first errors are statistical the second systematic.

	$< Q^2 >$=0.86 GeV^2	$< Q^2 >$=1.19 GeV^2	$< Q^2 >$=1.66 GeV^2	$< Q^2 >$=2.83 GeV^2
R_{ρ^0}	0.767±0.131±0.193	0.818±0.108±0.080	0.974±0.126±0.111	1.352±0.143±0.171
	$< \epsilon >$ = 0.793	$< \epsilon >$ = 0.830	$< \epsilon >$ = 0.818	$< \epsilon >$ = 0.790

Table D.14: The results of R_{ρ^0} for 1996-97 hydrogen. The first errors are statistical the second systematic.

	$< Q^2 >$=0.86 GeV^2	$< Q^2 >$=1.19 GeV^2	$< Q^2 >$=1.66 GeV^2	$< Q^2 >$=2.87 GeV^2
R_{ρ^0}	0.768±0.122±0.028	0.711±0.070±0.070	0.958±0.111±0.184	1.124±0.099±0.141
	$< \epsilon >$ = 0.792	$< \epsilon >$ = 0.828	$< \epsilon >$ = 0.821	$< \epsilon >$ = 0.790

Table D.15: The results of R_{ρ^0} for 1998-00 hydrogen. The first errors are statistical the second systematic.

	$< Q^2 >$=0.86 GeV^2	$< Q^2 >$=1.19 GeV^2	$< Q^2 >$=1.66 GeV^2	$< Q^2 >$=2.85 GeV^2
R_{ρ^0}	0.770±0.087±0.109	0.773±0.069±0.082	1.001±0.085±0.184	1.249±0.090±0.178
	$< \epsilon >$ = 0.793	$< \epsilon >$ = 0.829	$< \epsilon >$ = 0.820	$< \epsilon >$ = 0.790

Table D.16: The results of R_{ρ^0} for 1996-00 hydrogen. The first errors are statistical the second systematic.

	$< Q^2 >$=0.86 GeV^2	$< Q^2 >$=1.18 GeV^2	$< Q^2 >$=1.66 GeV^2	$< Q^2 >$=2.85 GeV^2
R_{ρ^0}	0.743±0.059±0.107	0.814±0.052±0.078	1.007±0.067±0.143	1.046±0.055±0.138
	$< \epsilon >$ = 0.792	$< \epsilon >$ = 0.831	$< \epsilon >$ = 0.822	$< \epsilon >$ = 0.787

Table D.17: The results of R_{ρ^0} for 1996-00 deuterium. The first errors are statistical the second systematic.

	$< Q^2 >$=0.87 GeV^2	$< Q^2 >$=1.19 GeV^2	$< Q^2 >$=1.66 GeV^2	$< Q^2 >$=2.88 GeV^2
R_{ρ^0}	0.669±0.117±0.158	0.752±0.086±0.116	0.816±0.089±0.126	1.063±0.083±0.158
	$< \epsilon >$ = 0.794	$< \epsilon >$ = 0.833	$< \epsilon >$ = 0.822	$< \epsilon >$ = 0.787

Table D.18: The results of R_{ρ^0} for 1996-00 incoherent deuterium. The first errors are statistical the second systematic.

	$< Q^2 >$=0.87 GeV^2	$< Q^2 >$=1.19 GeV^2	$< Q^2 >$=1.66 GeV^2	$< Q^2 >$=2.88 GeV^2
R_{ρ^0}	0.751±0.125±0.021	0.737±0.100±0.081	0.959±0.125±0.104	1.303±0.132±0.176
	$< \epsilon >$ = 0.791	$< \epsilon >$ = 0.829	$< \epsilon >$ = 0.818	$< \epsilon >$ = 0.789

Table D.19: The results of R_{ρ^0} for 1996-00 'incoherent' hydrogen. The first errors are statistical the second systematic.

Bibliography

[1] A. Sokolov and I. Ternov , *Sov. Phys. Doklady* 8 , (1964) 1203

[2] W. Lorenzon, *Beam Polarimetry at HERA* , 7th International Workshop on Polarised Gas Targets and Polarised Beams, Urbana-Champaign (1997)

[3] M. Dueren, *The HERMES Experiment: From the design to the first results* , Habilitationsschrift, Universitaet Erlangen-Nuernberg , DESY-HERMES 95-02 (1995)

[4] M. Beckmann *et. al.*, *The Longitudinal Polarimeter at HERA* , Submitted to Nucl. Intrument. Meth. *A*. (2000)

[5] J. Stewart, *The HERMES Polarised Hydrogen Internal Gas Target* , Proc. of the 7th Inernational Workshop on Polarised Gas Targets and Polarised Beams, Urbana-Champaign, USA, August 18-22, 1997, p69

[6] B. Braun, *Spin Relaxation of Hydrogen and Deuterium in Storage Cells* , PhD. Thesis, Ludwig-Maximilians-Universitaet Muenchen (1995)

[7] C. Baumgarten, *The HERMES Internal Polarised Hydrogen and Deuterium Targets* , The 13th International Symposium on High Energy Spin Physics, Protvino, Russia, 1998

[8] K. Ackerstaff *et. al.* (HERMES Collaboration), *Nucl. Instr. Meth.* A417 , (1998) 230

[9] W.R Leo, *Techniques for Nuclear and Particle Physics Experiments* , 2nd Edition Springer-Verlag (1994)

[10] The HERMES Collaboration , *Technical Design Report* , (1993)

[11] D. De Schepper *et. al.*, *The HERMES Cerenkov Detector* , HERMES Internal Note 00-021

[12] X. Artu, G.B. Yodh and G. Mennessier, *Practical Theory of Multi-Layered Transition Radiation Detector* , Phys. Rev.D12 (1975) 1289

[13] R. Kaiser, *Measurement of the Spin Structure of the Neutron using Polarised Deep Inelastic Scattering* , PhD Thesis, Simon Fraser University (1997)

[14] A. Fantoni, *Constrzione del calorimetro a contatori di vetro al piombo dell'esperimento HERMES per la misura delle funzioni di struttura di spin dei nucleoni* , PhD. Thesis, Universita degli Studi della Calabria (1996)

[15] T. Benisch, *Polarisierte Bhabha-Streuung und Luminositaetsmessung im HERMES Experiment* , PhD Thesis, Friedrich-Alexander-Universitaet Erlangen-Nuernberg (1998)

[16] B.Krauss, Ein Silizium Detektor fuer das HERMES Experiment,HERMES 01-041

[17] The Tracking and Imaging Gamma Ray Experiment (TIGRE)

[18] Micron Semiconductor Ltd., Curchill Industrial Estate, Lancing, Sussex, BN15 8UN, UK

[19] M. Murray, Nils Pickert and Benedikt Zihlmann, *HERMES Recoil Detector - Delivery and testing of the 1T Super-Conducting Magnet* (2004) Prelim. Int. Report.

[20] M. Diehl *et. al.*, *Phys. Lett.* B411 193 (1997) .

[21] X. Ji, *Phys. Rev. Lett.* 78, (1997) 610

[22] X. Ji, *Phys. Rev.* D55, (1997) 7114

[23] M. Diehl, T.Gouset and B.Pire, *Exclusive Electroproduction and Off-diagonal Parton Distributions*, DESY 98-168, hep-ph/9811220

[24] J.C. Collins, L.Frankfurt and M. Strikman *Phys. Rev.* D56, (1997) 2982

[25] X. Ji, *Phys. Rev. Lett.* 78 610 (1997); *Phys. Rev.* D55 7114 (1997)

[26] A. V. Radyushkin, *Phys. Rev.* D56 5524 (1997)

[27] J. Bluemlein and D. Robaschik, *Nucl. Phys.* B581 449 (2000)

[28] A. V. Belitsky *et. al.*, *Nucl. Phys.* B593 289 (2001) ; A. V. Belitsky *et. al.*, hep-ph/0112108

[29] Frank Ellinghaus, *Beam-Charge and Beam-Spin Azimuthal Asymmetries in Deeply-Virtual Compton Scattering*, DESY Thesis 03-044

[30] A. Airapetian *et. al.*, *Phys. Rev. Lett. 87* , (2001), hep-ph/0106068

[31] Hermes Collaboration, R. Kaiser (ed.) *The* Hermes *Recoil Detector TDR*, Hermes 02-003

[32] Bernhard Krauss, *Deeply Virtual Compton Scattering and the* HERMES-*Recoil-Detector*, DESY Thesis 04-054

[33] K. Goeke *et. al* , *Prog. Part. Nucl. Phys. 47*, (2001) 401-515

[34] Particle Data Group, *Review of Particle Physics* (1998), Eur. Phys. J. C 3

[35] H. Bichsel, C. Tschalaer, *A Range-Energy table for heavy particles in Silicon* Nucl. Data **A 3** (1967) 343-360

[36] C. Grupen, *Particle Detectors*, Cambridge University Press (1996)

[37] K. Fiedler, *Nachweis von Zuschauernukleonen im HERMES-Experiment*, Ph. D. Thesis, Erlangen (2000)

[38] W. Fallot-Burghardt et al., *Helix128 -3.0 User Manual*, ASIC Labor Heidelberg, HD-ASIC-33-0697

[39] Austria Mikrosysteme International GmbH.

[40] U. Koetz, ZEUS collaboration. Privat communications

[41] M. Milite, The internal structure of charmed jets in photoproduction at HERA and test of the ZEUS MVD silicon sensor. Ph.D. Thesis, University of Hamburg, 2001

[42] U. Trunk, Development and Characterization of the Radiation tolerant HELIX128-2 Readout Chip for the HERA-B Microstrip Detectors. Ph.D. Thesis, Rupertus Carola University, Heidelberg, Germany, 2000.

[43] I.M Gregor, I. Hristova, M.Kopytin, W.Lange, M. Reinecke, J.Stewart, A.Vandenbroucke, *A Laser test-stand for the new* Hermes *Recoil Silicon Detector*, Hermes 04-016

[44] M. Kopytin, I.M Gregor, W.Lange, W.-D Nowak, M. Reinecke, J.Stewart, A.Vandenbroucke, *HELIX128-3.0 Production Tests*, HERMES 05-002

[45] private communication with N. Meyners

[46] E. Switzer *Measurements of Electron Energy Deposition in the Hermes Silicon Recoil Detector (1 GeV-6 GeV)* DESY-Zeuthen Summer Program 2002

[47] J.J. Velthuis, *Results of ^{60}Co irradiation of the ZEUS-MVD frontend chips, the HELIX 3.0* ZEUS-Note 02-005, March 8 2002

[48] M. Morrissey, *SEQSI*, July 17 1996

[49] Technical Information Manual, *Mod. V550 CAEN*, June 2000

[50] M.Kopytin, W.Lange, C.Shearer, J.Stewart, A.Vandenbroucke, *Decision on the read-out chip for the new* HERMES *Silicon Recoil Detector*, HERMES 02-020

[51] J.J.M.Steijger, *The Hermes silicon project*, Nucl.Inst.Meth.A447 (2000) 55-60

[52] I. Hristova, M.J Murray, I.M Gregor, W.-D Nowak, M. Reinecke, J.Stewart, A.Vandenbroucke, HERMES *Recoil Silicon Detector Calibration to MIPs at T22 at DESY*, HERMES 05-014

[53] Slava Balashov, Bernhard Krauss, Nils Pickert, Klaus Rith, Friedrich Stinzing, Christian Vogel, *Energy Calibration of the Silicon Modules for the Recoil Detector with the Tandem Facility*, HERMES 05-020

[54] I.M Gregor, I. Hristova, M. Kopytin, W. Lange, M. Reinecke, J.Stewart, A.Vandenbroucke, *Helix128-3.0 Parameter Test for the* HERMES *Silicon Recoil Detector*, HERMES Preliminary Report, 2004

[55] private communication with MICRON Semiconductors Ltd. 2002

[56] A.Osborne, *Track Reconstruction for the* HERMES *Recoil Detector*, first Year PhD Report, University of Glasgow , August 2003

[57] D.Heesbeen, *Software for the Lambda Wheel* Internal Note.

[58] Private Communications, Maurice Bouwhuis

[59] Private Communications, Andreas Reischl

[60] CERN, *ADAMO Users manual*

[61] B.Krauss, *Optimisation of the Flex-Foil Layering for the* HERMES *Recoil Detector*, August 2003

[62] Private Communications, Mathias Reinecke

[63] I.M.Gregor, M.Kopytin, W.Lange, M.Reinecke, C.Shearer, J.Stewart, A.Vandenbroucke, *Test Beam results of the First Prototype for the* HERMES *Silicon Recoil Detector*, HERMES 02-053

[64] T.Chen, J.Stewart, C.Shearer, M.Ehrenfried, J.Volmer and E.-C.Aschenauer, *Report on the Monte Carlo Studies for a* HERMES *C3 Collimator, Draft 0.2*, HERMES 03-035

[65] Private Communications, A. Petrov

[66] Private Communications, M. Bouwhuis

[67] W.Wander, *Rekonstruktion Hochenenrgetischer Streuereignisse im* HERMES *Experiment*, HERMES Thesis 96-023

[68] B.Krauss,The Recoil Detector MC-Production Chain , February 2001, Software Report.

[69] F.L Pedrotti and L.S Pedrotti, *Introduction to Optics (2^{nd} Edition)*, Prentice-Hall 1993.

[70] Hans Guenther Dosch, Carlo Ewerz, Volker Schatz *The odderon in high Energy pp scattering*, hep-ph/0201294 (2002)

[71] A.B. Kaidalov, *Phys. Rep.* 50, (1979) 157

[72] D.H Perkins, *Introduction to High Energy Physics*, Addison- Wesley Publishing (1987)

[73] K. Goulianos, *Phys. Rep.* 101, (1983) 169

[74] P.D.B Collins, *An Intoduction to Regge Theory and High Energy Physics*, Cambridge University press (1977)

[75] V.N Bolotov et al. , *Nucl. Phys.*B73 , (1974) 365

[76] A. Donnachie and P.V Landshoff, *Phys. Lett.* B296 , (1992) 227

[77] T.H Bauer, R.D Spital, D.R Yennie and F.M Pipkin, *Rev. Mod. Phys.* 50, (1978) 261

[78] D.R Yennie, *Rev. Mod. Phys.* 47, (1975) 311

[79] J.J Sakuri, *Phys. Rev. Lett.* 22, (1969) 981

[80] C. del Papa et al, *Phys. Rev.* D19, (1979) 1303

[81] D. Schildknecht, G.A Schuler and B. Surrow *Phys. Lett.* B449, (1999) 328

[82] K. Schilling , P. Seyboth and G.Wolf *Nucl. Phys.* B15, (1970) 397

[83] K. Schilling , G.Wolf *Nucl. Phys.* B61, (1973) 381

[84] M.Tytgat, *Diffrative Production of ρ^0 and ω Vector Mesons at HERMES* , HERMES Thesis 01-014

[85] A.Donnachie and P.V Landshoff , *Phys. Lett.* B348 , (1995) 213

[86] J. Grosse-Knetter , *Measurement of Elastic ω Photoproduction at HERA* , PhD Thesis, University of Hamburg (1997)

[87] S.I. Manayenkov , *Eur. Phys. J.* C33 , (2004) 397

[88] S.J. Brodsky, L. Frankfurt, J.F. Gunion et al, *Phys. Rev.* D50 , (1994) 3134

[89] J.J Kokkedee, *The Quark Model* , Edited by W.A Benjamin (New York 1969)

[90] S.I. Manayenkov, DESY 99-016, 1999)

[91] K.G Boreskov et al, *Sov. J. Nucl. Phys.* 21 , (1975) 425

[92] K.G Boreskov et al, *Nucl. Phys.* B40 , (1972) 307

[93] K.G Boreskov et al, *Sov. J. Nucl. Phys.* 14 , (1972) 457

[94] A.D Martin et al, *Phys. Rev.*D55 , 4329 (1997);*Phys. Rev.*D62 , 014022 (2000)

[95] L. Frankfurt, W. Koepf and M. Strikman, *Phys. Rev.*D54 , (1996) 3194

[96] S.V Goloskokov and P. Kroll, hep-ph/0501242, (2005)

[97] W.Wander *Rekonstruktion hochenergetischer Steuereignisse im HERMES Experiment* , PhD Thesis , University Erlangen-Nuerenberg (1996)

[98] CERN-CN Division, *GEANT - Detector Description and Simulation Tool* , CERN Program Library Long Writeup W5013 , CERN (1993)

[99] http://www-hermes.desy.de/hmc/RhoMC

[100] M. Tygat , *Studies of the rho0 and omega Invariant mass distributions* , HERMES Internal Note 00-019

[101] T.G. O'Neill , no documentation available

[102] L.Lyons , *Statistics for Nuclear and Particle Physicists*, Cambridge University Press (1986)

[103] D.G Cassel et al , *Phys. Rev.* D24 , (1981) 2787

[104] Particle Data Group , C. Caso et al *Eur. Phys. J.* C3 , (1998) 1

[105] M.H Schmitt , PhD Thesis, Harvard University (1991)

[106] M. Kolstein , *Exclusive ρ^0 Meson Electroproduction at* HERMES , PhD Thesis, Vrije Universiteit Amsterdam (1998)

[107] HERMES g_1^n group, N. Akopov et al , *Determination of the 1995 Data Quality and the Extraction of the Spin Structure Function of the Neutron* , HERMES Internal Note 97-002

[108] Particle Data Group , K. Hagiwara et al, *Phys. Rev. D* 33 , 010001 (2002) and 2003 partial update for edition 2004

[109] P.Kitching and E.Kotik, *Determination of the ρ^0 Spin Density Matrix Elements from 1996 and 1997 H1 data* , Internal Report 00-048
G.Kotik, *Production and decay of Diffractive ρ^0 Mesons at HERMES* , HERMES Thesis 01-011

[110] G.Zech, *Comparing Statistical Data to Monte Carlo Simulation - Parameter Fitting and Unfolding*, DESY-Report 95-115

[111] CERN-CN Division, *MINUIT - Function Minimization and Error Analysis* , CERN Program Library Long Writeup, D506 CERN (1992)

[112] I. Akushevich and P. Kuzhir , *Phys. Lett.* B474 , (2000) 411

[113] R.Fabbri, *Hard Exclusive Electroproduction of Two Pions at HERMES* , DESY-Thesis 03-036

[114] J. Breitweg et. al. , *Eur. Phys. J.* C12 , (2000) 393 ; *Eur. Phys. J.* C6 , (1999) 603

[115] E. V. Kuraev, N. N Nikolaev and B. G. Zakharov , *JETP Lett.* 68 , (1998) 696

[116] I.P Ivanov, N.N Nikolaev and A.A Savin , *Diffractive Vector Meson Production at HERA: From Soft to Hard QCD* , DESY 04-243 (2004)

[117] C. Aldoff et al , *Eur. Phys. J* C13 , (2000) 371

[118] V. Eckardt et al , *Nucl. Phys.* B55 , (1973) 45

[119] P. Joos et al , *Nucl. Phys.* B113 , (1976) 53

[120] J.T. Dakin et al , *Phys. Rev.* D8 , (1973) 687

[121] J. Ballam et al , *Phys. Rev.* D10 , (1974) 765

[122] M.R. Adams et al , *Z. Phys.* C74 , (1997) 237

[123] P. Amaudruz et al , *Z. Phys.* C54 , (1992) 239 ; M. Arneodo et al, *Nucl. Phys.* B429, (1994) 503

[124] J.J. Aubert et al , *Phys. Lett.* B161 , (1985) 203

[125] W.R. Francis et al , *Phys. Rev. Lett.* 38 , (1977) 633; W.D. Shambroom et al, *Phys. Rev.* D26 , (1982) 1

[126] I.P Ivanov and N.N Nikolaev , *JETP Lett.* 69 , (1999) 294

[127] I.P. Ivanov , private communications, September 2004, June 2005

[128] S.V Goloskokov , private communications, September 2004

[129] S.I Manayenkov , private communications, December 2004

Acknowledgements

During the course of my PhD many people have contributed both directly and indirectly to my research and my approach to it. Here I take the opportunity to express my thanks and gratitude for their time, opinions and guidance.

During my PhD I worked on three distinct areas of research; hardware related work, software development and last of all my physics analysis. I will present my thanks in that order and for those who contributed in all three areas I will thank afterwards.

For the hardware work which I undertook I would like to thank Jim Stewart for his guidance and time especially in the initial stages of my PhD. Ingrid-Maria Gregor also deserves thanks for her kindness, time and patience. The students I worked with also deserve thanks, Mikhail Kopytin, Ivana Hristova, Arne Vandenbroucke. I thank Misha for an enjoyable work partner during the hardest days of my PhD, his help made the work seem less painful. Thanks also go to Herr. Botschik and Herr. Kretschmer for their patience and sharing of their work space during the initial testing of the HELIX128-3.0 chip. There are also those at ZEUS who I would like to thank for their help during the testbeam setup and work which we carried out. Thanks go to Uli Koetz for his kindness and support for our work in the testbeam area, also Nabile Goudbane deserves my thanks. On the technical side I would like to thank Wolfgang Lange, Mathias Reinecke and Scott Lumsden for their technical expertise and experience with regard to the electronics and their patience and understanding when dealing with a non-hardware person.

The second stage of my research involved the integration of the Recoil Detector into the HERMES Monte Carlo. In the course of this work many people had input and offered help and suggestions. The person without whom I would not have been anything approaching successful was Maurice Bouwhuis. His constant readiness to help and sit to read through my code was much appreciated and he deserves special mention here. Thanks also go to Bernhard Krauss for his help and readiness to assist even when he was working on other topics. Others who deserve thanks are Andreas Reischl, Benedikt Zihlmann, Jo Seele, Wolfgang Sommer and Ulrike Elschenbroich. Thanks also go to Bjoern Seitz for his advice and time spent helping me with the various problems that appeared during the course of my work. I would also like to thank Larry Felawka and Alexander Kissalev for their expertise and time spent answering the various questions that I had during my time at DESY.

The last stage of my research was focused on my physics analysis. Here thanks go to Moskov Amarian and Delia Hasch for their help and advice offered with regard to my analysis, in their roles as analysis coordinator. Thanks go to Bohdan Marianski with whom I worked with closely on the physics analysis for his friendly approach and hard work. Thanks also go to Alexander Borissov. Thanks go to Matthias Hartig who implemented the ρMC generator into GMC which we used to produce our Monte Carlo input files for the fitting program. Thanks also go to Elke-Caroline Aschenauer, Ami Rostoman and Delia Hasch for their comments and suggestions for how we should approach the analysis and for giving a different point of view and welcome advice. Thanks also go to Riccardo Fabbri for his advice and time regarding the approach to the determination of the DIS background

contribution. Thanks go to I.P. Ivanov, S.V Goloskokov and S.I Manaenkov for their theory calculations and advice offered on our analysis and results. The time taken to produce these calculations was much appreciated and here I take the time to thank them for their work. Above all however, I would like to thank Michael Tytgat, upon whose initial analysis my analysis and approach was based. His help, advice and constant readiness to assist when asked was very much appreciated and for this reason he deserves special acknowledgement and thanks.

In this section of my thesis I would like to thank those who had a global affect on my PhD. First of all thanks go to Prof. Guenther Rosner for giving me the opportunity to undertake a PhD in the nuclear physics group at the University of Glasgow. Thanks go to my supervisor and mentor Ralf Kaiser who always made the time to ensure that I stayed focused and on track even when he had greater responsibilities of his own running in parallel. The possibility to live in Hamburg and the challenges that that entailed were much appreciated and the freedom to choose the path my PhD took was also appreciated.

A special thanks goes to James Stewart, without whose help and time I feel my PhD would have faltered and stumbled in the early stages. His constant willingness to offer help and advice and to spend time making sure I was pushing my goals so that I made real progress was very much appreciated. For his help, time and patience I am in his debt.

Elke-Caroline Aschenauer deserves a mention in this section due to the help and advice and constant willingness to offer suggestions and opinions. Her help helped me throughout my PhD but especially in the physics analysis part of my research, where her opinions were highly valued.

Although already mentioned, Michael Tytgat deserves to be noted in this section and is singled out for special thanks. I would like to express my gratitude and thanks to Michael for his help and time spent with regard to the physics analysis. Without his help I feel that my analysis would not have reached the stage that it did and that the final one and half years of my PhD would have been extremely uncomfortable. For his help, time and patience I am most grateful.

There are many people at HERMES and DESY I have had contact with and if I have forgotten anyone then I apologise here. I would like to thank the HERMES collaboration as a whole. Without their collective contribution the work presented in this thesis would not have been possible.

I would also like to thank all those people from the Glasgow Nuclear Physics group. My time spent in Glasgow was limited but Glasgow always felt like a safe harbour for me and it was always nice to return to the department after a hard working trip in DESY.

Special thanks go to my parents and my younger brother for their constant support and understanding during my periods of research both away and at home. I would also like to thank all those who have had direct and indirect influence on my choice to pursue a PhD in physics. It has been a long road but with the sentence it comes to an end.

Declaration of Independent Research

I hereby declare that the work presented in this thesis is my own and that the research and physics analysis presented is original and independent except in those areas where research was done in collaboration with others as detailed below.

Signed:

Here I present an overview of the research activities I was involved with over the period of my PhD research. I explain below which tasks I worked on alone and those which were done in collaboration with others.

During my time spent working at HERMES at DESY Hamburg in Germany I worked for the Recoil Project. I worked both on hardware and software topics during my research. I then moved over to a vector meson analysis for the final part of my research.

The HELIX128-3.0 Readout Chip

- I carried out research on the HELIX128-3.0 readout chip for the silicon detector which is one of the Recoil Detectors subdetectors.
- The possibility to extend the dynamic range of the HELIX chip was studied in both a charge injection setup in the laboratory and also in the test beam setup at T22 in DESY, Hamburg.
- I worked on both of these tasks with other students from DESY, Zeuthen to present conclusions on both the choice of the final readout chip and also on the work done in the test beam setup.

The internal reports and papers I am co-author of are:

- M.Kopytin, W.Lange, C.Shearer, J.Stewart, A.Vandenbroucke, *Decision on the readout chip for the new* Hermes *Silicon Recoil Detector*, Hermes 02-020
- I.M.Gregor, M.Kopytin, W.Lange, M.Reinecke, C.Shearer, J.Stewart, A.Vandenbroucke, *Test Beam results of the First Prototype for the* Hermes *Silicon Recoil Detector*, Hermes 02-053

- I.M.Gregor, I. Hristova, M.Kopytin, W.Lange, M.Reinecke, C.Shearer, J.Stewart, A.Vandenbroucke, *Study of the First Prototype for the* HERMES *Silicon Recoil Detector with the ZEUS Beam Telescope*, HERMES 04-019

- M. Reinecke et al, *A Silicon Strip Recoil Detector for Momentum Measurement and Tracking at HERMES*, IEEE Trans. Nucl. Sci., Vol. 51, pp. 1111-1116, June 2004

The chapter in which my work is presented in my Thesis is in Chapter 4. Chapter 4.3 describes the charge injection research and Chapter 4.4 the test beam overview.

Recoil Detector Monte Carlo

- I worked for the main part of my non-analysis research time on the development and implementation of the Recoil Detector into the standard Hermes Monte Carlo (HMC) software scheme.

- My main job was to implement the necessary programs and tools for the silicon detector. I was solely responsible for this task and worked independently.

- I also produced a cosmic event generator which was used in code development for both my own and other tracking routines.

- I was also the code keeper for the Recoil Monte Carlo and was responsible for implementing the other subdetectors, coded by the other subgroups, into the Recoil Monte Carlo.

- I also had the task of porting over a stand alone version of a previous tracking code from Fortran into C and for making it compatible with the Hermes software scheme. I then worked on reproducing plots made in the Technical Design Report using the Recoil Monte Carlo.

The internal reports I am co-author of are:

- C. Shearer, *Implementation of the Recoil Detector into the* HERMES *Monte Carlo simulation.*, HERMES 04-007

- T.Chen, J.Stewart, C.Shearer, M.Ehrenfried, J.Volmer and E.-C.Aschenauer, *Report on the Monte Carlo Studies for a* HERMES *C3 Collimator, Draft 0.2*, HERMES 03-035

The chapter in which my work is presented in my Thesis is in Chapter 5. Chapter 5.1 presents the work done on the cosmic generator. Chapter 5.2 explains the research carried out to implement the Recoil Detector into the Monte Carlo. Chapter 5.3 presents the integration of the independent tracking code into the Recoil Monte Carlo scheme and a presentation of the kinematical plots is given.

Spin Density Matrix Element Extraction Analysis

- My analysis topic involved me working with the vector meson analysis group, which consisted of one other researcher, Bohdan Marianski and a subgroup coordinator, Alexander Borissov.

- My work involved using a previous analysis (Michael Tytgat) as a template to attempt to reproduce his results on the 1996/97 hydrogen data sample. Once this was achieved the work was extended to include the entire data sample for 1996-2000 for both the hydrogen and deuterium data samples.

- The majority of my work was carried out independently at DESY until the results became stable and well understood. Once this was achieved I worked in close collaboration with Bohdan Marianski for around 2 months to present our results for an attempted release.

- For the attempted release I produced both the release report and the results used in all of the plots independently. Bohdan produced all of the comparison plots which were presented in the final report and worked in close collaboration on the presentation.

The release report I am author of is:

- C. Shearer, B. Marianski, A. Borssov, *Spin Density Matrix Element Extraction from Hydrogen and Deuterium Targets*, HERMES Release Meeting, DESY Hamburg, 21^{st} February 2005.

The chapter in which the results of my analysis work is presented in my Thesis is in Chapter 8. The chapter presents each of the data subsets both separately and then combined for both the hydrogen and deuterium targets.